MECHANICAL BEHAVIOR AND CHARACTERIZATION OF SLS PROCESSED PA-11 FOR PA-11/SILICA NANOCOMPOSITES

by

Gabrielle Esposito

A Dissertation

Presented to the Graduate and Research Committee

of Lehigh University

in Candidacy for the Degree of

Doctor of Philosophy

in

Polymer Science & Engineering

Lehigh University

January 2020

CERTIFICATE OF APPROVAL

Approved and recommended for acceptance as a dissertation in partial fulfillment of the requirements for the degree of Doctor of Philosophy.

Gabrielle Esposito

Mechanical Behavior and Characterization of SLS Processed PA-11 for PA-11/Silica Nanocomposites

_____

Date

_____

Accepted Date

Dissertation Director:

_____
Professor Raymond A. Pearson
Lehigh University
Advisor & Chairperson

Committee Members:

_____
Professor John Coulter
Lehigh University

_____
Professor Lesley Chow
Lehigh University

_____
Dr. Binay Patel
Zzyzx Polymers
Research Scientist

ACKNOWLEDGEMENTS

I would like to thank my advisor, Professor Raymond Pearson, for all of your support, advice, patience and humor throughout my graduate studies. I greatly appreciate the opportunity you have given me toto be a part of your research group, and the time you have invested into my development as a researcher.

Thank you to Professor John Coulter, Professor Lesley Chow and Dr. Binay Patel for all of the advice and support you have given me during my doctoral research.

Special thanks to all of the Whitaker staff -- Mike Rex, Janie Carlin, Katrina Kraft, Lisa Arechiga, William Mushock, Dr. Robert Keyse and Dr. Laura Moyer – for all of your support during my graduate studies.

Thank you to all the past and present members of Professor Pearson's research group, especially our group sprit guide Stephen Antalics who teaches me every day to never stop learning.

Thank you to Arkema, Cabot Corporation, Zzyzx Polymers, and the Pennsylvania Department of Community and Economic Development (PA-DCED) for providing the materials and funding for this project.

Lastly, many thanks to my family who have supported me wholeheartedly throughout my entire college career, as well as the graduate student community in the Materials Science and Engineering department. Both of you have provided great support and levity during my graduate career with your kindness and humor, which I appreciate greatly.

TABLE OF CONTENTS

LIST OF TABLES

CHAPTER 1

CHAPTER 2

CHAPTER 3

LIST OF FIGURES

CHAPTER 1

CHAPTER 2

CHAPTER 3

APPENDIX

ABSTRACT

Advances in additive manufacturing (AM) continue to promise novel solutions for modeling and use of intricately shaped designs. At the forefront is a type of AM known as selective laser sintering (SLS), in which three dimensional shapes are produced through laser sintering and resurfacing of a powder bed. While advances have been made in using SLS to create functional parts in the aerospace and automotive industries, many challenges remain in using polymers for SLS printing to create high performance parts. Specifically, effectively characterizing the polymer powder to design the best printing environment, as well as diversifying the types of polymers and polymer systems that can excel in a SLS manufacturing environment.

In this dissertation, polyamide 11/carbon black (PA11/CB) SLS printing based nanocomposite powders were characterized through the printing process, with surface treated nanosilica added as both a processing aid and toughening agent to produce high performance polymer nanocomposites. PA11/CB was initially printed at increasing laser area energy density (A_N), using differential Scanning Calorimetry (DSC), x-ray diffraction (XRD), small angle x-ray scattering (SAXS), solution viscometry, tensile testing, essential work of fracture and fractography to determine microstructural changes in PA11 during the printing process. Separate iterations of developing a PA11/CB composite powder with surface treated silica nanoparticles (SNP) were accomplished through using 50 nm SNP and solid state shear pulverization, as well as 25 nm SNP with centrifugal mixing. A powder flow test adapted from the Freeman FT4 Powder Rheometer was developed for an existing hybrid rheometer (DHR2, TA Instruments), to test powder flow of the PA11/CB/SNP powders at increasing temperature. Additionally DSC, tensile testing, compression testing, essential work of fracture, linear reciprocating wear and fractography were used to evaluate the ability of SNP to improve both the powder flow and mechanical behavior of the printed material. Each study provided good insight into the SLS printing of polymer powders.

In Chapter 2, it was observed that the T_m, X_c, l_c and d_{hkl} spacing of PA11/CB have a large change in value upon printing, whereas the molecular weight was shown to have a rather gradual increase between the PA11/CB powder and printed parts. Amongst the printed samples, elongation to break, ultimate tensile stress and essential work of fracture were shown to modestly increase with increasing A_N from A_{N7} to A_{N11}. A_{N7} samples were shown to have significant residual powder within the sample from poorly sintered layers, while subtle structural differences were seen in the A_{N8} and A_{N9} samples as evidenced by melting, polymer chain rigidity, IR and d_{hkl} changes.

In Chapter 3, PA11/CB/50nmSNP samples were shown to effectively increase high temperature powder flow at 2 wt. % and 4 wt. % loading, however poor diffusion of the SNP from the PA11/CB particle surface during the printing process lead to noticeably high volume SNP boundary layers and premature fracture. Despite poor diffusion of SNP, particle debonding was evident of the 50 nm SNP as a toughening mechanism in the PA11 matrix. PA11/CB/25nmSNP samples similarly exhibited increased powder flow at as little as 0.25 wt. % loading, with marked increased in strength and stiffness with increasing SNP. It was found that loadings greater than 0.25 wt. % lead to SNP agglomeration, resulting in sheet-like SNP layers at the fracture surface and dramatically reducing elongation to break.

The Appendix additionally summarizes a separate, independent study utilizing SNP in a polymer composite system for a direct ink writing (DIW) based additive manufacturing process. SNP was added to a diglycidyl ether of bisphenol-A (DGEBA) based epoxy, short carbon fiber (CF) and fumed silica (FS) composite system to observe the effects of SNP composite shear flow, carbon fiber orientation and composite strength.

CHAPTER 1: INTRODUCTION

1.1 Selective Laser Sintering Overview

Additive manufacturing (AM) has expanded immensely within the past few decades, referring to any process involving a "layer by layer" building up of a 3D pre-designed model. At the forefront is a type of AM known as selective laser sintering (SLS), in which three dimensional shapes are produced through laser sintering and resurfacing of a powder bed [1]. The powder bed is typically heated to a temperature close to the polymer melting temperature, and the laser energy pushes the temperature of the polymer into the melt, creating fully densified parts as they cool. The thickness of the resurfaced powder bed, and ultimately layer thickness of the part is predetermined to enhance the diffusion of material between boundary layers upon laser interaction, without degrading material in subsequent laser passes. A more descriptive model of the SLS process is shown below in Figure 1-1.

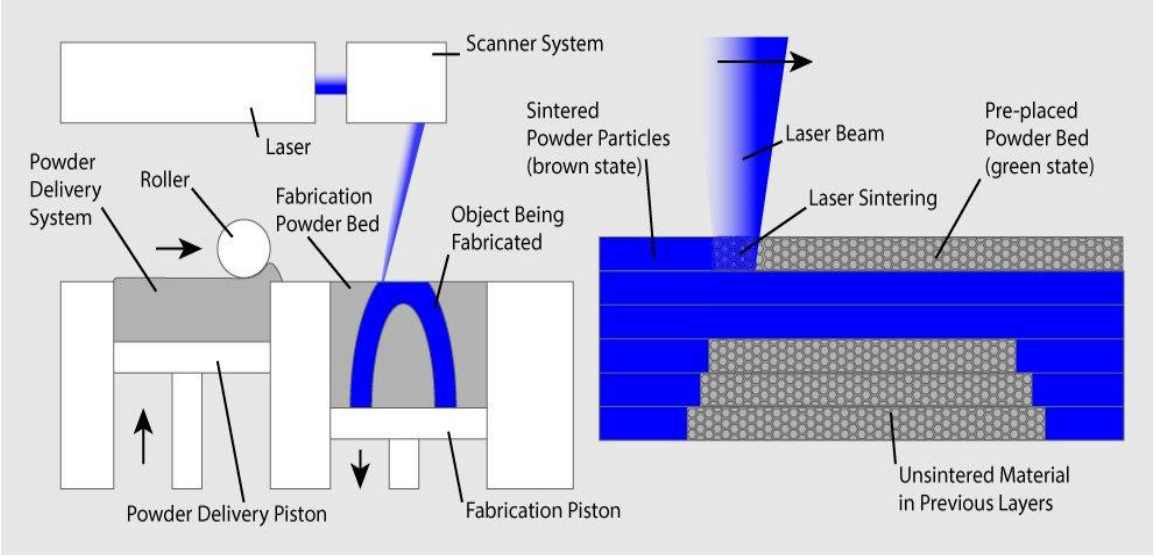

Figure 1-1: Model of the Selective Laser Sintering (SLS) process [2].

While advances have been made in using SLS to create functional parts in the aerospace and automotive industries [2], many challenges remain in using polymers for SLS printing to create high performance parts. The majority of challenges in the SLS process revolve around several powder properties, which if left unobserved and unmodified can lead to significant part distortion.

Most notably, particle size and shape distribution, as well as powder flow have an immense impact on evenly distributing layers of polymer powder and thus accurately depositing the correct layer thickness for printing. In addition to part resolution, the surface roughness of the sintered parts is highly dependent the particle size and shape distribution. Besides increased friction at the surface, a rough sintered part can also lead to unequal stress concentrations between inadequately sintered particles, necessitating a post processing polishing step for more homogenous surface properties. Residual stresses due to unequal thermal gradients and densification, as well as part porosity will also heavily depend on particle size distribution [2].

Other SLS powder parameters with immense influence over sintered part quality include material choice, aging stability and recyclability, thermal properties and sintering behavior, and laser absorption [2]. Similar to other additive manufacturing techniques, the commercial polymers available specifically for SLS printing are quite limited. The majority of these materials are semicrystalline polymers, as they provide a distinct "processing window" for efficient melting. This window is described as the range of temperatures between the crystallization and melting temperatures of the powders, with a wider window being more advantageous for flexible printing parameters [3]. While additive manufacturing in general is promising in reducing polymer waste, there remains uncertainty into how recyclable the excess powder in the print bed is after successive prints at high temperature [2]. Many commercial manufacturers of SLS powder report blends up to 30% recycled powder can be print efficiently, and it is proposed that this excess powder could be collected for alternate processing methods, such as extrusion [4].

1.2 Powder Flow Experiments for SLS Applications

Of specific recent interest has been the measurement of polymer powder flow for SLS printing. Many studies have focused on the tapped density as a quantifiable flow parameter. The tapped density is based on the concept that when a powder flows better, both adhesive and repulsive

particle interactions have reduced to diminish voids within the bulk powder matrix [5]. This reduced voiding would then lead to an increased measurable density of the powder. A commonly used parameter is known as the Hausner Ratio (HR) which compares the bulk powder density before and after physical tapping to better arrange powder particles and approach maximum packing of the material. The approximation for HR is shown below.

$$\frac{1}{\mathrm{HR}} = \frac{\rho_{\mathrm{bulk}}}{\rho_{\mathrm{tap}}} \tag{1}$$

More modern applications of the tapped density approach have been to mimic the actual layering of powder in an SLS process. Research led by Michael Van den Eynde has focused on building a custom powder spreading device that can measure the density of powder spread in an individual layer (ρ_{layer}) [6]. This measurement leads to an adapted HR, called the packing ratio (PR) which is a ratio of the ρ_{layer} to the tapped density ρ_{tap}. A model of their device is shown below in Figure 1-2.

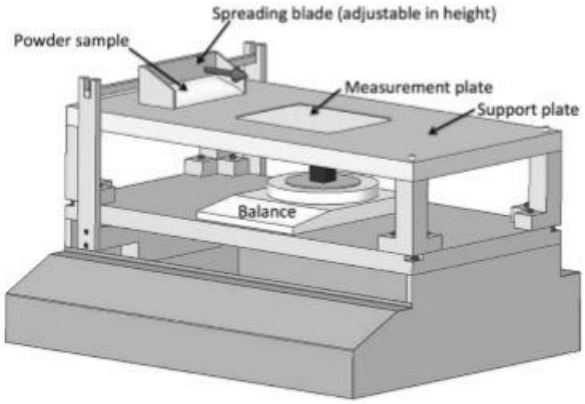

Figure 1-2: Custom powder spreading device to measure individual SLS layer density [6].

In addition to tapped density, there have been numerous other methods developed to measure and compare powder flow. Bed expansion ratio (BER) measures the change in powder bed height during and directly after fluidization of the particles with constant gas flow. This technique strives to model how powders react in a dynamic state when particles are in continuous motion and flow like a fluid [7]. Higher values of BER correlate with better powder flow, and can provide insight into possible particle agglomeration within a polymer powder system [7]. Angle of repose (AOR)

and avalanche angle measurements are two separate techniques that operate on statically or dynamically measuring the angles of bulk powders and relating these angles to powder flow. AOR is measured through passing powder through a lifted funnel, and measuring the angle the conical powder heap makes with the flat surface it was collected on. Avalanche angle measurements are taken more dynamically, and involve measuring the angle a bulk powder makes within a rotating drum prior to excess powder collapse as it reaches the top of the drum [7]. An increase in angle for both measurements correlate to decreased powder flow, as larger angles relate to higher cohesion of the particles and lower ability for individual particles to slip past each other. Lastly, rheometers have been used increasingly on powders, often using a modified concentric cylinder setup with custom spindles to apply shear to the powder system. The torque applied to the rotating blade can be related to powder flow, with increased torque relating to increased powder cohesion and decreased powder flow [7].

While there are many available powder flow measurement techniques, it is emphasized that the measurements chosen should reflect the eventual application. For SLS printing, it has been suggested both a dynamic and static powder flow experiment should be used to characterize the powder to predict performance in printed polymer parts [7, 8]. A recent study led by Stefan Ziegelmeier focused on relating both static and dynamic flow of a thermoplastic polyurethane (TPU) and Duraform Flex (DF) to the tensile behavior and Shore hardness of the printed powders. It was found that powders with higher sphericity and larger particle size had increased powder flow, as analyzed through tapping density, avalanche angle and powder rheology [8]. Of these, the tapped density was shown to have the most predictive nature for sintered mechanical behavior, relating well to the elongation at break and ultimate tensile strength [8]. Increased flow and sphericity also correlated well to decreased surface roughness and porosity in the sintered parts. Below are selected flow and mechanical behavior results from the study.

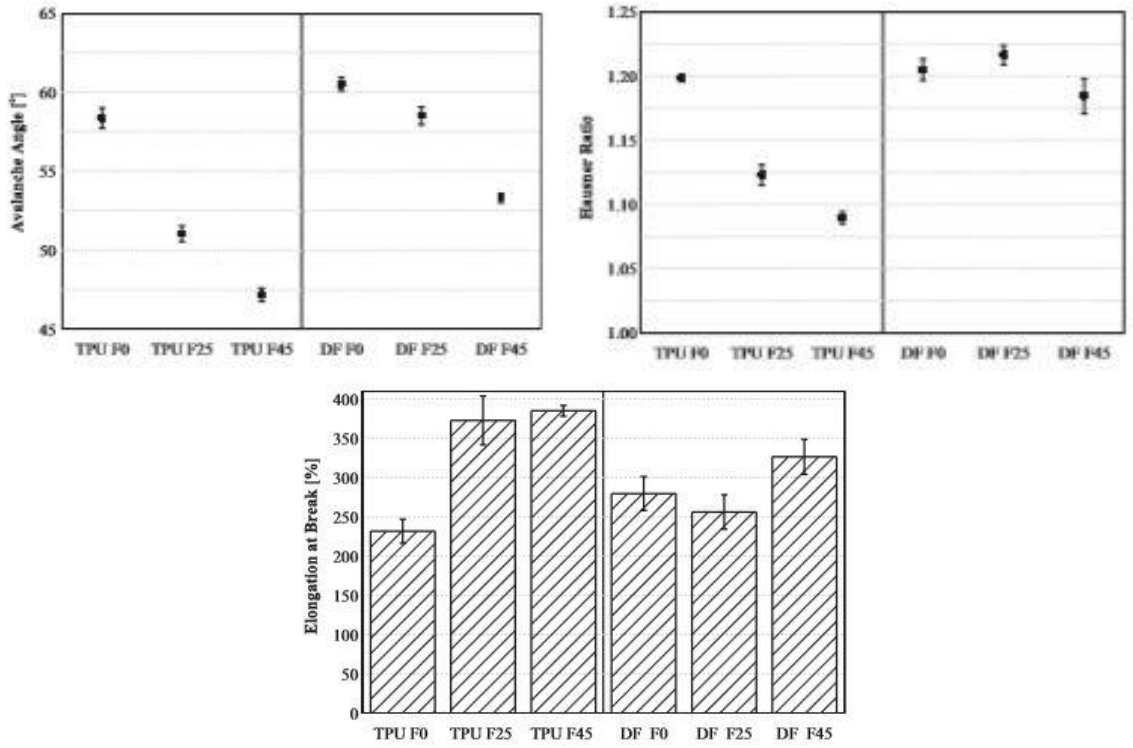

Figure 1-3: Avalanche angle, Hauser ratio and elongation at break for tested TPE and DF with increasing particle size [8].

An emerging powder flow measurement technique that has been used to measure both static and dynamic flow has been the one pioneered by the FT4 Powder Rheometer (Freeman Technology, UK) [9]. In this method, a traditionally helical impeller both rotates and compresses a powder in a cylindrical holding cell between two specified heights of the cylinder. Additionally, after the initial static or "confined" test the impeller can rotate in a tensile direction for a dynamic or "unconfined" flow measurement. Analysis of flow is based on characteristic changes in the measured torque and axial force as the impeller proceeds between the two cylindrical heights, as well as a measured flow energy (E_{flow}), as shown in the Equation below.

$$E_{flow} = \int_0^H \left(\left(\frac{T}{R \cdot \tan \alpha} \right) + F \right) dH \quad (2)$$

The T variable represents the measured torque, and the F represents the force acting at the front of the impeller. R is the radius of impeller, H the height of the cylinder and α the helix angle of the impeller [10]. While the helix is the most commonly used impeller, additional studies on rheometer

based powder flow measurements have noted success with using vane and serrated cylinder geometries [11]. In the case of alternate geometry impellers, the helix angle is calculated by the ratio of the vertical speed to the rotational velocity of the impeller. The Freeman rheology process is illustrated below in Figure 1-4.

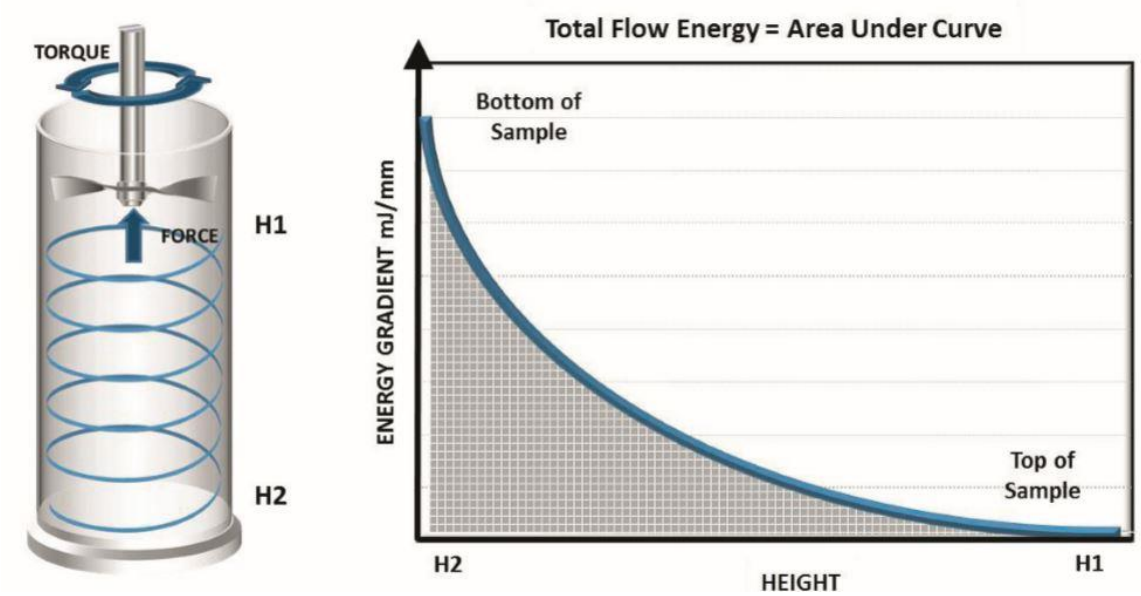

Figure 1-4: Illustration of the powder flow experiment in the Freeman method [12].

While powder flow has been shown to correlate well to sintered polymer mechanical properties, the powder flow measurements are typically performed at nominal room temperature. In actual SLS application, the powders are heated to specified bed temperature for effective sintering. Of real interest is measuring powder flow at elevated temperature to better predict the powder flow in the SLS environment. There have been preliminary results from Michael Van den Eynde's group, using a modified version of their previously shown device to measure packing ratio at higher temperatures. Measuring a polyamide 12 SLS powder, the packing ratio was calculated at room temperature (N/A), glass transition temperature (50^{o}C) and above glass transition temperature (N/A). A packing ratio of 0.87 was found at room temperature, with no noticeable change in packing ratio and layer quality at glass transition temperature [13]. Measurements were also performed above glass transition, however the exact temperature was not specified. The packing

ratio actually increased slightly, however this was attributed to the increased compressibility of the powder at higher temperature [13].

A separate study was found focusing on avalanche angle measurements for commercial SLS powders at increasing temperatures. There was a proposed limit to the testing temperatures, as temperatures above 110^{o}C as the powder would stick to the drum and prevent a clear image of the angle to be taken. In addition to avalanche angle, the surface fractal of the powder was measured, which is the fractal dimension of the powder surface [14]. This measurement relates to the roughness of the powder surface, and is measured after an avalanche to determine how the powder settles. Values closer to one relate to a more even surface, and as the surface becomes rougher the surface fractal becomes increasingly greater than one. It was found that all nine tested powders had diverse response to temperature, with some avalanche angles consistently increasing with temperature, some not changing at all, and some having an initial reduction followed by a slight increase [14]. The avalanche angle was not as sensitive to temperature variation as hypothesized, although this could be due to the linearization of the powder surface inside the drum [14]. The surface fractal seemed to have a more dramatic response with temperature variation, as it is able to capture minute changes in surface roughness and capture changes like powder agglomerates more rapidly than the avalanche angle [14]. The responses of the surface fractal were also varied, and likely dependent on other material properties like friction, modulus, and glass transition. Selected results are shown below, comparing three commercial polyamide 12 based SLS powders.

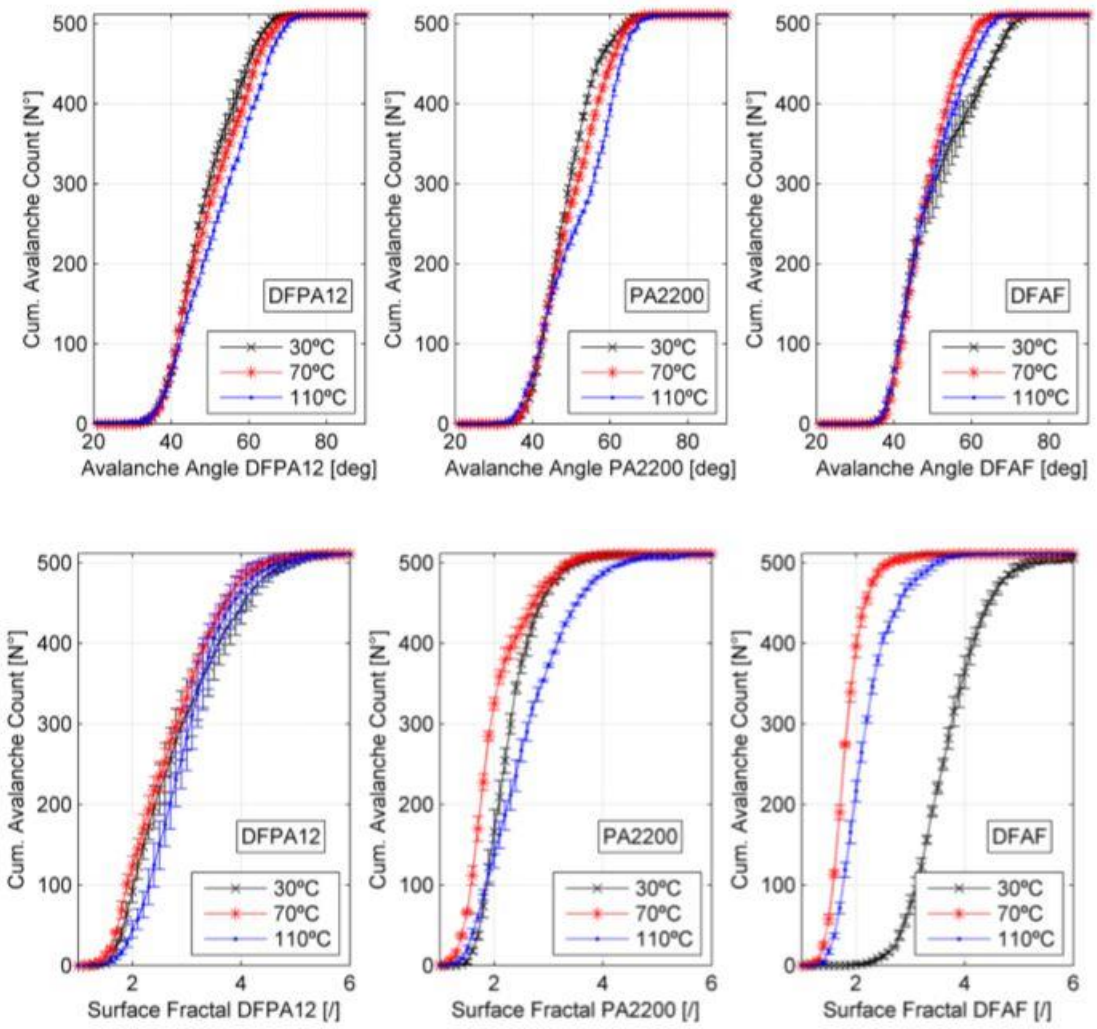

Figure 1-5: Avalanche angle and surface fractal with increasing temperature for three commercial PA12 based SLS powders.

1.3 PA11 Synthesis and Microstructure

As mentioned previously, another large constraint on the growth of SLS printing of polymers is the lack of commercial material diversity. Available polymer choices consist of the high performance PEEK and PEK, the polyamides 6, 11, and 12, thermoplastic elastomers (TPE) and commodity polymers such as polypropylene (PP) and high density polyethylene (HDPE). The most researched and referenced of these in literature is by far polyamide 12, as it was one of the earliest developed powders for the SLS process. Of increasing interest is the related polyamide 11 (PA11) as it demonstrates a unique combination of attractive potential properties. PA11 is unique among other

polyamides as it is non-petroleum sourced, specifically from castor oil. The monomer 11-aminoundecanoic acid that polymerizes to form PA11 is more accurately synthesized from recinoleic acid, which is in turn sourced from the castor oil [15]. Figure 1-6 shows the multitude of applications of the recinoleic acid, as well as steps of the full 11-aminoundecanoic acid synthesis from the castor oil source.

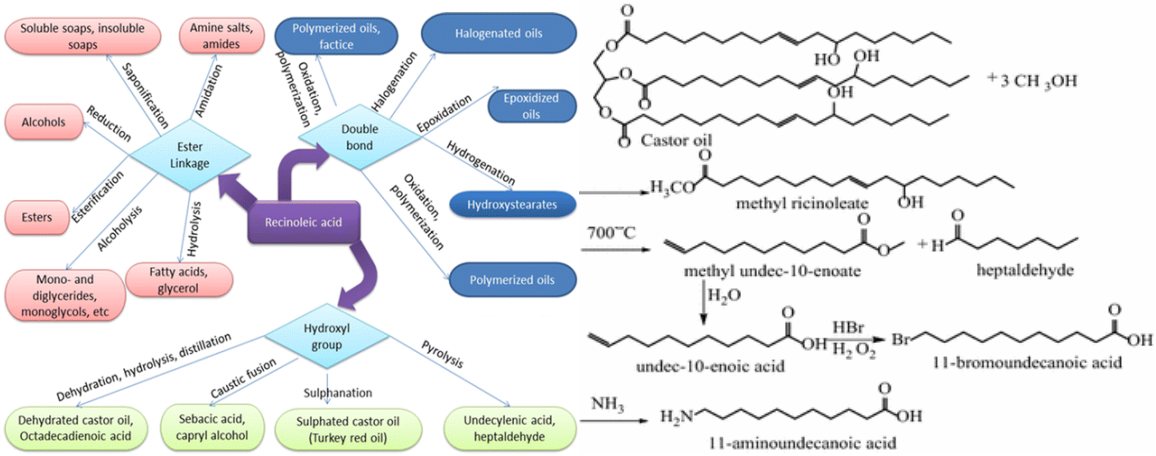

Figure 1-6: Applications of recinolecid acids, as well as the synthesis of 11-aminoundecanoic acid from methyl ricinoleate [15].

Like many polyamides, PA11 is a semicrystalline polymer, but with a hefty degree of polymorphism within the actual crystal structure of the unit cells. There have been six reported phases of PA11 with varying frequency and validation over the past few decades. The α phase is noted to be a stable triclinic phase, achieved primarily through solvent casting with *m*-cresol [16]. A stable triclinic phase with similar lattice parameters can also be achieved through slow melt crystallization, however there is debate whether this is the same α phase, or a separate α′ triclinic phase due to the difference in d_{hkl} spacing. A stable monoclinic β phase was discovered in a landmark 1981 study by casting in a formic acid/water solution, however this phase has not been readily studied and reported on since [17]. There are also three separate unstable pseudo-hexagonal phases,; γ, δ and δ′. The γ phase is typically achieved through casting in trifluoroacetic acid, the δ through heating PA11 α phase above 95°C, and the δ′ through quenching the PA11 melt rapidly

[16].The changes in crystal structure are largely driven by changes in the hydrogen bond polarization beween adjacent amide linkages in the folded polymer chain. The changes in phase have large influence on thermal and mechanical behavior, with the stable α and α′ phases having higher melting temperature, stiffness and strength [18]. Recently, the δ′ phase of PA11 has been found to have enhanced a piezoelectric response, suggesting future applications for sensors and actuators [18]. The hydrogen bond orientation as well as the triclinic cell for the α phase PA11 is shown below in Figure 1-7.

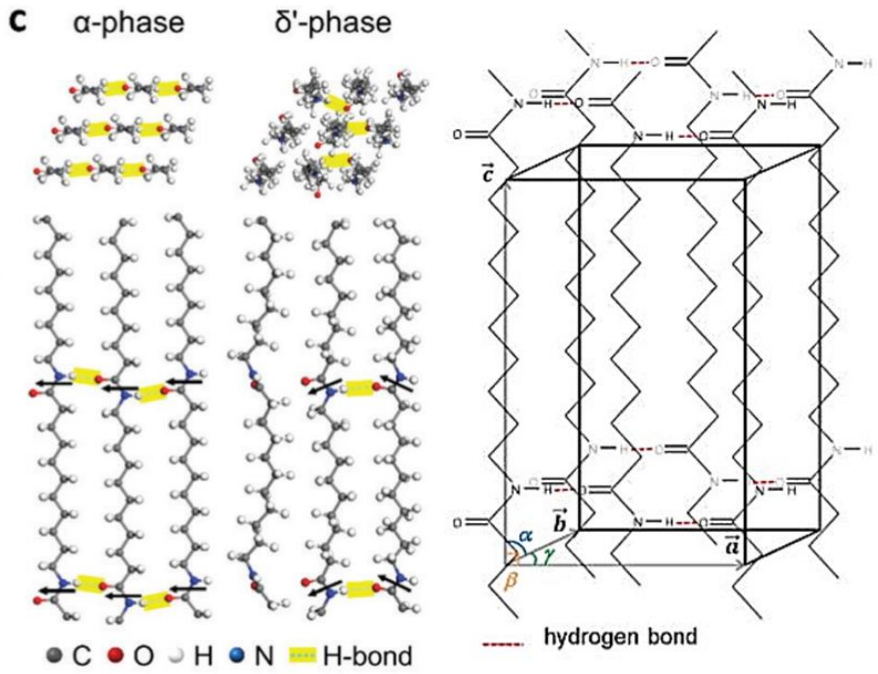

Figure 1-7: Illustration of amide hydrogen bonding and triclinic cell organization of PA11 [18].

General differences in PA11 polymer structure, as well as larger polymorphic changes in PA11 have been readily measured using X-Ray Diffraction (XRD) and Fourier Transform Infrared Sprctroscopy (FTIR). Standard XRD of an α phase PA11 reveals three peaks representing the [001], [100] and combination [110]/[010] triclinic cell faces. The [001] crystal face is representative of the linear polymer repeat unit in the direction of the polymer chain, whereas the [100] and [110]/[010] faces represent the distance between neighboring polymer chains and chain lattices, respectively [19]. Changes in $d_{[001]}$ are typically attributed to conformational changes in the 10 unit

methylene sequence upon heating and cooling, while the degree and orientation of hydrogen bonding has a large influence on both $d_{[100]}$and $d_{[110]/[010]}$ spacings, as well as Van der Waals bonding for the $d_{[110]/[010]}$ specifically [19]. Interestingly, PA11 passes a Brill transition zone when transitioning between α and δ phases, which is observed through XRD as a convergence of the [100] and [110]/[010] peaks [16]. Differences in d_{hkl} spacing and crystalline phase can also be inferred using FTIR. Particularly, changes in breadth and area in the amide A, II, V and VI bands are consistent with changes in $d_{[100]}$and $d_{[110]/[010]}$, while changes in methylene progression bands are consistent with changes in $d_{[001]}$ [19].

PA11 demonstrates other unique microstructural changes, especially in the polymerization process. Like PA12, PA11 is known to linearly post-polymerize, exacerbated by the addition of heat in a selected manufacturing process [20]. PA11 is typically a very linear polymer, however more interesting structures have been identifyed, including cyclization and star like structures. Cyclic PA11 strucures were studied using matrix-assisted laser desorption ionization (MALDI) [20]. Under heated mixing of 11-aminoundecanoic acid for 2.5 hours, the synthesized PA11 was shown to have a low molecular weight tail with peak weights correllating to cyclic oligomer structures [20]. A separate study focused on the ability of PA11 to form star stuctures in an attempt to tailor the rheological response to one that is more easily prcessible. The star shaped PA11 structures were synthesized via one-pot co-polycondensation of 11-aminoundecanoic acid with two separate multifunctional agents [21]. It was found that the branch lengths of these stars could be controlled to create both Newtonian and shear thinning rheological responses for the PA11, with the potential to tailor the rheology for specific manufacturing processes [21]. While research into these nonlinear structures is still accumulating, there appears to be great potential in exacerbating nonlinear PA11 chain structures for specific applications.

PA11 crystalline microstructure is noticeably very fine when compared to other polyamides, with spherulites consistently measured below 20 μm in diameter, and often only under 10 μm wide [22]. While crystallization is a kinetic process and largely dependent on a multitude of factors, PA11 has recently been found to have self-nucleating behavior upon repeated melting of the polymer. In other words, increased nucleation and nucleation rate due to the presence of self-seed crystal remnants [22]. Upon repeated melting and slow cooling, the spherulitic structure of PA11 will become finer without demonstrative changes to the percent crystallinity given the cooling rate is identical [22]. Such a fine spherulitic network likely leads PA11 to be so ductile, with extrusion and injection molding grades exceeding 300% strain [23,24]. Refinement of the spherulitic network upon reheating of PA11 is demonstrated below in Figure 1-8.

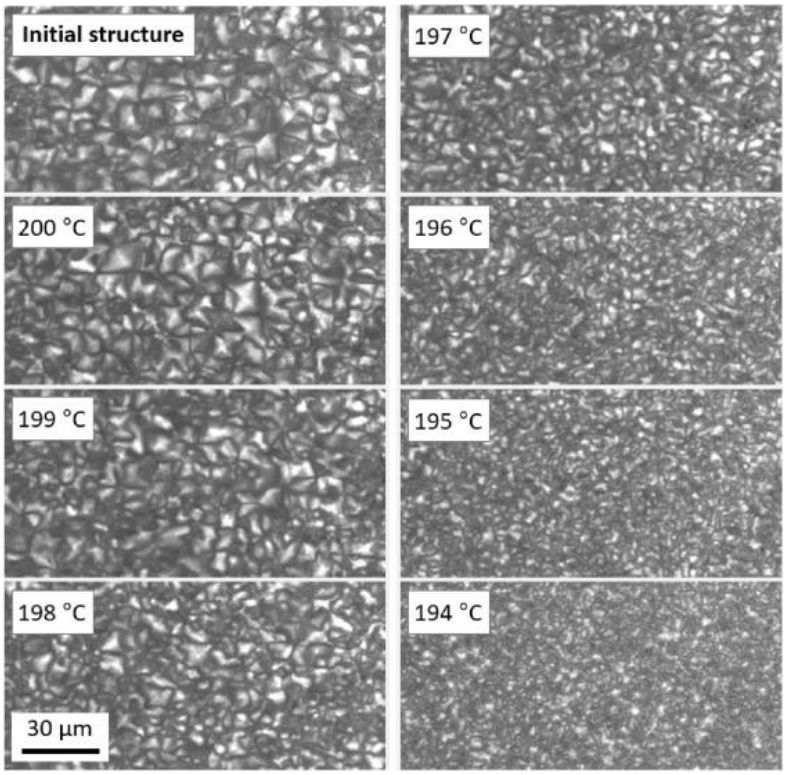

Figure 1-8: Spherulitic structure in PA11 revealing self-nucleating behavior as a refinement of spherulite size is visible upon remelting the polymer at different temperatures [22].

In addition to the crystalline and amorphous sections in a standard semicrystalline polymer, PA11 is also known to comprise of transitional chain rigidity between the two microstructures,

characterized by the rigid amorphous phase (RAP). Polyamides particularly have shown great sensitivity to cooling rates and their effect on the overall RAP. Interestingly, polyamides characteristically will show increased amount of RAP when cooled at a higher rate, contrasting with the majority of thermoplastic polymers that will increase in the mobile amorphous phase (MAP) with faster cooling rates [25,26]. This rigidity is associated with immediate antiparallel hydrogen bonding of the amide groups upon fast cooling of the polymer [26].

As compared to other polyamides, PA11 is noted to have much lower hydrophilicity at 1.9% water uptake as compared to the commonly used PA6 and PA66 with water absorption at 10.5% and 8.2%, respectively [27]. Aside from being non-petroleum based, other differences between PA11 and other commonly used polyamides lie within the mechanical properties. PA11 typically has a lower tensile strength and modulus when compared to other polyamides, although these values can vary greatly depending on the manufacturing process and molecular weight of the polymer. PA11 is noted to be very ductile however, with injection molded parts demonstrating tensile strains greater than 100% upon fracture [23]. There seems to be great promise in using PA11 for more environmental applications as the hydrophilicity is greatly reduced from other commonly used polyamides, however there is slight room for improvement in increasing the strength and stiffness of the material for more load bearing applications. Below in Table 1, properties of various polyamides are compared, including percent of bio-sourced monomer, life-cycle assessment (LCA), glass, crystallization and melting temperatures (T_g, T_s, and T_m) , tensile strength and modulus, and percent water absorption.

Table 1: Comparison of various physical and thermal properties of commonly used polyamides [27].

Polymer	Bio-sourcing	LCA*	Temperatures (°C)			Tensile (MPa)		Water adsorption
	Percentage of C-atom	$kgCO_{2eq}/kg$	T_g	T_s	T_m	Strength	Modulus	Uptake (%)
PA6	0	9.1	47	179	218	80	3000	10.5
PA66	0	7.9	50	230	258	72	2500	8.2
PA610	63	4.6	48	196	206	61	2100	2.9
PA1010	100	4.0	37	171	191	54	1800	1.8
PA1012	45	5.2	49	151	181	40	1400	1.6
PA10T	50	6.9	125	280	285	73	2700	3.0
PA11	100	4.2	42	154	183	34	1100	1.9
PA12	0	6.9	138	151	176	45	1400	1.5

1.4 Advances in PA11 and PA12 SLS Printing

While PA11 has been used increasingly in SLS printing, published results on printed PA11 properties are still not as widely accessible as its PA12 counterpart. Comprehensive PA11 technical results presented at the 23rd annual International Solid Freeform Fabrication Symposium from Harvest Technologies compared SLS printed, injection molded and compression molded PA11 mechanical properties. PA11 SLS fracture surface micrographs were shown, however the mechanical behavior data provided for SLS printed PA11 seems to be data generated from modeling software. The PA11 used were Duraform EX and ALM FR-106, and the printer used was a Systems sPro 60 with a 70 W CO2 laser. When comparing tensile strength and elongation to break between the three manufacturing methods, the injection molded specimens demonstrated the highest elongation at break the 241.7%, however the standard deviation was quite high at 86.3%. The compression molded parts had a much lower elongation at $38.5 \pm 19.4\%$, and the fully optimized SLS printed parts only had an average reported value of >50% [23]. The ultimate tensile strength was comparable between the compression molded and modeled SLS printed PA11 parts, with averages of 7254.9 ± 90.6 psi and 7391 psi respectively. The injection molded ultimate tensile strength tested much lower at 5917.8 ± 106.1 psi. The modeling of PA11 SLS performance was done to evaluate the role of porosity on tensile failure mode in SLS printed parts. ASTM D638

PA11 type 1 tensile bars were modeled with 100 μm radius particles and increasing melted sublayer h. Tensile performance with increasing h/r ratio was compared to determine at what melted or fully sintered percentage the part has to achieve to promote ductile fracture. Selected results are shown below in Figure 1-9.

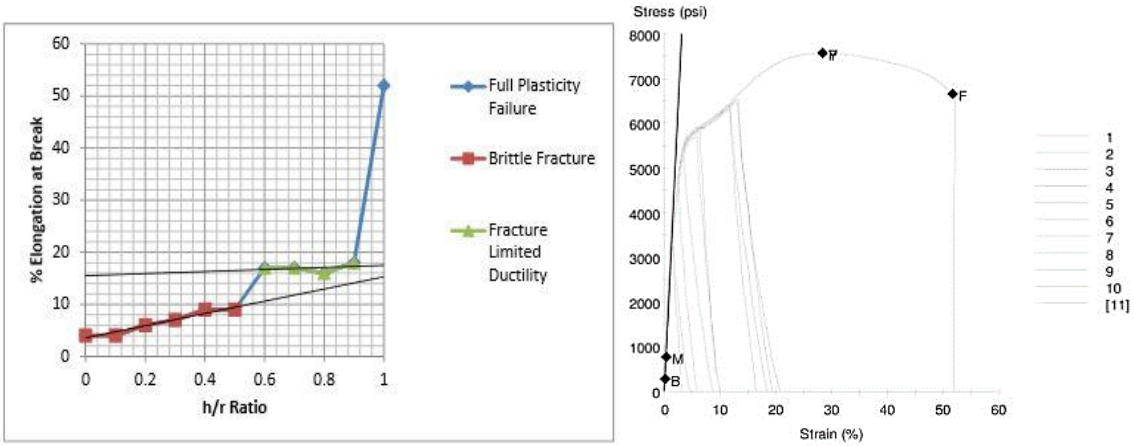

Figure 1-9: Elongation ant break and stress vs. strain curves for modeled PA11 SLS parts with increasing h/r ratio [23].

It was determined that an h/r ratio of at least 1 must be achieved to promote full ductile or plastic failure [18]. While the modeled PA11 SLS printed results are encouraging, there seems to be a lack of published research on experimentally sintered PA11. Other recent findings of SLS printed polyamide have been more robustly measuring the fracture toughness of SLS printed PA12, using compact tension specimens to differentiate the fracture toughness in separate printing directions [28]. Samples comprised of PA 2200 powder were print in an EOS Formiga P100 printer with laser power at 21 W, laser speed at 2500 mm/s, and layer thickness of 100 μm. Samples were print in three directions (xy, xz, and yz), half with a manual crack initiation, and half with a crack incorporated into the printing design. There was a direct dependence of printing orientation on K_{1C} fracture toughness, as samples printed in the xy and xz directions had greater K_{IC} of 4.77 MPa/m$^{1/2}$ and 4.66 MPa/m$^{1/2}$ respectively than the 3.25 MPa/m$^{1/2}$ average value calculated for the yz direction. This was due to the printing layers running in the same direction as the crack, allowing for more efficient propagation during testing. It was also discovered that the SLS initiated crack

was more blunt on average, which led to slightly higher K_{1C} values than the manually initiated crack specimens. Despite the slightly larger values, the general behavior and trend in behavior between the separate printing directions was the same, providing promise for that printing initiated cracks in SLS printed fracture toughness specimens with more complex geometries [28]. Below are the force vs. displacement curves and K_{1C} results for the PA12 sintered specimens in all three printing directions, and with both manual and printed crack initiations.

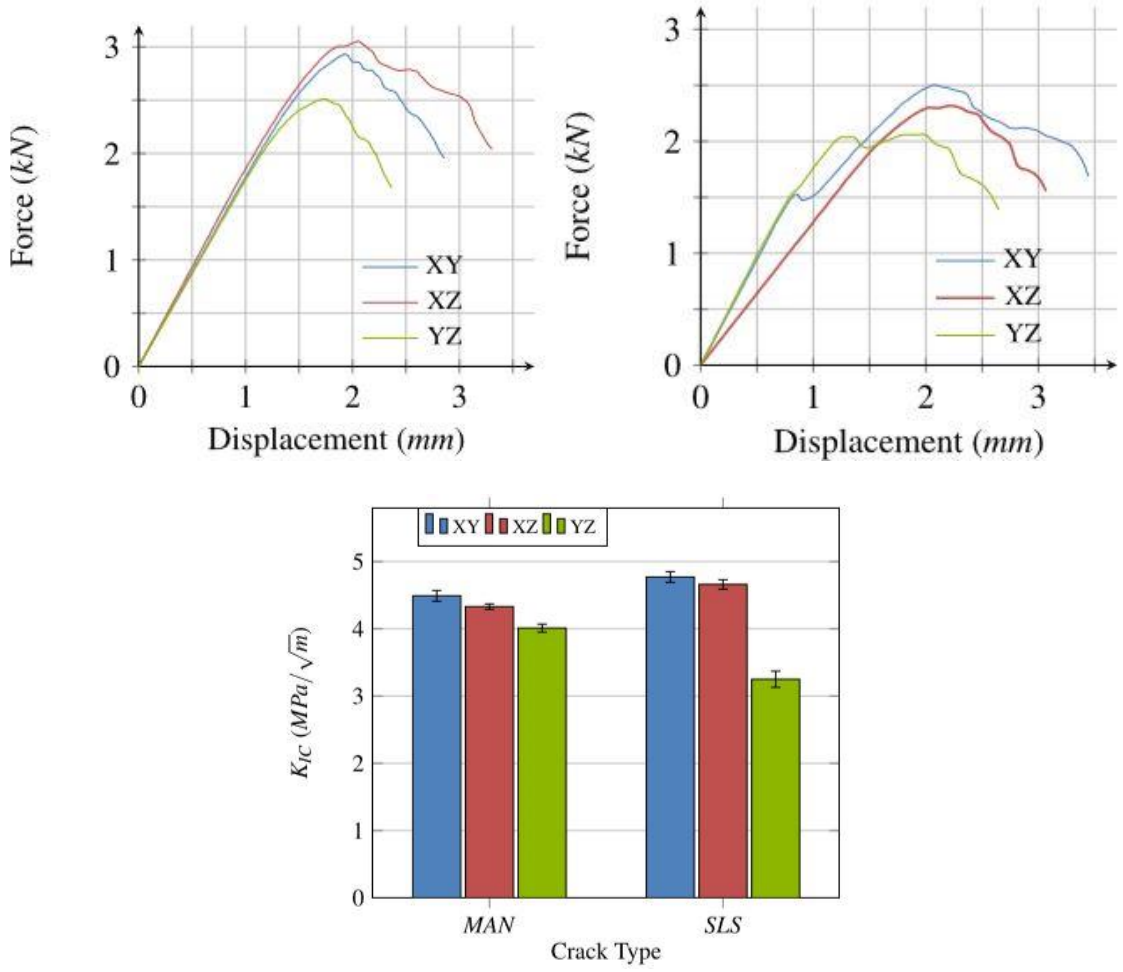

Figure 1-10: Force vs. displacement curves for the manual (left) and SLS (center) crack initiated CT specimens. The K_{1C} for these CT specimens in three different printing directions are shown on the right [28].

1.5 SLS printing of polymer nanocomposites

SLS printing of polymer nanocomposites have also been increasingly proposed and studied. As with most polymer SLS research, the majority of studies and proposed nanocomposites have been with PA12, with increasing exploration into PA11 based composite and nanocomposite SLS systems. Nanocomposites comprising of PA12 and carbon black (CB) have been sold commercially and published regularly, with the carbon black primarily added to increase the thermal conductivity/laser absorbance of the polymer and generate more effective melting. Adding carbon black in excess (greater than 1 wt. %) has been studied to increase electrical conductivity of the polymer as well. A PA12/CB printed nanocomposite comprising of 4 wt. % CB was found to increase the electrical conductance by five times the order of magnitude when compared to the neat PA12 [29]. Other studied nanocomposite systems have included PA12 with nanoclay, graphene and carbon nanotubes [29].

Of the proposed polyamide nanocomposite systems for SLS printing, the general trends seem to be adding nanoparticles for reinforcement, or for flame retardancy. A recent study investigated using both nanoclays and carbon nanofibers to increase the flame retardancy and stiffness of PA11 and PA12 for SLS printing [30]. Nanocomposites using Rilsan PA11 and Vestamid PA12 were formed through twin screw extrusion for testing, with initial powder production established using cryogenic grinding. TEM analysis proved good dispersion of both the nanoclays and carbon nanofibers at increasing weight percent [30]. In general, the thermal stability and flame retardancy were greatly improved by the addition of nanoclay in both systems, with the carbon nanofibers having more of an improvement in the PA11 system. The carbon nanofibers in general led to increased tensile strength in both PA11 and PA12, while the nanoclay had more of an influence on increasing tensile modulus. Flexural strength was more varied, with nanoclay increasing the PA12 flexural strength more dramatically, and carbon nanofibers having a larger impact on the PA11 resin. The tensile and flexural strength with increasing nanoclay and carbon nanofiber are shown below.

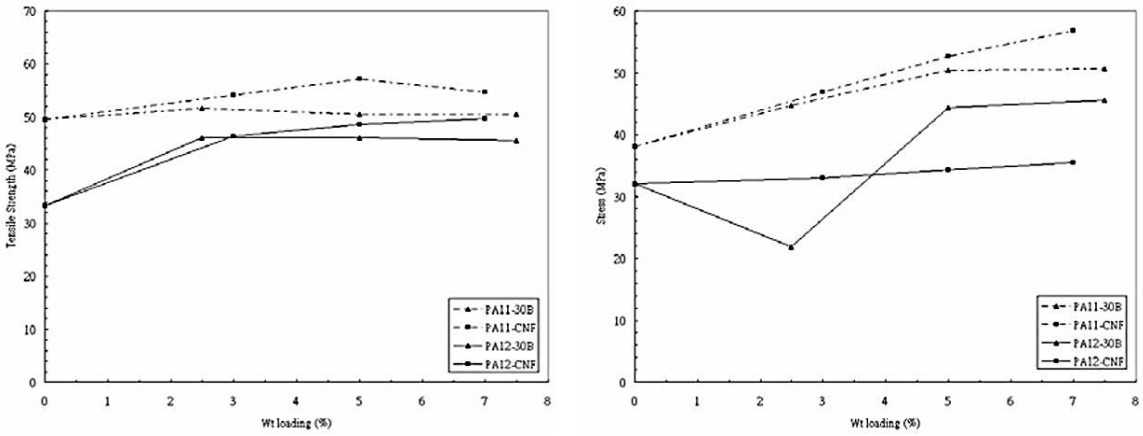

Figure 1-11: Tensile and flexural strength of PA11 and PA12 with increasing nanoclay (30B) and carbon nanofibers (CNF) [30].

Nanosilica as both a reinforcing agent and powder aide in both PA11 and PA12 has also been studied for a promising SLS nanocomposite material. A dissolution–precipitation process was shown to be successful in distributing nanosilica onto PA12 particles supplied from Degussa [31]. The nanosilica was surface modified with 3-aminopropyl triethoxysilane to better attach to the PA12 surface during the precipitation step. The samples were sintered using an HRPS-III SLS system CO2 laser power between 8 and 24 W, laser speed of 2000 mm/s and hatch spacing of 100 μm. The dissolution-precipitation of the silica on the PA12 produced well dispersed nanosilica coverage, and differential scanning calorimetry (DSC) provided evidence of the nanosilica acting as a heterogenous nucleating agent [31]. The impact strength, tensile modulus and tensile strength were 8.54%, 39.4% and 20.9% higher respectively in the nanosilica reinforced SLS parts [31]. When compared to a melt processed PA12/nanosilica nanocomposite at the same 3 wt. % loading, the samples reached a maximum tensile strength at a lower laser energy density than the neat material, however the value was not much improved. Figure 1-12 demonstrated the good surface dispersion of silica, as well as the change in tensile strength with laser energy density for all three tested PA12 systems.

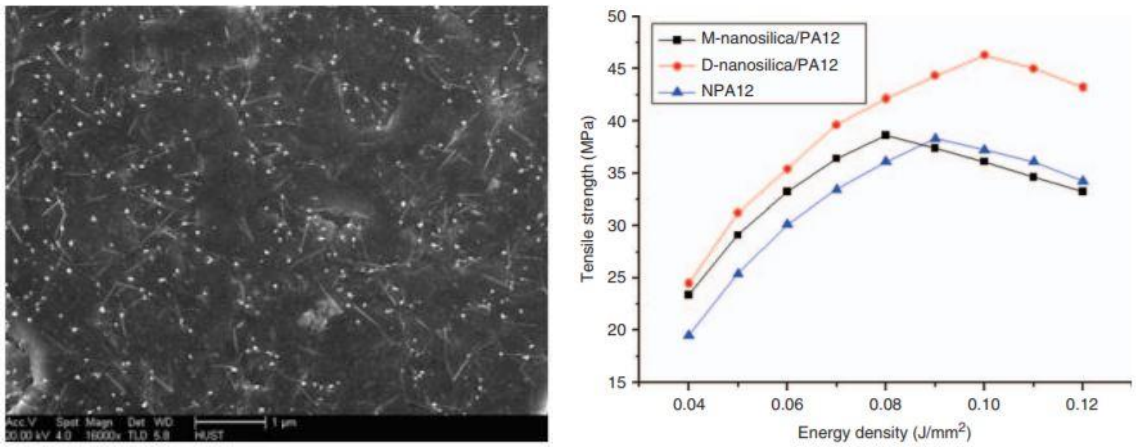

Figure 1-12: Nanoslica dispersion on a PA12 particle (left) and influence of nanosilica and laser energy density on tenisle strength of SLS printed PA12 (right) [31].

There have also been select studies on printing PA11/nanosilica nanocomposites using SLS. One noted experiment attempted to manufacture functionally graded polymer nanocomposites with SLS printing, utilizing PA11 with 0 to 10 volume percent of 15nm fumed silica [32]. The aim of this project was to create functionally graded materials with three dimensionality, instead of the one dimensional graded materials often achieved using more traditional manufacturing [32]. The PA11 polymer used was Rilsan D80, with the composites combined using a rotary tumbler and print on a Sinterstation 2000 printer, using a CO_2 laser with 4.5 W of power for printed specimens. The fabrication of these functionally graded materials with increasing silica content was very successful, with the creation of a graded complient gripper and a rotator cuff scaffold. The mechanical properties of the printed PA11 with increasing nanosilica volume were not as straightforward. The elongation at break change was nominal up to 4 vol % nanosilica, but decreased with increasing nanosilica past that volume [32]. The tensile and compressive modulus both initially decreased with additional nanosilica, but became significantly stiffer at 6 vol % and 10 vol % nanosilica in the printed PA11 [32]. While this stands as a unique study actually testing SLS printed PA11 nanocomposites, there seems to be a need for more investigation into the nanosilica interaction with the polymer matrix and nanosilica dispersion to help explain the variance in mechanical behaviors wih increasing nanosilica content.

1.6 Objectives and Content of this Dissertation

There are two primary objectives to the research study:

1) To fully characterize a commercial Polyamide 11/Carbon Black (PA11/CB) SLS printing powder before and after the printing process, elucidating changes to the polymer structure and orientation with increasing laser energy density.
2) To evaluate the role of surface treated nanosilica in enhancing both powder and sintered solid properties; namely powder flow and essential work of fracture.

There is one secondary objective to the proposed research study:

1) To evaluate the role of surface treated nanosilica in a separate polymer composite system manufactured via a separate additive manufacturing process. Namely, an epoxy/carbon fiber polymer composite processed with a direct ink writing based additive manufacturing setup.

In Chapter 1 a general overview of SLS printing was provided, with emphasis on powder flow measurements of SLS powders. In addition, an overview of PA11 and progress in using SLS printing to manufacture polymer nanocomposites was discussed. Finally, direct ink writing was introduced as an additive manufacturing method with great promise in creating high fiber anisotropy.

In Chapter 2, in an effort to better elucidate the structural changes of PA11 during the SLS printing process, a PA11/CB printing powder was print at increasing laser area energy density (A_N). Differential Scanning Calorimetry (DSC), x-ray diffraction (XRD), small angle x-ray scattering (SAXS), solution viscometry, tensile testing, essential work of fracture and fractography are utilized to determine microstructural changes in PA11 sintered with increasing laser energy during

the printing process. Finally, a solidification mechanism unique to the printing processed is proposed to explain the structural changes observed in the printed material with increasing A_N.

In Chapter 3, the role of surface treated silica nanoparticles (SNP) in improving the powder flow and mechanical behavior is examined. Separate iterations of developing a PA11/CB composite powder with surface treated silica nanoparticles (SNP) are accomplished through using 50 nm SNP and solid state shear pulverization, as well as 25 nm SNP with centrifugal mixing. A powder flow test adapted from the Freeman FT4 Powder Rheometer is developed for an existing hybrid rheometer (DHR2, TA Instruments), to test powder flow of the PA11/CB/SNP powders at increasing temperature. Additionally DSC, tensile testing, compression testing, essential work of fracture, linear reciprocating wear and fractography are used to evaluate the ability of SNP to improve both the powder flow and mechanical behavior of the printed materials.

In Chapter 4, the main conclusions of this dissertation are summarized. Five recommendations for future studies are suggested to best follow the results as presented in this dissertation. The Appendix that follows chronicles recent successes in utilizing SNP for a carbon fiber filled epoxy resin, designed for the direct ink writing process.

1.7 References

[1]. Stansbury, J. W., and Idacavage, M. J. (2016). 3D printing with polymers: Challenges among expanding options and opportunities. *Dental Materials* , 32, 54–64.

[2]. Ligon, S. C., Liska, R., Stampfl, J., Gurr, M. and Mülhaupt R. (2017). Polymers for 3D Printing and Customized Additive Manufacturing. *Chemical Reviews*, 117, 10212-10290.

[3]. Schmid, M., Amado, A., Wegener, K. (2015). Polymer powders for selective laser sintering (SLS). *AIP Conference Proceedings 1664*, 160009-1 – 160009-5.

[4]. Majewski, C., Zarringhalam, H. and Hopkinson, N. (2008). Effect of the degree of particle melt on mechanical properties in selective laser-sintered Nylon-12 parts. *J. of Eng. Manufacture*, 222, 1055.

[5]. Guerin, E., Tchoreloff, P., Leclerc, B., Tanguy, D., Deleuil, M. and Couarraze, G. (1999). Rheological Characterization of Pharmaceutical Powders Using Tap Testing, Shear Cell and Mercury Porosimeter. *International Journal of Pharmaceutics*, 189(1), 91–103.

[6]. Van den Eynde M., Verbelen L., Van Puyvelde P. (2015). Assessing Polymer Powder Flow for the Application of Laser Sintering. *Powder Technology*, 286, 151–155.

[7]. Krantz M., Zhang, H. and Zhu, J. (2009). Characterization of Powder Flow: Static and Dynamic Testing. *Powder Technology*, 194(3), 239–245.

[8]. Ziegelmeier S., Christoua, P., Wölleckea, F., Tuck, C., Goodridge, R., Hague, R., Krampec, E. and Wintermantel, E. (2015). An Experimental Study into the Effects of Bulk and Flow Behaviour of Laser Sintering Polymer Powders on Resulting Part Properties. *Journal of Materials Processing Technology*, 215, 239–250

[9]. Freeman Technology. Measuring and understanding the flow properties of powders with the FT4 Powder Rheometer. FM 85958, 1/2018.

[10]. Hare, C., Zafar, U., Ghadiri, M., Freeman, T., Clayton, J. and Murtagh M.J.(2015). Analysis of the dynamics of the FT4 powder rheometer. *Powder Technology*, 285, 123-127.

[11]. Barnes, H. A. and Nguyen Q. D. (2001). Rotating vane rheometry — a review. *Journal of Non-Newtonian Fluid* Mechanics, 98, 1–14.

[12]. Freeman, T., Brockbank, K. and Armstrong, B. (2015). Measurement and quantification of caking in powders. *Procedia Engineering*, 102, 35-44.

[13]. Van den Eynde M., Verbelen L., Van Puyvelde, P. (2017). Influence of temperature on the flowability of polymer powders in laser sintering. *AIP Conference Procedings 1914*, 190007-1 – 190007-5.

[14]. Amado Becker A. (2016). *Characterization and prediction of SLS processability of polymer powders with respect to powder flow and part warpage.* Thesis, ETH Zurich.

[15]. Mubofu E. B. (2016). Castor Oil as a Potential Renewable Resource for the Production of Functional Materials. *Sustainable Chemical Processes*, 4(11), 1-12.

[16]. Nair, S. (2006). *Studies on the development of structure and morphology in nylons*. Thesis, University of Pune.

[17]. Kawaguchi, A., Ikawa, T., Fujiwara, Y., Tabuchi, M. and Monobe, K. J. (1981). Polymorphism in lamellar single crystals of nylon 11. *Macromol. Sci. Phys*., B20, 1-20.

[18]. Choi, Y. S., Kim, S.K., Williams, F., Calahorra, Y., Elliott, J.A. and Kar-Narayan, S. (2018). The Effect of Crystal Structure on the Electromechanical Properties of Piezoelectric Nylon-11 Nanowires. *Chemical Communications*, 54(50), 6863–6866.

[19]. Yoshioka,Y. and Tashiro, K. (2003). Structural change in the Brill transition of Nylon m/n (1) Nylon 10/10 and its model compounds. *Polymer*, 44, 7007-70019.

[20]. Barrère, C., Hubert-Roux, M., Lange, C.M., Rejaibi, M., Kebir, N., Desilles, N., Lecamp, L., Burel, F. and Loutelier-Bourhis C. (2012). Solvent-Based and Solvent-Free Characterization of Low Solubility and Low Molecular Weight Polyamides by Mass Spectrometry: a Complementary Approach. *Rapid Communications in Mass Spectrometry*, 26(11), 1347–1354

[21]. Martino L., Basilissi L., Farina H., Ortenzi M., Zini E., Di Silvestro G., Scandola M. (2014). Bio-based polyamide 11: Synthesis, rheology and solid-state properties of star structures. *European Polymer Journal*, 59, 69-77.

[22].Jariyavidyanont, K., Janke, A., and Androsch, R. (2019). Crystal self-nucleation of polyamide-11. *Thermochimica Acta*, 677, 139-143

[23]. Leigh, D. K. (2012). A Comparison of Polyamide 11 Mechanical Properties Between Laser Sintering and Traditional Molding. *23rd Annual International Solid Freeform Fabrication Symposium*. 574-605.

[24]. Arkema. Rilsan PA-11: Created From a Renewable Source. 3720E, 6/2005.

[25]. Mollova, A., Androsch, R., Mileva, D., Schick, C. and Benhamida, A. (2013). Effect of Supercooling on Crystallization of Polyamide 11. *Macromolecules*, 46, 828-835.

[26]. Xenopoulos, A. and Wunderlich, B. (1990). Thermodynamic Properties of Liquid and Semicrystalline Linear Aliphatic Polyamides. *J. of Polymer Science Part B,* 28, 2271-2290.

[27]. Kabasci, S. (2014). Bio-Based Plastics: Materials and Applications. *John Wiley & Sons*, London, 275-293.

[28]. Brugo, T., Palazzetti, R., Ciric-Kostic, S., Yan, X.T., Minak, G. and Zucchelli, A. (2016). Fracture Mechanics of Laser Sintered Cracked Polyamide for a New Method to Induce Cracks by Additive Manufacturing. *Polymer Testing*, 50, 301–308

[29]. de Leon, Al C., Chen, Q., Palaganas, N.B., Palaganas J.O., Manapat, J. and Advincula, R.C. (2016). High performance polymer nanocomposites for additive manufacturing applications. *Reactive and Functional Polymers* 103, 141-155.

[30]. Koo, J; Lao, S; Ho, W; Ngyuen, K; Cheng, J; Pilato, Louis; Wissler, G; Ervin, M. (2006). Polyamide nanocomposites for selective laser sintering. *17th Solid Freeform Fabrication Symposium, SFF 2006*. 392-409.

[31]. Yan, C., Shi, Y., Yang, J. and Liu, J. (2008). A Nanosilica/Nylon-12 Composite Powder for Selective Laser Sintering. *Journal of Reinforced Plastics and Composites*, 28(23), 2889–2902.

[32]. Chung, H, and Das, S. (2008). Functionally Graded Nylon-11/Silica Nanocomposites Produced by Selective Laser Sintering. *Materials Science and Engineering: A,* 487(1-2), 251–257.

CHAPTER TWO: CHARACTERIZING POLYAMIDE 11 POLYMER STRUCTURE AND MECHANICAL BEHAVIOR WITH INCREASING LASER AREA ENERGY DENSITY

2.1 Introduction

Selective laser sintering (SLS) of polymer powders has made tremendous strides in the past decade, particularly in creating functional parts for the aerospace and automotive industries [1]. However, many challenges remain in using polymers for SLS printing. Specifically, effectively characterizing the polymer powder to design the best printing environment, as well as diversifying the types of polymers and polymer systems that can excel in an SLS manufacturing environment [1]. There has been recent success in better characterizing the mechanical behavior of SLS printed parts with variable printing parameters. Specifically, altering parameters like powder layer thickness, laser speed, laser power, and hatch spacing to observe changes primarily in tensile and flexural behavior [2]. Ultimately, these parameters can combine to create a laser area energy density term, which has shown great promise in printer parameter optimization for enhanced mechanical properties [2,3].

While there have been detailed characterizations of traditional mechanical properties in SLS printed polymer parts, major lapses in characterization still exist within the available literature. Broadly, any results on changes in microstructure and crystal structure of printed polymers seem sparse, despite noted differences in melting behavior and molecular weight between virgin SLS powder and printed material [4]. Polymer diversity also seems to be lacking, with the vast majority of results characterizing polyamide 12 (PA12), despite the commercial availability of other polymer powder for SLS printing [1]. One of these available powders is polyamide 11 (PA11), which has seen increased interest in general use due to its sustainable nature and diminished water absorption compared to more commonly used nylons. Though very similar in monomer structure, there are distinct differences in behavior between PA12 and PA11, with PA11 showing greater ductility and flexural strength [5]. Lastly, the lasers used in the majority of SLS literature are the infrared CO_2 variety, even with the increasing availability of blue diode based lasers for use in SLS printers. In

general, there seem to exist larger gaps in expanding SLS literature past select characterization techniques, materials and printer choice that limit the potential expansion of the SLS manufacturing process.

To address these gaps, this chapter involves characterizing a polyamide 11/carbon black (PA11/CB) printing based nanocomposite powder. While some experiments will be dedicated to measuring properties solely in the unsintered powder, the majority of characterization will compare the unsintered powder to sintered material with varying laser energy density applied in the printing process. A wide range of characterization techniques will be employed, with an emphasis on correlating mechanical properties such as tensile strength and toughness to the microstructural changes determined in each characterization step. The results will then be used to develop a PA11/CB/silica nanoparticle (SNP) composite powder for use in SLS printing, using SNP as both a processing aid and toughening agent to produce high performance polymer nanocomposites. It is imperative to measure the extent of any polymer structure changes through the printing process prior to the production of the PA11/CB/SNP nanocomposite in order to:

1. Optimize the printing parameters to produce consistent yet desirable properties in the printed PA11/CB material.
2. Determine what, if any, changes to the PA11 polymer chain occur as a result of increasing laser area energy density in the SLS process.
3. Decipher the mechanisms of property changes in the PA11/CB nanocomposite system for future reference when characterizing the PA11/CB/SNP material, determining if property changes are a result of the SNP addition or the printing process itself.

By thoroughly characterizing the changes in the PA11/CB system through the SLS printing process, the printer can be more efficiently utilized to produce polymer parts with favorable microstructure for high performance applications, and the results can be used for future development and characterization of a nanocomposite printing powder.

2.2 Experimental

2.2.1 Materials

A PA11/CB composite powder under the commercial name Rilsan Invent Black was provided by the Arkema corporation. The polymer powder used in this study has a nominal average size of 50 μm, as determined by dynamic light scattering. The shape of these particles varied from slightly rounded to triangular, with an incredibly rough particle surface. Carbon black was determined to be dispersed homogenously throughout the polymer particle, with an approximate composite weight contribution of 1 wt. % as measured using thermogravimetric analysis.

2.2.2 SLS Printing Parameters

The powder was processed using the commercial Sintratec Kit SLS printer, equipped with a 2 W blue diode (445 nm) laser. Prior to printing, powder was dried at 80°C overnight (16 hours) to reduce the effects of humidity on the printing process. Powder was additionally passed through a 150 μm sieve to remove uncharacteristically large particles from the bulk powder. The printer chamber temperature was set to 178°C and left to equilibrate for 3 hours prior to the start of printing. The powder bed was set to 150°C during the chamber equilibration and increased to 178°C for the actual print. Samples were consistently print in the same envelope to prevent any influence of the powder bed location on printed part performance.

Samples were printed with increasing area laser energy density, also known as Andrew Number (A_N) [6]. The equation for A_N is shown below with P, LS, and HS representing laser power, laser speed and hatch spacing, respectively.

$$A_N = \frac{P}{LS \times HS} \quad (1)$$

Five separate A_N were chosen for this study to elucidate the effect of increasing area laser energy density on polymer structure. The chosen A_N were selected based off internal findings demonstrating a transitional regime in elongation at break midway through the selected range,

proposed to be related to changing polymer structure. For this study, the laser power and hatch spacing were kept constant at 2 W and 100 μm for each A_N studied. The specific A_N and their corresponding laser speed as used in this study are shown below in Table 2-1.

Table 2-1: List of laser speed used for each tested A_N in the present study.

A_N (J/cm^2)	7 J/cm^2	8 J/cm^2	9 J/cm^2	10 J/cm^2	11 J/cm^2
Laser Speed (mm/s)	285 mm/s	250 mm/s	225 mm/s	200 mm/s	180 mm/s

2.2.3 Thermal Analysis of PA11/CB

Differential Scanning Calorimetry (DSC) was utilized to evaluate the melting temperature (T_m), crystallization temperature (T_c), weight percent crystallinity (X_c), glass transition temperature (T_g) and mobile amorphous fraction (MAF). DSC samples were extracted from the internal bulk of a ½″ x ¼″ x ¼″ specimen printed in the same print bed coordinates for each A_N. Samples weighing approximately 10 mg were placed into hermetically sealed aluminum pans and placed onto the DSC sample stage (DSC Q2000, TA Instruments). For determination of the T_m, T_g, T_c, X_c and MAF of printed PA11/CB with increasing A_N, samples were equilibrated at 0°C and heated at a rate of 10°C/min to 230°C, followed by a cooling cycle at the same ramp rate to 0°C. For determination of the effect of cooling rate on the PA11/CB melting behavior, powder samples weighing approximately 10 mg were similarly placed into hermetically sealed aluminum pans and experienced an equilibration at 0°C followed by a heating rate of 10°C/min to 230°C. Samples were then subjected to cooling rates of 50°C/min, 40°C/min, 30°C/min, 20°C/min, 10°C/min, 5°C/min, 2.5°C/min or 1°C/min to 0°C. Samples then underwent a second heating cycle at 10°C/min to 230°C to measure the changes in X_c and subsequent T_m with different cooling rates. All tests were conducted under nitrogen environment.

For the calculation of X_c, the enthalpy of melting (ΔH_f) was measured using Universal Analysis software (TA Instruments), and the standard enthalpy of melting ($\Delta H_f{}^o$) used in this study was 226.4 J/g [7]. The calculation of X_c is shown below in Equation 2.

$$X_c = \frac{\Delta H_f}{\Delta H_f^o} \tag{2}$$

MAF was evaluated through calculating the change in heat capacity (ΔCp) during T_g for each tested sample. The change in heat capacity was measured using Universal Analysis software. Both MAF and X_c were used to calculate the Rigid Amorphous Fraction (RAF) with varying standard amorphous heat capacity (ΔCp_{am}) in accordance with the Equations 3 and 4 below [8].

$$MAF = \frac{\Delta Cp}{\Delta Cp_{am}} \tag{3}$$

$$RAF = 1 - MAF - X_c \tag{4}$$

2.2.4 X-Ray Analysis of PA11/CB

Both X-Ray Diffraction (XRD) and Small Angle X-Ray Scattering (SAXS) were used to characterize the crystal structure of both the powder and printed PA11/CB. XRD (Panalytical Empyrean) was performed using a CuKα radiation source at 0.15406 nm. Symmetric scans were taken from the bulk of ½″x ¼″ printed PA11/CB squares at 2θ= 5º to 30º. The d_{hkl} spacing was also analyzed using experimental data in accordance with Bragg's Law as shown below.

$$d_{hkl} = \frac{n\lambda}{2\sin\theta} \tag{5}$$

SAXS (SAXSspace, AntonPaar GmbH) was performed using a CuKα radiation source at 0.15406 nm and a sample-to-detector distance of 327.0652 mm. Printed and powder PA11/CB samples of approximate 100μm thickness were used in each measurement. The long period (Lp) was determined using the equation below, with intensity profiles corrected by the Lorentz factor $I(q)^2 = f(q)$. The qmax term refers to the q wave vector at maximum scattering intensity.

$$L_p = \frac{2\pi}{q_{max}} \tag{6}$$

The lamellae thickness (Lc) can then be derived from the following equation, where ρ is the PA11 density (1.013 kg/L) and ρ_c is the PA11 crystalline density (1.130 kg/L) [7].

$$L_c = L_p \left(\frac{\rho}{\rho_c}\right) X_c \quad (7)$$

2.2.5 Infrared Spectroscopy of PA11/CB

Fourier Transform Infrared Spectroscopy (FTIR) (PerkinElmer Spectrum 100) was used to further characterize changes in the polymer structure with increasing Andrew Number. The universal ATR sampling accessory with diamond crystal was chosen to measure the IR spectra. IR transmission was measured from 4000 cm^{-1} to 530 cm^{-1} for each sample with an average of 100 scans per measurement. FTIR solid samples were extracted from the internal bulk of a ½″ x ¼″ x ¼″ specimen printed in the same print bed coordinates for each AN.

2.2.6 Imaging of PA11/CB Tensile and Fracture Surface

Scanning electron microscopy (Zeiss 1500) was used to examine fracture surfaces as produced through tensile testing and essential work of fracture. Samples were sputter coated with iridium to reduce charging during the imaging process. Carbon tape was administered to both promote adhesion to the SEM stub as well as ground the electron conduction. Necked regions of representative tensile specimens as well as fracture surfaces of the 12.5 ligament length EWF samples were chosen for imaging. An accelerating voltage of 3 kV was used in conjunction with the SE2 lens detector. Select samples were additionally sent to the Core Electron Microscopy Facility at the University of Massachusetts Medical School for transmission electron microscopy (TEM) analysis. Samples were prepared using cryo-ultramicrotomy to section 90 nm samples and osmium tetroxide staining to promote contrast.

2.2.7 Molecular Weight Evaluation of PA11/CB

Molecular weight was measured for the PA11/CB powder as well as printed PA11/CB with increasing A_N. Molecular weight was measured primarily through solution viscometry, performed following ASTM D2857 standards with a size 75 Cannon-Ubbelohde viscometer in a 35ºC water

bath. 2 g/dL stock solutions of the PA11/CB in hexafluoro-2-propanol (HFIP) were created through placing the solutions in a room temperature sonicating bath for 24 hours. Five dilutions were created from the stock solutions for molecular weight analysis, including 0.2 g/dL, 0.4 g/dL, 0.6 gdL, 0.8 g/dL and 1 g/dL. Mark-Houwink constants for the PA11/HFIP pair were established through the work of Laun and Pasch [9], and determined to be 3.3 $x10^{-2}$ mL/g for K and 0.75 for a at 35°C.

2.2.8 Mechanical Behavior Analysis of PA11/CB

Tensile testing and essential work of fracture (EWF) were performed using a screw-driven universal testing machine (Instron 5567), with strain measured through use of a digital extensometer. Type V tensile specimens (ASTM D638-14) and essential work of fracture (EWF) were test at 1 mm/min. EWF was chosen to measure PA11/CB fracture toughness as the method can better characterize ductile polymer fracture, and that preliminary fracture studies on PA11/CB confirmed deviation from linear elastic fracture mechanics. EWF analysis was performed on double edge notched (DENT) specimens with dimensions of 75 mm x 45 mm x 3 mm. The ligament lengths (l) tested were 5, 7.5, 10, 12.5 and 15 mm. This method relies on the theory that for quasi-static cracking, the external work done is equal to the sum of the essential and inessential work, as illustrated by the equation below [10].

$$W_f = w_e l t + \beta w_p l^2 t \quad (8)$$

The essential work ($w_e lt$) and inessential work ($\beta w_p l^2 t$) are both shown to comprise the work of fracture (W_f). Additionally, t represents the sample thickness, β represents the plastic zone shape factor and w_p represents the specific plastic work. W_f was determined by integrating the area under the load vs. displacement curve after crack propagation for each sample. The point selected for this study was chosen to be maximum load, and the left bound of the integration was chosen as a line parallel to the linear elastic region of the curve and intersecting with the maximum load value.

Essential work of fracture (w_e) was determined through linear regression of the specific work of fracture ($w_f = W_f / lt$), as shown in the equation below [10].

$$w_f = w_e + \beta w_p l \tag{9}$$

The specific work of fracture is found for each tested sample and plot against the ligament length to comprise data points for the linear regression. This process is additionally demonstrated in Figure 2-1, below.

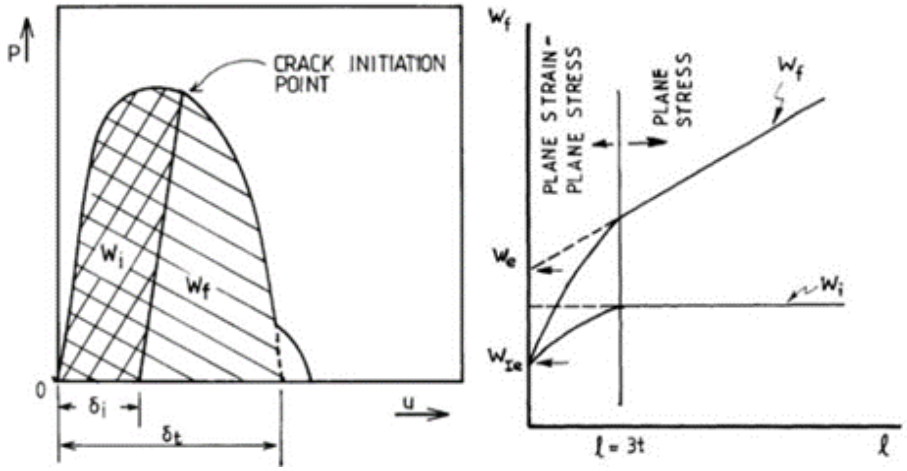

Figure 2-1: Load vs. displacement and linear regression curves used to determine essential work of fracture [10].

2.3 Results and Discussion

2.3.1 Thermal Analysis of PA11/CB

Melting temperatures (T_m) of a representative printed PA11/CB (A_{N8}) sample was compared to that of the virgin printing powder, as well as some recycled PA11/CB powder that was recovered from the printing bed. The melting behavior was strikingly different, with the melting temperature reducing from 201.2°C to 191.4°C between the virgin powder and the printed sample. It should be mentioned that typical T_m for the α, α' and δ crystalline phases for PA11 fall between 180°C and 190°C, suggesting the powder PA11 T_m is likely due to differences in lamellar structure or molecular weight [11]. The printed sample additionally showed a smaller residual peak closer to the melting temperature of the virgin powder, which has been shown to represent an unmelted core

of the powder particle [4]. The recycled powder had a similar melting temperature to that of the virgin powder at 201.3ºC, however the breadth of the curve was much broader as compared to that of the virgin powder. The percent crystallinity was also greatly changed between the powders and the printed sample, with the virgin and recycled powders containing 38.3% and 37.1% crystallinity respectively, and the printed sample exhibiting 21.0% crystallinity. Upon printing, the PA11/CB shows marked changes in both percent crystallinity as well as melting behavior. The results are summarized below in Figure 2-2 and Table 2-2.

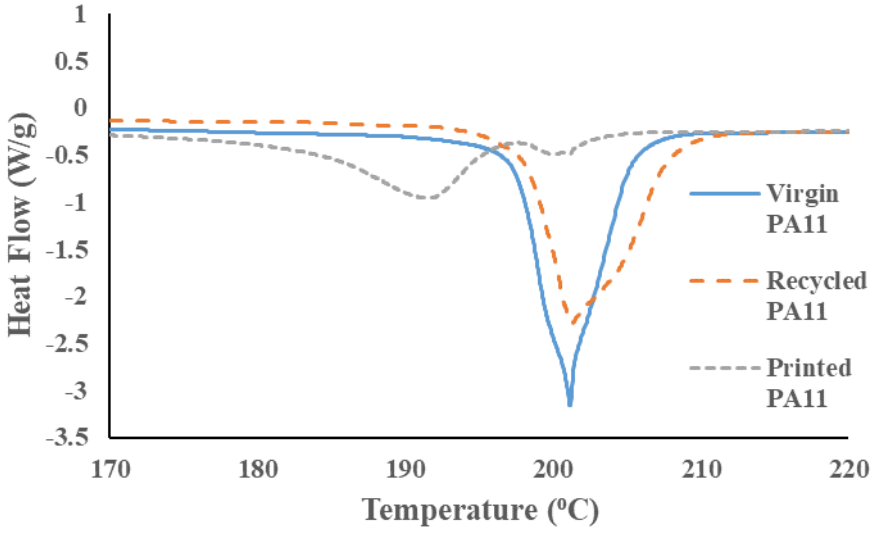

Figure 2-2: The melting behavior of the virgin, recycled and A_{N8} printed PA11/CB.

Table 2-2: Melting temperatures and percent crystallinity of the virgin, recycled and printed PA11/CB

PA11/CB Sample	Melting Temperature (ºC)	Percent Crystallinity (%)
Virgin	201.2ºC	38.3%
Recycled	201.3ºC	37.1%
Printed (A_{N8})	191.4ºC	21.0%

The melting behavior was subsequently compared of printed samples with increasing A_N, increasing from A_{N7} to A_{N11}. The samples showed a reduction in the residual powder peak before completely disappearing at the A_{N9} melting curve. Additionally, the A_{N8} and A_{N9} samples showed small shoulders on the melting peaks, indicative of the α crystal structure with larger d_{hkl} spacing referred to as α′ [11]. Otherwise, the melting temperature and percent crystallinity was nominally

the same between samples printed with increasing A_N. The results are summarized below in Figure 2-3 and Table 2-3.

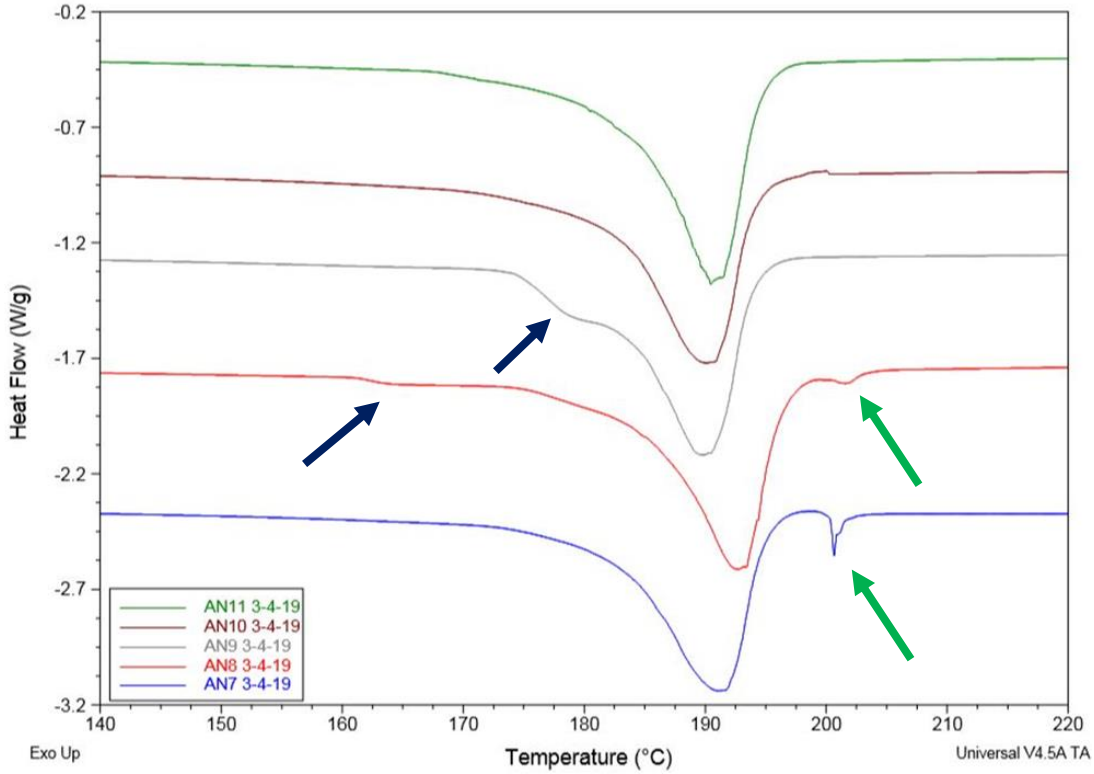

Figure 2-3: Melting behavior of printed PA11/CB at A_N of 7,8,9,10 and 11. The blue arrows highlight melting shoulders, while the green arrows show the residual powder melting peak.

Table 2-3: Thermal behavior and crystallinity of PA11/CB at increasing A_N.

Andrew Number (J/cm^2)	**Tg (ºC)**	**ΔCp (J/gºC)**	**Tm (ºC)**	**Xc (%)**
7	48.7ºC	0.28 J/gºC	191.1ºC	19.4 %
8	47.8ºC	0.24 J/gºC	192.8ºC	22.5 %
9	46.2ºC	0.26 J/gºC	189.6ºC	20.6 %
10	47.2ºC	0.32 J/gºC	190.2ºC	19.5 %
11	48.0ºC	0.30 J/gºC	190.5ºC	21.2 %

After examining the change in melting behavior with increasing A_N, it was hypothesized that the change in laser energy density may alter the effective cooling rate of the polymer between successive laser passes. The change in cooling rate would possibly influence the subsequent

melting behavior as the crystallization kinetics would be altered. Samples were analyzed using DSC, varying the cooling rate after the PA11/CB powder had already been melted. Cooling rates were first increased from 10°C/min to 50°C/min in 10°C/min intervals. The crystallization peak increased in magnitude, with T_C additionally shifting to lower temperatures with increasing cooling rate. The largest change was between the 10°C/min and 20°C/min cooled samples, with the T_C dropping from 168.8°C and 165.4°C. The change in crystallization behavior with increasing cooling rate is shown below in Figure 2-4.

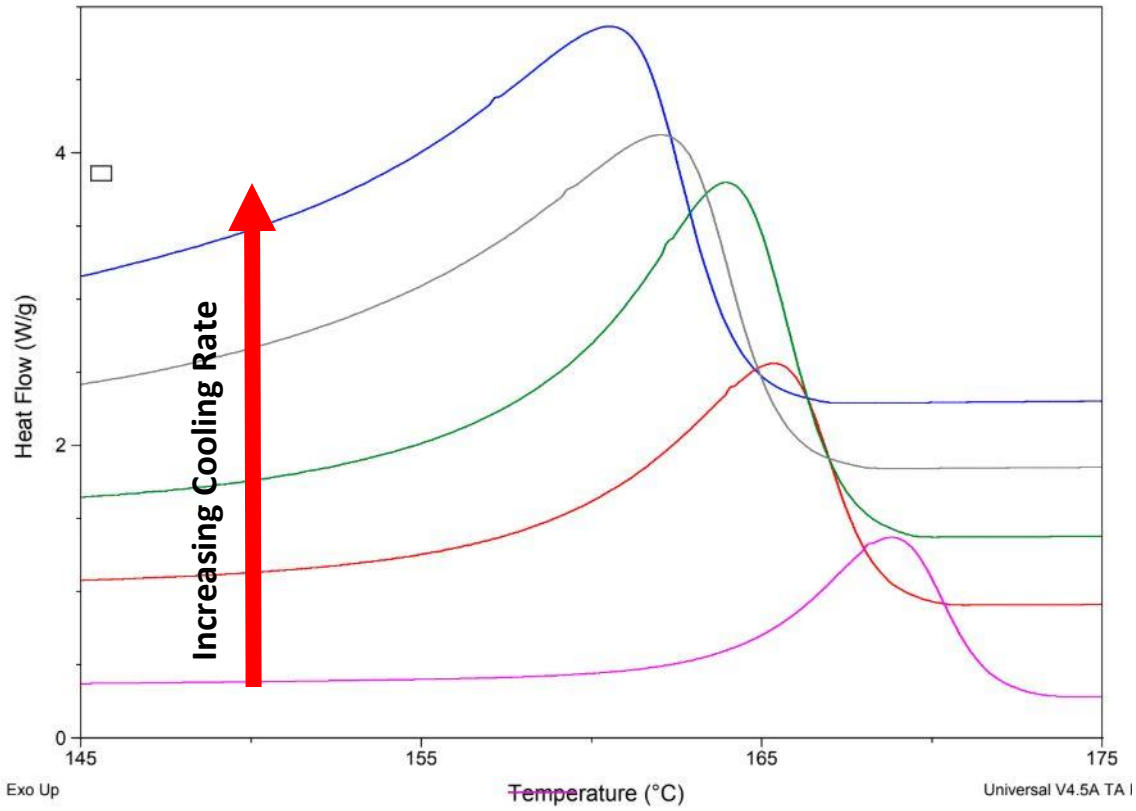

Figure 2-4: Crystallization of PA11/CB at increasing cooling rates of 10°C/min (pink), 20°C/min (red), 30°C/min (green), 40°C/min (grey), and 50°C/min (blue).

The subsequent melting behavior of the PA11/CB cooled at increasing rates were also compared to elucidate the effect of effective cooling rate on the melting temperature, specifically the appearance of a shoulder. All tested PA11/CB powder samples showed a primary T_M between 189.0°C and 190.3°C. Additionally, all samples demonstrated presence of a shoulder prior to the

major melting peak. The shoulder initiated at lower temperatures for samples cooled at increasing rates, suggesting larger changes in d-spacing of the α crystal phase. Changes in d spacing and crystalline phase with increasing cooling rates have been studied and noted previously by Mollova et al. [12]. The change in melting behavior with increasing cooling rate is shown below in Figure 2-5, and the change in both T_C and T_M with increasing cooling rate are summarized in Table 2-4.

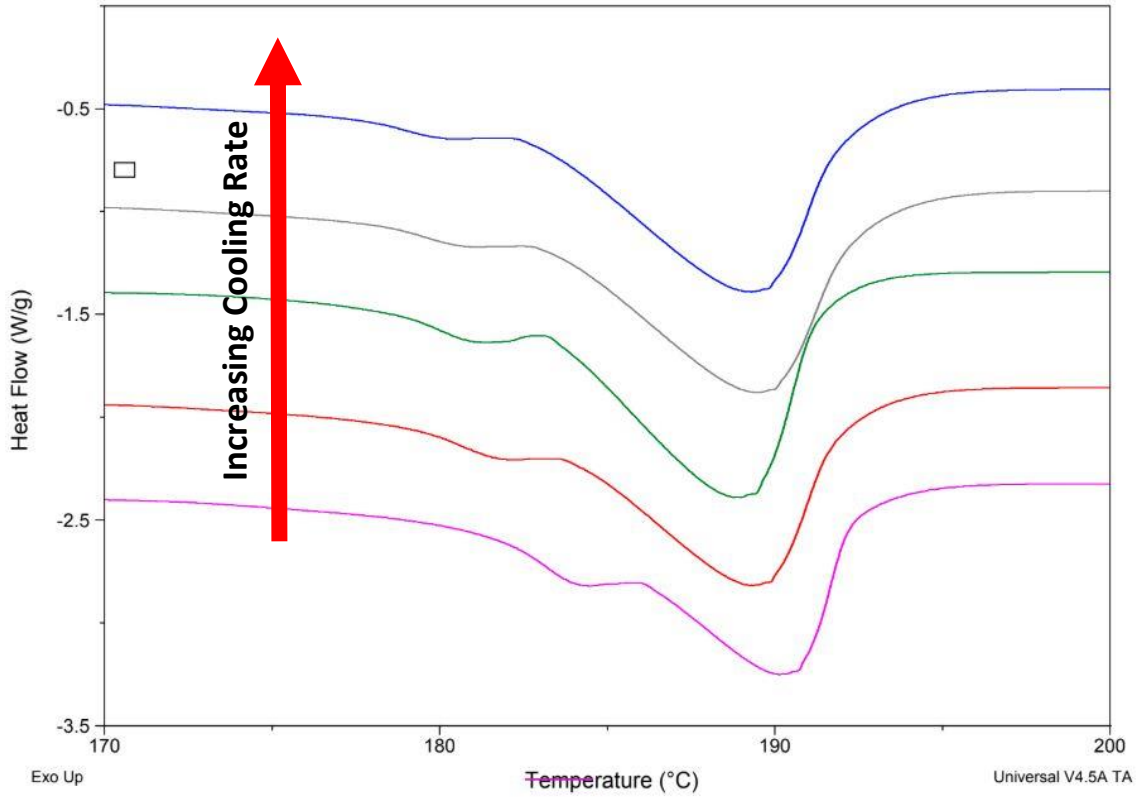

Figure 2-5: Melting behavior of PA11/CB crystallized at increasing cooling rates of 10°C/min (pink), 20°C/min (red), 30°C/min (green), 40°C/min (grey), and 50°C/min (blue).

Table 2-4: Change in T_c and T_m with increasing cooling rates of PA11/CB.

Cooling Rate (ºC/min)	**10ºC/min**	**20ºC/min**	**30ºC/min**	**40ºC/min**	**50ºC/min**
Tc (ºC)	168.8ºC	165.4ºC	164.1ºC	162.1ºC	160.6ºC
Tm (ºC)	190.3ºC	189.4ºC	189.0ºC	189.4ºC	189.3ºC

After observing persistent presence of a melting peak shoulder with increased cooling rate of the PA11/CB, the effect of slower cooling rate on the crystallization and subsequent melting peaks were studied. Cooling rates of 5°C/min, 2.5°C/min and 1°C/min were used, with crystallization and melting behavior additionally compared to the 10°C/min cooled sample. The crystallization peak decreased in magnitude, with T_C additionally shifting to higher temperatures with decreasing cooling rate. The largest change was between the 2.5°C/min and 1°C/min cooled samples, with the T_C increasing from 171.5°C to 174.9°C. The change in crystallization behavior with increasing cooling rate is shown below in Figure 2-6.

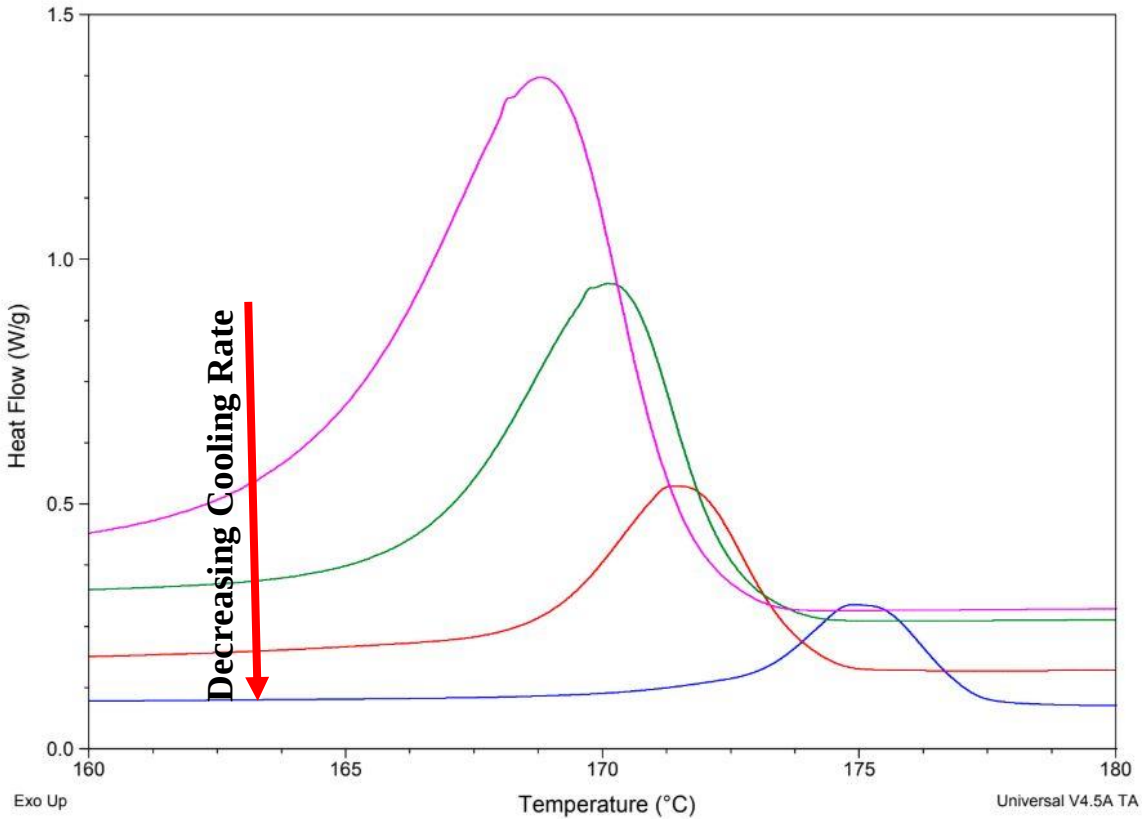

Figure 2-6: Crystallization of PA11/CB at decreasing cooling rates of 10°C/min (pink), 5°C/min (green), 2.5°C/min (red), and 1°C/min (blue).

The subsequent melting behavior of the PA11/CB cooled at decreasing rates were also compared to elucidate the effect of effective cooling rate on the melting peak. Like the 10°C/min cooled

sample, the 5°C/min cooled sample showed a melting peak shoulder, although not as prominent. The shoulder was not present for both the 2.5°C/min and 1°C/min cooled samples, suggesting higher uniformity in the d-spacing of the crystal lattice. There was also a consistent decrease of T_M with decreasing cooling rate, lowering from 190.3°C for the 10°C/min cooled sample to 187.0°C for the 1°C/min cooled sample. The change in melting behavior with decreasing cooling rate is shown below in Figure 2-7, and the change in both T_C and T_M with decreasing cooling rate are summarized in Table 2-5.

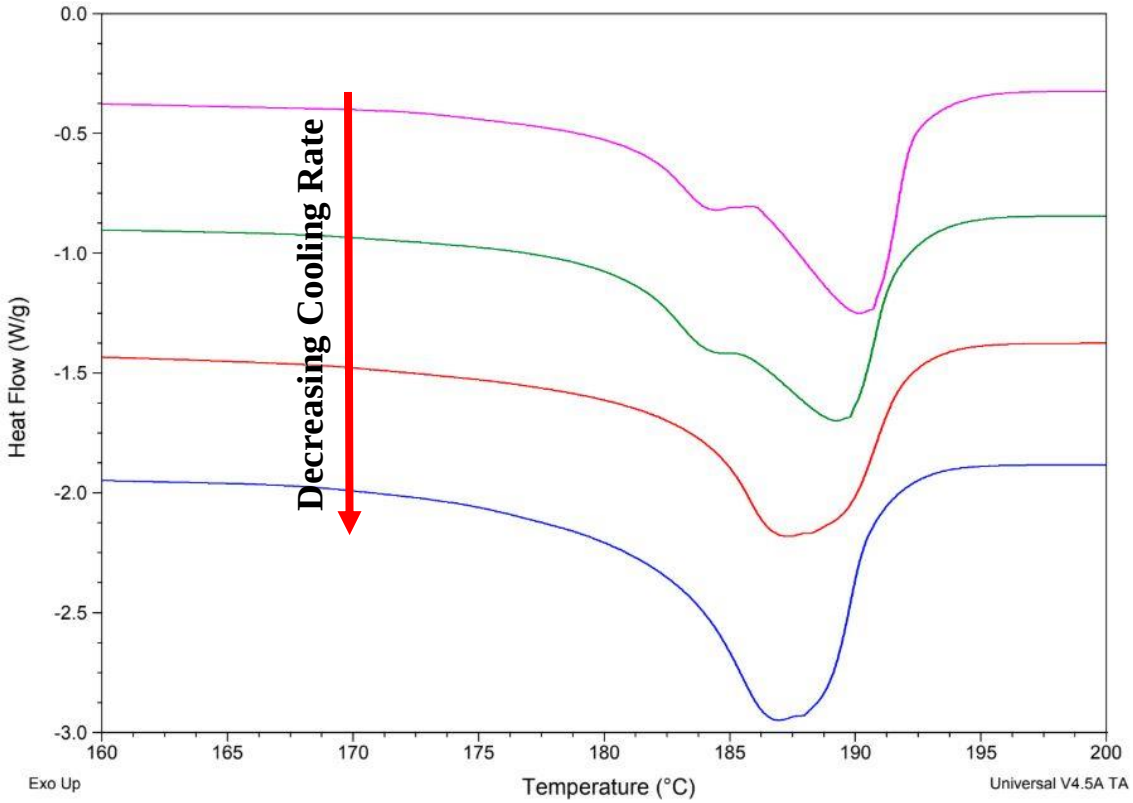

Figure 2-7: Melting behavior of PA11/CB crystalized at decreasing cooling rates of 10°C/min (pink), 5°C/min (green), 2.5°C/min (red), and 1°C/min (blue).

Table 2-5: Change in Tc and Tm with decreasing cooling rates of PA11/CB.

Cooling Rate (°C/min)	**10°C/min**	**5°C/min**	**2.5°C/min**	**1°C/min**
Tc (°C)	168.8°C	170.1°C	171.5°C	174.9°C
Tm (°C)	190.3°C	189.3°C	187.5°C	187.0°C

In addition to the melting behavior, polyamide polymer structure can also be inferred by transitional chain rigidity, characterized by the rigid amorphous phase (RAP). Polyamides particularly have shown great sensitivity to cooling rates and their effect on the overall RAP. Interestingly, polyamides characteristically will show increased RAP when cooled at a higher rate, contrasting with the majority of thermoplastic polymers that will increase in the mobile amorphous phase (MAP) with faster cooling rates [13]. MAP can be easily determined through the change in heat capacity at glass transition, as compared to a fully amorphous standard. The heat capacity change at T_g was subsequently compared of printed samples with increasing A_N, increasing from A_{N7} to A_{N11}. There seemed to be a clear divide in the transition, with the A_{N7}, A_{N8} and A_{N9} showing a similar yet lower change in heat capacity than compared to the A_{N10} and A_{N11} samples. Considering that these samples have comparable crystalline content, the A_{N10} and A_{N11} samples have a higher MAP than the samples printed at lower A_N. These results compliment the cooling rate results well, as the samples with lower A_N that would experience a faster effective cooling from successive laser passes additionally show more rigidity. The change in heat capacity for all printed samples is shown below in Figure 2-8.

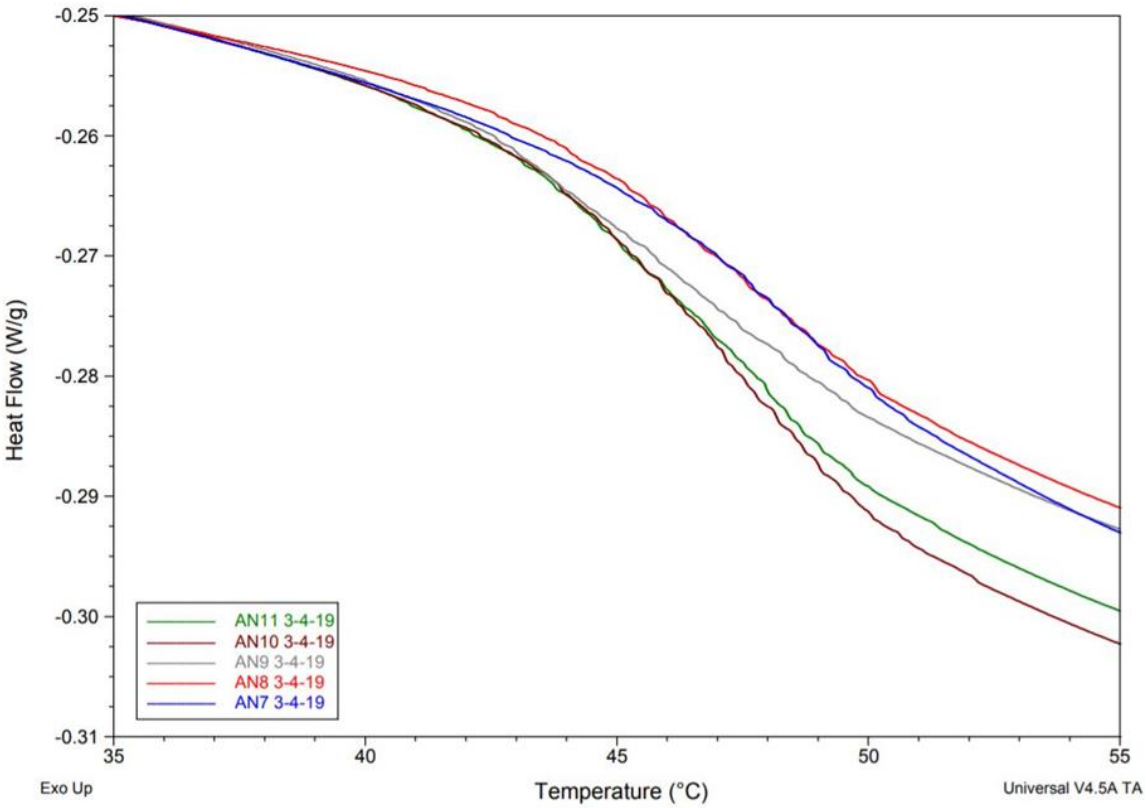

Figure 2-8: Heat capacity change for printed samples at T_g.

The specific change in RAP for increasing A_N is shown below in Figure 2-9, with varying standard amorphous heat capacity at T_g. A standard amorphous heat capacity for PA11 was determined through a model developed by Xenopoulos and Wunderlich at 68.4 J/K-mol [13]. When corrected with the PA11 monomer molecular weight and put into the equation for RAP, the values become negative for all printed samples. An experimental value of the standard amorphous heat capacity for PA11 has not presently been calculated, however a fully amorphous sample has been achieved through cooling at 1000 ^{o}K/s [12]. Considering the present material is actually a PA11/CB composite, it is likely that the modeled standard does not accurately apply. When plotting the RAP for a range of possible standard amorphous heat capacities, the separation between the A_{N7}, A_{N8}, A_{N9} and the A_{N10}, A_{N11} printed samples can be seen, especially for lower possible standards. This reduced rigidity coupled with the knowledge of increased chain rigidity with increased cooling rate of PA11 again suggests a reduction in the effective resolidification rate of the PA11 with increasing

A_N. Alternatively, this could also suggest a better ability of the A_{N10} and A_{N11} laser energy densities to re-melt areas of high rigidity with successive laser passes, especially knowing that laser depth scales well with A_N [2]. In other words, this rapid cooling could be occurring in all tested samples with the addition of the next powder layer, but the energy densities at A_{N10} and A_{N11} may be more penetrative to re-melt this transitional area and increase the contribution to the entangled bulk rather than the RAP.

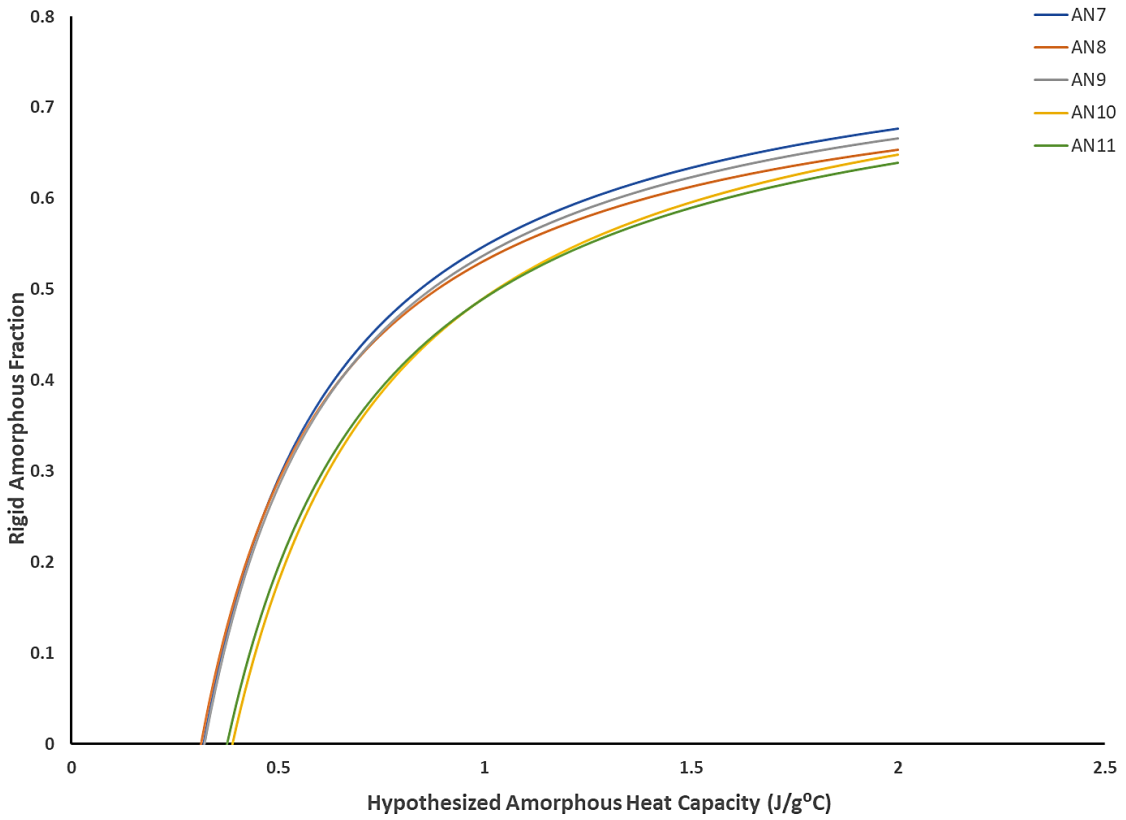

Figure 2-9: Change in RAP with increasing values of hypothesized amorphous heat capacity for all printed and tested PA11/CB.

2.3.2 X-Ray Analysis of PA11/CB

After observing the calorimetric differences between the PA11/CB powder and the printed samples at increasing A_N, both SAXS and XRD were utilized to elucidate any changes to the PA11 crystal structure during the printing process. SAXS was first performed to determine changes in the lamellae thickness during the printing process. Due to the overall similarity between the T_m for the

printed polymer, the lamellae thickness was thought to only significantly change between the powder and a representative printed sample. Thus, spectra was taken for the virgin PA11/CB powder, recycled PA11/CB powder, and a PA11/CB sample printed at A_{N9}. The calculated L_p and L_c for each sample is summarized below in Table 2-6.

Table 2-6: Changes in L_p and L_c for the virgin, recycled and A_{N9} printed PA11/CB.

PA11/CB Sample	**L_p (nm)**	**L_c (nm)**
Virgin	11.2 nm	3.8 nm
Recycled	11.3 nm	3.7 nm
Printed (A_{N8})	10.6 nm	2.0 nm

All calculated values of L_p seemed to agree quite favorably to the L_p measured in previous SAXS studies of PA11 [7]. As expected, there was not a discernible change between the L_p and L_c of the virgin and recycled powder, suggesting little to no changes of the PA11/CB powder crystalline structure in the time span of printing at elevated temperature. The printed PA11/CB showed more significant changes to the L_p and L_c, with the L_c decreasing by nearly 50% upon printing and slow cooling of the PA11/CB powder. This change in L_c between the printed and powder samples suggests the vast difference in T_m is due to a reduction of L_c of the printed PA11/CB upon cooling of the sintered part. It should be noted that while L_c is a function of T_c, there were no discernible changes in T_c and overall crystallization behavior between the powder and printed samples. The noted molecular weight increase in the printed PA11/CB could be a reason for the change, as longer polymer chains will have greater difficulty participating in chain folding and thus increasing the L_c thickness in a spherulitic structure.

XRD was utilized to analyze any changes in the PA11 unit cell upon printing, specifically changes to the crystalline phase and the d_{hkl} spacing of the crystal lattice. Upon observation of the measured spectra, all tested samples seem to show crystalline peaks consistent with the α crystalline phase, with no indication of the Brill transition into the less stable δ phase. However like the SAXS results,

there largest difference in d_{hkl} spacing was between the PA11/CB powder and the printed PA11/CB. The changes in diffraction and ultimately d_{hkl} spacing are shown in Figure 2-10 and Table 2-7.

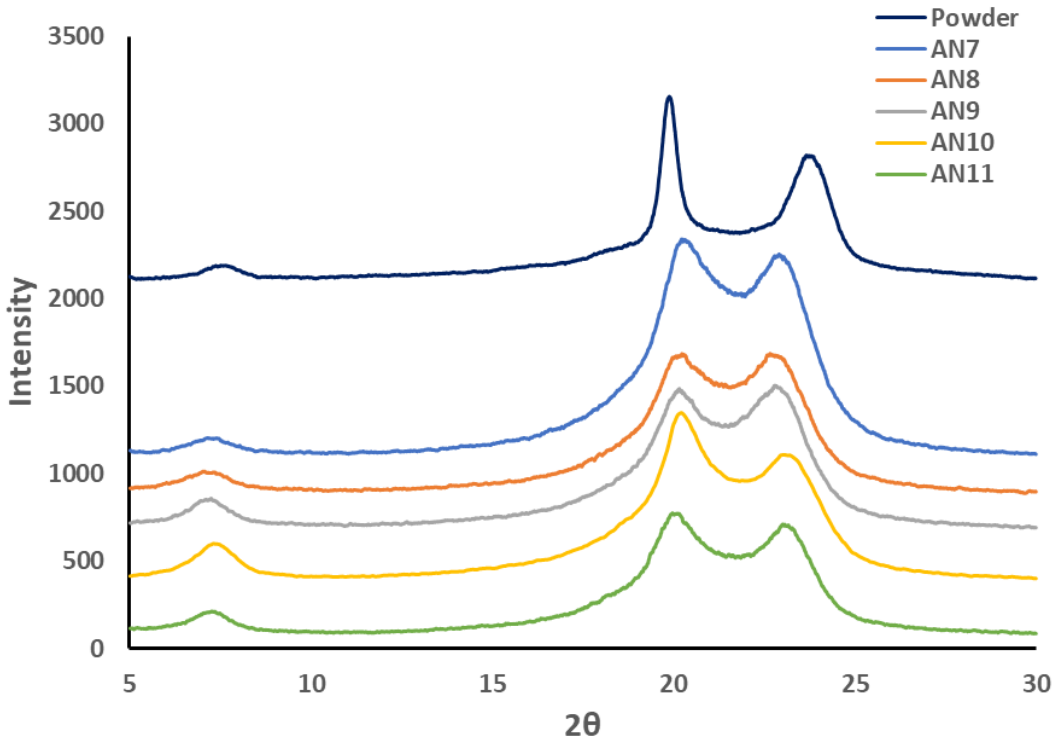

Figure 2-10: XRD diffraction peaks for powder and printed PA11/CB

Table 2-7: Changes in d_{hkl} spacing for powder and printed PA11/CB

PA11/CB	**d[001] (nm)**	**d[100] (nm)**	**d[110]/d[010] (nm)**
Virgin powder	1.165 nm	0.446 nm	0.373 nm
A_{N7}	1.215 nm	0.437 nm	0.388 nm
A_{N8}	1.233 nm	0.438 nm	0.392 nm
A_{N9}	1.220 nm	0.440 nm	0.390 nm
A_{N10}	1.208 nm	0.439 nm	0.385 nm
A_{N11}	1.213 nm	0.443 nm	0.385 nm

The [001] crystal face is representative of the linear polymer repeat unit, that is in the direction of the polymer chain. As seen in Table above, the $d_{[001]}$ spacing is much lower for the PA11/CB

powder than for the printed polymer samples. The overall changes in $d_{[001]}$ are typically attributed to conformational changes in the 10 unit methylene sequence upon heating and cooling [14]. The shortest spacing would be for a fully trans conformation throughout the chain, whereas additional gauche orientation would start to increase the chain length and ultimately $d_{[001]}$. The largest $d_{[001]}$ spacing occurred in the A_{N8} sample, followed by A_{N9}. Congruent with the concluded results in the thermal analysis section, if the lower A_N result in faster partial solidification, then it would be expected that some of the conformational disordering would be retained considering there less time for the polymer chain to reorganize favorably. The smaller value of $d_{[001]}$ calculated for the A_{N7} sample could be due to the residual unmelted powder in the printed polymer skewing the diffraction angle a bit higher. Overall, changes in $d_{[001]}$ are due to retention of conformational disorder of the methylene sequence within the PA11 upon cooling from the sintered state.

The changes in $d_{[100]}$ and $d_{[110]/[010]}$ are related to the distance between neighboring polymer chains and chain lattices, respectively [14]. The degree and orientation of hydrogen bonding has a large influence on both d_{hkl} spacings, as well as Van der Waals bonding for the $d_{[110]/[010]}$ specifically. The largest change between the PA11/CB powder and the printed samples was in the $d_{[110]/[010]}$, with a discernible change in the 2θ phase angle from 23.8° to 22.7°-23.1° for the printed samples. For a shift of this large in the lattice direction, PA11 is typically reported as α', as opposed to the solution crystalized α phase. These changes are consistent with other studies investigating the difference in d_{hkl} spacing with melt-crystalized and cooled PA11 [11]. In general, this change is likely due to a reduction of Van der Waals bonding between lattices with the introduction of gauche conformations reducing some of the interaction potential of the chains. While all printed samples demonstrated an increase in $d_{[110]/[010]}$, the A_{N8} and A_{N9} were slightly more elevated at 0.392 nm and 0.390 nm respectively. Previous studies investigating the change in d_{hkl} spacing with temperature of PA11 have shown similar values in the 40°C to 50°C range [11]. The changes in $d_{[100]}$ were more gradual,

with an overall increase in spacing with increasing A_N from 0.437 nm to 0.443 nm. For comparison, the $d_{[100]}$ for PA11/CB powder was measured at 0.446 nm. If the changes in $d_{[110]/[010]}$ are combined with the changes seen in the $d_{[100]}$ between the powder and printed PA11/CB, it is likely there have been some introduction of antiparallel hydrogen bonding between PA11 chains. This potential introduction of antiparallel hydrogen bonding would add some twisting to the extended polymer chain, which would not only slightly change the plane angle of the stacked lattices but increase the space between polymer lattice planes. Interestingly, the slight deviations in d_{hkl} spacing for both the A_{N8} and A_{N9} samples correlate well to the small shoulders in the melting peaks observed in the sample thermograms, which have been previous linked to differences in d_{hkl} spacing [11]. The changes in $d_{[001]}$, $d_{[100]}$ and $d_{[110]/[010]}$ with increases in A_N are shown below in Figures 2-11 and 2-12.

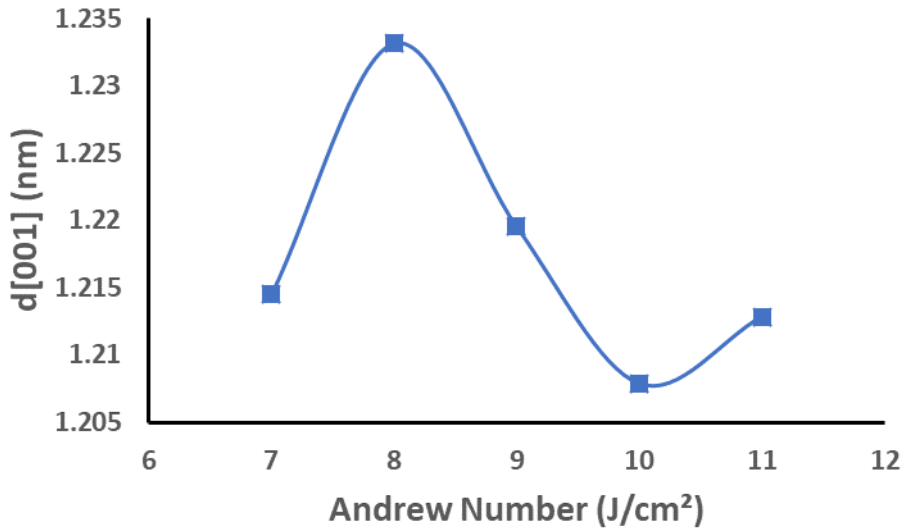

Figure 2-11: Change in $d_{[001]}$ spacing with increasing A_N

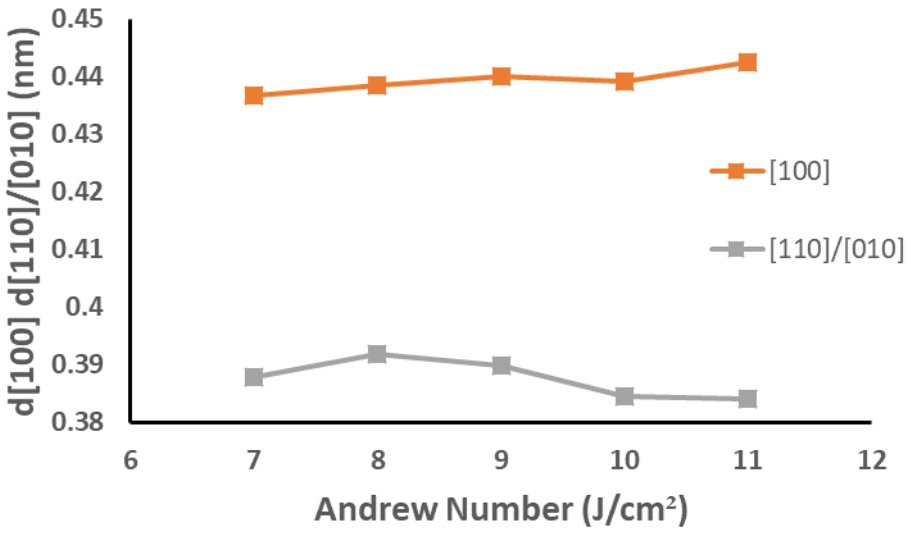

Figure 2-12: Change in $d_{[100]}$ and $d_{[110]/[010]}$ with increasing A_N

2.3.3 Infrared Spectroscopy of PA11/CB

Fourier transform infrared spectroscopy (FTIR) was utilized to further examine changes in the PA11 molecular structure through the printing process. It should be mentioned that while PA11 is extremely IR active, past studies on using FTIR to discern changes of PA11 structure between the α and α′ phase have shown only very minor differences, as compared to more significant peak changes in the δ phase [11]. The amide V and VI peaks are shown below in Figure 2-13, traditionally appearing at approximately 680 cm^{-1} and 580^{-1} respectively. The amide V peak arises from the NH out of plane stretching, whereas the amide VI peak represents the C=O out of plane stretching mode. When comparing the PA11/CB powder spectra to the printed samples, the amide V and VI peaks are more intense and narrower in the powder samples. Generally, both a broadening and intensity reduction are associated with increased torsional motion around the H_2C–C=O and H_2C–NH bonds [14]. The peak positions alternatively seem unchanged between the powder and printed samples. The combination of both phenomena confirms the transition from the α to α′ phases during the printing process, as determined in previous studies [11]. When comparing the printed samples, both amide V and VI peak area trends are similar, with a somewhat parabolic

relationship with the highest values found in A_{N7} and A_{N11} and a minimum peak area for the A_{N9} sample. As mentioned before, the unsintered powder in the A_{N7} samples are likely altering some of the spectroscopic values, creating an artificially higher peak area than the A_{N8} sample with less retained powder. The IR spectra and peak areas for both amide V and VI are shown below in Figure 2-13 and Table 2-8.

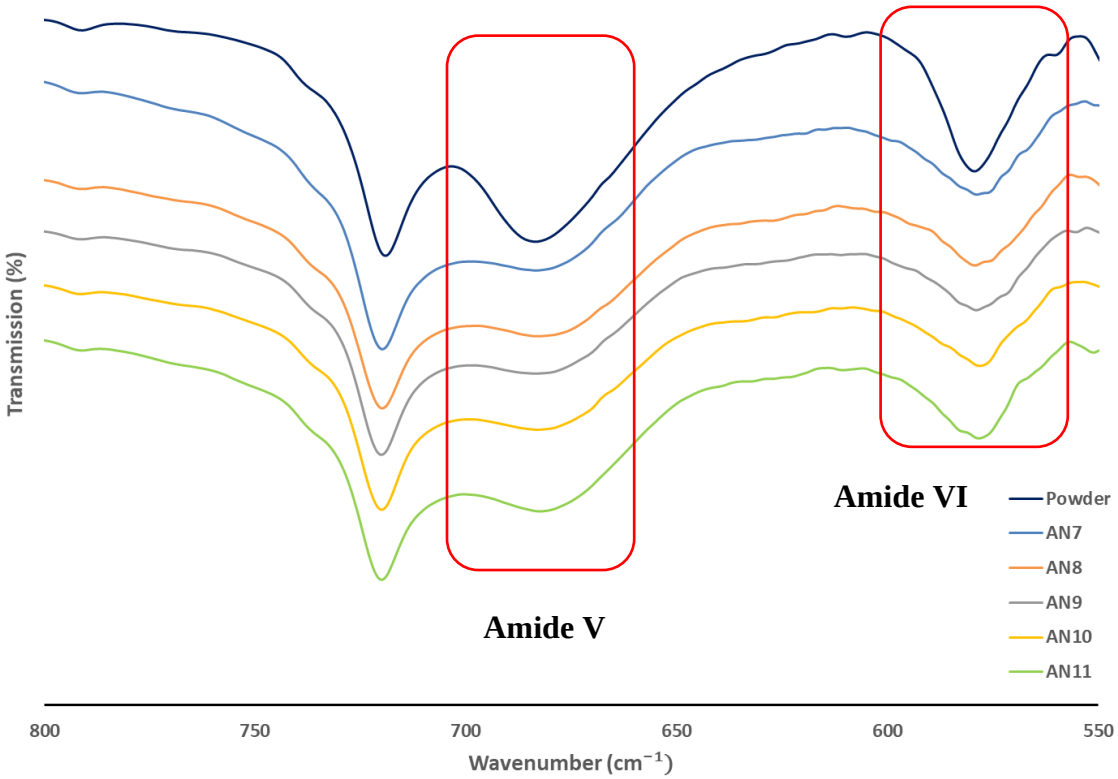

Figure 2-13: Amide V and VI bands for powder and printed PA11/CB samples.

Table 2-8: Change in peak area for the Amide V and VI bands in powder and printed PA11/CB samples.

PA11/CB sample	Amide V (%T)	Amide VI (%T)
Powder	97.4 %T	250.5 %T
A_{N7}	30.1 %T	191.1 %T
A_{N8}	25.5 %T	161.8 %T
A_{N9}	24.9 %T	151.7 %T
A_{N10}	26.8 %T	153.6 %T
A_{N11}	35.6 %T	168.9 %T

Another area of interest in the IR spectra of polyamides are the methylene progression bands, appearing between 900 cm^{-1} and 1400 cm^{-1}. The multitude of peaks are representative of CH_2 rocking and C–C stretching modes of the methylene sequence [14]. Three of these peaks show considerable change; the C–C(O) stretching at 938 cm^{-1}, and two CH_2 wagging peaks at 1190 cm^{-1} and 1240 cm^{-1}. The peak at 938 cm^{-1} shows a lowering in intensity and broadening when comparing the powder and printed PA11/CB spectra, reflecting a conformational fluctuation of the typically *trans*-zigzag methylene segment. A similar trend in broadening and intensity can be observed in the 1240 cm^{-1} peak, with the intensity particularly low in the A_{N8} and A_{N9} samples. The 1190 cm^{-1} peak shows the appearance of a small shoulder at 1198 cm^{-1} upon printing, again with a more prominent reduction in intensity for the A_{N8} and A_{N9} samples. In general, a complete disappearance and reappearance of these peaks at a higher wavenumber suggests a full transformation of the trans conformation of the methylene segment to the gauche [14]. While there is definite broadening and lowering of intensity in the aforementioned peaks upon printing, there is no complete disappearance. Thus, upon printing and recrystallization, the larger trans-zigzag methylene segment within the PA11 polymer structure likely becomes disrupted by a few gauche conformations, shortening the trans segment and producing the changes in the IR spectra shown below in Figure 2-14. The A_{N8} and A_{N9} samples specifically showed lower peak intensities,

suggesting that these two samples have a higher concentration of CH_2 units in the gauche conformation. These changes correlate well with the calculated $d_{[001]}$ and $d_{[110]/[010]}$ as measured by XRD, as the A_{N8} and A_{N9} samples demonstrated the larger changes in d_{hkl} spacing traditionally due to changes in the methylene segment in the polyamide monomer unit.

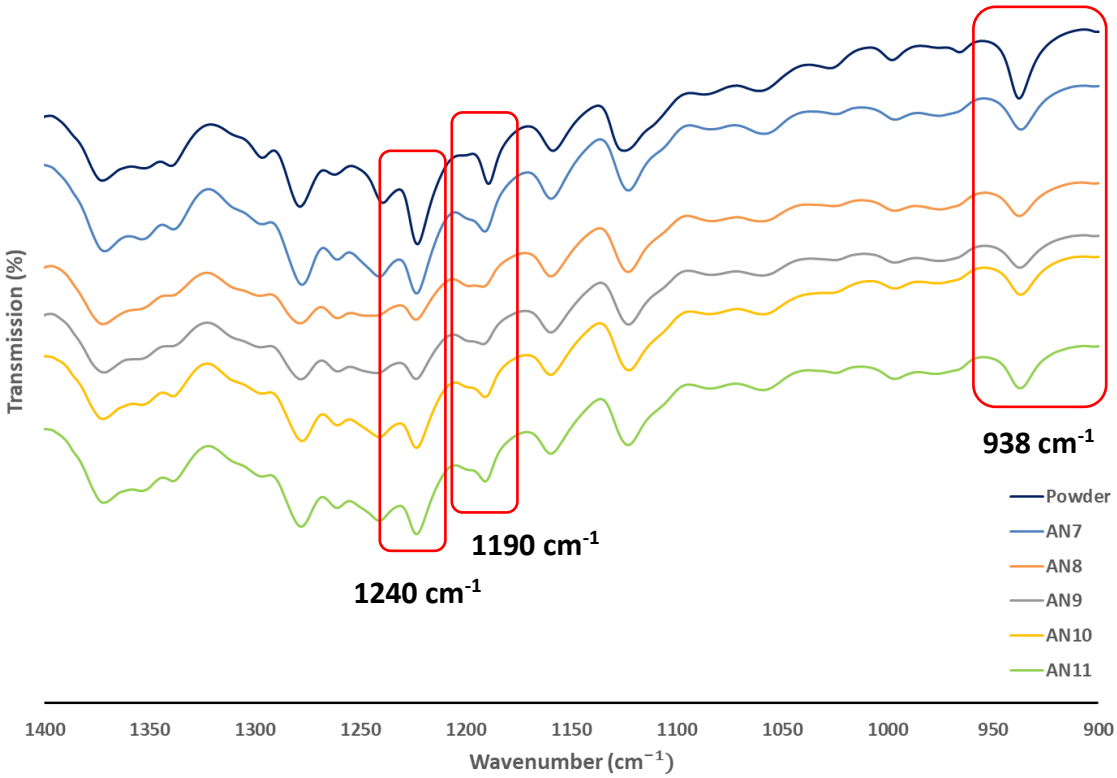

Figure 2-14: FTIR spectra of the methylene sequence in powder and printed PA11/CB.

The amide I and II bands are also sensitive to hydrogen bonding, and typically occur around 1640 cm^{-1} and 1540 cm^{-1} respectively [11]. Both peaks show definite shifting between the powder and printed PA11 samples. The amide I band was primarily shifted for the A_{N7} and A_{N8} samples, at approximately 1639 cm^{-1} and 1638 cm^{-1} respectively. The rest of the tested sample wavenumbers fell between 1634 cm^{-1} and 1635^{-1} cm. The peak area, alternatively, did not change significantly between any of the measured samples. The amide band I arises from stretching of the carbonyl group in both the hydrogen bonded crystalline and amorphous regions, as well as non-hydrogen bonded carbonyl stretching. While amide I peak shifting in PA11 has been shown not to be

influenced by change in crystalline phase, the wavenumber has been increased through a rise in temperature [11]. However, this rise in wavenumber is also associated with reduced absorbance, whereas in the present study the peak area has remained relatively unchanged. There is likely some change in the distribution of carbonyl stretching for the A_{N7} and A_{N8} samples, but none that can be specified from the present study. The amide II band stems from the bending of ordered, disordered and free N–H groups. This peak is more illustrative of crystalline phase, with larger shifts between the α, α′, and δ phases, and subsequently the prevalence of parallel or antiparallel hydrogen bonding between the amide groups. The PA11/CB powder amide II peak was at the lowest wavenumber of 1537 cm^{-1}, followed by the A_{N10} sample at 1139 cm^{-1} and the A_{N7} and A_{N11} samples at 1540 cm^{-1}. The A_{N8} and A_{N9} both had slightly elevated peak wavenumbers of 1544 cm^{-1} and 1543 cm^{-1} respectively. This shift to higher wavenumbers is indicative of the change from α to α′ of PA11, whereas the δ phase is typically represented by an amide II peak at 1555 cm^{-1}. Regardless, the change in wavenumber again for the A_{N8} and A_{N9} samples remains consistent with the other structural changes determined by DSC and XRD. The amide I and II bands are shown below for all tested samples of PA11/CB in Figure 2-15.

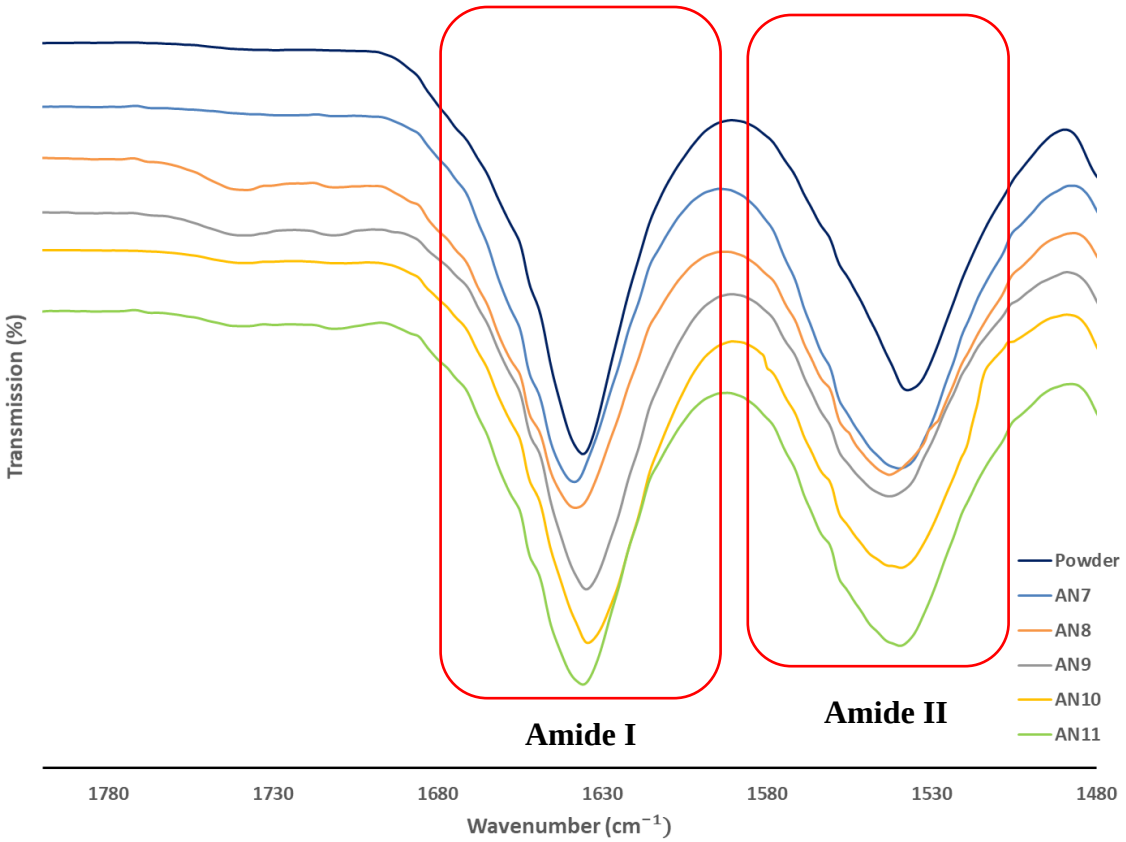

Figure 2-15: FTIR spectra of amide I and II bands for powder and printed PA11/CB

The last peak used for comparison in the powder and printed PA11/CB samples is the amide A. This composite band is due to the free, crystalline and amorphous N–H stretching of the amide group. The amide A peak for the PA11/CB powder is strikingly narrower when compared to the printed sample spectra. This is likely due to the higher X_C in the PA11 powder as compared to the printed samples, as the peak is narrowed to the wavenumber most specifically representing the crystalline N–H stretching at 3300 cm^{-1}. The peak maximums show some shifting as well, with the largest wavenumber measured in the PA11/CB powder sample at 3303 cm^{-1}. The A_{N7}, A_{N10} and A_{N11} followed with peak maximums at 3302 cm^{-1}, 3301 cm^{-1} and 3301 cm^{-1} respectively. The A_{N8} and A_{N9} samples had amide A peak maximums at slightly lower wavenumbers, each at 3300 cm^{-1}. Peak shifting of the amide A band has been noted in PA11, with shifting to lower wavenumbers indicative of the change from an α or α′ crystalline phase to the δ. The reported amide A wavenumber for the δ phase is 3297 cm^{-1}, which is a bit lower than the measured values in the

present study. While all of the printed samples show an amide A peak consistent with the α or α′ crystalline phase, the peak shift could be due to an introduction of antiparallel hydrogen bonding between amide groups in the polymer chain, particularly in the A_{N8} and A_{N9} samples. This concentration of antiparallel hydrogen bonding would be very low, but not insignificant as demonstrated by the small changes in peak wavenumbers and d_{hkl} spacing between the printed and powder PA11/CB. The amide A spectra for all tested samples is shown below in Figure 2-16.

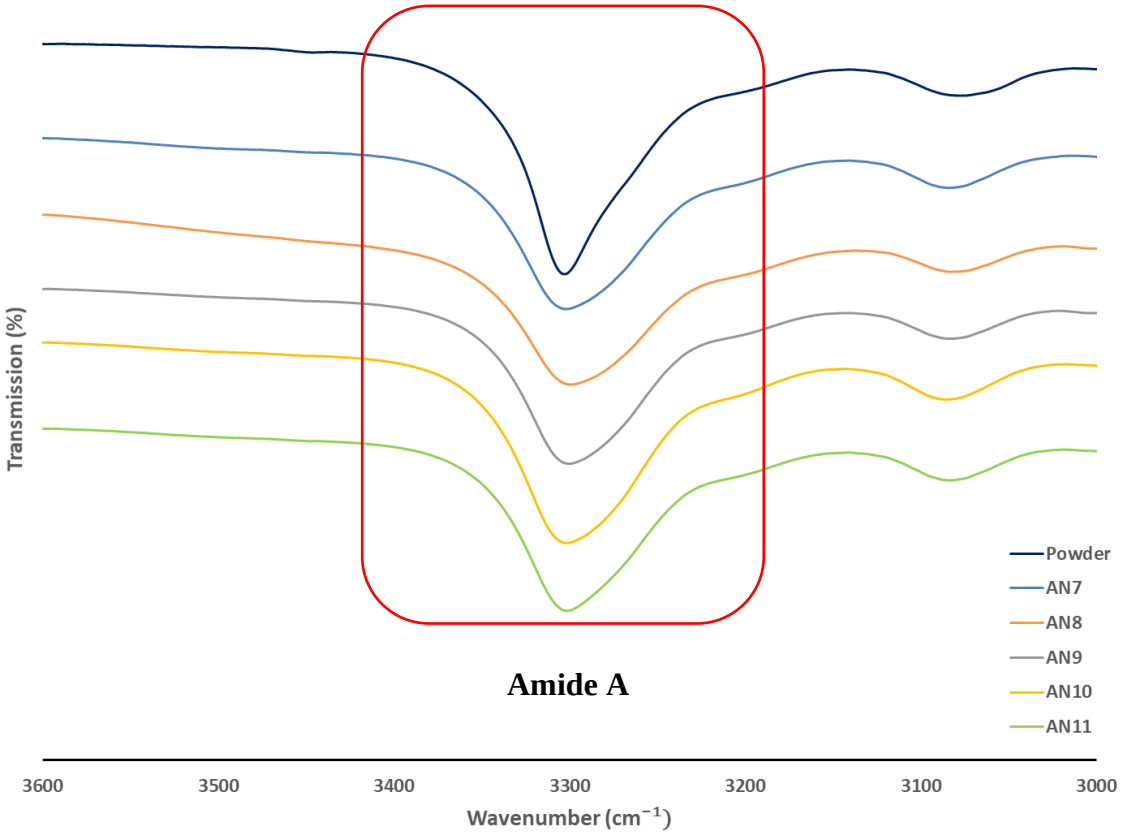

Figure 2-16: FTIR spectra of the amide A band in powder and printed PA11/CB.

2.3.4 Molecular Weight Evaluation of PA11/CB

Molecular weight evaluation was carried out on the PA11/CB powder, as well as samples printed at increasing A_N to determine any changes to molecular weight of the material through the printing process. Interestingly, polyamides are noted to engage in a linear post-polymerization if the chains are not properly terminated after primary polymerization [15]. This post-polymerization is highly

dependent on the humidity and oxidation levels [17, 18]. The humidity level in relation to the amount of acceptable water as determined by the thermodynamic equilibrium constant will control the reaction direction, with dry environments leading to further polycondensation and wet environments leading to hydrolysis and ultimately degradation. [16, 18]. High oxidation can lead to increased thermo-oxidative degradation, increasing chain scission and ultimately lowering the molecular weight [19, 20]. Characterizing the molecular weight can subsequently elucidate if any degradative or post-polymerization processes are occurring, revealing details of likely changes to the polymer structure.

As calculated through dilute solution viscometry, the PA11/CB demonstrated a consistent molecular weight (M_V) increase with increases in A_N. The M_V increase upon printing was immediately apparent between the PA11/CB powder and the samples printed at the lowest area laser energy density A_{N7}, increasing from 40.1kg/mol to 48.4 kg/mol. The M_V increase between successive increases of A_N was surprisingly very linear, with the largest M_V calculated for the A_{N11} sample at 58.1 kg/mol. This is encouraging, as it demonstrates that not only does polyamide 11 demonstrate a post-condensation molecular weight increase upon printing, but it is optimizable through controlling A_N. Select samples were additionally tested via gel permeation chromatography (GPC) under identical solvent and temperature conditions to better gauge the validity of the solution viscometry results. The selected samples (PA11/CB powder, A_{N7} and A_{N11}) weight average molecular weight (M_W) all fell within 5% difference of the M_V results of the respective samples, suggesting good validity within the solution viscometry results.

The results compare well with similar studies measuring the molecular weight of printed polyamide samples, however the vast majority have been performed on polyamide 12 [15,16,19]. The degree of increase is a bit lower, as previous studies have shown up to a tripling of M_W upon printing. Besides a change in printing material, a much higher power CO_2 laser is typically used for said

studies which could potentially alter the kinetics of post-condensation within the printed part. It should also be noted that solid state polymerization has been confirmed in the printing powder before the sintering begins [15, 16, 19]. While this undoubtedly has an effect on the molecular weight changes between the virgin powder and printed solid, the printed samples were subjected to the same thermal history prior to printing, and likely has a marginal impact as the exposure to high temperature was relatively short as compared to the exposure times in leading solid state polymerization studies of SLS powders [15, 16]. The dilute solution viscometry results are shown in Figures 2-17 to 2-22 and summarized in Table 2-9.

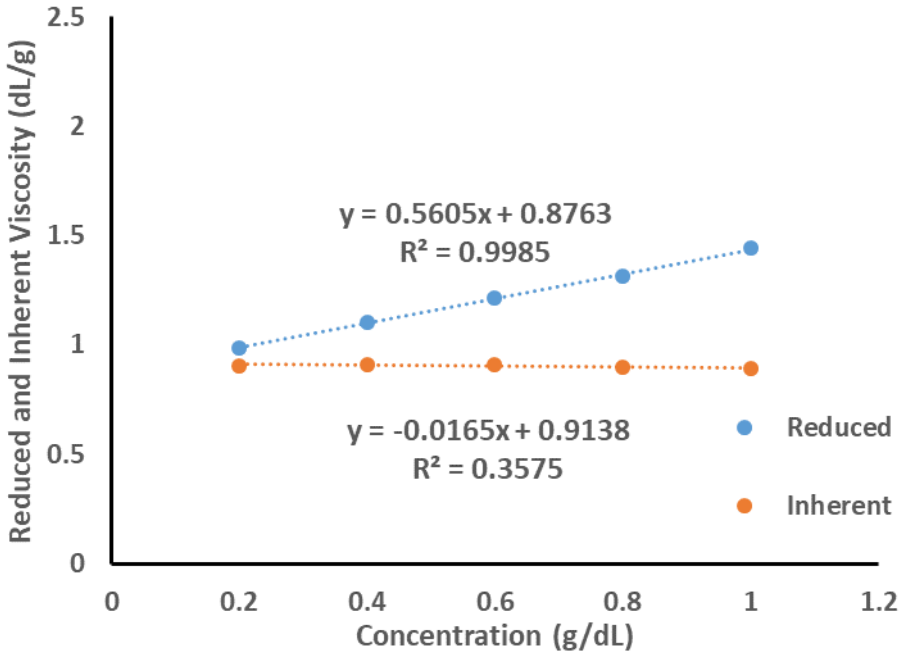

Figure 2-17: Reduced and inherent viscosity of PA11/CB powder.

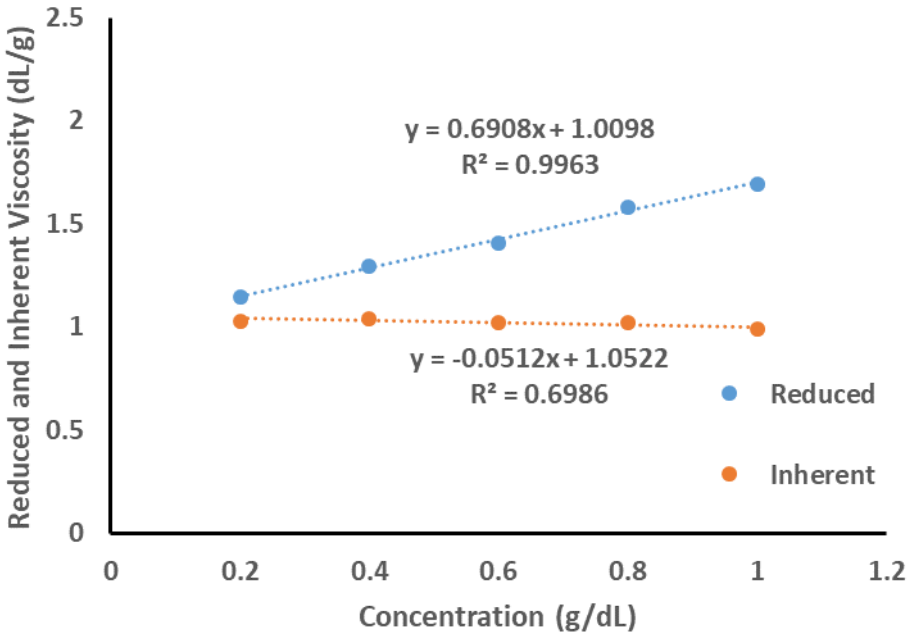

Figure 2-18: Reduced and inherent viscosity of A_{N7} printed PA11/CB

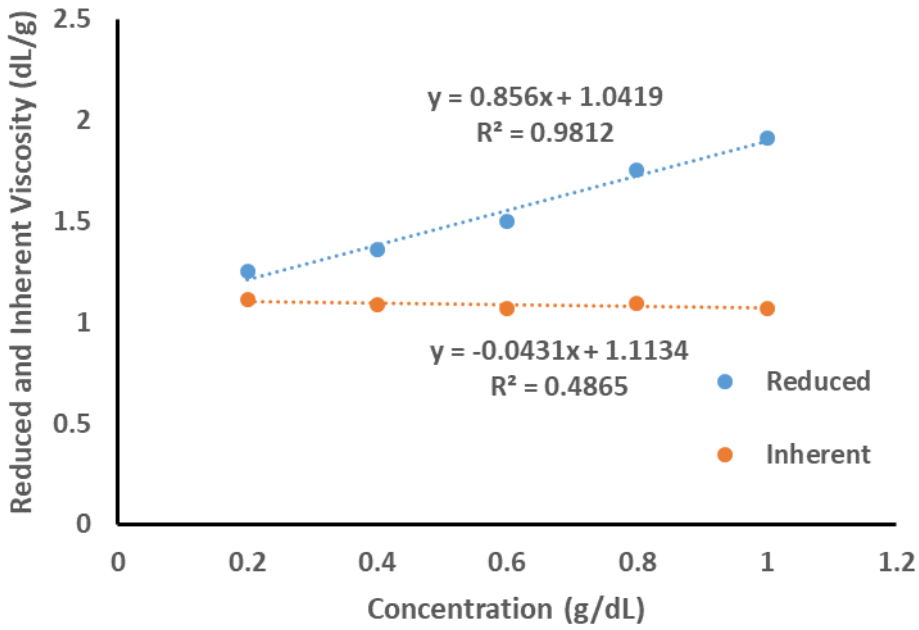

Figure 2-19: Reduced and inherent viscosity of A_{N8} printed PA11/CB

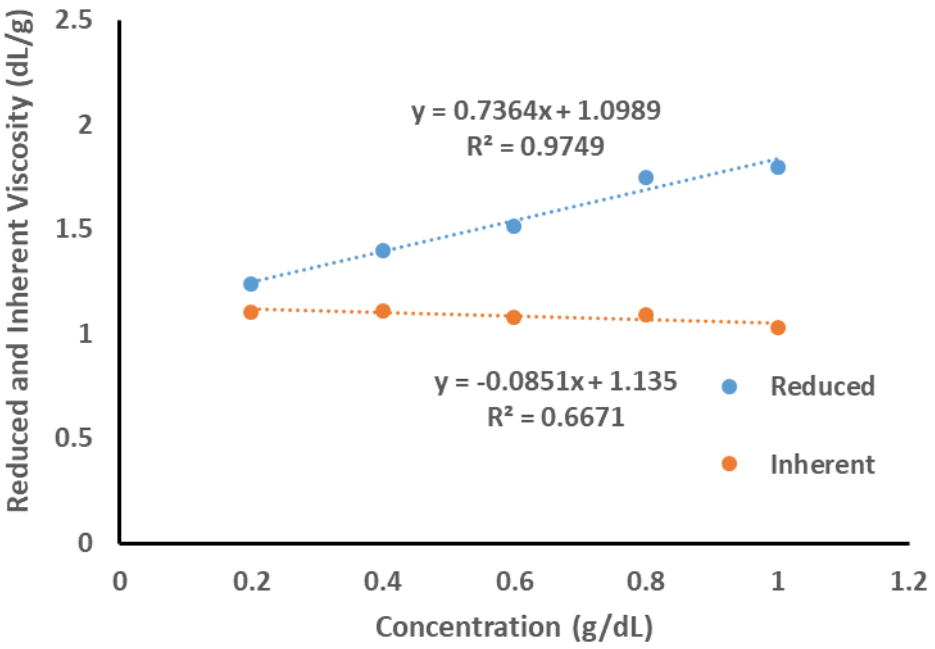

Figure 2-20: Reduced and inherent viscosity of A_{N9} printed PA11/CB

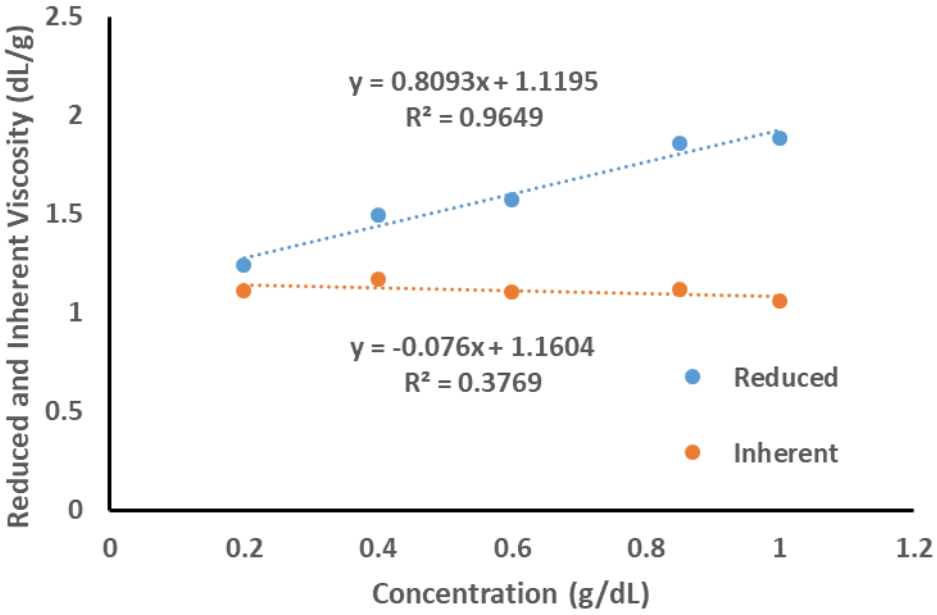

Figure 2-21: Reduced and inherent viscosity of A_{N10} printed PA11/CB

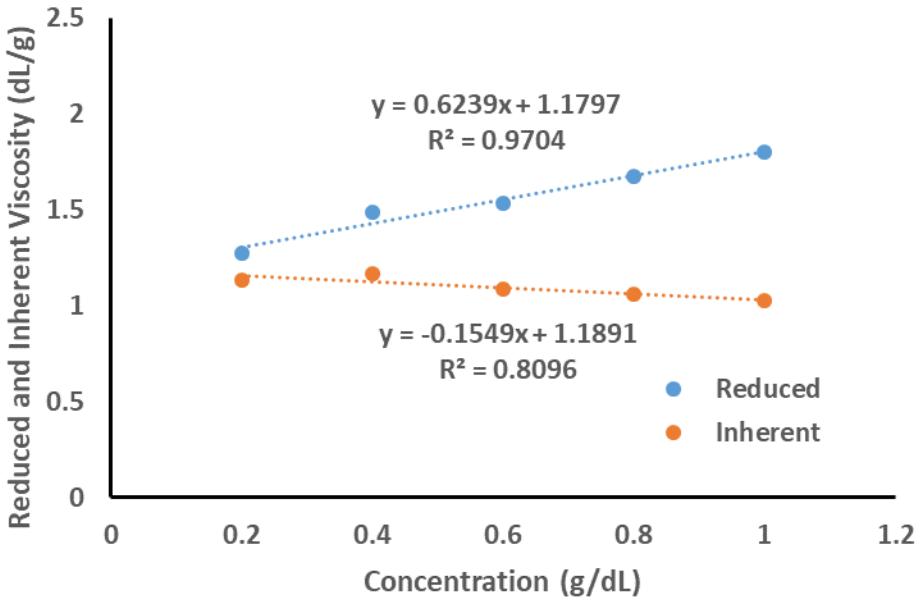

Figure 2-22: Reduced and inherent viscosity of A_{11} printed PA11/CB

Table 2-9: Intrinsic viscosity and M_V of PA11/CB powder and printed samples

Andrew Number (J/cm^2)	**Powder**	**7**	**8**	**9**	**10**	**11**
[η] (dL/g)	0.90	1.03	1.08	1.12	1.14	1.18
Mv (kg/mol)	40.1	48.4	51.4	54.0	55.4	58.1

2.3.5 Mechanical Behavior Analysis of PA11/CB

Both tensile testing (ASTM D638-14) and essential work of fracture were employed to gauge the effect of increasing A_N on the printed PA11/CB mechanical behavior. Tensile samples demonstrated a gradual increase of ultimate tensile strength and elongation to break with increasing A_N, with more of a stepwise increase in tensile modulus. Similar increases in mechanical properties of SLS printed polymer parts with increasing energy density have been studied before, however predominately focused on PA12 printed with CO_2 lasers [2,21]. Finding similar respective trends in mechanical properties with increasing laser energy density for PA11 with a blue diode laser serves not only as a benchmark for the material/laser combination, but evidence for the tailorability of mechanical properties with differing A_N.

Ultimate tensile strength, elongation to break and tensile modulus were found to increase 6.7%, 81.7% and 17.6% respectively when increasing the A_N from 7 J/cm^2 to 11 J/cm^2. Elongation to break demonstrated the most responsive change with increasing A_N, whereas the increases to ultimate tensile strength and modulus were more modest. When compared to extrusion and injection molding grades of PA11, both the ultimate tensile strength and modulus compare quite favorably. Specifically referencing Rilsan technical reports, the tensile modulus is reported lower than the measured values of this study at 1450 MPa [22]. In comparison, the highest measured average modulus in the present study (A_{N10} at 1.9 GPa) is approximately 31.0% higher than the advertised value. The ultimate tensile stress is listed at 53 MPa, which is consistent with the average values measured for this study among all tested A_N.

The key difference among the present tested samples and typical PA11 mechanical behavior lies in the elongation to break, which typically exceeds 300% in most PA11 extrusion and injection molding grades [22,23]. The average measured values for the present study ranged from 43.1% to 78.8% strain, up to a 700% difference between the standard strain values for PA11 and the printed PA11/CB samples. Data on compression molded PA11 compares well, with average tensile modulus and elongation at break measured to be 1.3 GPa and 38.4% respectively [23]. Listed yield stress values are additionally very similar to ones observed in the present study. Representative tensile behavior and comparison of mechanical properties of all tested A_N are shown below in Figures 2-23 and 2-24, respectively.

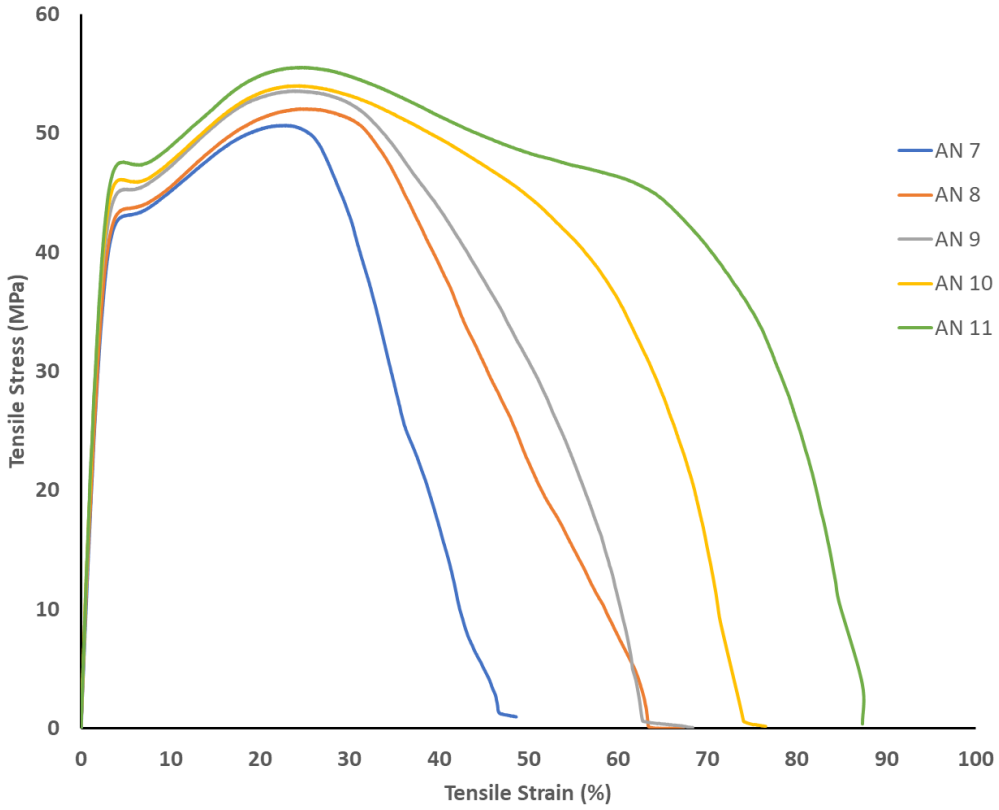

Figure 2-23: Representative tensile behavior of printed PA11/CB with increasing A_N

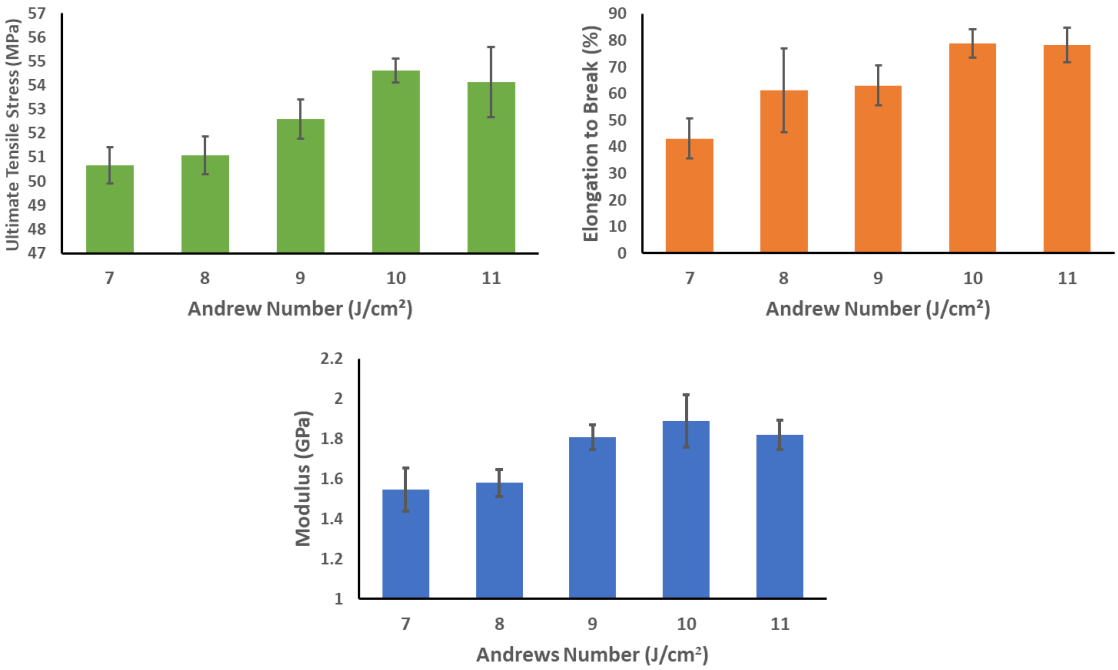

Figure 2-24: Change in ultimate tensile stress, modulus and elongation to break of PA11/CB with increasing A_N

In addition to tensile testing, essential work of fracture (w_e) was performed to elucidate the change in fracture behavior and calculated fracture toughness of the PA11/CB with increasing A_N. The w_e was found to steadily increase from 23.5 kJ/m^2 at A_{N7} to 29.6 kJ/m^2 for A_{N11}, a 26.0% change. In addition to the w_e values, the slope of the work of fracture line (βw_p) also increases with A_N. The β constant is representative of the geometry and size of the outer plastic dissipation zone, thus the increase in slope suggests increases in the plastic zone size with increasing A_N. The w_e values determined in the present study compare quite favorably to toughened polyamide 66, with reported values close to 18 kJ/m^2[24]. Interestingly, the w_e of the printed PA11/CB seems more comparable to toughened polyamide, with present values larger than w_e for 3 vol. % TiO_2 toughened polyamide 6 at 19.49 kJ/m^2 [25] and the carbon fiber toughened polyamide Onyx at 24.14 kJ/m^2 [26]. The load/displacement curves and work of fracture linear regressions for each tested A_N are shown below in Figures 2-25 to 2-29, and all of the mechanical behavior results of printed PA11/CB are summarized in Table 2-10.

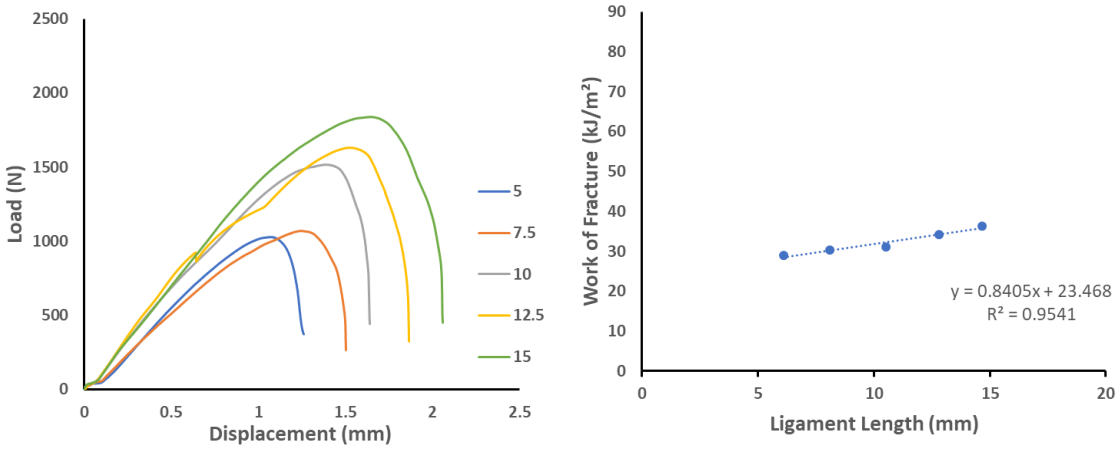

Figure 2-25: Essential work of fracture results for the A_{N7} printed PA11/CB

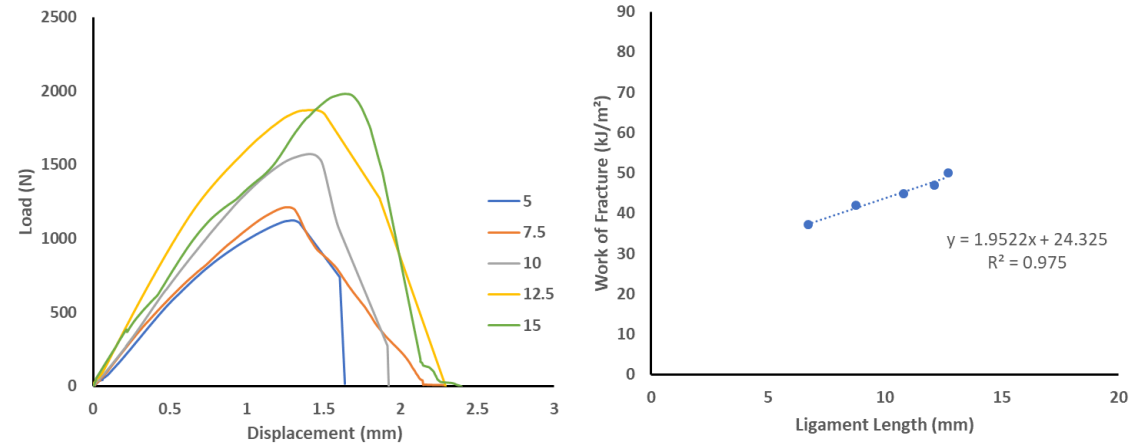

Figure 2-26: Essential work of fracture results for the A_{N8} printed PA11/CB

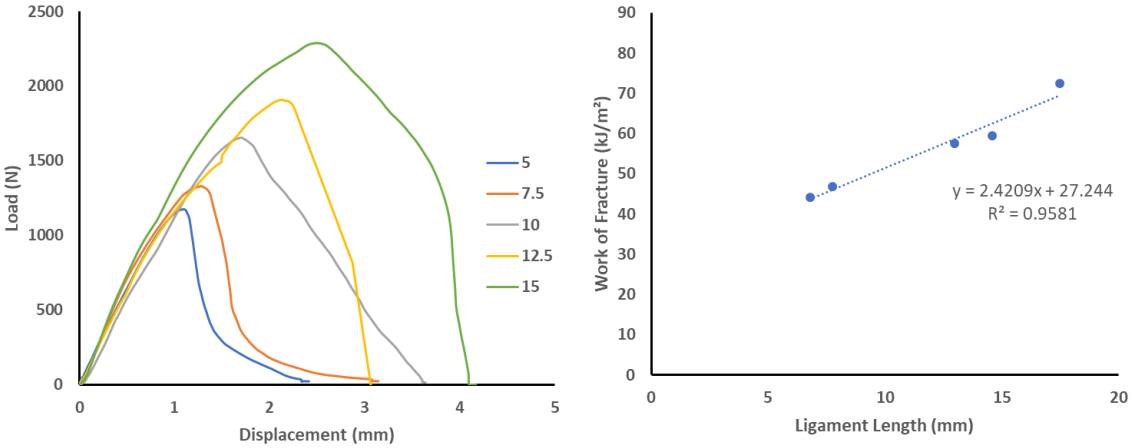

Figure 2-27: Essential work of fracture results for the A_{N9} printed PA11/CB

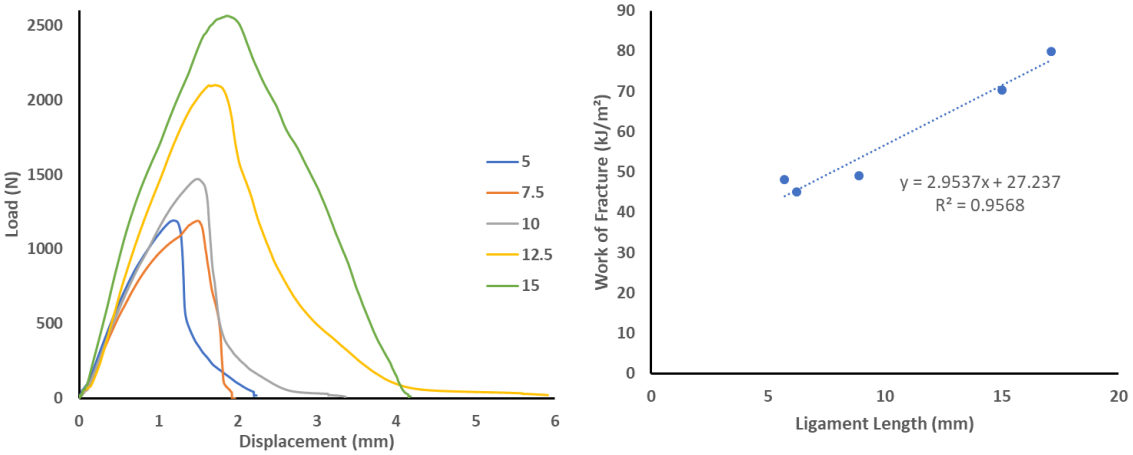

Figure 2-28: Essential work of fracture results for the A_{N10} printed PA11/CB

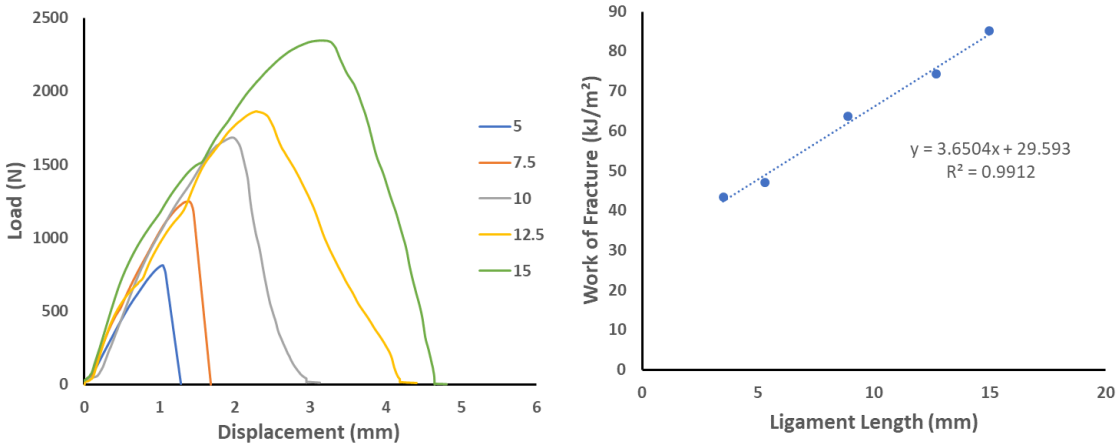

Figure 2-29: Essential work of fracture results for the A_{N11} printed PA11/CB

Table 2-10: Summary of tensile and fracture testing results for printed PA11/CB

Andrew Number (J/cm^2)	**Ultimate Tensile Strength (MPa)**	**Elongation to Break (%)**	**Tensile Modulus (GPa)**	**W_e (kJ/m^2)**	**Work of Fracture R^2 Fit**
7	50.7 ± 0.8 MPa	43.1 ± 7.5%	1.5 ± 0.1 GPa	23.5 kJ/m^2	0.95
8	51.1 ± 0.8 MPa	61.4 ± 15.8%	1.6 ± 0.1 GPa	24.3 kJ/m^2	0.98
9	52.6 ± 0.8 MPa	63.1 ± 7.5%	1.8 ± 0.1 GPa	27.2 kJ/m^2	0.96
10	54.6 ± 0.5 MPa	78.8 ± 5.4%	1.9 ± 0.1 GPa	27.2 kJ/m^2	0.96
11	54.1 ± 1.5 MPa	78.3 ± 6.5 %	1.8 ± 0.1 GPa	29.6 kJ/m^2	0.99

While the modulus and ultimate tensile stress values compare favorably to standard PA11 measured mechanical properties, the elongation to break still stands starkly different between the printed and injection molded PA11. The sources of these large changes are difficult to narrow, as numerous changes to the polymer structure can result in vastly different mechanical properties. Crystalline structure of semicrystalline polymers and its relation to mechanical properties has been studied vastly, with clear connections to both the crystalline and amorphous regions. Generally, when crystallinity increases in aliphatic nylons, the yield stress and stiffness increase with a decrease with a decrease in elongation [27]. Similarly, increased lamellae thickness has also demonstrated a resulting increase in yield stress [27]. Spherulite size also has a definite effect on mechanical behavior, with decreasing spherulite size leading to increasing impact strength and elongation to

break [27]. Within the amorphous region, entanglement density and presence of tie molecules have been linked favorably to elongation to break, fatigue lifetime and fracture toughness [27]. Chain mobility has shown similar effects on mechanical behavior as entanglement density, with specific enhancements in plastic deformation and post-yield strain hardening or necking [27]. The spherulitic structure of the printed and powder PA11/CB proved very difficult to ascertain using traditional polarized light optical microscopy, likely due to the addition of carbon black obscuring the light. Very limited studies were performed using scanning electron microscopy on etched A_{N9} samples, with average spherulite diameter ~4µm. Selected spherulite images are shown below in Figure 2-30.

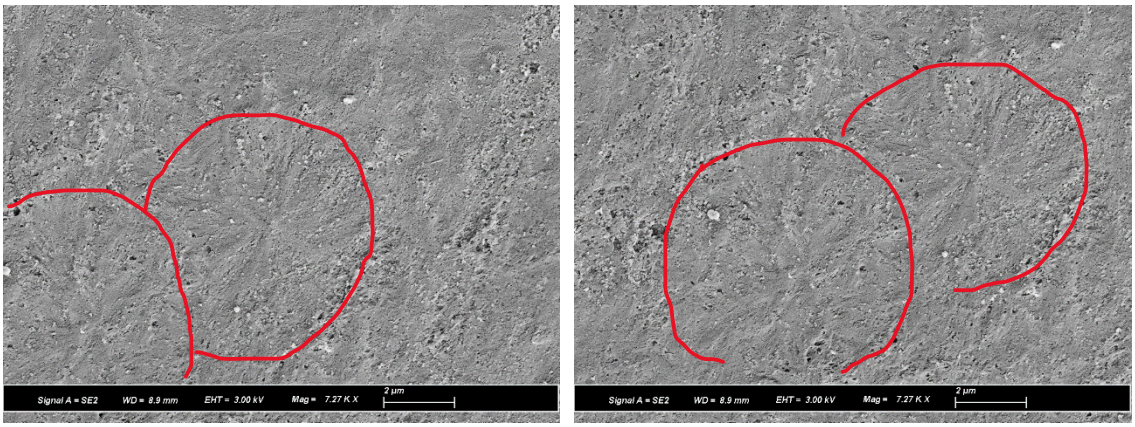

Figure 2-30: Isolated spherulites outlined in red on an etched PA11/CB A_{N9} cryogenically fractured DENT fracture surface.

Printed PA11/CB A_{N7} and A_{N11} samples were additionally imaged through TEM to better analyze potential change in spherulite size with increasing A_N. Spherulites were identified through the presence of CB at the impinged spherulite interfaces, as shown below in Figure 2-31. In general, the spherulite dimensions were 5 µm or less for both samples, however the PA11/CB A_{N11} samples exhibited impinged spherulites with visually smaller size, some with single micron diameters. While this is very qualitative and not conclusive on the role of increasing A_N with spherulite microstructure, the TEM study does suggest potential refinement of spherulites with increasing

laser intensity. Representative TEM images of both the A_{N7} and A_{N11} are shown below in Figure 2-31.

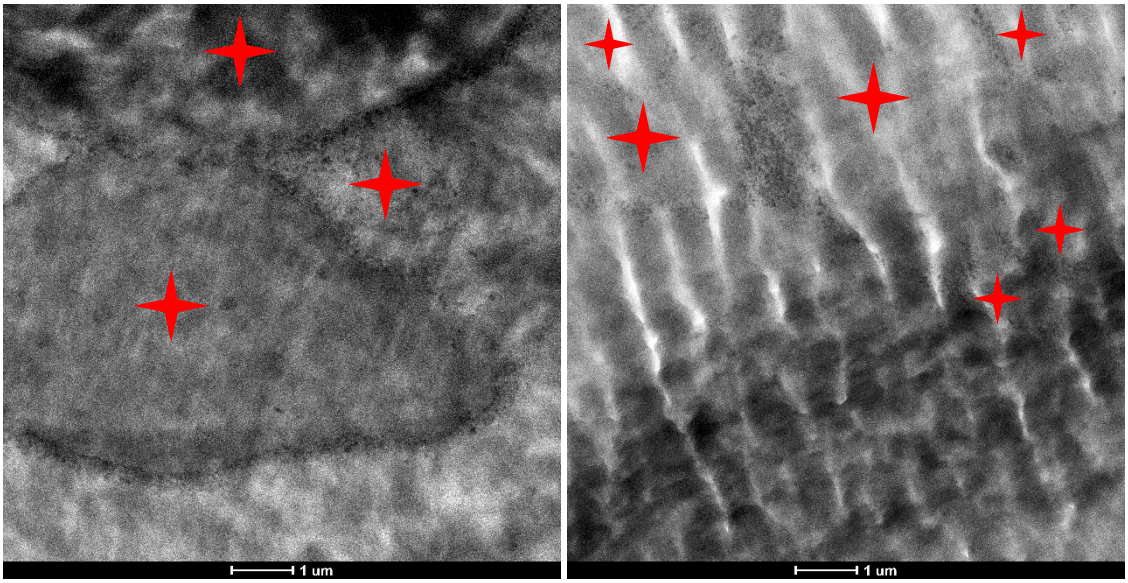

Figure 2-31: Impinged spherulites on stained PA11/CB A_{N7} (left) and PA11/CB A_{N11} (right) samples. Red stars indicate the center of each spherulite, with high volumes of carbon black visible at the spherulitic boundaries.

When reviewing the proposed crystal structure changes in the printed PA11/CB, the percent crystallinity, lamellae thickness and crystal phase were determined to likely be very similar with increasing A_N. The presence of a residual unsintered powder melting peak in the A_{N7} and A_{N8} samples suggested incomplete melting of the powder, the unmelted sections possibly acting as a source of stress concentration resulting in more brittle fracture. The PA11/CB powder itself additionally has a much higher crystallinity and rigidity than the melted PA11/CB, possibly acting as a source of brittle failure within the printed polymer samples. Another significant change was found in chain mobility, with the A_{N10} and A_{N11} samples having lower calculated RAP as compared to the printed samples at lower A_N. There have not been any significant correlations proposed currently between the RAP and mechanical behavior, however increased chain mobility in general leads to more ductile polymers. With a lower RAP and a subsequent larger percentage of polymer chains in the mobile amorphous phase, it could provide some reasoning to the increases in elongation to break and w_e at higher A_N.

Unfortunately, the spherulitic structure of all printed samples and the PA11/CB powder were not as easily ascertained in the present study. Interestingly, it should be noted that PA11 specifically has noted self-nucleating behavior, that is increased nucleation and nucleation rate due to the presence of self-seed crystal remnants [28]. Specifically, upon repeated melting and slow cooling, the spherulitic structure of PA11 will become more fine without demonstrative changes to the percent crystallinity given the cooling rate is identical [28].With increasing A_N, the laser penetration depth will subsequently increase, likely melting not just the topmost layer of powder but the previous layers underneath. After undergoing successive sintering cycles, the polymer is likely to crystallize in smaller spherulites due to the self-nucleating behavior or post-condensation of PA11. The diffusion of chains between neighboring particles and printing layers is also likely to increase with successive laser rasters over the same area, reducing sources of stress concentration and enhancing the entanglement density of the polymer. This could be a reason for continuous increase in w_e with increasing A_N, as both refinement of spherulitic size and higher entanglement density would improve the toughness of a semicrystalline polymer. In summary, a number of separate microstructural and crystalline structure changes during the printing process may have influenced the resulting mechanical behavior of the printed PA11/CB. Namely:

1. Unsintered PA11/CB powder acting as a stress concentrator within the printed sample.
2. Increased chain mobility and percentage of polymers constituting the mobile amorphous phase, possibly in higher contribution to the entangled bulk.
3. Smaller spherulitic size due to molecular weight increase and self-nucleating behavior of PA11 with successive laser passes at increasing laser penetration depth.

2.3.6 Imaging of PA11/CB Tensile and Fracture Surface

Fractography proved very revealing about the potential changes in polymer microstructure of PA11 with increasing A_N. In general, all tested samples demonstrated ductile fracture and failure. The

major change was the diminishing of separate polymer bulk tears and voids into a more prominent necked region stretched through the entire width of the tensile specimen. The most prominent shift occurred between the A_{N7} and A_{N8} samples, where higher density of tearing and voiding occurred only near the edges of the A_{N8} sample, whereas this tearing and voiding occurred throughout the entire A_{N7} tensile surface. The progression of a defined neck region with increasing A_N is demonstrated below in Figure 2-32.

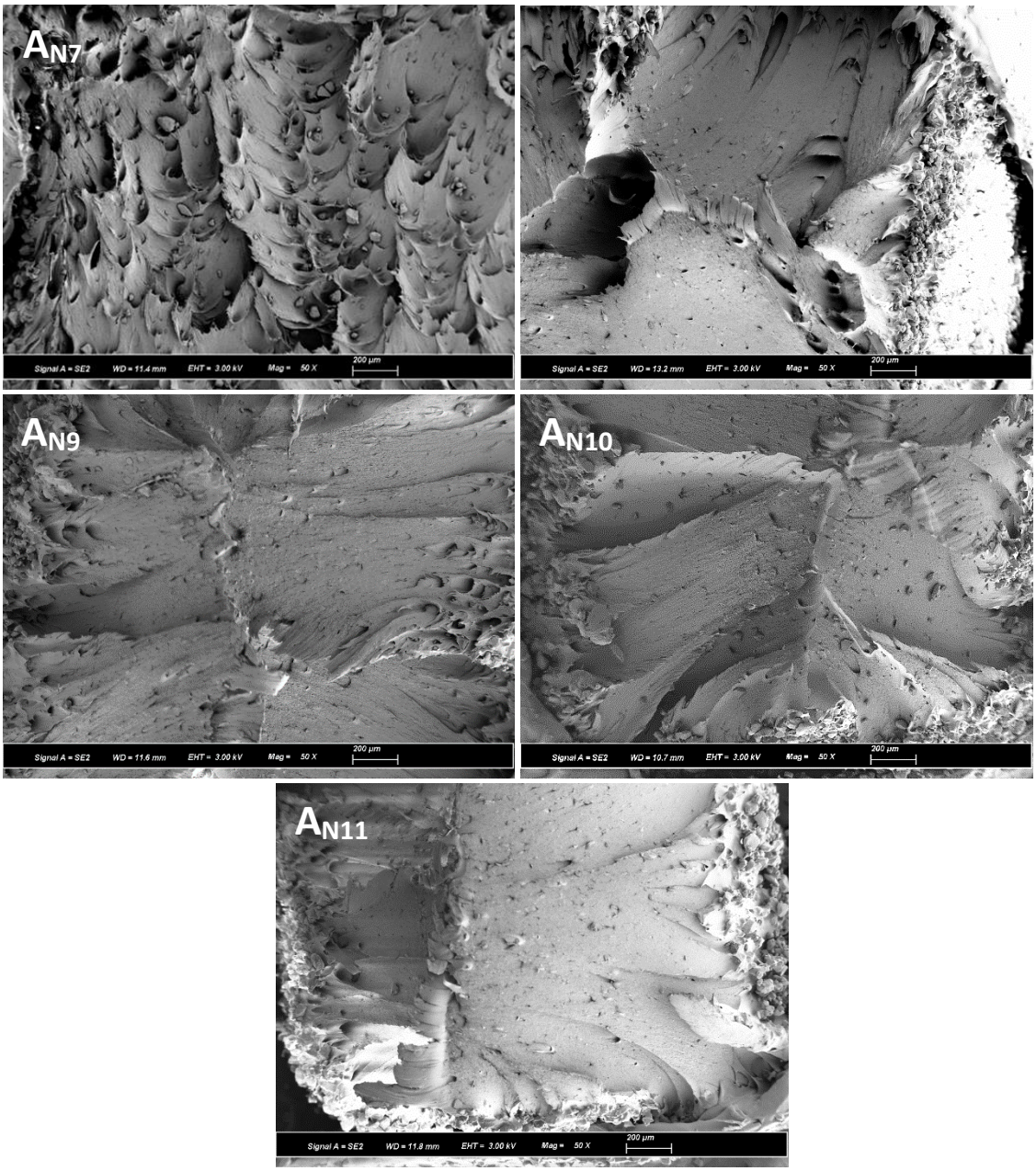

Figure 2-32: Progression of necked region in tensile specimens with increasing A_N

The source of the larger voids found in the A_{N7}, A_{N8} and A_{N9} samples seem to derive from unsintered or partially sintered polymer particles remaining within the bulk. The vast majority of these particles were found in the A_{N7} sample, with the ductile tearing of the bulk advancing on the outside of these particles. The presence of these particles in the bulk coupled with the measured tensile elongation in break suggests the presence of these particles act as a source of stress concentration within the tensile sample. Additionally, the polymer powder has shown to be incredibly more crystalline than the fully sintered polymer, likely with increased average spherulite size. Thus in addition to acting as a stress concentrator, these unsntered particles may promote brittle fracture through failure at the spherulitic boundaries instead of the slipping, unfolding and void coalescence of the ordered lamellae. The texture of the bulk polymer matrix shown an elongated and oriented fibrillar network, especially in the necked region of the tested region. When observed closer, small microvoids can be seen between the oriented fibrils, consistent with documented microvoid formation in the amorphous phase of semicrystalline polymers between oriented fibrils [27,29]. Figure 2-33 contrasts images of unsintered particles with the ductile polymer matrix of tested samples. Additionally, selected images of the tensile surface are shown for tested samples at each A_N in Figures 2-34 to 2-38.

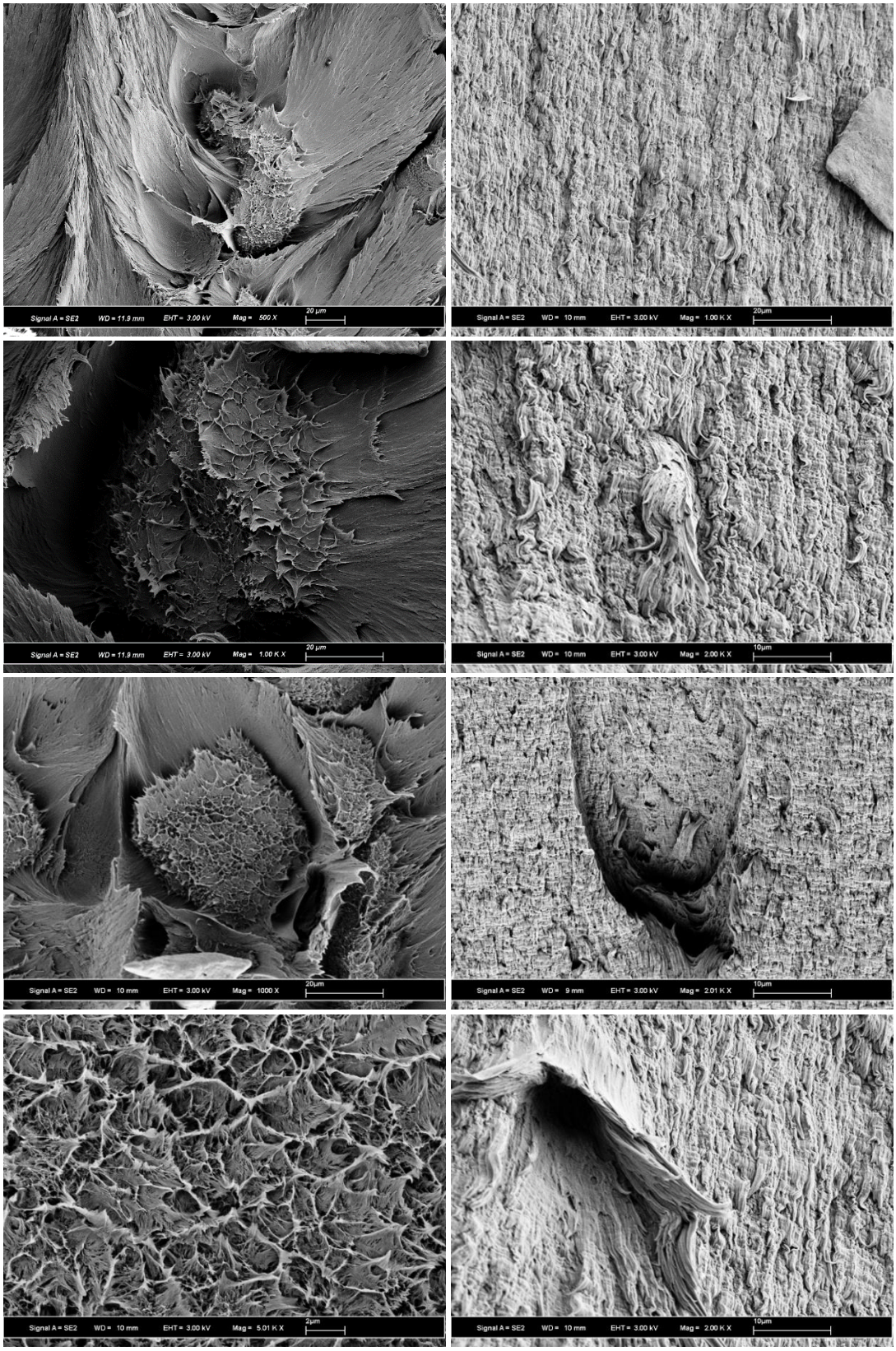

Figure 2-33: Comparison of unsintered PA11/CB particles and ductile tearing in printed PA11/CB A_{N7} (left) and A_{N9} (right) tensile specimens.

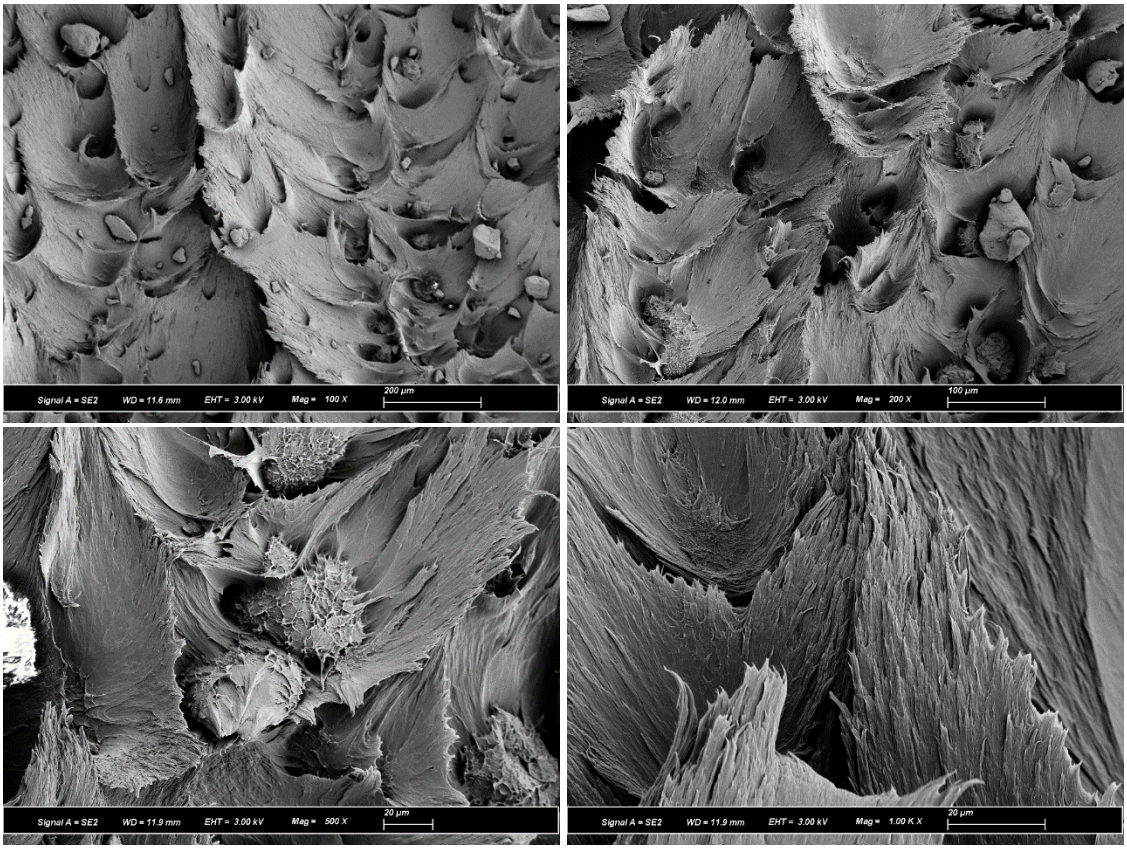

Figure 2-34: Selected tensile fracture surface images of A_{N7} printed samples.

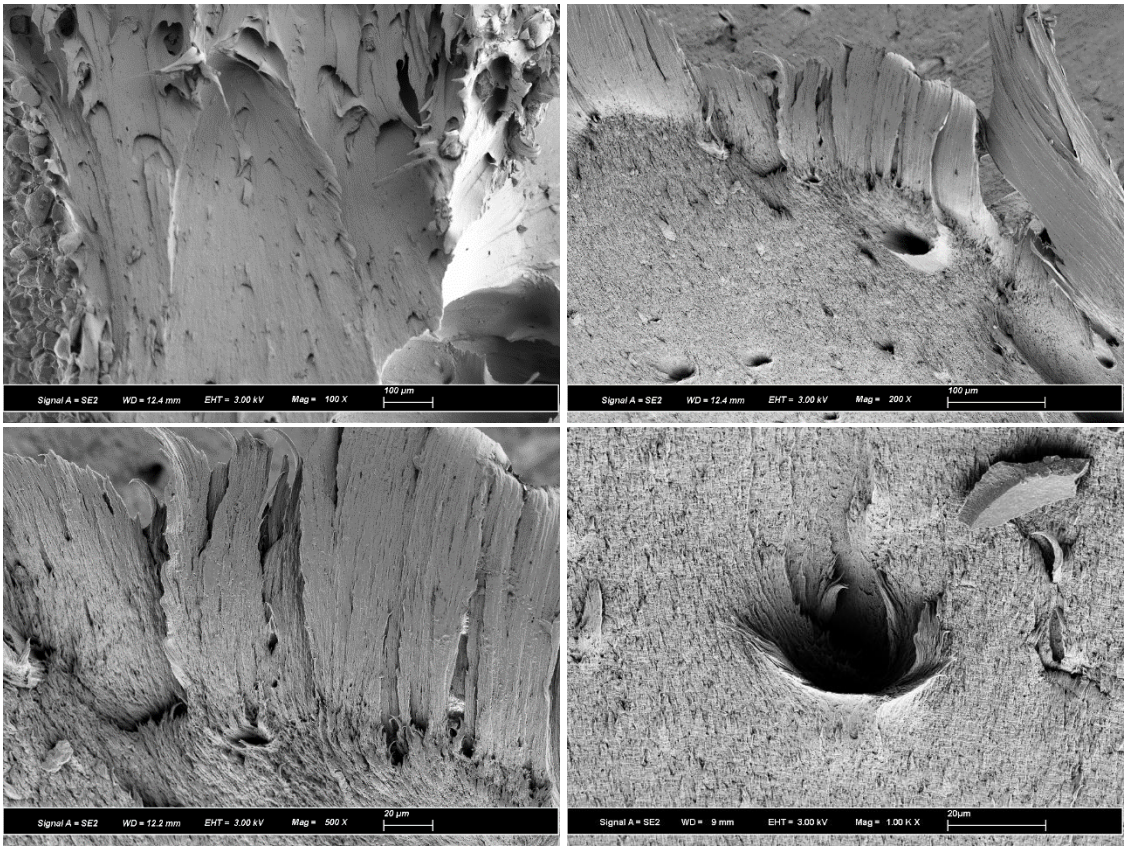

Figure 2-35: Selected tensile fracture surface images of A_{N8} printed samples.

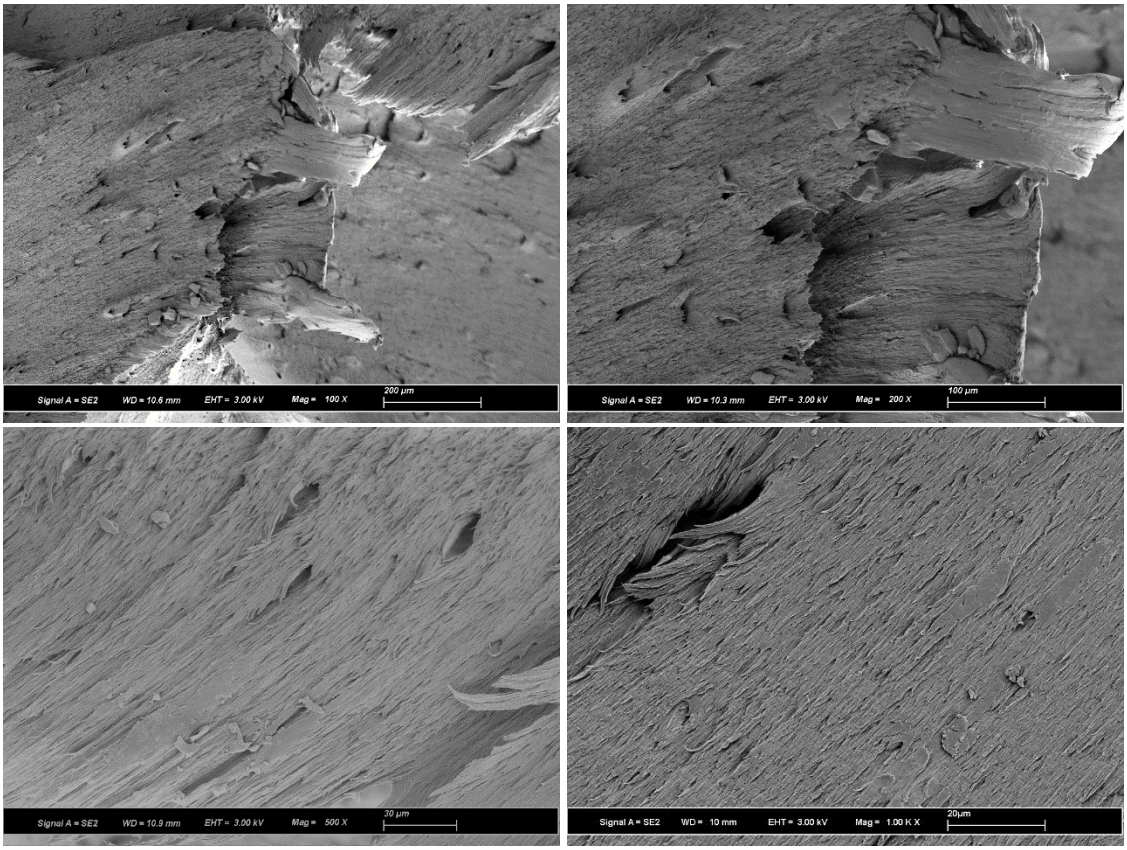

Figure 2-36: Selected tensile fracture surface images of A_{N9} printed samples.

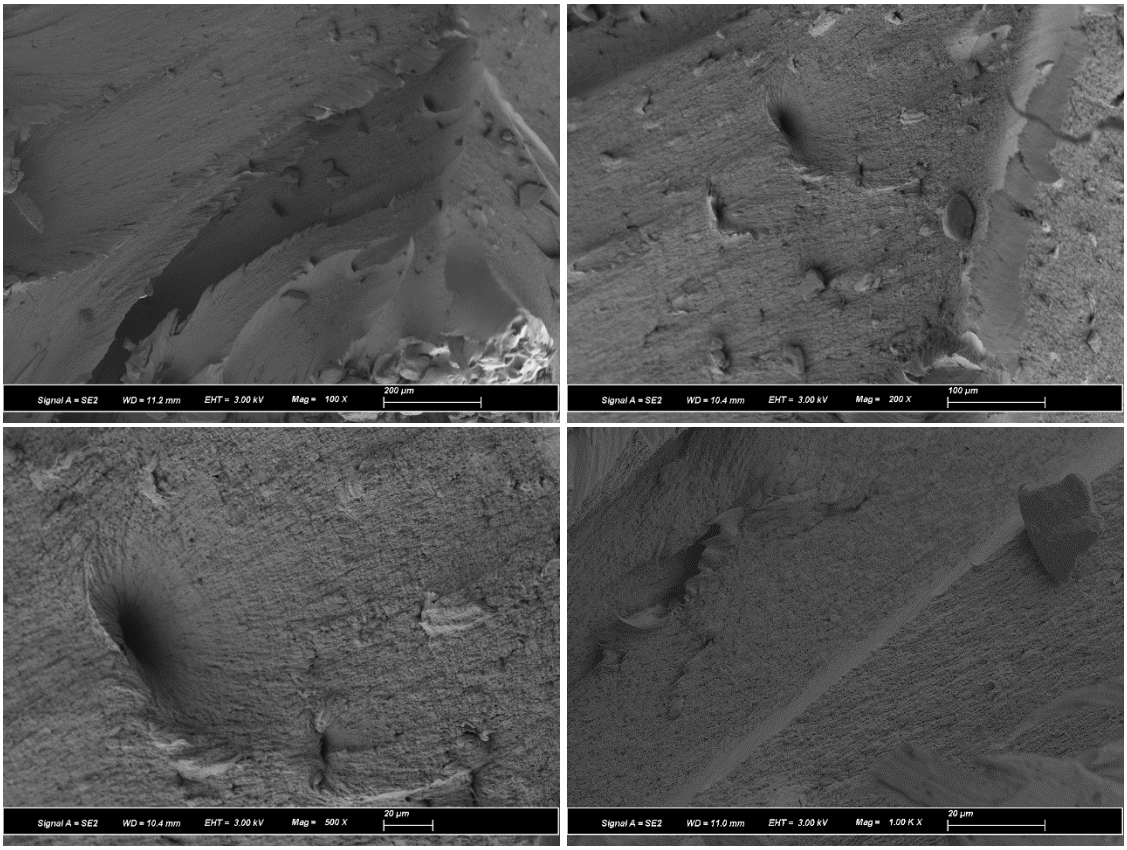

Figure 2-37: Selected tensile fracture surface images of A_{N10} printed samples.

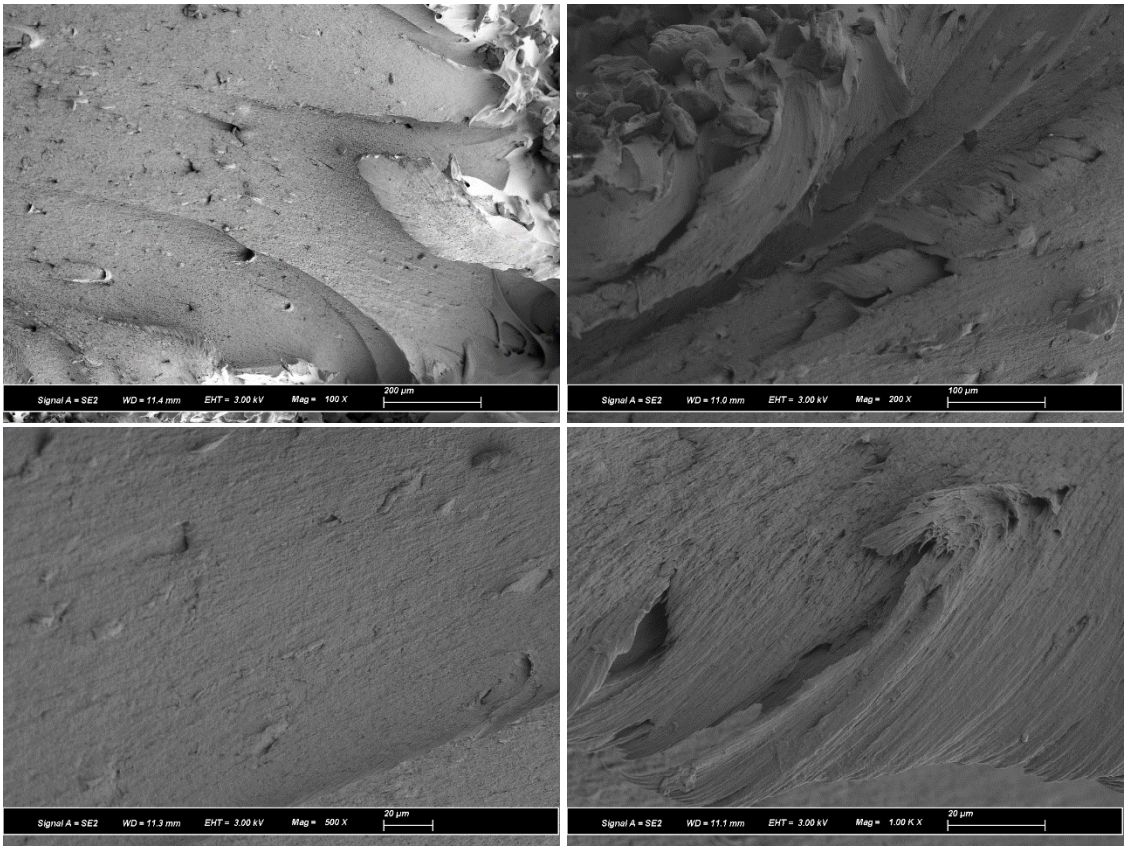

Figure 2-38: Selected tensile fracture surface images of A_{N11} printed samples.

In addition to the tensile surfaces, the essential work of fracture surfaces were examined. The samples demonstrated a unique "dimpled" surface, documented in previous essential work of fracture studies on nylons [24, 30]. In general, the spacing of these dimples are dependent on the number and type of inclusions (sources of stress concentration), whereas the shape is based on the stress state of the sample upon fracture [29]. The size is most correlated with increasing fracture energy and plastic work done by the sample upon fracture. In semicrystalline polymers, common inclusions include spherulite nuclei and general matrix defects [29,30]. In the case of filled semicrystalline polymers, particle aggregates and their subsequent cavitation can additionally act as inclusions [30]. For a dimpled fracture surface, the primary source of dimple formation and crack propagation is through microvoid coalescence nucleated at any of the aforementioned inclusion

sites, however in filled polymer systems cavitation or debonding of the particle from the matrix can also contribute [30].

In the PA11/CB samples tested for this study, the prominent inclusion sources seemed to change with increasing A_N. In the A_{N7} and A_{N8} samples, layer defects can be easily seen on the fracture surface, with poorly sintered particles visible in a straight line along the crack direction. A high density of dimples can be seen germinating from the direction of these poorly sintered bed layers, suggesting the crack propagated through these faulty print layers before deflecting into the sintered bulk. In between these faulty layers, the dimples in both samples seem well aligned in the direction of fracture, suggesting more stable crack propagation through the sintered bulk. Evidence of these poorly sintered layers in the A_{N7} and A_{N8} samples are shown below in Figure 2-39.

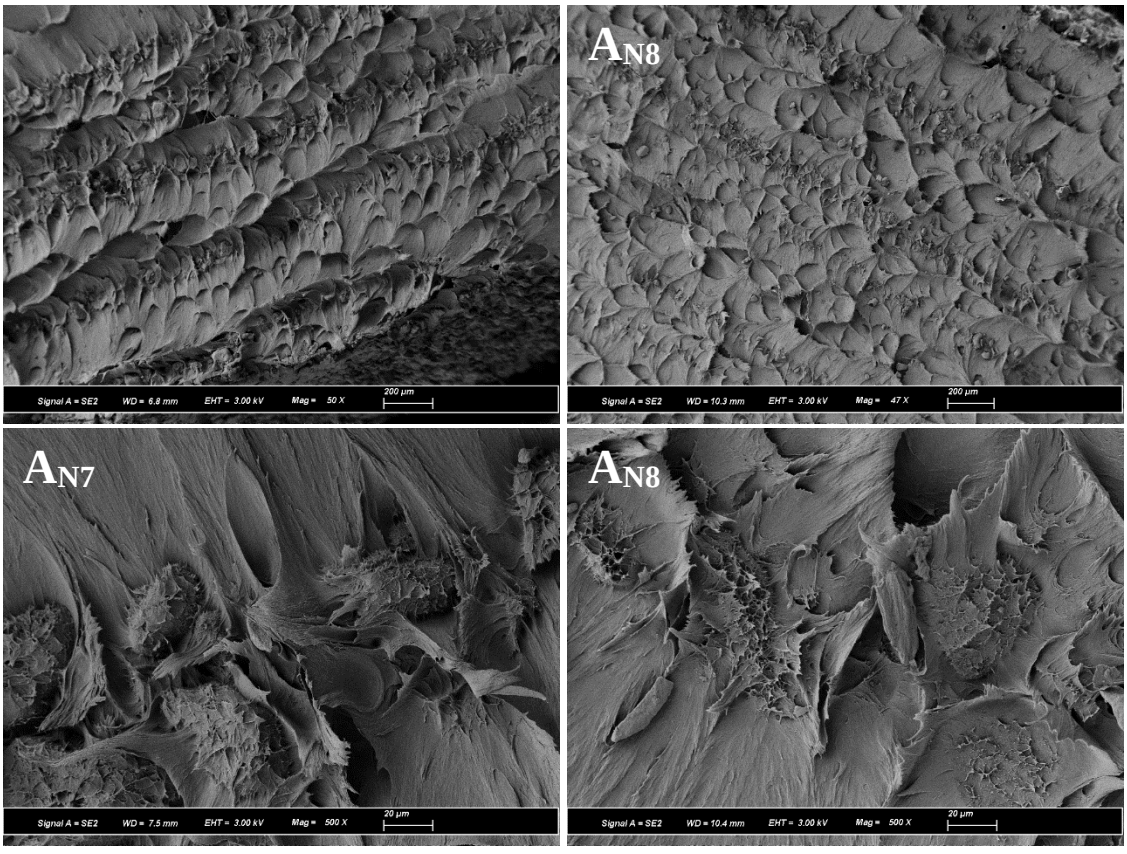

Figure 2-39: Poorly sintered particle layers in A_{N7} and A_{N8} printed PA11/CB samples.

The average size of the dimples seemingly increased with A_N, which follows the increase in plastic work (βw_p) calculated from the essential work of fracture study. That is, samples with larger βw_p

were found to have larger dimple sizes on the fracture surface. In addition to size, the frequency or density of impinging dimples changed with A_N, with the number of dimples decreasing with increasing A_N. The lower number of dimples on the fracture surface correlates to the number of independent inclusion sites in the sample. Many dimples in the lower A_N samples seem to be directed from obvious defects (mostly unsintered particles), so the reduced frequency with increasing A_N likely derives from fewer printing errors in the higher A_N samples. Lastly, the directionality of the dimples changes with increasing A_N, with the dimples gradually orienting more in the direction of the crack propagation direction with higher A_N. This again likely stems from the reduction in unsintered or partially sintered particles with higher A_N, as poorly sintered layers will accelerate crack growth and change the propagation direction. These changes can be illustrated in selected fracture surface images of the A_{N7}, A_{N9} and A_{N11} samples shown below in Figure 2-40.

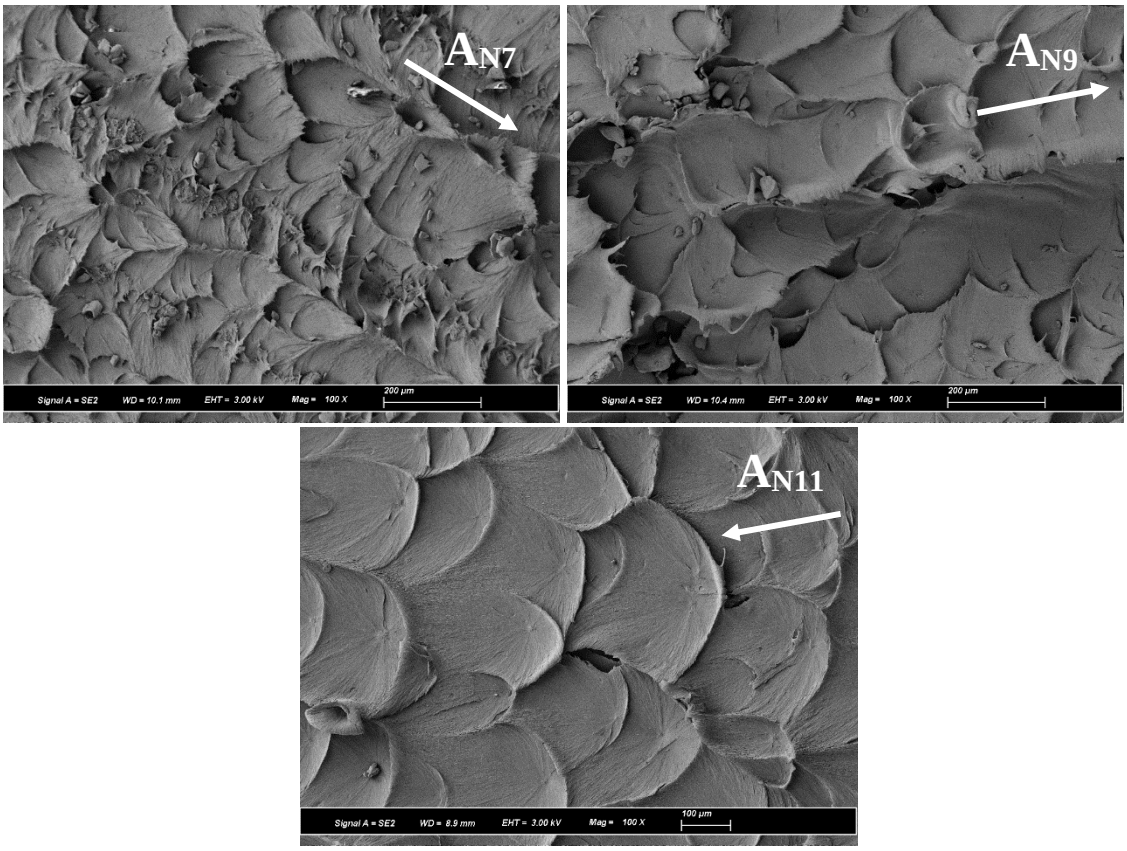

Figure 2-40: Change in size and directionality of dimples with increasing A_N. The crack direction is indicated by the white arrow on each image.

The source of the microvoid coalescence needed to facilitate the dimpled fracture surface can easily be elucidated by imaging the node of the dimple, closer to the larger frontal shear lips of the individual dimple. Interestingly, it seems as though the carbon black used in the PA11 primarily for laser absorption plays a nontrivial role in the creation of the dimpled structure under fracture. When investigating a number of the "nodes" or initiation points for these dimples, a large population of very small particles (roughly 50 nm to 100 nm) were present throughout the node, reducing in frequency further away from the suspected site of initiation. Considering that the only known additive to the polymer was carbon black, it is safe to assume that there are carbon black aggregates. The node itself is highly porous, with parabolic tearing of the dimple extending from the node. The positioning of the carbon black is mostly on the edges of voids and the parabolic tears, suggesting the carbon black may be initiating and propagating the microvoid coalescence needed to create the dimpled tearing of the fracture surface. Figure 2-41 highlights a representative node and the presence of carbon black particles extending from the nodal center.

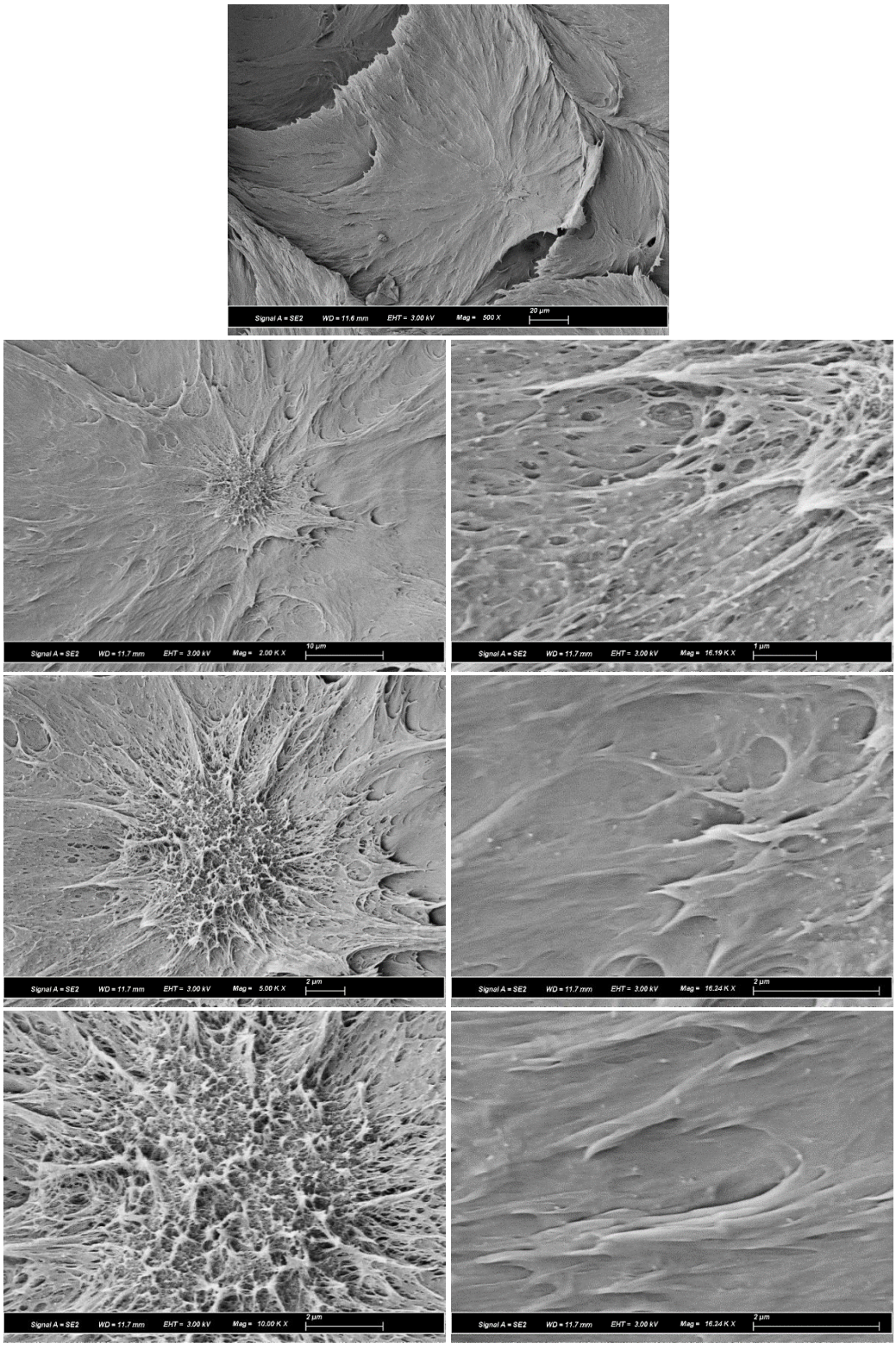

Figure 2-41: Representative dimple node in an A_{N9} sample with the smaller white dots representing the carbon black agglomerates. The images on the right show the reduction in carbon black with increasing distance from the node.

While the nodal architecture in Figure 2-41 was the most commonly found structure in the tested samples, there seemed to be some diversity in the type of initiation points for the dimpled fracture surface, but more so for samples at increasing A_N. Below in Figure 2-42, a compilation of the unique dimple nodes found in the PA11/CB fracture surface are shown. The top two images show a similar highly voided and protruding feature, with the left demonstrating a more web-like structure than the right image. Both nodes are highly populated by carbon black particles, and are reminiscent of the poorly sintered particle structure as shown previously. These nodes may be the inner nucleus of a poorly sintered particle, with extensive voiding additionally propagated by the presence of carbon black aggregates. The bottom left node seems more representative of traditional microvoid coalescence, with a more planar arrangement of circular voids in the matrix. The bottom right node has significantly less observable voiding, but still more similar to the planar node in the bottom left image. Interestingly, the bottom two images correlate well to the surfaces of fatigued nylon samples, with the more elongated and sheared boundaries said to represent the spherulite nuclei [31]. The high density of these elongated striations represents the density and impingement of the spherulitic structure, as opposed to the dimple initiated by a singular intra-spherulitic fracture. The bottom right image additionally shows elongation and deformation of spherulites parallel to the crack direction, with average size between 1-2 microns. Thus, the main inclusion sources are likely poorly sintered particle cores, carbon black aggregates and impinged spherulite nuclei.

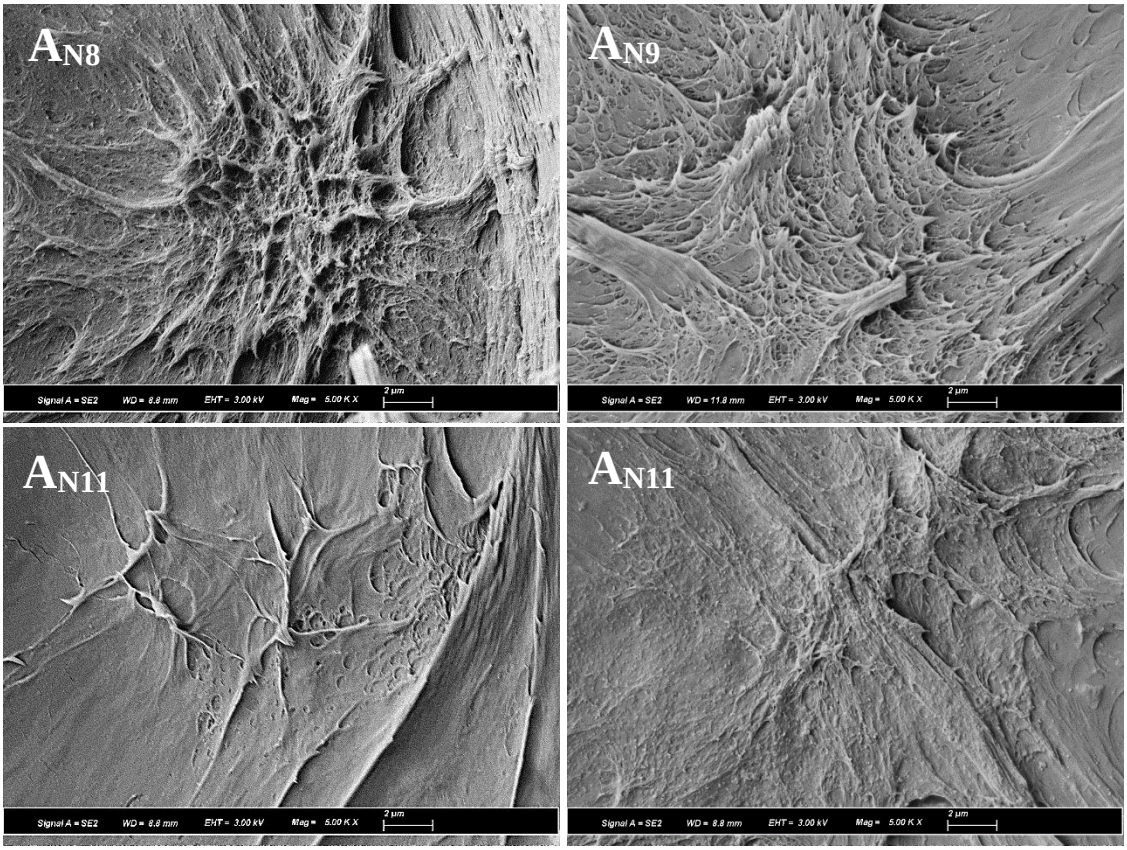

Figure 2-42: Diversity of dimple nodes found in the printed PA11/CB fracture surface.

2.4 Conclusions

Various characterization techniques were employed to elucidate significant changes to the PA11 microstructure during the SLS printing process. It was shown that there are specific microstructural changes that occur in PA11, some gradual and others more striking between the PA11/CB powder and printed material. The T_m, X_c, l_c and d_{hkl} spacing of PA11/CB were all shown to have a large change in value upon printing, whereas the molecular weight was shown to have a rather gradual increase between the PA11/CB powder and printed parts. Amongst the printed samples, elongation to break, ultimate tensile stress and essential work of fracture were shown to modestly increase with increasing A_N from A_{N7} to A_{N11}. These values compared quite well to available literature on PA11, with the exception of elongation to break which was quite lower than values for injection molded PA11. Subtle structural differences were particularly seen in the A_{N8} and A_{N9} samples, with

the appearance of a shoulder on the melting peak and complimentary changes in d_{hkl} spacings and several FTIR peak shifts. The A_{N7} sample was shown to have significant residual powder within the sample from poorly sintered layers, likely skewing DSC, XRD and FTIR data with the highly crystalline retained powder. Polymer chain rigidity, as characterized by RAP, was also seen to reduce at A_N above the A_{N9}. Fractography proved useful in determining the sources of stress concentration within the printed samples, with all tested samples showing a "dimpled" surface characteristic of ductile fracture. The A_{N7} and A_{N8} samples were largely defect driven, with the unmelted cores of PA11 particles acting as a major source of voiding and crack propagation on the fracture surface. Other sources of stress concentrations include carbon black aggregates and impinged spherulite nuclei.

While seeming disjointed, these results help to create a better understanding of the printing process, specifically the effect of partial sintering on PA11 structure and mechanical performance. Processing temperatures for SLS printing are chosen to lie within a defined processing window to prevent full solidification of the polymer part as it is being printed. PA11 crystal structure will initially change prior to sintering as it passes through the Brill transition zone around 110°C. Both the bed and chamber temperatures were set to 178°C, however fluctuations in temperatures likely exist, particularly between the bed and powder reservoir. As a new powder layer is spread across the print bed, it will have a cooling effect on the recently melted polymer, possibly causing some immediate crystallization of PA11 in the δ phase at the melted polymer/powder interface. With the next laser pass, if the laser area energy density is not penetrative enough to not only melt the new layer of powder but the transitional phase at the powder interphase, at the very least this transitional layer will remain, if not fully unsintered particles. Given the similarities between the melt behavior of PA11/CB at higher cooling rates, the larger RAP, complimentary d_{hkl} spacing and FTIR peak shifting of the A_{N8} and A_{N9} samples, it is likely that both of these samples contain this highly rigid

transitional layer. It is likely that it is not until A_{N10} that the laser depth is long enough to successfully remelt the transitional layer and not just the top layer of powder. While there have not been definitive studies that have linked the presence of RAP to specific mechanical behavior, there subsequently would be a reduced presence of polymer chains in the entangled bulk, which has been shown to favorably increase semicrystalline polymer ductility. Thus, to maximize mechanical performance, it is not just imperative to print at an that fully melts the PA11 powder, but possibly the more rigid transitional phase that is proposed to germinate at the PA11 melt/powder interphase.

With this proposed mechanism in mind, it is also concluded that characterization techniques other than tensile testing have proved immensely helpful in optimizing the printing process. Namely, characterizing the melt behavior, RAP and fractography of the w_e surface have proved enormously useful in determining the existence of poorly sintered powder, a rigid transitional phase and the sources of failure in printed PA11/CB. Using these characterization techniques in tandem can create a fuller picture of the printing process, and help identify sources of error within the printed samples to further help optimize the printing parameters to create high performance printed parts.

2.5 References

[1]. Ligon, S. C., Liska, R., Stampfl, J., Gurr, M. and Mülhaupt R. (2017). Polymers for 3D Printing and Customized Additive Manufacturing. *Chemical Reviews*, 117, 10212-10290.

[2]. Pilipovic, A., Brajlih, T., and Drstvensek, I. (2018). Influence of Processing Parameters on Tensile Properties of SLS Polymer Product. *Polymers*, 10, 1208-1226.

[3]. Beal, V.E., Paggi R.A., Salmoria, G.V., and Lago, A. (2009). Statistical Evaluation of Laser Energy Density Effect on Mechanical Properties of Polyamide Parts Manufactured by Selective Laser Sintering. *J. of Applied Polymer Scienc*e, 113, 2910–2919.

[4]. Majewski, C., Zarringhalam, H. and Hopkinson, N. (2008). Effect of the degree of particle melt on mechanical properties in selective laser-sintered Nylon-12 parts. *J. of Eng. Manufacture*, 222, 1055.

[5]. Kabasci, S. (2014). Bio-Based Plastics: Materials and Applications. *John Wiley & Sons*, London, 275-293.

[6]. Bourell, D.L, Watt, T. J., Leigh, D.K., and Fulcher, B. (2014). Performance limitations in polymer laser sintering. *Physics Procedia*, 56 , 147-156.

[7]. Okamba-Diogo, O., Richaud, E., Verdu, J., Fernagut, F., Guilment, J. (2016). Investigation of polyamide 11 embrittlement during oxidative degradation. *Polymer, Elsevier*, 82, 49-56.

[8]. Chen, H and Cebe, P. (2007). Investigation of the rigid amorphous fraction in nylon-6. *J. of Thermal Analysis and Calorimetry*, 89, 417–425.

[9]. Laun, S., Pasch, H., Longieras, N., and Degoulet, C. (2008). Molar mass analysis of polyamides-11 and -12 by size exclusion chromatography in HFiP. *Polymer*, 49(21), 4502-4509.

[10]. Mai, Y., and Cotterell, B. (1986). On the essential work of ductile fracture in polymers.*Int. J. Fracture*, 32, 105-125

[11]. Nair, S. (2006). *Studies on the development of structure and morphology in nylons*. Thesis, University of Pune.

[12]. Mollova, A., Androsch, R., Mileva, D., Schick, C. and Benhamida, A. (2013). Effect of Supercooling on Crystallization of Polyamide 11. *Macromolecules*, 46, 828-835.

[13]. Xenopoulos, A. and Wunderlich, B. (1990). Thermodynamic Properties of Liquid and Semicrystalline Linear Aliphatic Polyamides. *J. of Polymer Science Part B*, 28, 2271-2290.

[14]. Yoshioka,Y. and Tashiro, K. (2003). Structural change in the Brill transition of Nylon m/n (1) Nylon 10/10 and its model compounds. *Polymer*, 44, 7007-70019.

[15] Drummer, D., Wudy, K., and Drexler, M. (2015). Modelling of the Aging Behavior of Polyamide 12 powder during Laser Melting Process. *AIP Conference Proceedings*, 1664, 160007

[16] Acierno, S. and Van Puyvelde, P. (2004). Rheological Behavior of Polyamide 11 with Varying Initial Moisture Content. *J. of App. Polymer Science*, 97, 666–670

[17] Wudy, K. and Drummer D. (2019). Aging effects of polyamide 12 in selective laser sintering: Molecular weight distribution and thermal properties. *Additive Manufacturing*, 25, 1-9

[18] Vouyiouka, S. N., Karakatsani, E. K., and Papaspyrides, C.D. (2005). Solid state polymerization. *Prog. In Polymer Science*, 30, 10-37

[19] Zarringhalam, H., Hopkinson, N., Kamperman, N.F, and de Vlieger, J.J. (2006). Effects of processing on microstructure and properties of SLS Nylon 12. *Mat. Science and Engineering A*, 435, 172-180.

[20] Drummer, D., Wudy, K., Kuhnlein, F., and Drexler, M. (2014). Influence of degradation behavior of polyamide 12 powders in laser sintering process on produced parts. *AIP Conference Proceedings*, 1593, 691-695.

[21] Hofland, E.C., Baran, I., and Wismeijer, D.A. (2017). Correlation of Process Parameters with Mechanical Properties of Laser Sintered PA12 Parts. *Adv. In Mat. Sci. and Engineering*, 207, 1-11.

[22] Arkema. Rilsan PA-11: Created From a Renewable Source. 3720E, 6/2005.

[23] Leigh, D. K. (2012). A comparison of polyamide-11 mechanical properties between laser sintering and traditional molding. *SSF Symposium*, 23, 574-605.

[24] Pegoretti, A and Ricco, T. (2006). On the essential work of fracture of neat and rubber toughened polyamide-66. *Engineering Fracture Mechanics*, 73, 2486-2502.

[25] Ching, E., Li, R., Tjong, S.C., and Mai, Y. W. (2003). Essential Work of Fracture (EWF) Analysis for Short Glass Fiber Reinforced and Rubber Toughened Nylon-6. *Polymer Engineering and Science*, 43, 558-569.

[26] Cuesta, L.I., Martinez-Paneda, E., Diaz, A., and Alegre, J.M. (2019). The essential work of fracture parameters for 3D printed polymer sheets. *Materials and Design*, 181, 1-9.

[27] Hussein, N. *Enhancement of the mechanical performance of semi-crystalline polyamides by tailoring the intermolecular interaction in the amorphous phase*. Thesis, INSA de Lyon.

[28] Jariyavidyanont, K., Janke, A., and Androsch, R. (2019). Crystal self-nucleation of polyamide-11. *Thermochimica Acta*, 677, 139-143.

[29] Hertzberg, R.W., Vinci, R.P., and Hertzberg, J.L. (2012). Deformation and Fracture Mechanics of Engineering Materials, 5th Edition. *Wiley Global Education*, Westford, 277-291.

[30] Yang, J.L., Zhang, Z., Zhang, H. (2005). The essential work of fracture of polyamide 66 filled with TiO_2 nanoparticles. *Composites and Science Technology*, 65, 2374-2379.

[31] Raphael, J., Saintier, N., Robert, G., Bega, J. and Laiarinandrasana, L. (2019). On the role of the spherulitic microstructure in fatigue damage of pure polymer and glass-fiber reinforced semi-crystalline polyamide 6.6. *International J. of Fatigue*, 126, 44-54.

CHAPTER THREE: DEVELOPMENT OF A POLYAMIDE 11/CARBON BLACK/NANOSILICA NANOCOMPOSITE FOR USE IN SELECTIVE LASER SINTERING

3.1 Introduction

Commercially available selective laser sintering (SLS) polymer powders have dramatically increased in the past decade, with polyamide 12 (PA12) being the most popular and most cited in polymer SLS focused research [1]. There are concerted interests and efforts in improving polymer powder for SLS printing, however the breadth of polymer powder properties needed to succeed and improve upon in an SLS process can be quite large. Broadly, some of the main areas of polymer powder improvement for the SLS process include diversifying material choice, optimizing powder size distribution, shape distribution and powder flow, and increasing aging stability, laser absorption and recyclability. Separate studies have elucidated and improved upon singular powder development areas [2], but understandably creating polymer powder that can address multiple development areas of improvement can be a real challenge.

Easily the largest area of improvement of SLS printing powder is increasing the diversity of polymer powder that can be processed through SLS printing. Some of the difficulty in developing new polymers for SLS printing lies in the necessity of a processing window that is wide enough to suspend immediate solidification after melting, as well as a specified melting temperature low enough to halt thermoxidative degradation of the polymer powder [3]. PA12 has been utilized heavily both commercially and academically due to meeting both aforementioned requirements, as well as having relatively good mechanical properties associated with the polyamides [4]. While there would be interest in using more standard polyamides in the SLS printing process, the melting temperatures of standard polyamides like PA6 and PA6,6 are often too high for operation in a standard commercial SLS printer. The main differences in properties between the commercially available PA12 and PA11 with the more commonly used PA6 and PA6,6 are the stress and modulus values, which can be upwards of double the value of the PA12 and PA11 properties. A key research

avenue would be to modify already processible SLS powders to have similar mechanical performance to polymers like PA6 and PA6,6 while still retaining the necessary thermal properties to print well in a commercial SLS printer.

Another key area of development would be improving powder flow to best suit the SLS printing process. There have been studies relating specific powder flow tests to mechanical performance of sintered parts, however the powder flow results are predominantly measured at room temperature whereas the SLS printer will operate at a much higher temperature [5]. Quantifying powder flow at processing temperature would provide a more accurate estimation of flow behavior during the printing process, allowing for a better optimization of powder flow to decrease printed sample defects. Powder flow is especially hindered in cryogenically ground SLS powders, as the particles lack the sphericity and smoothness needed to reduce friction and assist powder flow.

To address both of these SLS powder development areas, this chapter involves the development of a polyamide 11/carbon black/silica nanoparticle (PA11/CB/SNP) printing powder. Both 50 nm and 25 nm diameter aminosilane surface treated colloidal silica were chosen to coat the PA11/CB particle as both a processing aid and toughening agent to produce high performance polymer nanocomposites. The goal was for the presence of SNP to reduce friction between PA11/CB particles and increase powder flow at printing temperatures, while acting as a reinforcing agent at the particle and layer boundaries in the printed material. Increasing powder flow at SLS printing temperature will help remove printing defects associated with unequal powder spreading on the print bed, whereas reinforcing the particle boundaries and printing layers will help strengthen the common sources of stress concentration within a SLS printed material, particularly in the z or build direction. With potential to further improve mechanical performance, the PA11/CB/SNP composite would both diversify the available polymer powders for SLS printing, while possibly increasing

mechanical properties like strength and stiffness to have more comparable properties with currently unavailable printing polymers like PA6 and PA6,6.

3.2 Experimental

3.2.1 Materials

A PA11/CB composite powder under the commercial name Rilsan Invent Black was provided by the Arkema corporation. The polymer powder used in this study has a nominal average size of 50 μm, as determined by dynamic light scattering. The shape of these particles varied from slightly rounded to angular, with an incredibly rough particle surface. Carbon black was determined to be dispersed homogenously throughout the polymer particle, with an approximate composite weight contribution of 1 wt. % as measured using thermogravimetric analysis. Surface treated colloidal nanosilica with 50 nm and 25 nm diameter were provided by the Cabot corporation for this study. Both sizes of nanoparticles were surface treated with an amine terminated silane to promote silica dispersion and adhesion to the PA11/CB particle surface. Density of the 50 nm nanoparticles was previously measured by Patel at 2.27 g/cm^3 [6], and both tensile and shear modulus of SNP have been previously referenced at 70 GPa and 30 GPa, respectively [6].

Two processing methods were used to combine the nanoparticles to the PA11/CB powder, specifically to promote adhesion of the silica nanoparticles (SNP) to the polymer particle surface. The first method attempted was a proprietary solid state shear pulverization, provided by the Zyzzx Polymers company. This processing was performed on the 50 nm NS particles, creating composite powder with 2 wt. % and 4 wt. % NS. The second processing method involved centrifugal mixing of the 25 nm NS powder and PA11/CB. 50 g composite powder samples were mixed at 1200 rpm for a total of 20 minutes, stopping halfway in between to shake the powder container and loosen any compacted powder from the bottom of the container. In addition to the composite powder, 10 g of 3 mm ceramic beads were added to the container for the printing process to aid with mixing.

Using this method, a PA11/CB/25nmNS composite powder was successfully created with 0.25 wt. %, 0.5 wt. %, 1 wt. % and 2 wt. % additions of NS.

3.2.2 SLS Printing

The powder was processed using the commercial Sintratec Kit SLS printer, equipped with a 2 W blue diode (445 nm) laser. Prior to printing, powder was dried at 80°C overnight (16 hours) to reduce the effects of humidity on the printing process. Powder was additionally passed through a 150 µm sieve to remove uncharacteristically large particles from the bulk powder. The printer chamber temperature was set to 178°C and left to equilibrate for 3 hours prior to the start of printing. The powder bed was set to 150°C during the chamber equilibration and 178°C for the actual print. Samples were consistently printed in the same envelope to prevent any influence of the powder bed location on printed part performance. The PA11/CB/50nmNS samples were print at A_{N9}, using the parameters as outlined in Chapter 2. Select samples were additionally printed at $A_{N12.5}$, using a hatch spacing of 80 µm and laser speed of 200 mm/s. The PA11/CB/25nmNS samples were all printed at A_{N9}, using the parameters outlined in Chapter 2.

3.2.3 Powder Flow Measurements

An experimental setup was designed to measure powder flow for the composite powders, specifically to evaluate the ability of added SNP to increase the powder flow of the PA11/CB powder at increasing temperatures. The method used was designed heavily using the methodology behind the FT4 Powder Rheometer (Freeman Technology, UK) [7]. In this method, a traditionally helical impeller both rotates and compresses a powder in a cylindrical holding cell. The measured torque required to flow the powder and force acting at the top of the impeller are used to calculate a total flow energy (E_{flow}) of the powder [8]. The equation for E_{flow} is shown below, in Equation 1.

$$E_{flow} = \int_0^H \left(\left(\frac{T}{R \cdot \tan\alpha} \right) + F \right) dH \quad (1)$$

The T variable represents the measured torque, and the F represents the force acting at the front of the impeller. R is the radius of impeller, H the inner height of the cylinder and α the helix angle of the impeller. It should be mentioned that a vane rotor was used for the present study, so α was alternatively calculated by the ratio of the vertical speed to the rotational velocity of the impeller. The process can additionally be reversed, with a rotating motion of the powder in the tensile direction, typically used to characterize less restrained powder flow. The setup was designed to fit into a DHR2 discovery hybrid rheometer (TA Instruments) with an environmental chamber that can enclose an attached geometry. A cylindrical vessel was machined to fit an existing disposable parallel plate fixture that could additionally fit inside the attached furnace. The dimensions of the attached cylinder and vane impeller are shown below in Figure 3-1.

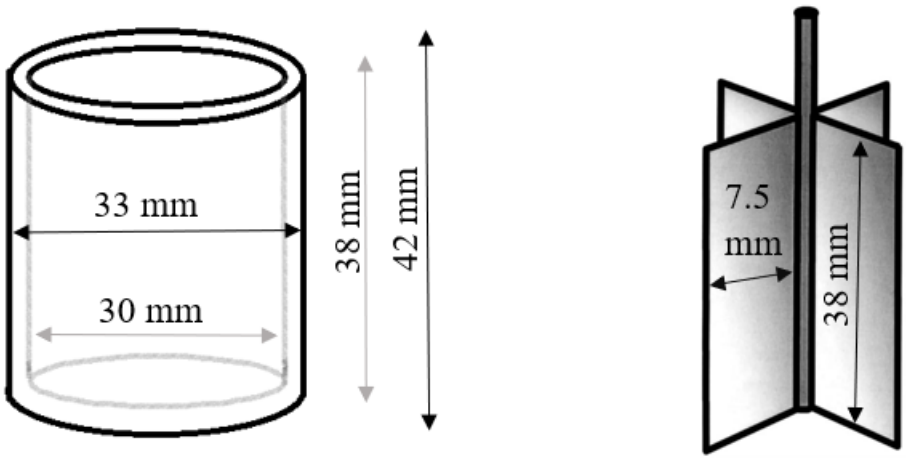

Figure 3-1: Cylinder and vane dimensions used for the powder flow tests at increasing temperature.

For each test, powder is filled and tapped 200 times at room temperature, each time to the 33 mm inner cylindrical height. The vane is then lowered to just above the powder surface, at which point the furnace would be closed. The sample is then left to equilibrate for an hour at the testing temperature, at which point the test would begin. The vane impeller compresses at a rate of 500 μm/s while rotating at an angular velocity of 5 rad/s. This continues until a final depth of 15 mm. Immediately afterward, the impeller then proceeds in the opposite vertical direction, at the same

vertical and rotational speeds as in the first step. The temperatures tested for each PA11/CB/SNP powder were 25°C, 40°-120°C in 20°C intervals, and 130°C-180°C in 10°C intervals. This totals out to 12 separate testing temperatures.

3.2.4 Thermal Behavior

Differential Scanning Calorimetry (DSC) was utilized to evaluate the melting temperature (T_m), crystallization temperature (T_c), and weight percent crystallinity (X_c). DSC samples were extracted from the internal bulk of a ½″ x ¼″ x ¼″ specimen printed in the same print bed coordinates for each A_N. Samples weighing approximately 10 mg were placed into hermetically sealed aluminum pans and placed onto the DSC sample stage (DSC Q2000, TA Instruments). For determination of the T_m, T_c and X_c of printed PA11/CB/SNP with increasing SNP content, samples were equilibrated at 0°C and heated at a rate of 10°C/min to 230°C, followed by a cooling cycle at the same ramp rate to 0°C. For the calculation of X_c, the enthalpy of melting (ΔH_f) was measured using Universal Analysis software (TA Instruments), and the standard enthalpy of melting ($\Delta H_f{}^o$) used in this study was 226.4 J/g [9]. The calculation of X_c is the same as Equation 2 as shown in Chapter 2.2.3.

Thermogravimetric analysis (TGA, Q500 T.A. Instruments) was additionally performed on the PA11/CB/SNP samples to characterize the amount of SNP present in representative printed parts. Samples weighing approximately 20 mg were placed in a platinum crucible and heated from 25 °C to 700 °C at a ramp rate of 10 °C/min under an air environment. Weight loss was measured with increasing temperature, with residual weight of the SNP and carbon black taken after polymer degradation. Representative PA11/CB samples were also tested to determine the average amount of carbon black present in the Rilsan Invent powder in order to subtract the value from the final remaining weight and isolate the silica content. Two samples were tested from each PA11/CB/SNP printed part.

3.2.5 Mechanical Behavior

Tensile testing and dynamic mechanical analysis (DMA) were performed for both the PA11/CB/50nmSNP and PA11/CB/25nmSNP samples. Type V tensile specimens (ASTM D638-14) were tested using a screw-driven universal testing machine (Instron 5567), with strain measured through use of a digital extensometer. DMA analysis was done using rectangular torsion fixtures on a hybrid rheometer (T. A. Instruments DHR2). Samples were print to 2″ x ½″ x $^1/_8$″ rectangular sample dimensions and subjected to 0.2 % strain at 1 Hz frequency from 25°C to 170°C at 1°C/min temperature increase. Experimental tensile modulus for both PA11/CB/SNP samples were compared to the expected values as predicted by the Halpin-Tsai model, as shown below in Equation 2 [10]. E_c, E_f and E_m are the modulus of the composite, filler and matrix, respectively, ξ is the shape factor of the filler and is equal to 2 for spherical particles, and Φ_f is the volume fraction of filler.

$$E_c = \frac{1+\xi\eta\emptyset_f}{1-\eta\emptyset_f} E_m \text{ with } \eta = \frac{{E_f}/{E_m}-1}{{E_f}/{E_m}+\xi} \quad (2)$$

The PA11/CB/25nmSNP samples went through additional mechanical tests, including essential work of fracture (EWF) as described in Chapter 2.2.5. It should be mentioned that EWF was attempted on the PA11/CB/50nmSNP samples, however yielding was not observed prior to crack propagation, leading to an invalid test condition. Compression testing was also performed on the PA11/CB/25nmSNP with increasing SNP content. Samples were printed to ¼ ″ x ¼ ″ x ½ ″ dimensions in both the x (bed layer) and z (build) directions to help determine the effect of increasing SNP on reinforcing the layer and particle boundaries. Compression testing was performed via ASTM D695-15 standard at a 1 mm/min crosshead speed. Lastly, linear reciprocating wear was performed on PA11/CB A_{N9} samples print in the x, y and z directions as shown below in Figure 3-2, with dimensions matching those of the printed compression samples.

Additionally, PA11/CB/25nmSNP samples with increasing SNP were printed in the z direction for wear studies to help analyze the effect of increasing SNP on improving mechanical properties in the build direction. Figure 3-2 additionally shows the linear reciprocating wear setup, where samples were subjected to 100,000 cycles wear experiments performed at a sliding speed of 50.8 mm/s and 25.4 mm stroke length under a 250 N normal load. Wear rate was calculated using Archard's wear law, shown below in Equation 3 [11]. K represents the wear rate in mm^3/Nm, V_l as the volume lost, F_N as the normal load, and d as the sliding distance. The volume lost can also be rewritten in terms of mass loss (Δm) and density (ρ) which are also illustrated in Equation 3.

$$K = \frac{V_l}{F_N \cdot d} = \frac{\Delta m/\rho}{F_N \cdot d} \tag{3}$$

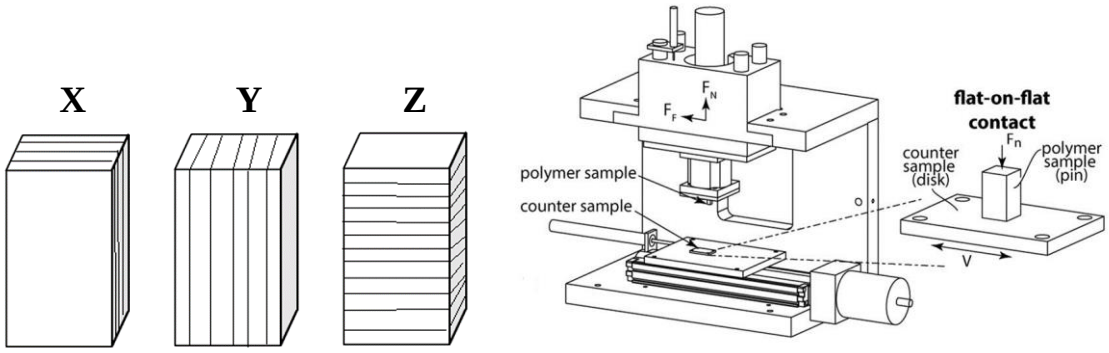

Figure 3-2: Wear and compression sample layer organization (left) and linear reciprocating wear setup used for the present study (right) [11].

3.2.6 Imaging

Scanning electron microscopy (Zeiss 1500) was used to examine PA11/CB/NS powder and fracture surfaces as produced through essential work of fracture. Samples were sputter coated with iridium to reduce charging during the imaging process. Carbon tape was administered to both promote adhesion to the SEM stub as well as ground the electron conduction. Powder was gently tapped onto the surface of the carbon tape to reduce crowding of the powder particles prior to the iridium coating. Fracture surfaces of the 12.5 ligament length EWF samples were chosen for imaging. An accelerating voltage of 3 kV was used in conjunction with the SE2 lens detector.

3.3 Results and Discussion

3.3.1 PA11/CB/50nmSNP Powder Processing

PA11/CB/50nmSNP powder was mixed with 2 wt. % and 4 wt. % SNP loadings using solid state shear pulverization. Upon initial observation, the powder appeared somewhat homogenous, with some apparent SNP agglomerates easily visible against the carbon black concentrated particles. SEM proved extremely helpful in determining the dispersion of SNP in the PA11/CB system with selected images of the PA11/CB/50nmSNP powder shown below in Figure 3-4. The powder with 2 wt. % SNP is shown in the left column, and the powder with 4 wt. % SNP is illustrated in the right column. The PA11/CB particle shape and size appeared unchanged with the addition of SNP, with angular geometry nominally 50 μm in size. Upon higher magnification, it is shown that the SNP adhered quite well to the PA11/CB surface, with multiple layers of the SNP appearing to be on most particles. The PA11/CB/50nmSNP at 4 wt. % SNP loading additionally showed some 1 μm to 2 μm SNP agglomerates on the powder surface, which are more likely to impede polymer diffusion upon sintering and act as a major source of stress concentration upon fracture.

In addition to SEM, TGA was also employed on the powder sample to determine the distribution of SNP in the composite powder. The PA11/CB powder was test first to establish the average weight percent of CB found within the PA11/CB powder. The average remaining CB weight was approximately 0.95%, which for SLS printing powders is somewhat large. For the PA11/CB/50nmSNP powder, the average measured SNP content for the 2 wt% loaded samples was 1.95 wt. %, demonstrating good homogenization of mixing. The 4 wt. % SNP loaded samples had a slightly higher than expected average SNP content at 4.22 wt. %, which could have been due to the presence of agglomerates on the particle surface. Regardless, solid shear pulverization proved fairly successful in producing homogenously blended powders for SLS printing. The degradation results are illustrated in Figure 3-3 and summarized in Table 3-1.

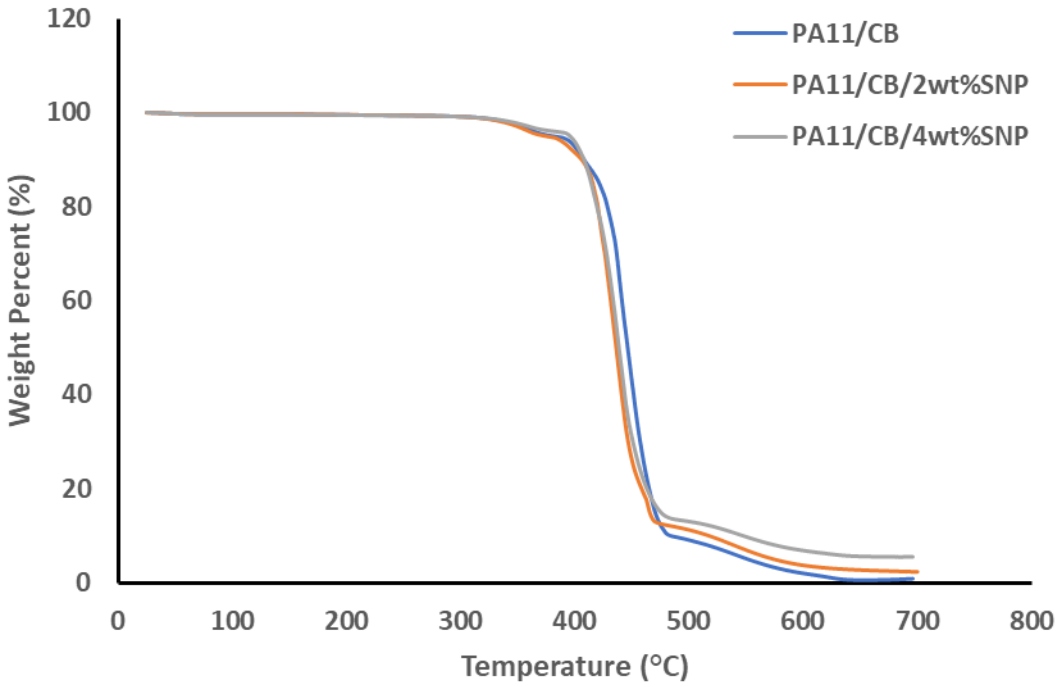

Figure 3-3: Degradation of solid state shear pulverized PA11/CB/50nmSNP powder samples.

Table 3-1: Summary of calculated SNP and CB content for PA11/CB and PA11/CB/50nmSNP powder samples

PA11/CB Sample	**Weight % 1**		**Weight % 2**		**Average Weight %**	
	CB (%)	SNP (%)	CB (%)	SNP (%)	CB (%)	SNP (%)
PA11/CB	0.99 %	0 %	0.91%	0 %	0.95%	0 %
PA11/CB/2wt%50nmSNP	0.95 %	1.91 %	0.95 %	1.98 %	0.95%	1.95 %
PA11/CB/4wt%50nmSNP	0.95 %	4.32 %	0.95 %	4.11 %	0.95%	4.22 %

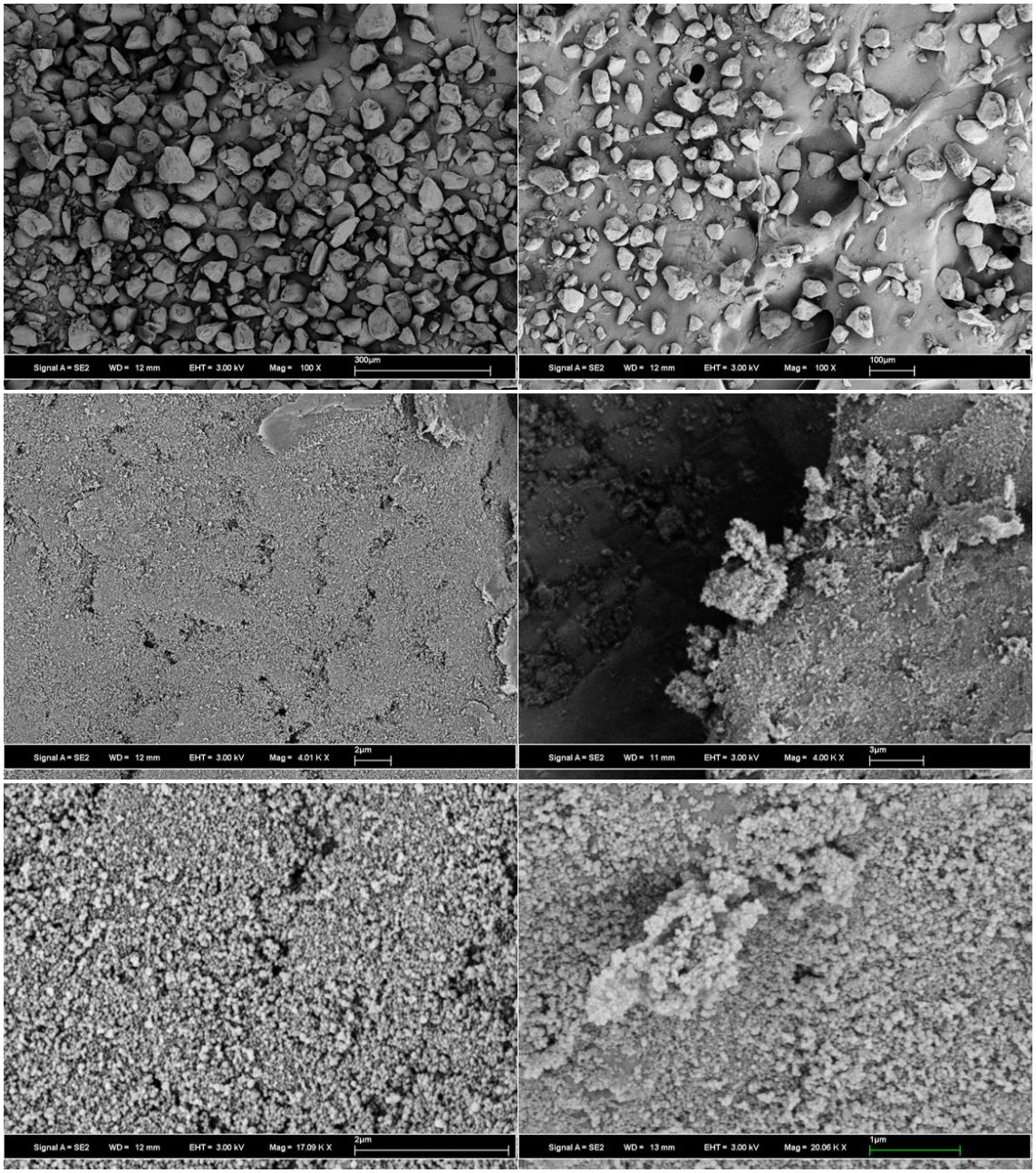

Figure 3-4: Images highlighting SNP coverage of the PA11/CB particle surface in the PA11/CB/2wt%50nmSNP (left) and PA11/CB/4wt%50nmSNP (right) powder samples.

3.3.2 Thermal Analysis of PA11/CB/50nmSNP

Peak melting temperatures (T_m) and weight percent crystallinity (X_C) of printed PA11/CB/2wt%50nmSNP and PA11/CB/4wt%50nmSNP were compared to that of a representative printed PA11/CB (A_{N9}) sample. The melting behavior was somewhat similar, with

the melting temperatures at 192.2°C, 190.3°C and 189.6°C for the PA11/CB/2wt%50nmSNP, PA11/CB/4wt%50nmSNP and PA11/CB samples respectively. While the PA11/CB A_{N9} sample showed a significant shoulder in the melting peak, neither SNP containing sample had similar melting shoulders, suggesting the SNP containing samples do not have as large of changes in d_{hkl} spacing as was demonstrated in Chapter 2.3.2. The PA11/CB/4wt%50nmSNP sample did show a very slight shoulder close to the T_m, but not nearly as striking and prominent as the shoulder in the PA11/CB sample. Both the PA11/CB/2wt%50nmSNP and PA11/CB/4wt%50nmSNP samples additionally showed a smaller residual peak closer to the melting temperature of the virgin powder, which has been shown to represent an unmelted core of the powder particle [12]. The residual peak grew with area with increase in SNP, suggesting the presence of SNP reduced the sintering and diffusion of the PA11 through the SNP particle boundaries. The values of X_C remained fairly constant with increasing SNP content, with the PA11/CB/2wt%50nmSNP and PA11/CB/4wt%50nmSNP samples having 21.1% and 20.4% crystallinity, as compared to the PA11/CB A_{N9} sample with 20.6% crystallinity. The melting behavior for all three mentioned samples is shown in Figure 3-5.

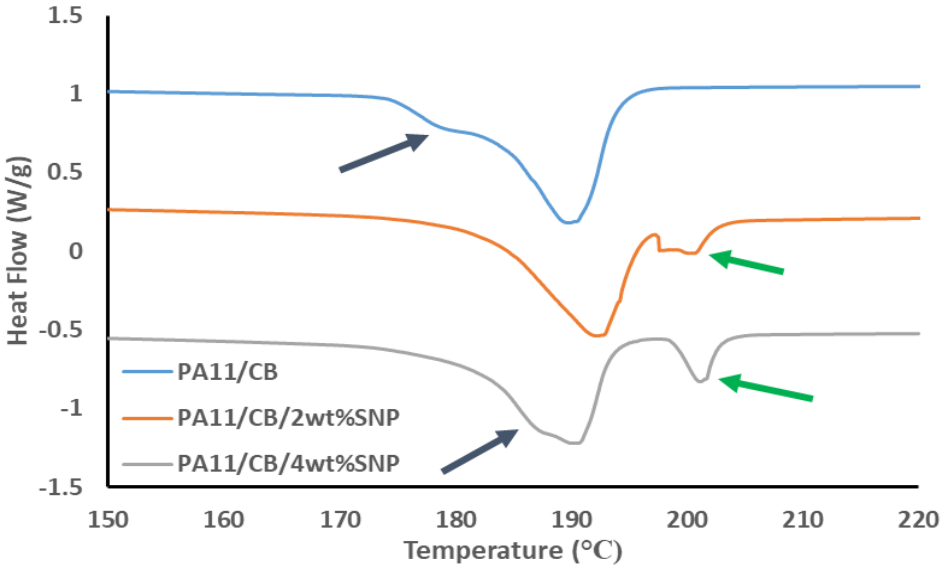

Figure 3-5: Melting behavior of printed PA11/CB A_{N9}, PA11/CB/2wt%50nmSNP and PA11/CB/4wt%50nmSNP samples. The blue arrows highlight melting shoulders, while the green arrows show the residual powder melting peak.

After observing the significant residual powder peaks in the SNP containing samples, it was briefly considered that if the samples were print at a high enough A_N, the polymer would be able to diffuse through the silica boundary. Conversely, it was also proposed that at a high enough A_N, the laser would be able to help the SNP diffuse through the melted polymer matrix. A PA11/CB/2wt%50nmSNP sample was print at $A_{N12.5}$ to evaluate the effectiveness of increasing the A_N on reducing the residual powder peak and improving polymer diffusion through the silica boundary. While the residual powder peak did reduce in area with the increase in A_N, it did not go completely disappear, suggesting the average silica boundary layer between two adjacent SLS coated PA11/CB particles is too large for the PA11 to effectively diffuse through with the printing parameters available for this specific printer. The T_m and X_C for both samples otherwise remained the same with increase in A_N. It was hypothesized that the increased presence of SNP reduced laser absorption of the PA11/CB particles, however brief analysis of UV absorption at 445 nm in the PA11/CB and PA11/CB/50nmSNP showed no discernible changes in intensity. The melting behavior of both samples is shown below in Figure 3-6.

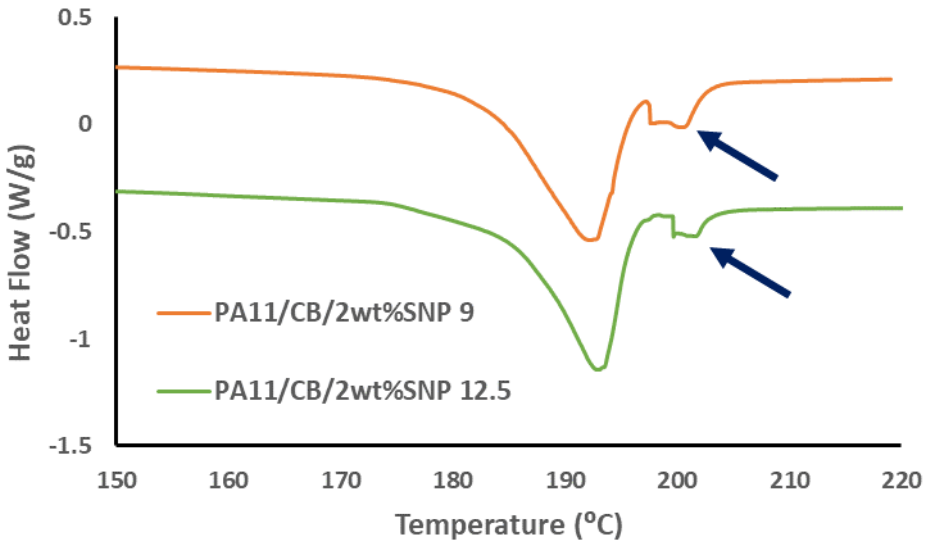

Figure 3-6: Melting behavior of printed PA11/CB/2wt%50nmSNP at A_{N9} and $A_{N12.5}$. The blue arrows highlight residual powder melting peaks.

There was concern that the presence of SNP could act as an additional nucleating agent in the PA11/CB polymer system [13]. To help answer this, the crystallization peaks of the PA11/CB/2wt%50nmSNP, PA11/CB/4wt%50nmSNP and PA11/CB A_{N9} samples were analyzed and are shown below in Figure 3-7. The value of T_C remained relatively unchanged with increases of SNP, with the highest T_m measured in the A_{N9} sample at 168.8°C. The PA11/CB/2wt%50nmSNP and PA11/CB/4wt%50nmSNP had measured T_m at 168.0°C and 167.8°C respectively. Both the breadth and area of the crystallization peak remained virtually unchanged between the three tested samples, suggesting that the crystallization kinetics were not significantly changed with 2 wt. % and 4 wt. % loadings of 50nm SNP. The crystallization peaks of all three samples are shown below in Figure 3-7, and the results for all mentioned DSC analyses are summarized in Table 3-2.

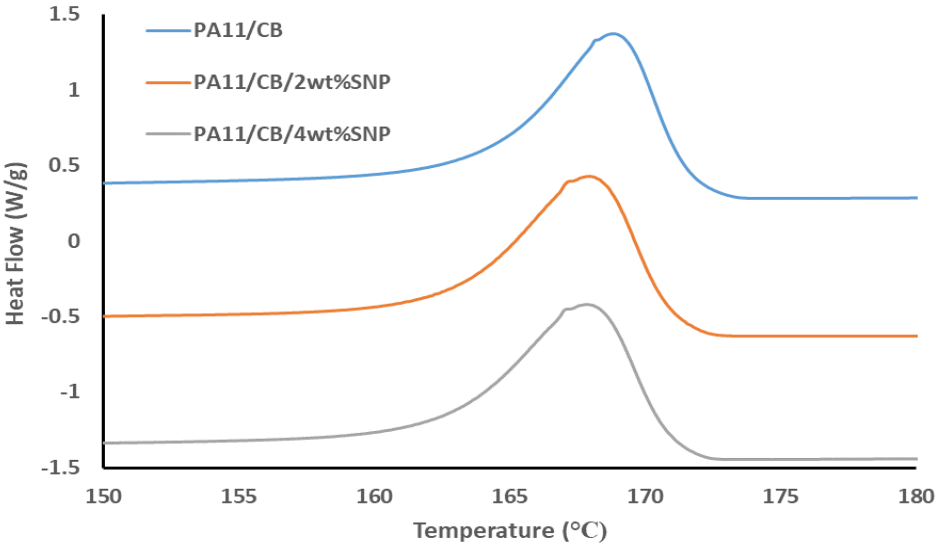

Figure 3-7: Crystallization behavior of printed PA11/CB A_{N9}, PA11/CB/2wt%50nmSNP and PA11/CB/4wt%50nmSNP samples.

Table 3-2: Thermal behavior summary of printed PA11/CB and PA11/CB/50nmSNP samples.

PA11/CB Sample	**T_m (°C)**	**T_C (°C)**	**X_C (%)**
PA11/CB	189.6°C	168.8°C	20.6%
PA11/CB/2wt%50nmSNP	192.2°C	168.0°C	21.1 %
PA11/CB/4wt%50nmSNP	190.3°C	167.8°C	20.4 %

A key processing step for the powder prior to printing is passing the dried powder through a 150 µm sieve, removing any larger particle outliers from the bulk composite powder. TGA was performed on the printed SNP containing PA11/CB to evaluate any loss in SNP through the sieving step, and to get a more accurate estimation of the weight percent of SNP in the printed material. The average residual silica weight in the PA11/CB/2wt%50nmSNP sample was 1.76%, a 9.75% reduction from the average powder SNP weight. The PA11/CB/4wt%50nmSNP had a slightly higher SNP weight reduction of 12.33%, with an average residual SNP weight in the printed material of 3.70%. The loss of SNP was likely due to the removal of PA11/CB with larger agglomerates of the nanoparticles on the surface, ultimately increasing the effective particle size. While there was a reduction of SNP through the sieving process, the average SNP weight in the printed materials was relatively close to the intended weight percent. The TGA results are shown below in Figure 3-8 and summarized in Table 3.

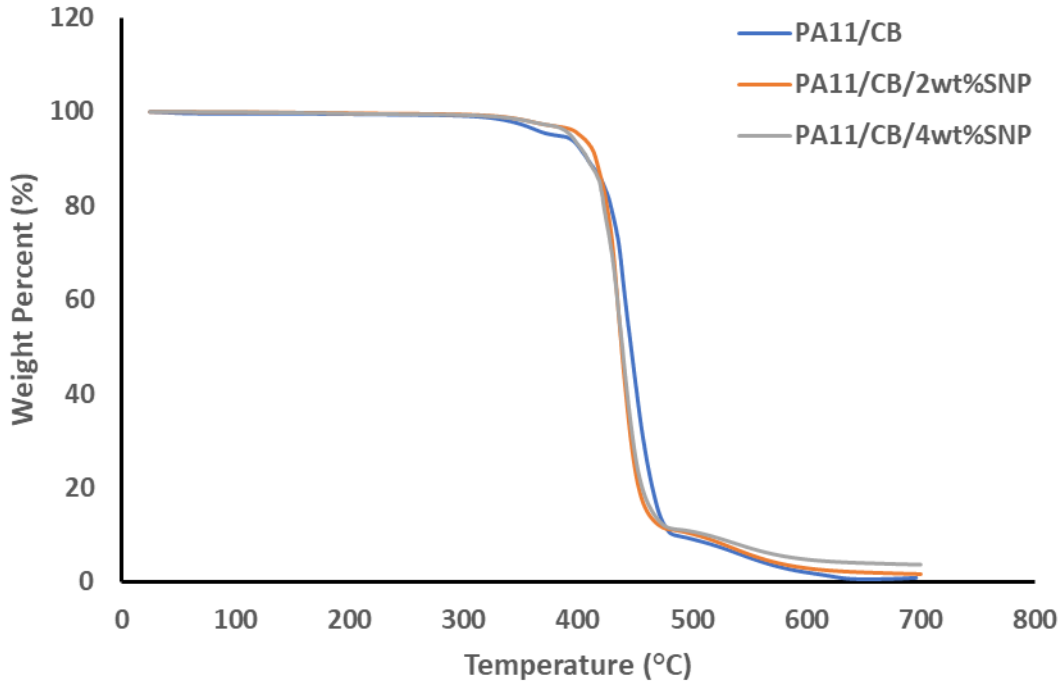

Figure 3-8: Degradation of solid state shear pulverized PA11/CB/50nmSNP printed samples.

Table 3: Summary of calculated SNP and CB content for PA11/CB and PA11/CB/50nmSNP printed samples

PA11/CB Sample	**Weight % 1**		**Weight % 2**		**Average Weight %**	
	CB (%)	SNP (%)	CB (%)	SNP (%)	CB (%)	SNP (%)
PA11/CB	0.99 %	0 %	0.91%	0 %	0.95%	0 %
PA11/CB/2wt%50nmSNP	0.95 %	1.72 %	0.95 %	1.79 %	0.95%	1.76 %
PA11/CB/4wt%50nmSNP	0.95 %	3.74 %	0.95 %	3.65 %	0.95%	3.70 %

3.3.3 Powder Flow of PA11/CB/50nmSNP

Powder flow experiments were carried out on the PA11/CB/50nmSNP powder and compared to that of the PA11/CB powder to measure the effectiveness of 50 nm SNP of increasing powder flow at increasing temperature, specifically temperatures close to SLS processing temperatures. The confined (compressive) PA11/CB powder flow did not discernably change up to 120°C, after which there was an immediate tripling of E_{flow}. The E_{flow} continued to consistently increase with increasing temperature, with the torque signal eventually showing a characteristic plateau at the 150°C, 160°C and 170°C temperatures. This plateau is associated with strong cohesion of the particles [14], leading to a yielding of the powder bulk instead of flow. The PA11/CB powder at 180°C had such strong cohesion and pre-diffusion of the polymer particles that the axial force limit for the instrument was reached, resulting in the vane rotor suspending vertical motion and prematurely stopping the test. For the unconfined (tensile) PA11/CB powder flow, E_{Flow} values were expectedly much lower, and did not discernibly change until 160°C, increasing from 0.079 mJ to 0.129 mJ. The change in torque with penetration depth for both confined and unconfined flow of PA11/CB with increasing temperature are shown below in Figures 3-9 to 3-10 and summarized in Table 3-4.

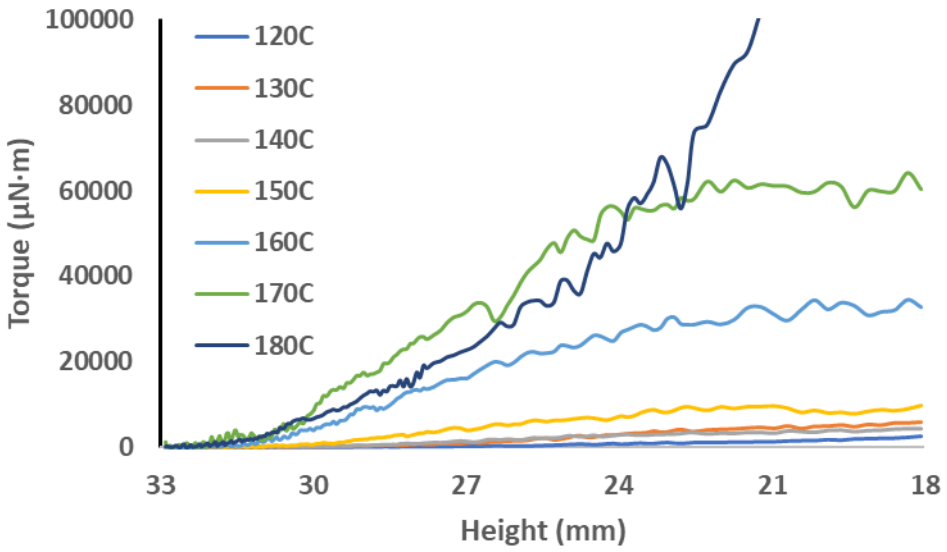

Figure 3-9: Torque signals for PA11/CB confined powder flow at increasing temperature.

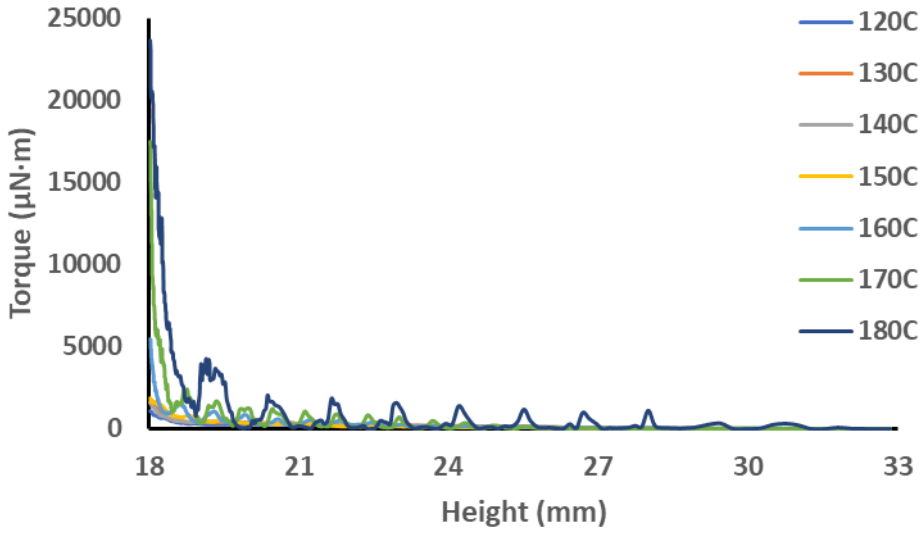

Figure 3-10: Torque signals for PA11/CB unconfined powder flow at increasing temperature.

Table 3-4: Calculated confined and unconfined E_{Flow} at increasing temperatures for PA11/CB powder

Testing Temperature (°C)	**Confined E_{Flow} (mJ)**	**Unconfined E_{Flow} (mJ)**
25°C	0.660 mJ	0.074 mJ
40°C	0.640 mJ	0.065 mJ
60°C	0.680 mJ	0.066 mJ
80°C	0.694 mJ	0.064 mJ
100°C	0.940 mJ	0.053 mJ
120°C	1.198 mJ	0.067 mJ
130°C	3.428 mJ	0.078 mJ
140°C	3.157 mJ	0.075 mJ
150°C	7.289 mJ	0.079 mJ
160°C	22.883 mJ	0.129 mJ
170°C	47.910 mJ	0.302 mJ
180°C	N/A	N/A

The powder flow of PA11/CB/2wt%50nmSNP revealed some key differences when compared to the PA11/CB standard. Both the confined and unconfined E_{Flow} was surprisingly larger for the PA11/CB/2wt%50nmSNP powder, with room temperature values of 1.118 mJ and 0.111 mJ respectively. Despite slightly higher base E_{Flow} values, the PA11/CB/2wt%50nmSNP powder proved much more stable, with increases to the confined flow not occurring until 130°C. The increases in confined E_{Flow} past 130°C were significantly less rapid, with confined E_{Flow} of PA11/CB/2wt%50nmSNP at 170°C calculated to be 14.03 mJ, as compared to the confined E_{Flow} of PA11/CB at the same temperature calculated to be 47.91 mJ. The unconfined E_{Flow} of PA11/CB/2wt%50nmSNP demonstrated no significant changes with increasing temperatures, suggesting good spreadability of the composite powder in the printer at high temperatures. While the test at 180°C was able to protrude farther with the PA11/CB/2wt%50nmSNP powder than the PA11/CB powder, the test again exceeded the axial force limit and thus stopped prematurely. The

change in torque with penetration depth for both confined and unconfined flow of PA11/CB/2wt%50nmSNP with increasing temperature are shown below in Figures 3-11 to 3-12 and summarized in Table 3-5.

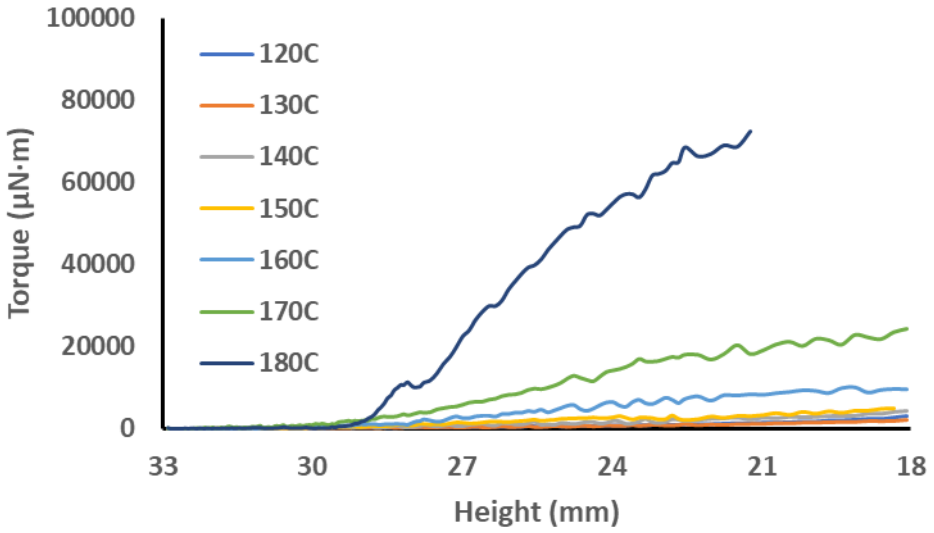

Figure 3-11: Torque signals for PA11/CB/2wt%50nmSNP confined powder flow at increasing temperature.

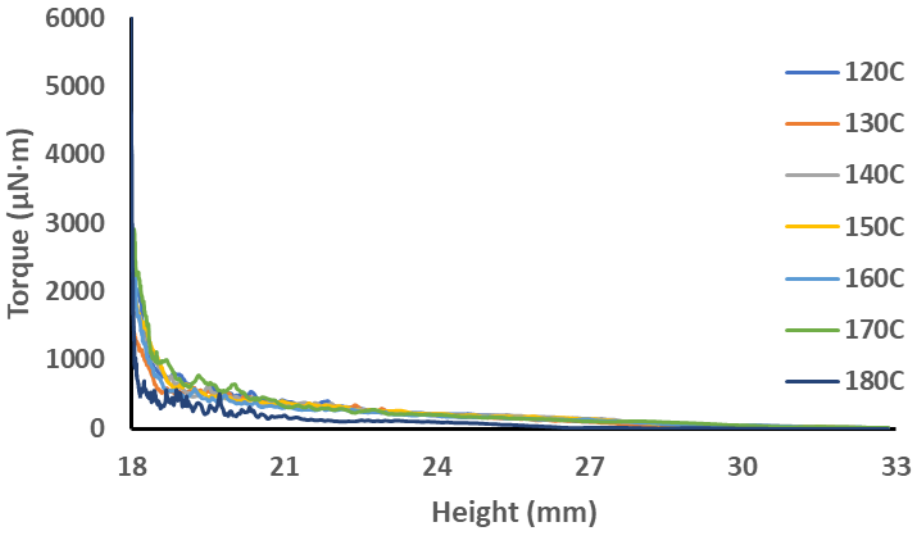

Figure 3-12: Torque signals for PA11/CB/2wt%50nmSNP unconfined powder flow at increasing temperature.

Table 3-5: Calculated confined and unconfined E_{flow} at increasing temperatures for PA11/CB/2wt%50nmSNP powder

Testing Temperature (°C)	**Confined E_{Flow} (mJ)**	**Unconfined E_{Flow} (mJ)**
25°C	1.118 mJ	0.111 mJ
40°C	1.142 mJ	0.121 mJ
60°C	1.037 mJ	0.109 mJ
80°C	1.721 mJ	0.107 mJ
100°C	1.264 mJ	0.120 mJ
120°C	1.138 mJ	0.103 mJ
130°C	1.140 mJ	0.095 mJ
140°C	2.389 mJ	0.102 mJ
150°C	3.269 mJ	0.104 mJ
160°C	7.031 mJ	0.095 mJ
170°C	14.030 mJ	0.110 mJ
180°C	N/A	N/A

The powder flow of PA11/CB/4wt%50nmSNP demonstrated superior and more stable powder flow for the tested temperature range as compared to the PA11/CB and PA11/CB/2wt%50nmSNP powders. Similar to the PA11/CB/2wt%50nmSNP powder, the base E_{Flow} values for both the confined and confined flow were elevated as compared to the PA11/CB values. However, the confined E_{Flow} did not significantly increase until 170°C, increasing from 1.78 mJ to 3.72 mJ. Additionally, powder flow at 180°C was readily measured, with a confined E_{Flow} of 10.80 mJ. The torque behavior was also markedly different, without the yielding at lower depths of the powder as seen in the PA11/CB and PA11/CB/2wt%50nmSNP samples. This suggests lower cohesion of the PA11/CB/4wt%50nmSNP powder at higher temperatures, increasing the confined powder flow. The unconfined powder flow did not discernibly change with increase in temperature, again suggesting improved dynamic flow of the powder during the transfer of an additional powder layer in the SLS printing process. The change in torque with penetration depth for both confined and

unconfined flow of PA11/CB/4wt%50nmSNP with increasing temperature are shown below in Figures 3-13 to 3-14 and summarized in Table 3-6.

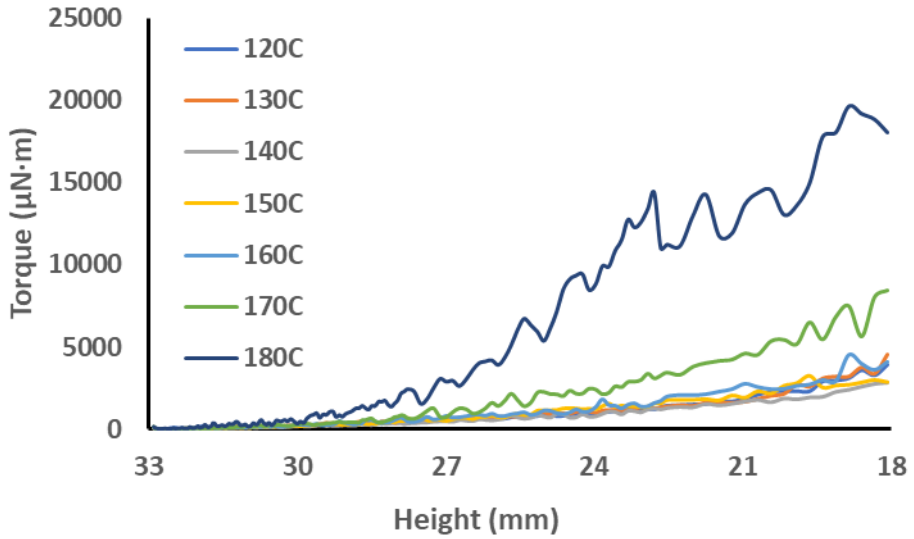

Figure 3-13: Torque signals for PA11/CB/4wt%50nmSNP confined powder flow at increasing temperature.

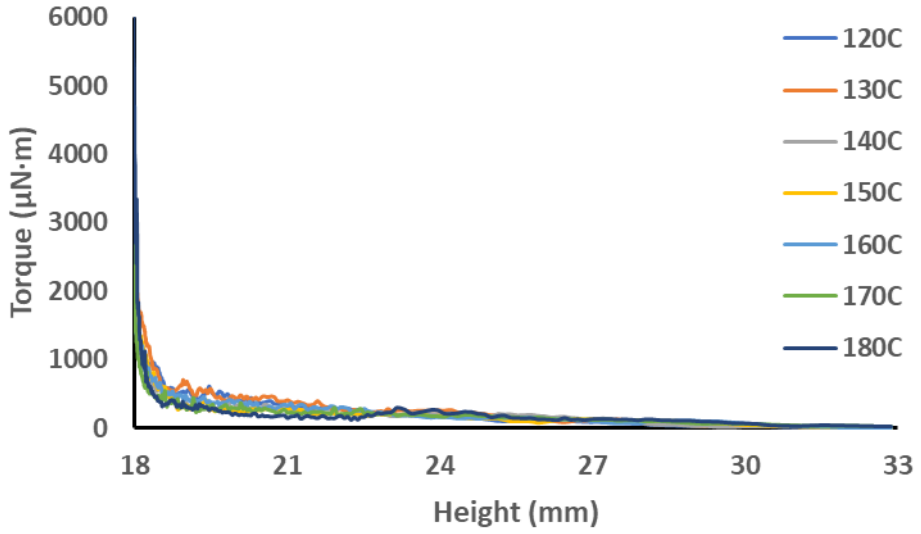

Figure 3-14: Torque signals for PA11/CB/4wt%50nmSNP unconfined powder flow at increasing temperature.

Table 3-6: Calculated confined and unconfined E_{flow} at increasing temperatures for PA11/CB/4wt%50nmSNP powder

Testing Temperature (°C)	Confined E_{Flow} (mJ)	Unconfined E_{Flow} (mJ)
25°C	1.114 mJ	0.086 mJ
40°C	1.068 mJ	0.084 mJ
60°C	1.139 mJ	0.108 mJ
80°C	1.372 mJ	0.085 mJ
100°C	1.744 mJ	0.094 mJ
120°C	1.490 mJ	0.087 mJ
130°C	1.540 mJ	0.094 mJ
140°C	1.386 mJ	0.076 mJ
150°C	1.546 mJ	0.077 mJ
160°C	1.776 mJ	0.078 mJ
170°C	3.718 mJ	0.062 mJ
180°C	10.803 mJ	0.079 mJ

3.3.4 Mechanical Behavior of PA11/CB/50nmSMP

Both tensile testing (ASTM D638-14) and dynamic mechanical analysis (DMA) (ASTM D5279-13) were employed to gauge the effect of increasing SNP on the SLS printed PA11/CB mechanical behavior. PA11/CB/2wt%50nmSNP and PA11/CB A_{N9} tensile samples demonstrated no discernible change in tensile modulus, with the average tensile modulus of both being 1.8 GPa. The average tensile modulus of the PA11/CB/4wt%50nmSNP was slightly lower at 1.7 GPa, likely as a result of the amount of unsintered PA11/CB powder in the polymer matrix. Ultimate tensile strength remained consistent for the PA11/CB/2wt%50nmSNP samples as compared to the PA11/CB A_{N9} samples, however the PA11/CB/4wt%50nmSNP samples revealed a lower average ultimate tensile strength of 49.8 MPa. The largest change in tensile behavior between the PA11/CB and PA11/CB/50nmSNP samples was the elongation at break, which reduced substantially with the addition of SNP. The average elongation at break for the PA11/CB/2wt%50nmSNP samples

was 21.1%, while the average elongation to break for the PA11/CB/4wt%SNP samples was 17.9% as compared to the average PA11/CB A_{N9} values of 63.1%. It is likely again that poor polymer diffusion and SNP agglomerates across the SNP boundary have led to diminished elongation at break, however previous results of Nylon 6 and functionalized SNP composites have shown a similar decrease in strain with SNP loading [15]. The tensile behavior of the PA11/CB/50nmSNP composites is illustrated below in Figure 3-15, with the results summarized in Table 3-7.

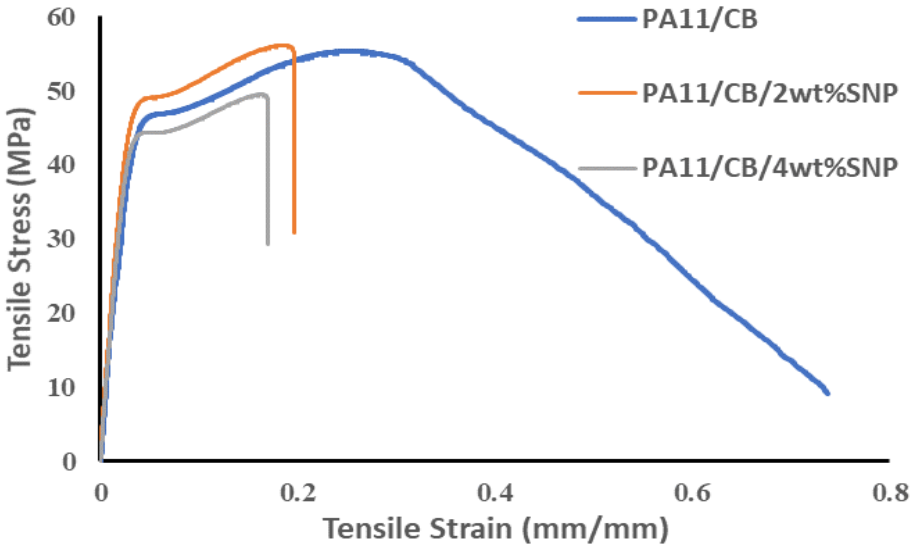

Figure 3-15: Tensile behavior of PA11/CB and PA11/CB/50nmSNP samples.

Table 3-7: Tensile behavior summary of PA11/CB and PA11/CB/50nmSNP samples.

PA11/CB Sample	**Ultimate Tensile Strength (MPa)**	**Elongation to Break (%)**	**Tensile Modulus (GPa)**
PA11/CB A_{N9}	52.6 ± 0.8 MPa	63.1 ± 7.5%	1.8 ± 0.1 GPa
PA11/CB/2wt%50nmSNP	53.3 ± 0.7 MPa	21.1 ± 3.1%	1.8 ± 0.1 GPa
PA11/CB/4wt%50nmSNP	49.8 ± 0.9 MPa	17.9 ± 1.9 %	1.7 ± 0.1 GPa

The PA11/CB/50nmSNP tensile (E′) and shear (G′) modulus values were compared to those as expected by the Halpin-Tsai model, and the comparison is illustrated below in Figure 3-16. E′ was determined through finding the slope of the PA11/CB and PA11/CB/50nmSNP tensile stress/strain

curves between 0 and 20 MPa. Within standard error, the PA11/CB/2wt%50nmSNP fall into the predicted values well. The PA11/CB/4wt%50nmSNP moduli alternatively do not compare well to that as predicted by the Halpin-Tsai model, although this again is likely due to poor polymer diffusion across the SNP boundaries. There could also be a slight lowering of modulus due to reduced molecular weight of the total PA11 phase, as Section 2.3.4 demonstrated a significant change in molecular weight between the PA11/CB powder and the printed material. X_C remains fairly constant between the PA11/CB and PA11/CB/50nmSNP samples, which combined with nominal changes in T_m suggests minimal changes in spherulite size within the printed samples. If there was more efficient sintering of the PA11/CB in the PA11/CB/50nmSNP composites, it is likely that the both experimental moduli would be in better agreeance with the Halpin-Tsai model.

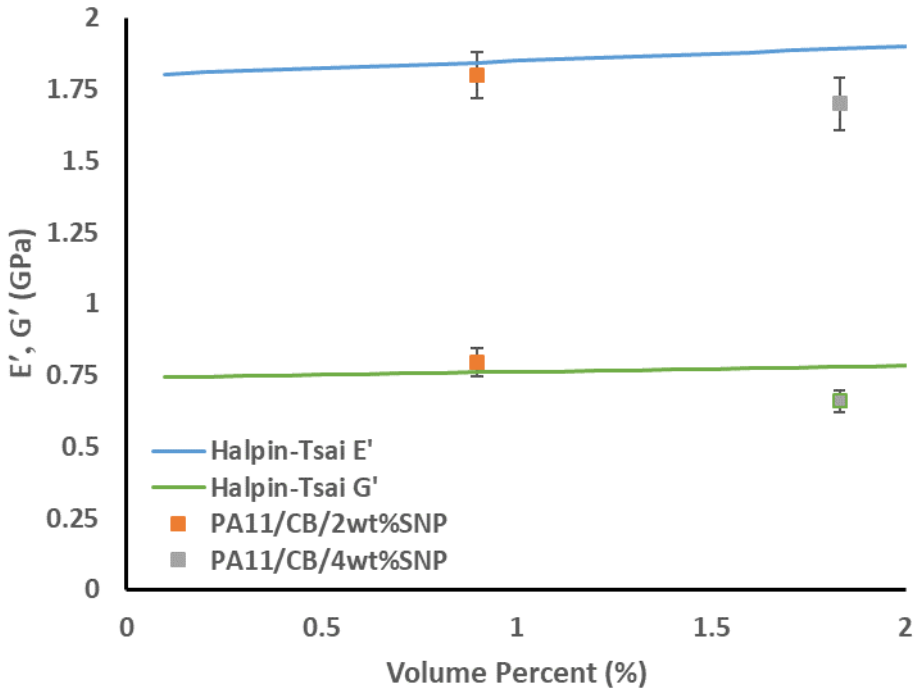

Figure 3-16: Comparison of experimental and Halpin-Tsai predicted modulus of PA11/CB/50nmSNP samples.

In addition to tensile testing, DMA was additionally performed on the composite materials, and compared to a PA11/CB A_{N9} standard. The storage modulus (G′) of the PA11/CB/2wt%50nmSNP

and PA11/CB A_{N9} was very similar, with room temperature shear modulus values of 0.80 GPa and 0.74 GPa, respectively. The G′ for the PA11/CB/4wt%50nmSNP was noticeably lower, with room temperature G′ of 0.66 GPa. The PA11/CB/50nmSNP samples did demonstrate lower degrees of stress relaxation, as quantified by the difference in G′ at room temperature and the rubbery plateau, taken at 100°C for the present study. The smallest change in G′ was seen in the PA11/CB/4wt%50nmSNP sample at 0.54 GPa, followed by the PA11/CB/2wt%50nmSNP sample at 0.61 GPa and the PA11/CB A_{N9} sample at 0.64 GPa. The G′ and loss modulus (G″) for each tested sample are shown below in Figure 3-17. The glass transition temperature (T_g) was additionally evaluated using the maximum of the tan(δ) peak, shown in Figure 3-18. The T_g for the PA11/CB A_{N9} and the PA11/CB/2wt%50nmSNP sample were very similar at 59.4°C and 59.0°C respectively. The T_g for the PA11/CB/4wt%50nmSNP was measured lower at 54.4°C, possibly as a result of lower molecular weight of the polymer due to the larger presence of unsintered PA11.

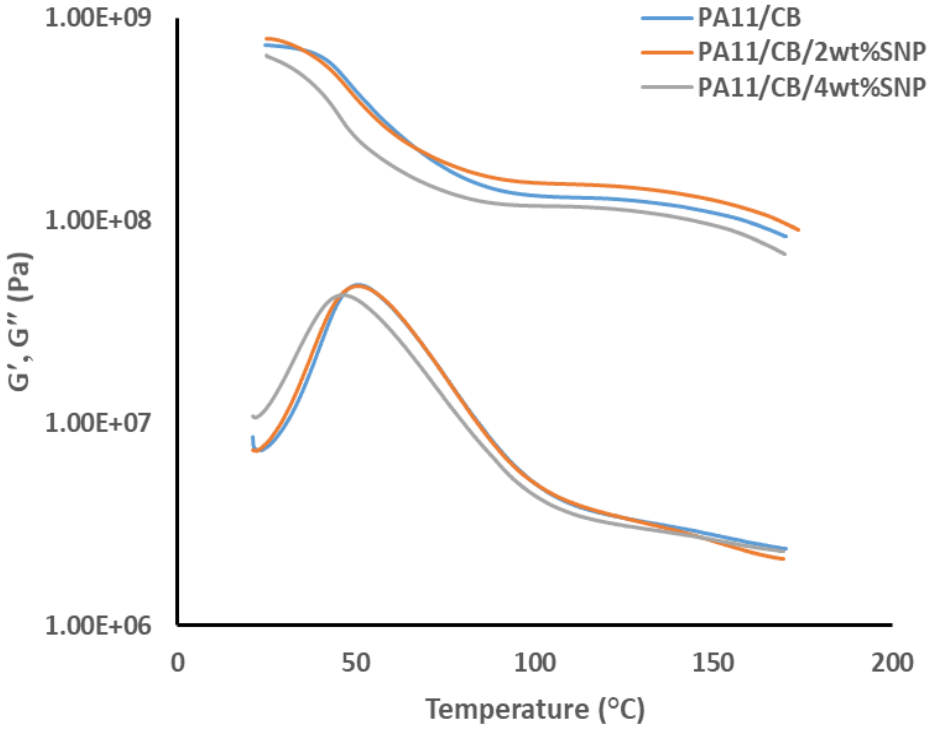

Figure 3-17: Storage and loss modulus of PA11/CB and PA11/CB/50nmSNP samples with increasing temperature.

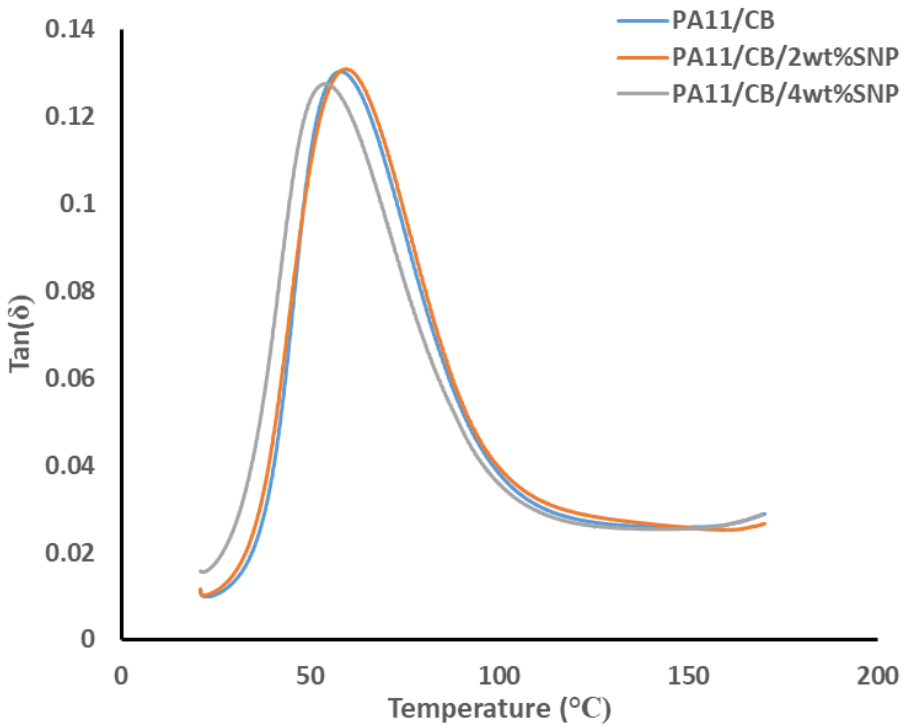

Figure 3-18: Tan(δ) of PA11/CB and PA11/CB/50nmSNP samples with increasing temperature.

3.3.5 PA11/CB/50nmSNP Tensile Surface

Tensile fracture surfaces of the PA11/CB/50nmSNP were characterized using SEM. Both the PA11/CB/2wt%50nmSNP and PA11/CB/4wt%50nmSNP demonstrated small areas of ductile tearing that transitioned into very brittle and planar failure. The brittle section in both samples exhibited signs of crazing, whereas the ductile sections demonstrated similar elongated and oriented fibrillar networks as highlighted in Section 2.3.6. In the both PA11/CB/2wt%50nmSNP PA11/CB/4wt%50nmSNP tensile fracture surfaces, both the brittle and ductile section revealed cracks that seemingly appeared between individual sintered particle boundaries. The PA11/CB/4wt%50nmSNP sample additionally showed cracking in the printing direction, suggesting poor diffusion of the PA11 polymer across printed polymer layers. Figure 3-19 compares brittle, ductile and brittle/ductile transitional tensile surfaces of both the PA11/CB/2wt%50nmSNP and PA11/CB/4wt%50nmSNP samples.

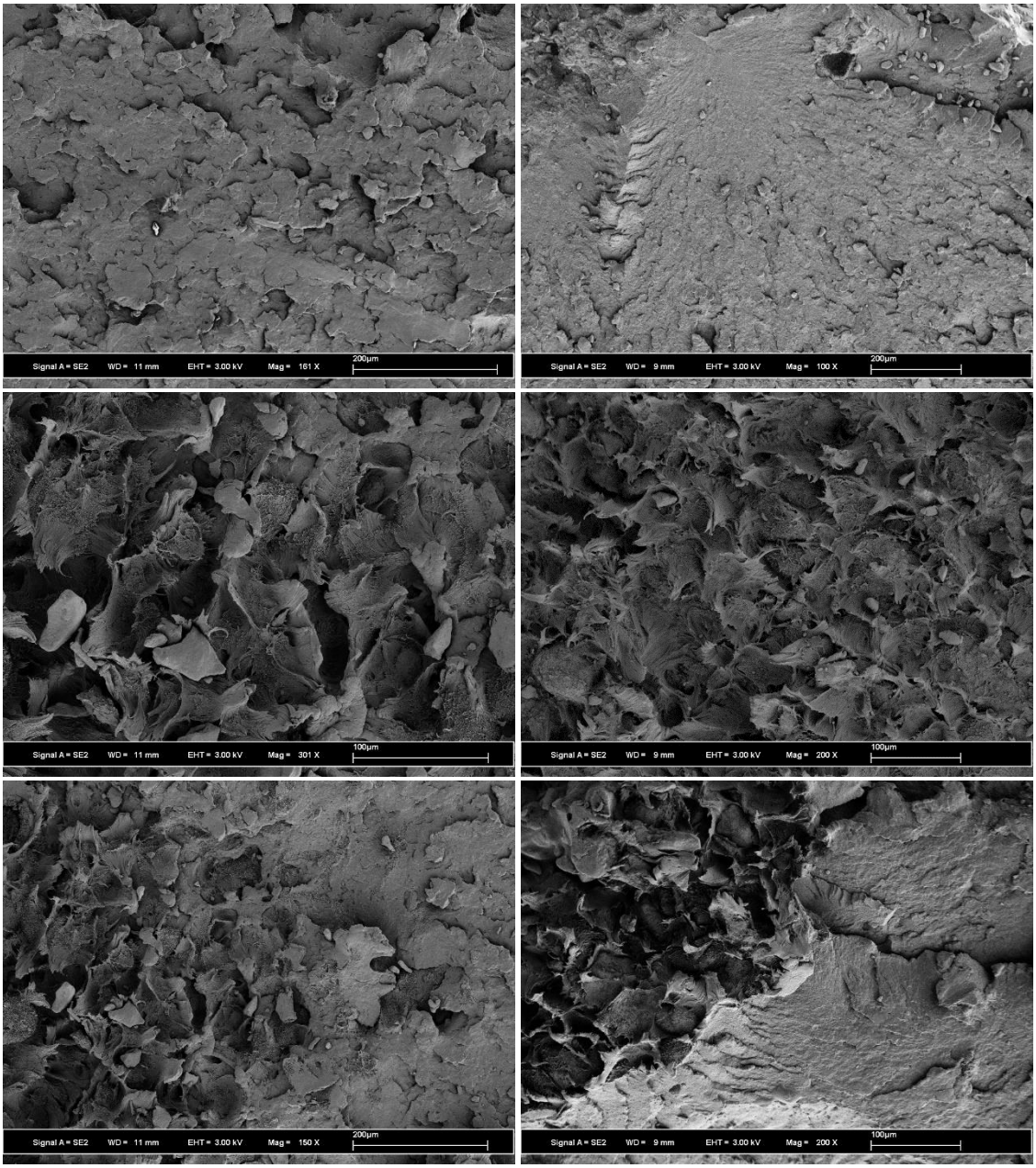

Figure 3-19: Images highlighting both ductile and brittle tensile behavior of PA11/CB/2wt%50nmSNP (left) and PA11/CB/4wt%50nmSNP (right) samples.

Sources of stress concentration within both samples were easy to identify, with unsintered particles evident in the PA11/CB/2wt%50nmSNP, and at a higher concentration in the PA11/CB/4wt%50nmSNP samples. This confirms the DSC results in Section 3.3.2 showing large residual peaks of unsintered virgin PA11/CB powder in both PA11/CB/50nmSNP samples. Additionally, SNP agglomerates were present in both samples, but seen in a higher frequency in

the PA11/CB/4wt%50nmSNP sample. In many cases, cracks and tearing of the polymer matrix were shown to germinate from these stress concentration sources. Examples of stress concentrators in the PA11/CB/4wt%50nmSNP tensile samples are shown below in Figure 3-20.

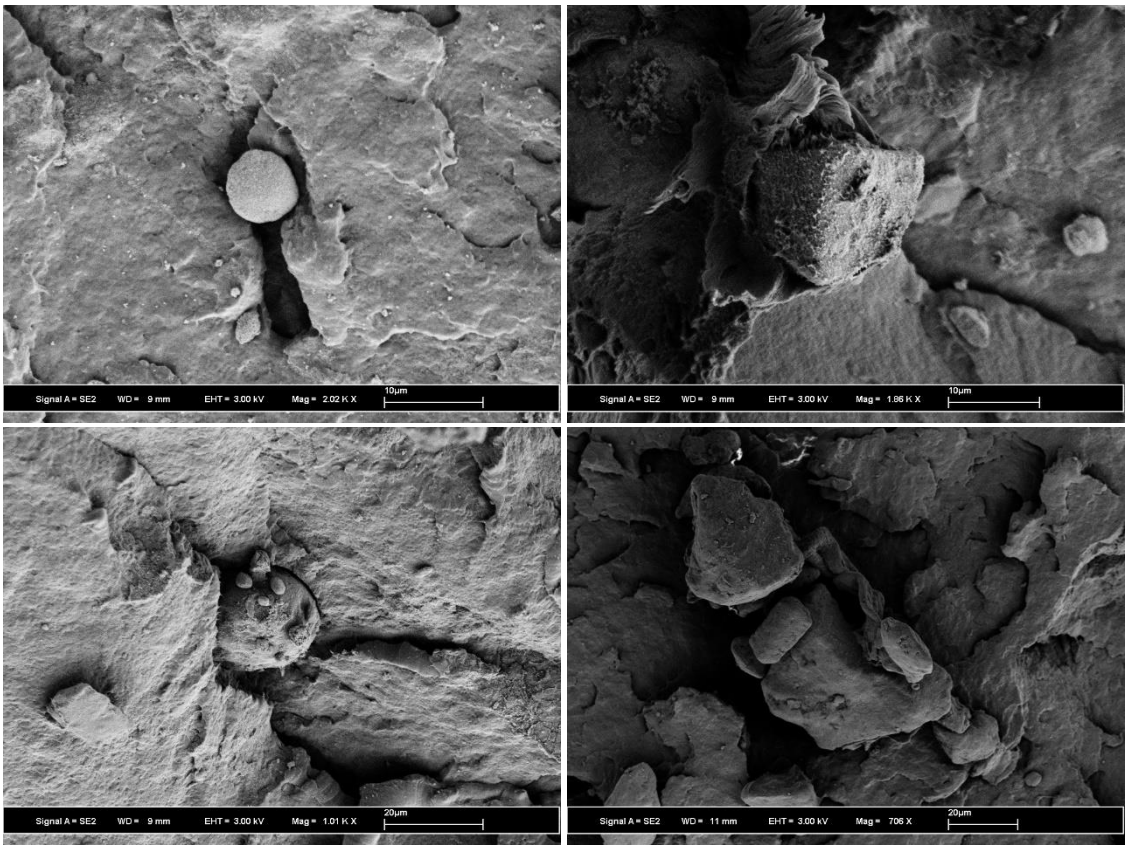

Figure 3-20: Images highlighting unsintered PA11/CB particles and SNP agglomerates in the PA11/CB/4wt%50nmSNP tensile samples.

As mentioned before, the more planar and brittle sections of the tensile specimens showed signs of crazing, which was especially evident in the PA11/CB/2wt%50nmSNP sample. Linearly elongated and oriented fibrils were found connecting separate fractured planes of the polymer matrix, indicative of polymer bridging or crazing, and are shown in Figure 3-21. In general, there have been many reported studies of SNP increasing polymer crazing as a primary deformation mechanism, however this is predominantly seen in amorphous, glassy polymer matrices [16]. Incidentally, polyamides have been known to undergo crazing as a deformation mechanism,

although typically as a result of environmental stress cracking [17]. It is possible that the addition of SNP not only increases the stiffness and rigidity of the matrix, but also participates in toughening mechanisms such as debonding that help increase the incidence of craze formation in the PA11/CB/2wt%50nmSNP samples.

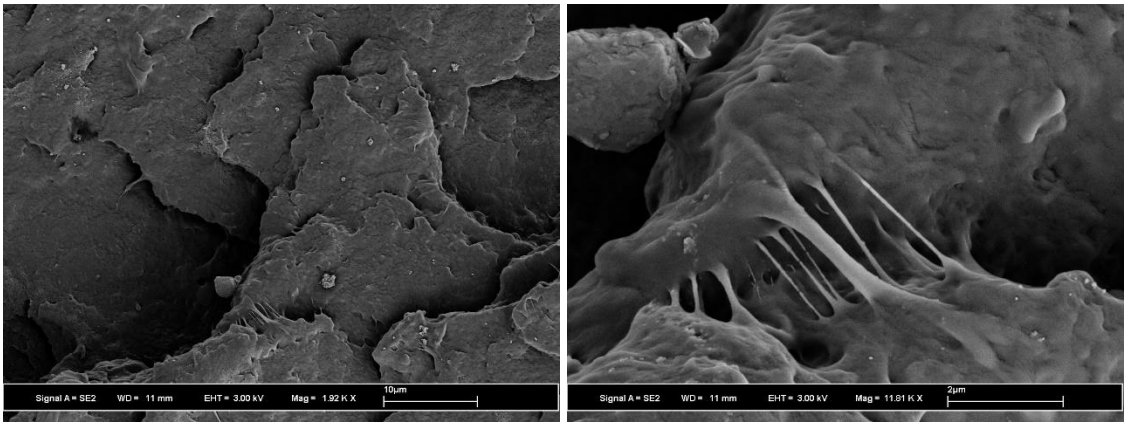

Figure 3-21: Images highlighting fibril bridge and craze formation in the PA11/CB/2wt%50nmSNP tensile failure surface.

The SNP boundaries between adjacent particles were noticeable in both PA11/CB/50nmSNP polymer matricies, emerging as clear SNP rich linear boundaries surrounded by PA11 matrix. The average thickness of this boundary increased with increasing SNP, with a 1 µm boundary present in the PA11/CB/2wt%50nmSNP samples and a 2 µm boundary in the PA11/CB/4wt%50nmSNP samples. These clearly SNP rich sections illustrate the poor diffusion of both the SNP into the PA11 matrix, and in the case of the PA11/CB/4wt%50nmSNP samples PA11 through the SNP boundary. The poor polymer diffusion in the PA11/CB/4wt%50nmSNP is supported by the netted and fibrous matrix of the silica boundaries in contrast with the more dense and solid brittle bulk. Examples of these SNP boundaries for each PA11/CB/50nmSNP sample are shown below in Figure 3-22.

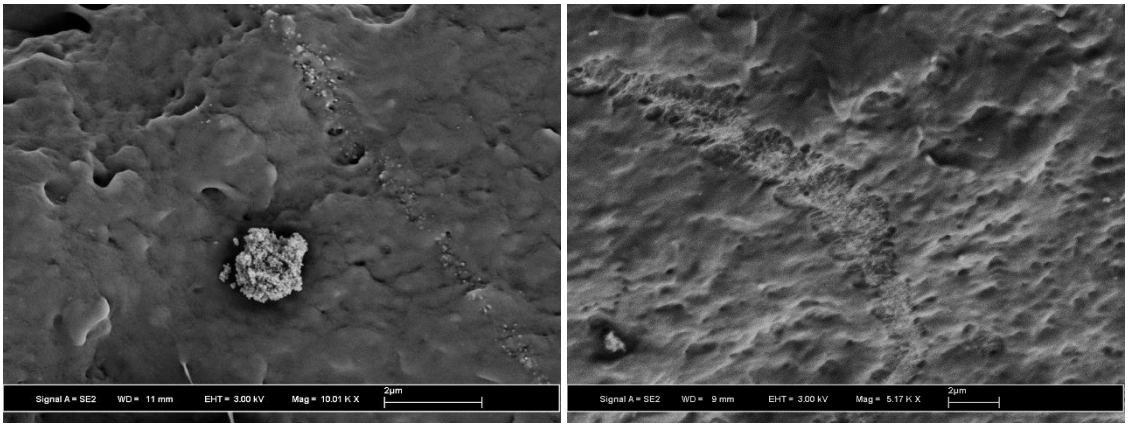

Figure 3-22: Evidence of SNP particle boundaries in the PA11/CB/2wt%50nmSNP (left) and PA11/CB/4wt%50nmSNP (right) powder samples.

In the PA11/CB/2wt%50nmSNP samples, it should be noted that these SNP rich boundaries were present in both the brittle and ductile tensile failure sections. In the brittle failure sections, smaller voids are present surrounding individual particles, indicative of particle debonding from the PA11/CB matrix [18]. When analyzing the SNP rich boundaries in the ductile failure sections, the microstructure appeared incredibly similar to the microvoided dimple nodes present in Section 2.3.6, as a result of the carbon black in the PA11/CB. The SNP rich seams are highly porous, with parabolic tearing extending from the boundary to the ductile polymer tears. The SNP is present throughout the boundary, but positioned mostly on the edges of voids and the parabolic tears, suggesting the SNP may be initiating and propagating the microvoids observable in the area. While the PA11/CB/2wt%50nm SNP samples were too brittle to undergo a valid essential work of fracture study, the presence of SNP engaging in toughening mechanisms at the particle boundaries is incredibly encouraging. These observations suggest that while the SNP layers on the PA11/CB particles were likely too thick for PA11 to diffuse through, the SNP itself shows promise in effectively reinforcing and toughening the PA11/CB matrix. Select toughened SNP boundaries in the PA11/CB/2wt%50nmSNP sample are shown below in Figure 3-23.

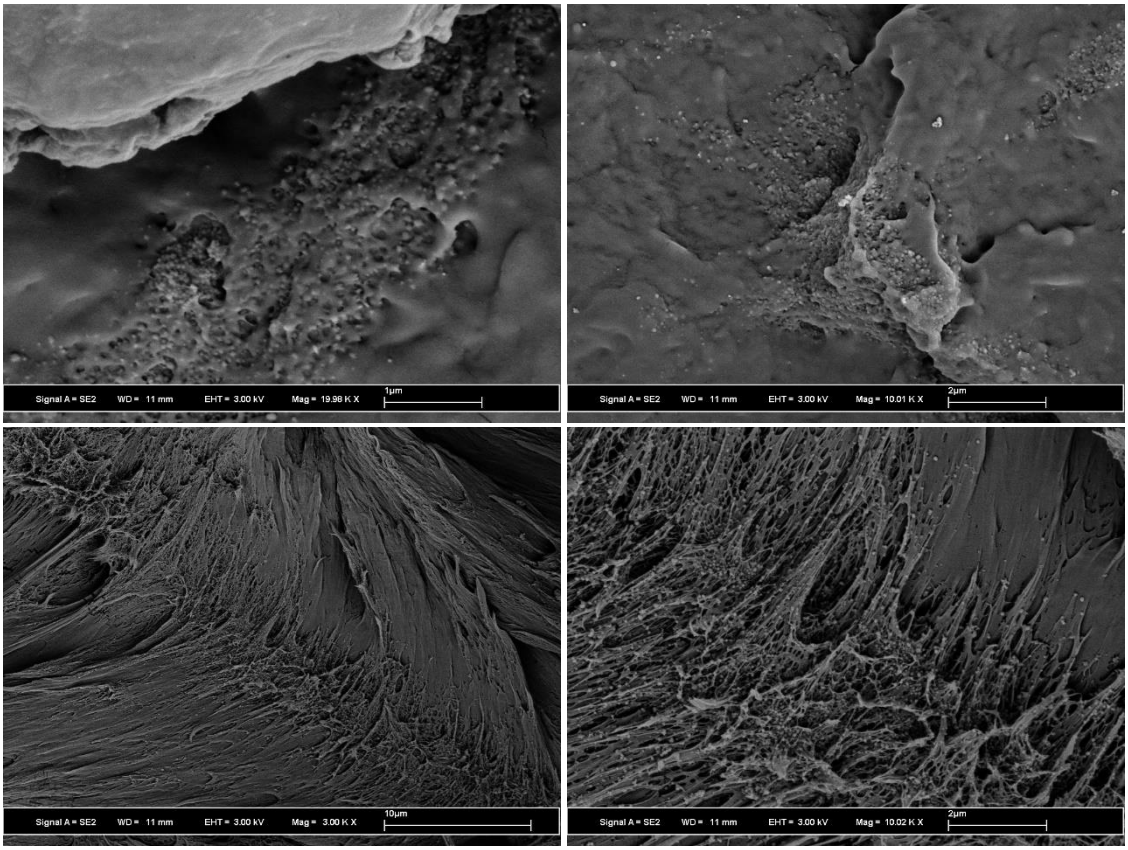

Figure 3-23: Evidence of SNP debonding and toughening in the PA11/CB/2wt%50nmSNP tensile failure surface.

3.3.6 PA11/CB/25nmSNP Powder Processing

PA11/CB/25nmSNP powder was mixed with 0.25 wt. %, 0.5 wt. %, 1 wt. % and 2 wt. % SNP loadings using centrifugal mixing. At every increased loading of SNP, the powder remained exceptionally homogenous with little to no visible SNP agglomerates. Selected SEM images are shown for samples of each PA11/CB/25nmSNP powder below in Figures 3-24 to 3-27. The PA11/CB particle shape and size appeared unchanged with the addition of SNP, with angular geometry nominally 50 μm in size. Upon higher magnification, it is shown that the SNP adhered quite well to the PA11/CB surface with each SNP loading. The PA11/CB/0.25wt%25nmSNP samples demonstrated partial PA11/CB surface covering, with a full single layer of SNP on the PA11/CB particle observed at the 0.5 wt. % SNP loading. Emerging multiple layers of SNP were visible for the PA11/CB/1wt%25nmSNP and PA11/CB/2wt%25nmSNP powders, with thicker

SNP layers collected at concavities on the PA11/CB particle surfaces. Additionally, SNP aggregates of several particles were apparent on the PA11/CB/1wt%25nmSNP and PA11/CB/2wt%25nmSNP surface, but no signs of larger SNP agglomerates.

In addition to SEM, TGA was also employed on the powder sample to determine the distribution of SNP particles in the composite powder. The average CB wt. % used in calculations was that as reported in Chapter 3.3.1. The average measured SNP content for the 0.25 wt. %, 0.5 wt. %, 1 wt. % and 2 wt. % loaded samples were 0.26 wt. %, 0.52 wt. % 1.00 wt. % and 1.95 wt. % respectively, demonstrating good homogenization of mixing. Centrifugal mixing with the aid of ceramic beads proved immensely useful in producing homogenous powder blends for SLS printing. The degradation results are illustrated in Figure 3-28 and summarized in Table 3-8.

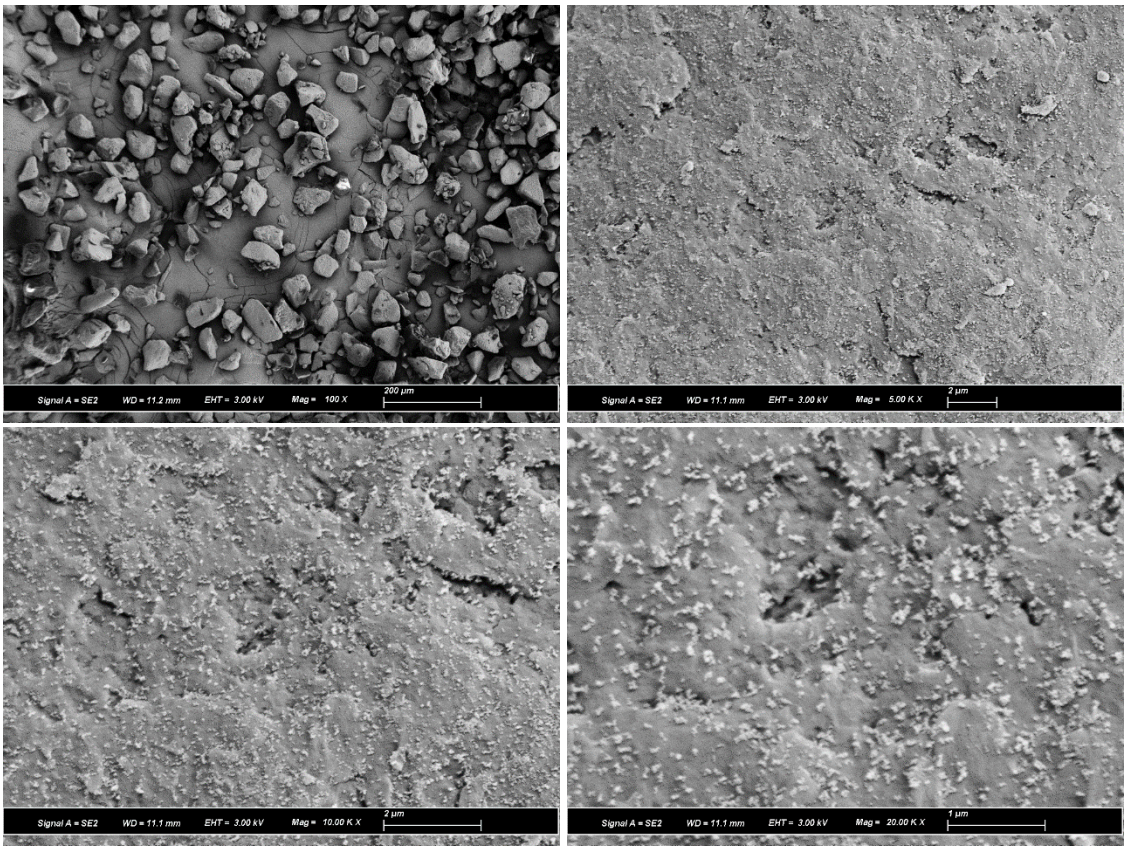

Figure 3-24: Images highlighting SNP coverage of the PA11/CB/0.25wt%25nmSNP particle surface.

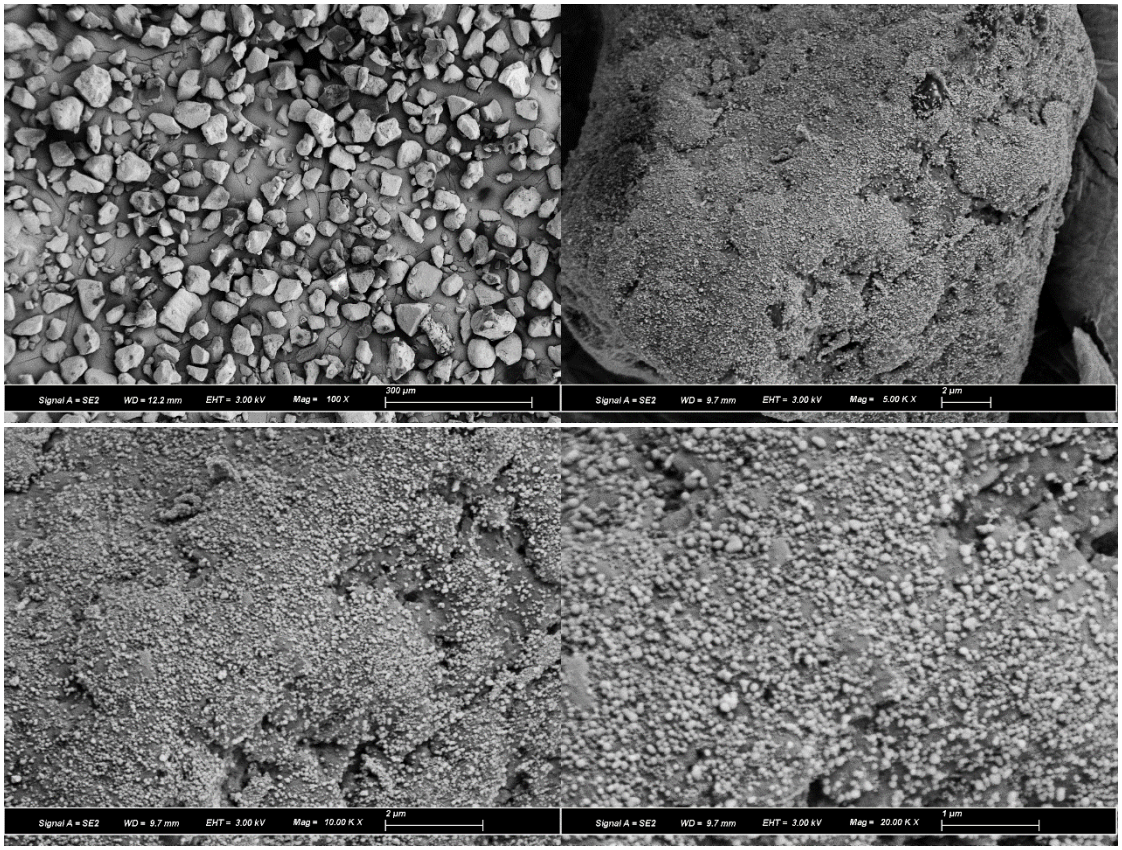

Figure 3-25: Images highlighting SNP coverage of the PA11/CB/0.5wt%25nmSNP particle surface.

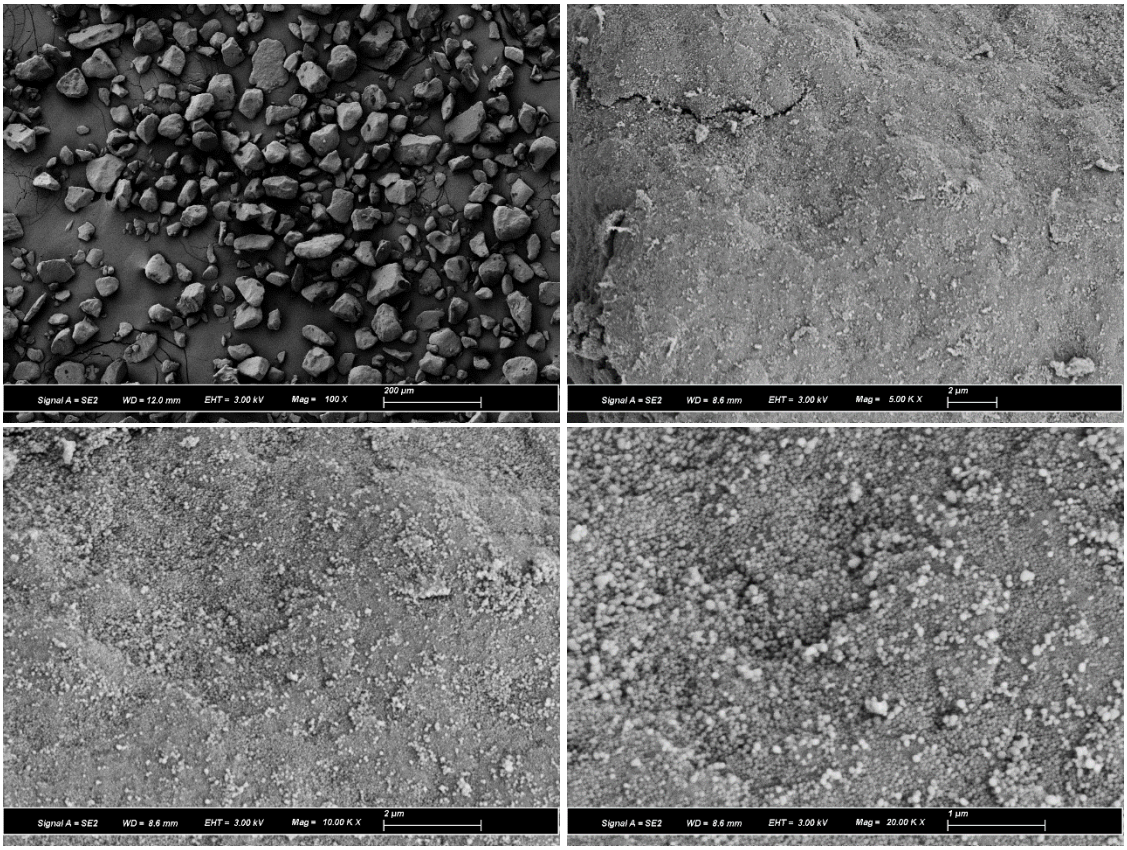

Figure 3-26: Images highlighting SNP coverage of the PA11/CB/1wt%25nmSNP (left) particle surface.

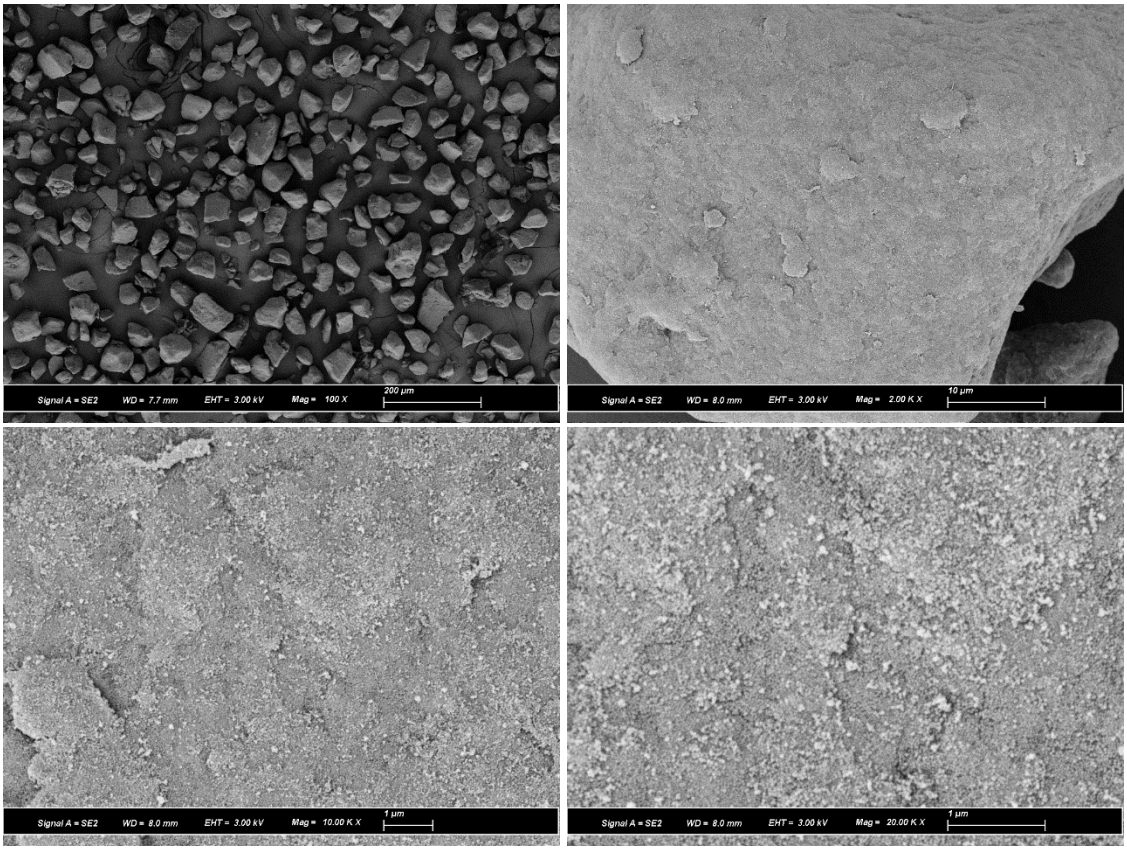

Figure 3-27: Images highlighting SNP coverage of the PA11/CB/2wt%25nmSNP particle surface.

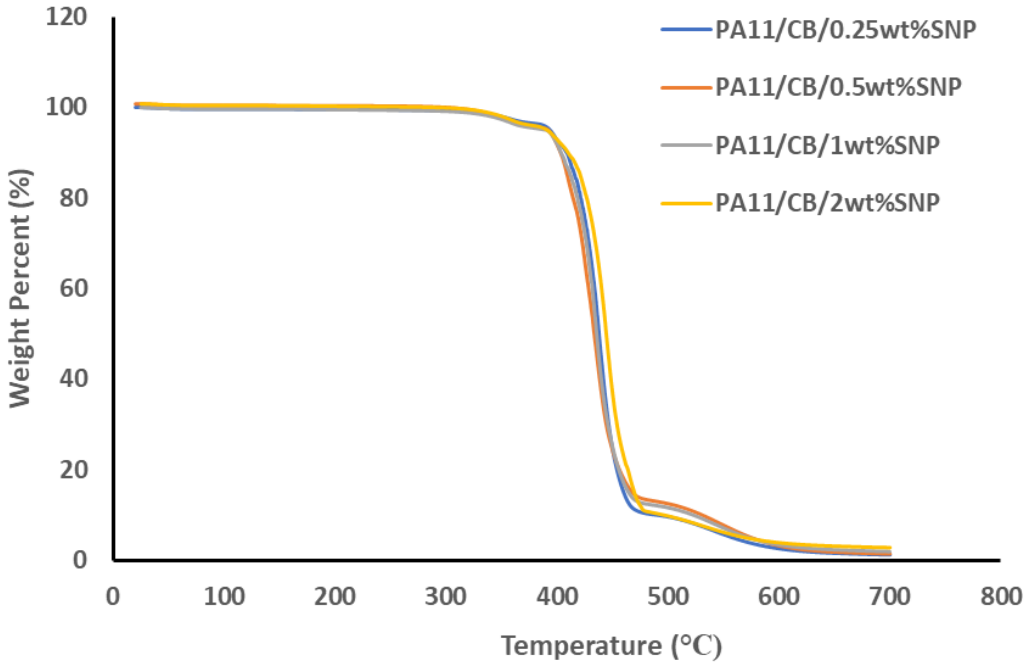

Figure 3-28: Degradation of mixed PA11/CB/25nmSNP powder samples.

Table 3-8: Summary of calculated SNP and CB content for PA11/CB and PA11/CB/25nmSNP powder samples

PA11/CB Sample	Weight % 1		Weight % 2		Average Weight %	
	CB (%)	SNP (%)	CB (%)	SNP (%)	CB (%)	SNP (%)
PA11/CB/0.25wt%25nmSNP	0.95 %	0.29 %	0.95 %	0.22 %	0.95 %	0.26 %
PA11/CB/0.5wt%25nmSNP	0.95 %	0.50 %	0.95 %	0.53 %	0.95 %	0.52 %
PA11/CB/1wt%25nmSNP	0.95 %	1.03%	0.95 %	0.96 %	0.95 %	1.00 %
PA11/CB/2wt%25nmSNP	0.95 %	2.02 %	0.95 %	1.88 %	0.95 %	1.95 %

3.3.7 Thermal Analysis of PA11/CB/25nmSNP

Melting temperatures (T_m) and weight percent crystallinity (X_C) of printed PA11/CB/25nmSNP with 0.25 wt. %, 0.5 wt. %, 1 wt. % and 2 wt. % SNP loadings were compared to elucidate changes in melting behavior. The melting behavior was somewhat similar, with T_m ranging from 191.3°C to 192.6°C for all tested samples. Both the PA11/CB/0.25wt%25nmSNP and PA11/CB/0.5wt%25nmSNP samples demonstrated slight shoulders in the melting peaks, occurring at approximately 188°C and 170°C respectively. These shoulders compare well to those noted in the A_{N8} and A_{N9} samples in Chapter 2, suggesting the SNP containing samples likely have changes in d_{hkl} spacing, also highlighted in Chapter 2 [19]. All tested PA11/CB/25nmSNP samples showed smaller residual peaks closer to the melting temperature of the virgin powder, which has been shown to represent an unmelted core of the powder particle [12]. The residual peak grew with area with increase in SNP as with the PA11/CB/50nmSNP powder samples, suggesting again that the presence of SNP reduced the sintering and diffusion of the PA11 through the SNP particle boundaries. The values of X_C remained constant with increasing SNP content, with X_C ranging from 20.9% to 22.6% for all tested PA11/CB/25nmSNP samples. The melting behavior for all four PA11/CB/25nmSNP samples is shown in Figure 3-29.

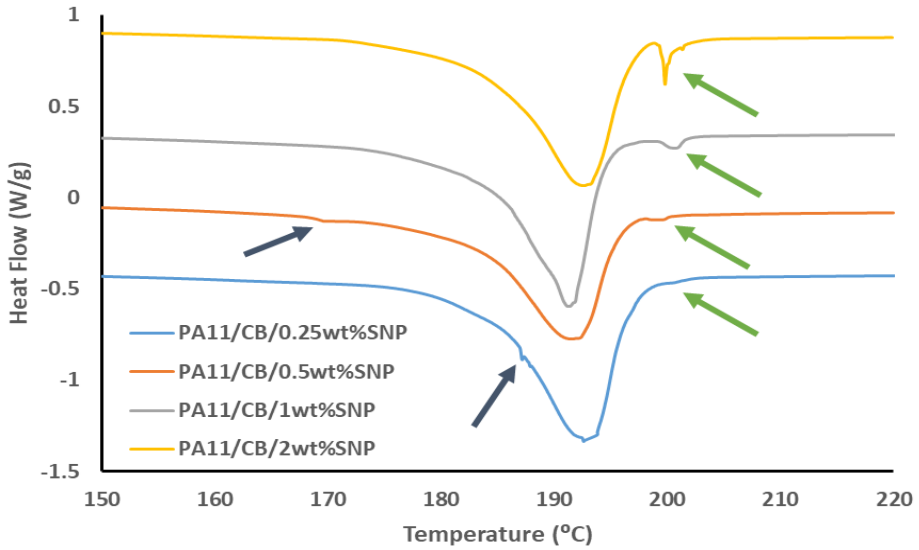

Figure 3-29: Melting behavior of printed PA11/CB PA11/CB/25nmSNP samples. The blue arrows highlight melting shoulders, while the green arrows show the residual powder melting peak.

As mentioned in Section 3.3.2, there was concern that the presence of SNP could act as an additional nucleating agent in the PA11/CB polymer system. The crystallization peaks of the PA11/CB/25nmSNP samples were analyzed and are shown below in Figure 30. The value of T_C remained relatively unchanged with increases of SNP, varying between 167.9°C and 168.0°C for the 25nm SNP containing samples. Both the breadth and area of the crystallization peak remained unchanged between the three tested samples, suggesting that the crystallization kinetics were not significantly changed with 0.25 wt. %, 0.5 wt. %, 1 wt. % and 2 wt. % loadings of 25nm SNP. The crystallization peaks of all four samples are shown below in Figure 3-30, and the results for all mentioned DSC analyses are summarized in Table 3-9.

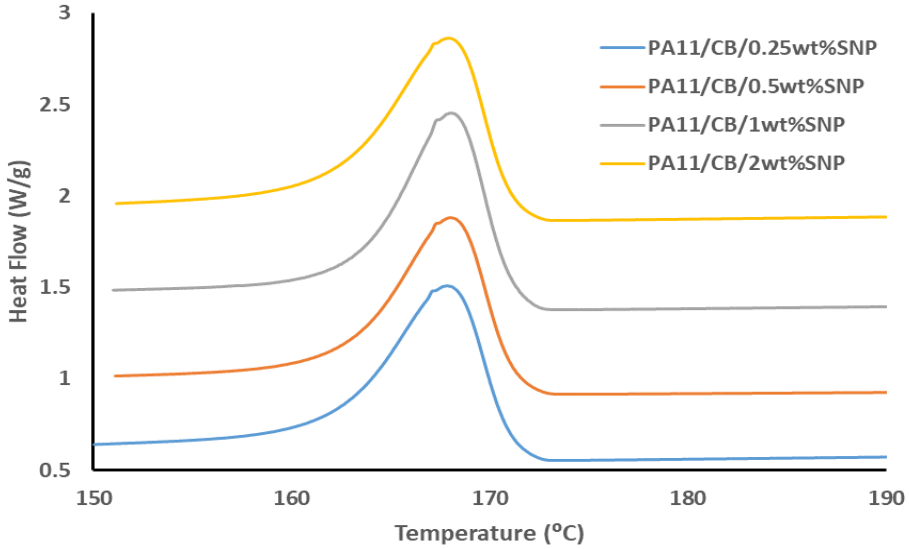

Figure 3-30: Crystallization behavior of printed, PA11/CB/25nmSNP samples.

Table 3-9: Thermal behavior summary of printed PA11/CB and PA11/CB/25nmSNP samples.

PA11/CB Sample	**T_m (°C)**	**T_C (°C)**	**X_C (%)**
PA11/CB	189.6°C	168.8°C	20.6%
PA11/CB/0.25wt%25nmSNP	192.5°C	167.9°C	22.6 %
PA11/CB/0.5wt%25nmSNP	191.5°C	168.0°C	21.5 %
PA11/CB/1wt%25nmSNP	191.3°C	168.0°C	20.9 %
PA11/CB/2wt%25nmSNP	192.6°C	167.9°C	21.7 %

Lastly, TGA was performed on the printed SNP containing PA11/CB to evaluate any loss in SNP through the powder sieving step prior to printing, and to get a more accurate estimation of the weight percent of SNP in the printed materials. The average residual silica weight in the PA11/CB/0.25wt%25nmSNP sample was 0.25%, technically 3.8% reduction from the average powder SNP weight but still well within range of the separate powder values. The PA11/CB/0.5wt%25nmSNP had a similarly negligible SNP weight change, this time a 1.9% increase to 0.53% SNP in the printed material. The PA11/CB/1wt%25nmSNP sample showed an even lower change in weight percent between the printed and powder samples of 1.0% for an average SNP weight percent in the printed material of 1.01%. The PA11/CB/2wt%25nmSNP sample demonstrated a 3.1% change in SNP content after sieving, with an average residual SNP weight in the printed material of 1.89%. The negligible change in SNP between the powder and

printed samples suggests a low likelihood of large agglomerates of SNP on the PA11/CB surfaces, and confirms the average SNP weight in the printed materials was very close to the intended weight percent. The TGA results are shown below in Figure 3-31 and summarized in Table 3-10.

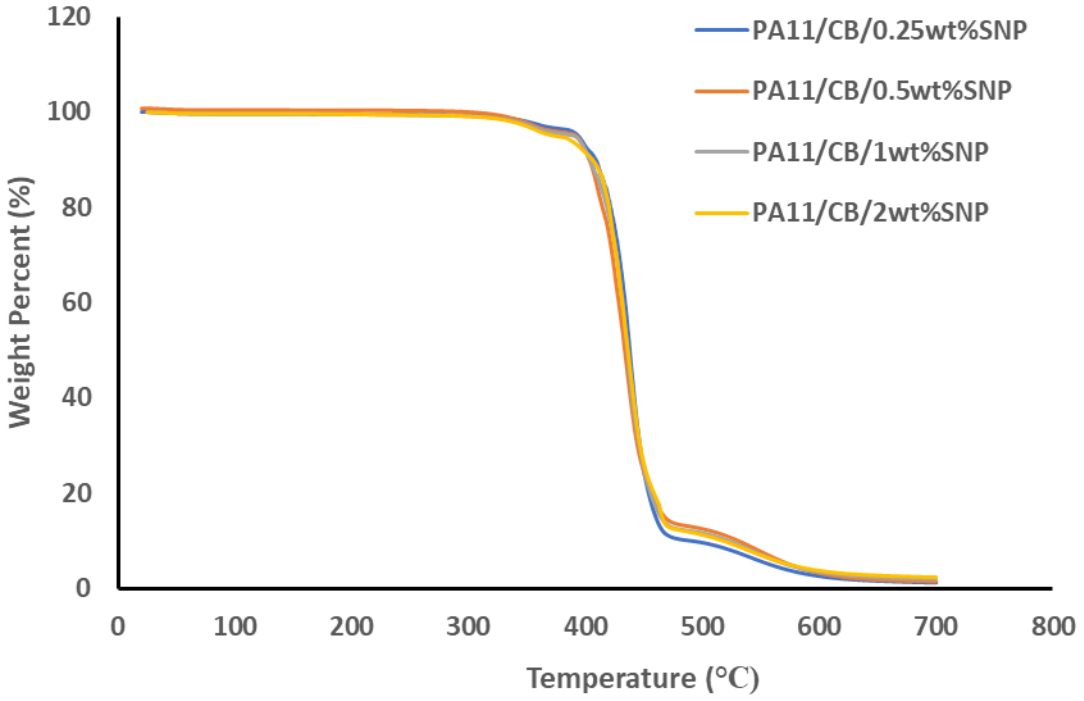

Figure 3-31: Degradation of printed PA11/CB/25nmSNP samples.

Table 3-10: Summary of calculated SNP and CB content for printed PA11/CB/25nmSNP samples.

PA11/CB Sample	**Weight % 1**		**Weight % 2**		**Average Weight %**	
	CB (%)	SNP (%)	CB (%)	SNP (%)	CB (%)	SNP (%)
PA11/CB/0.25wt%25nmSNP	0.95 %	0.31 %	0.95 %	0.19 %	0.95 %	0.25 %
PA11/CB/0.5wt%25nmSNP	0.95 %	0.48 %	0.95 %	0.55 %	0.95 %	0.53 %
PA11/CB/1wt%25nmSNP	0.95 %	0.97%	0.95 %	1.05 %	0.95 %	1.01 %
PA11/CB/2wt%25nmSNP	0.95 %	1.97 %	0.95 %	1.81 %	0.95 %	1.89 %

3.3.8 Powder Flow of PA11/CB/25nmSNP

Powder flow experiments were carried out on the PA11/CB/25nmSNP powder to measure the effectiveness of 25 nm SNP of increasing powder flow at increasing temperature, specifically temperatures close to SLS processing temperatures. The powder flow of PA11/CB/0.25wt%25nmSNP initially mirrored that to the PA11/CB standard, albeit with slightly elevated confined and unconfined E_{Flow}, calculated at 0.852 mJ and 0.083 mJ respectively. Despite slightly higher base E_{Flow} values, the PA11/CB/0.25wt%50nmSNP powder proved much more stable, with increases to the confined flow not occurring until 130°C. Past 130°C, the confined flow increased gradually until the transition of 170°C to 180°C, at which point the E_{Flow} increased from 19.690 mJ to 45.721 mJ. Despite such a high E_{Flow} value at 180°C, the confined powder was still able to flow for the entire test and did not exceed the axial force limit as the PA11/CB powder sample did when tested at the same temperature. The unconfined E_{Flow} of PA11/CB/0.25wt%25nmSNP demonstrated no significant changes with increasing temperatures until 180°C, increasing to 0.487 mJ. As the test could not be completed at 180°C for the PA11/CB powder, it is difficult to compare the PA11/CB/0.25wt%25nmSNP unconfined flow directly, but it is likely that the PA11/CB/0.25wt%25nmSNP powder would have issues with powder fluidization and spreading with such a relatively high unconfined E_{Flow} value. The change in torque with penetration depth for both confined and unconfined flow of PA11/CB/0.25wt%25nmSNP with increasing temperature are shown below in Figures 3-32 to 3-33 and summarized in Table 3-11.

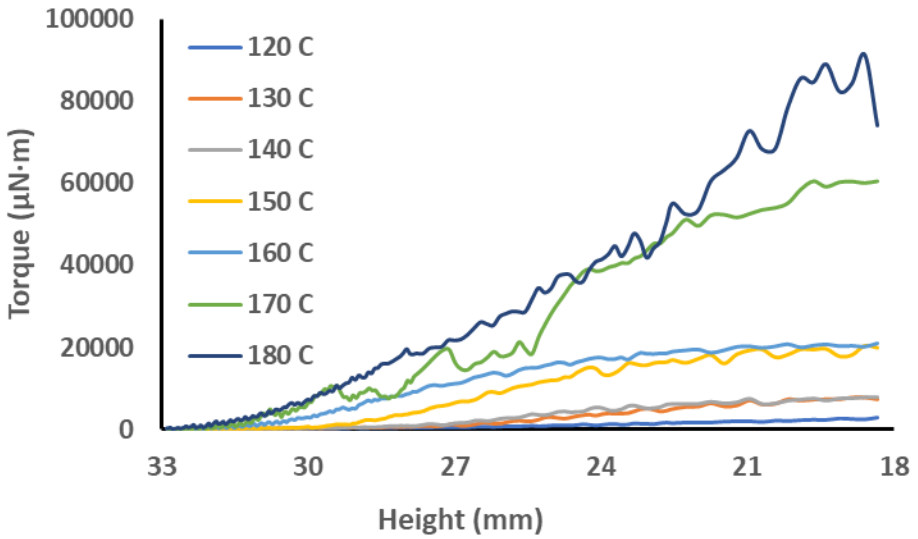

Figure 3-32: Torque signals for PA11/CB/0.25wt%25nmSNP confined powder flow at increasing temperature.

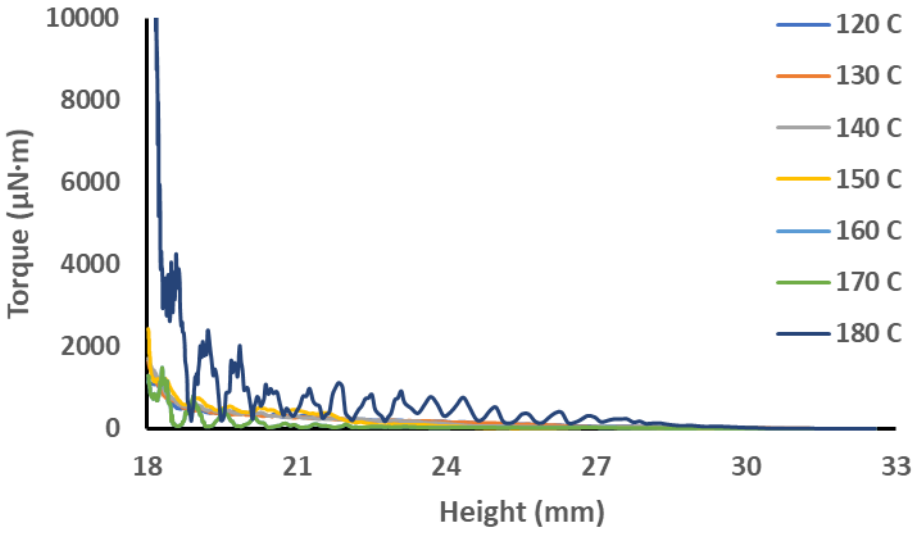

Figure 3-33: Torque signals for PA11/CB/0.25wt%25nmSNP unconfined powder flow at increasing temperature.

Table 3-11: Calculated confined and unconfined E_{flow} at increasing temperatures for PA11/CB/0.25wt%25nmSNP powder

Testing Temperature (°C)	Confined E_{Flow} (mJ)	Unconfined E_{Flow} (mJ)
25°C	0.852 mJ	0.083 mJ
40°C	0.871 mJ	0.084 mJ
60°C	0.853 mJ	0.077mJ
80°C	0.862 mJ	0.078 mJ
100°C	1.104 mJ	.088 mJ
120°C	1.591 mJ	0.081 mJ
130°C	4.951 mJ	0.087 mJ
140°C	4.972 mJ	0.081 mJ
150°C	13.961 mJ	0.097 mJ
160°C	16.153 mJ	0.121 mJ
170°C	19.690 mJ	0.121 mJ
180°C	45.721 mJ	0.487 mJ

The powder flow of PA11/CB/0.5wt%25nmSNP demonstrated similar trends in confined and unconfined powder flow for the tested temperature range as the PA11/CB/0.25wt%25nmSNP powder sample. The base E_{Flow} values for the confined flow were slightly elevated as compared to the PA11/CB values, however the E_{Flow} for the unconfined powder flow was quire comparable. The room temperature PA11/CB/0.5wt%25nmSNP E_{Flow} for confined and unconfined flow were 0.901 mJ and 0.051 mJ respectively. Similar to the PA11/CB/0.25wt%25nmSNP samples, the confined E_{Flow} did not start to significantly increase until 130°C, afterwards gradually increasing to 33.699 mJ at 180°C. The unconfined flow did not discernibly change until 180°, with E_{Flow} of 0.311 mJ. With a lower unconfined E_{Flow}, the PA11/CB/0.5wt%25nmSNP powder likely has improved dynamic flow of the powder during the powder layer transfer when compared to the PA11/CB/0.25wt%25nmSNP powder. Powder flow was also readily measured at 180°C, showing enhanced confined powder flow when compared to the PA11/CB powder. The change in torque

with penetration depth for both confined and unconfined flow of PA11/CB/0.5wt%25nmSNP with increasing temperature are shown below in Figures 3-34 to 3-35 and summarized in Table 3-12.

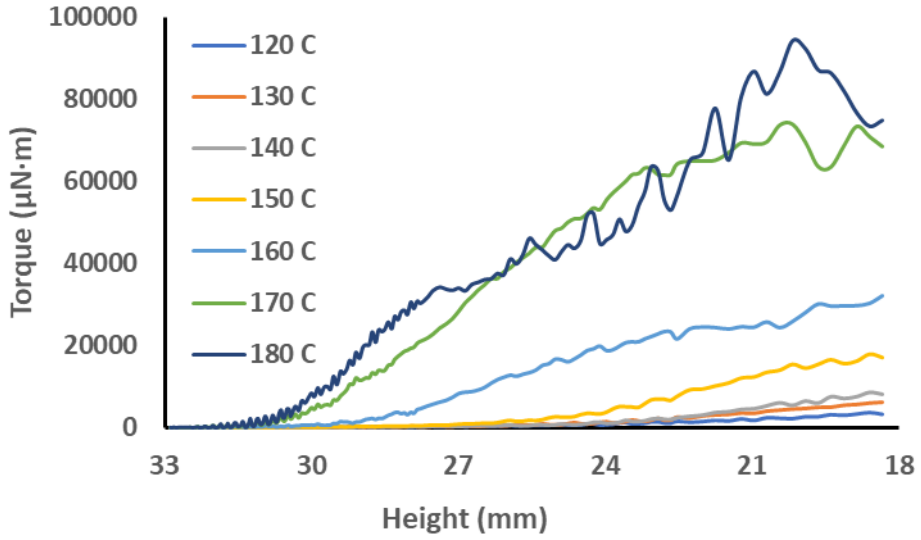

Figure 3-34: Torque signals for PA11/CB/0.5wt%25nmSNP confined powder flow at increasing temperature

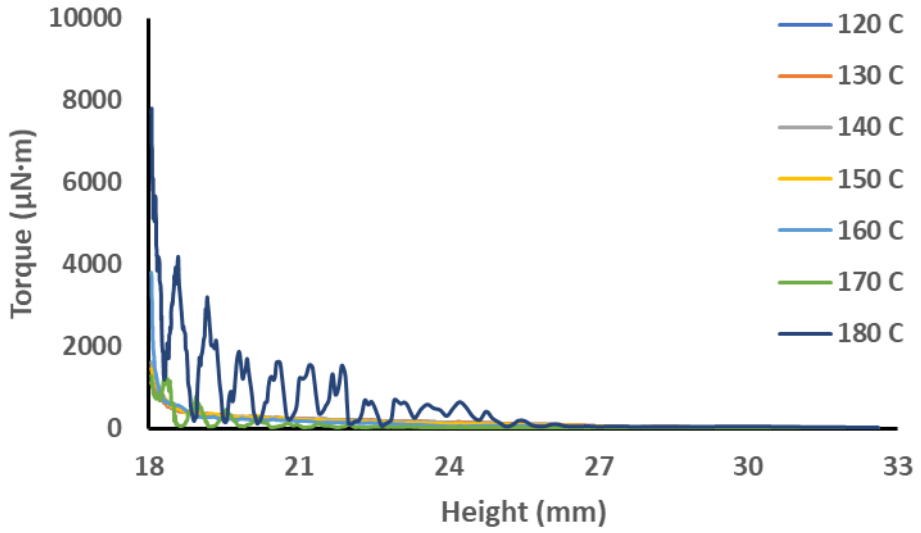

Figure 3-35: Torque signals for PA11/CB/0.5wt%25nmSNP unconfined powder flow at increasing temperature

Table 3-12: Calculated confined and unconfined E_{flow} at increasing temperatures for PA11/CB/0.5wt%25nmSNP powder

Testing Temperature (°C)	**Confined E_{Flow} (mJ)**	**Unconfined E_{Flow} (mJ)**
25°C	0.901 mJ	0.051 mJ
40°C	0.893 mJ	0.089 mJ
60°C	0.939 mJ	0.093 mJ
80°C	0.931 mJ	0.097 mJ
100°C	1.095 mJ	0.089 mJ
120°C	1.681 mJ	0.071 mJ
130°C	3.154 mJ	0.070 mJ
140°C	4.066 mJ	0.074 mJ
150°C	9.068 mJ	0.073 mJ
160°C	19.674 mJ	0.086 mJ
170°C	23.212 mJ	0.081 mJ
180°C	33.699 mJ	0.311 mJ

The powder flow of PA11/CB/1wt%25nmSNP demonstrated superior and more stable powder flow for the tested temperature range as compared to the PA11/CB/0.25wt%25nmSNP and PA11/CB/0.5wt%25nmSNP powders. Similar to the aforementioned 25 nm SNP loaded powders, the PA11/CB/1wt%25nmSNP powder began to show increasing confined E_{Flow} values at 130°C. The increase of E_{Flow} after this temperature was at a markedly lower rate, reaching a maximum value of 20.880 mJ at 180°C. The torque behavior was also noticeably different, with rapid increases in torque not occurring until larger depths of the powder. This suggests lower cohesion of the PA11/CB/1wt%25nmSNP powder at higher temperatures, increasing the confined powder flow. The unconfined powder flow did not discernibly change with increase in temperature, reaching a maximum E_{Flow} of 0.155 mJ at 180°C. This again suggests improved dynamic flow of

the powder during the transfer of an additional powder layer in the SLS printing process. The change in torque with penetration depth for both confined and unconfined flow of PA11/CB/1wt%25nmSNP with increasing temperature are shown below in Figures 3-36 to 3-37 and summarized in Table 3-13.

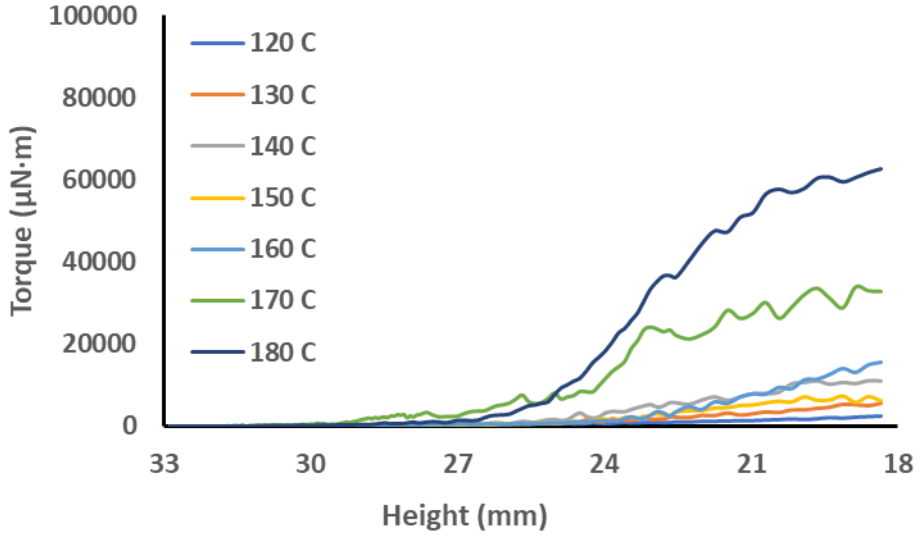

Figure 3-36: Torque signals for PA11/CB/1wt%25nmSNP confined powder flow at increasing temperature

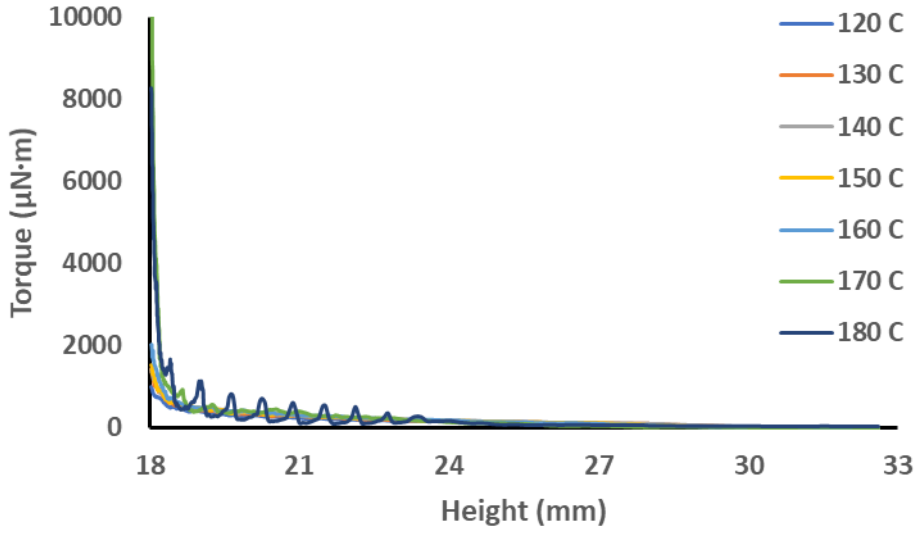

Figure 3-37: Torque signals for PA11/CB/1wt%25nmSNP unconfined powder flow at increasing temperature

Table 3-13: Calculated confined and unconfined E_{flow} at increasing temperatures for PA11/CB/1wt%25nmSNP powder

Testing Temperature (°C)	**Confined E_{Flow} (mJ)**	**Unconfined E_{Flow} (mJ)**
25°C	0.465 mJ	0.069 mJ
40°C	0.769 mJ	0.070 mJ
60°C	0.745 mJ	0.062 mJ
80°C	0.804 mJ	0.062 mJ
100°C	0.849 mJ	0.068 mJ
120°C	1.175 mJ	0.078 mJ
130°C	3.286 mJ	0.090 mJ
140°C	6.364 mJ	0.095 mJ
150°C	3.509 mJ	0.090 mJ
160°C	7.647 mJ	0.096 mJ
170°C	13.153 mJ	0.139 mJ
180°C	20.880 mJ	0.155 mJ

Lastly, the powder flow of PA11/CB/2wt%25nmSNP demonstrated a similarly highly stable powder flow for the tested temperature range as the PA11/CB/1wt%25nmSNP powder. The confined E_{Flow} did not significantly increase until 170°C, increasing from 2.602 mJ to 10.401 mJ. Additionally, powder flow at 180°C was readily measured, with a confined E_{Flow} of 21.190 mJ. The torque did not significantly increase until the rotor reached 7 mm of powder depth, similar to the PA11/CB/1wt%25nmSNP samples. The torque behavior with increasing powder depth continued to show yielding, suggesting while the E_{Flow} is much lower than the PA11/CB/25nmSNP powders with 0.25 wt. % and 0.5 wt. % SNP, there are still signs of polymer particle cohesion at SLS processing temperatures. The unconfined powder flow did not discernibly change with increase in temperature, reaching a maximum E_{Flow} of 0.158 mJ at 180°C. This again suggests improved dynamic flow of the powder during the transfer of an additional powder layer in the SLS printing

process. The change in torque with penetration depth for both confined and unconfined flow of PA11/CB/2wt%25nmSNP with increasing temperature are shown below in Figures 3-38 to 3-39 and summarized in Table 3-14.

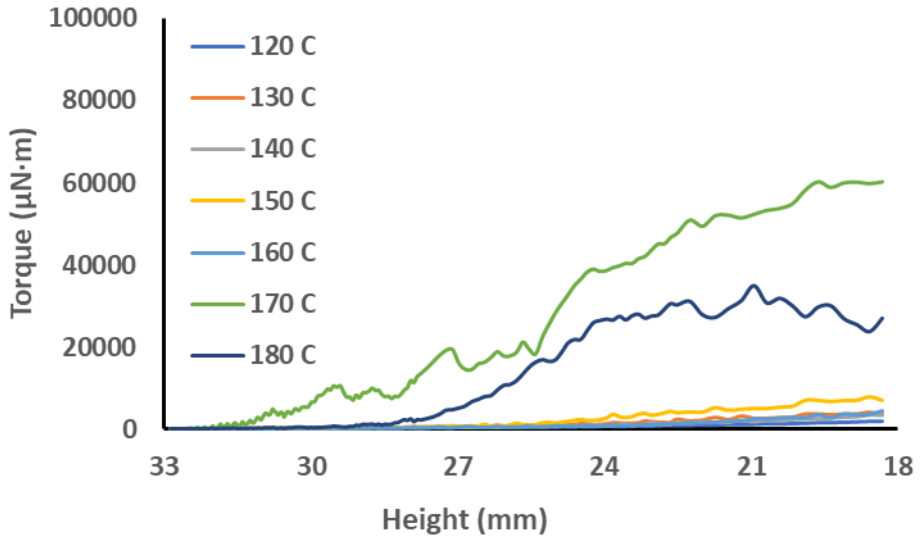

Figure 3-38: Torque signals for PA11/CB/2wt%25nmSNP confined powder flow at increasing temperature

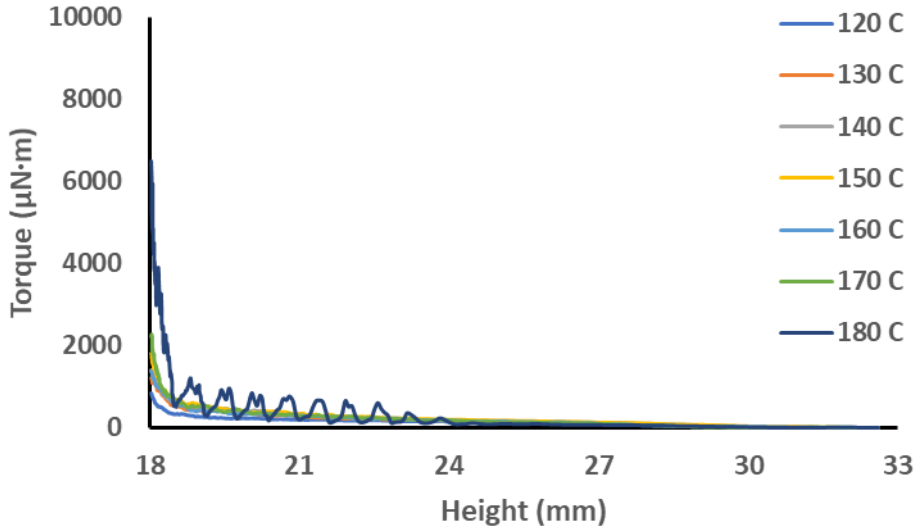

Figure 3-39: Torque signals for PA11/CB/2wt%25nmSNP unconfined powder flow at increasing temperature

Table 3-14: Calculated confined and unconfined E_{flow} at increasing temperatures for PA11/CB/2wt%25nmSNP powder

Testing Temperature (ºC)	**Confined E_{Flow} (mJ)**	**Unconfined E_{Flow} (mJ)**
25ºC	0.908 mJ	0.072 mJ
40ºC	0.889 mJ	0.078 mJ
60ºC	0.857 mJ	0.077 mJ
80ºC	0.907 mJ	0.077 mJ
100ºC	0.957 mJ	0.077 mJ
120ºC	1.014 mJ	0.069 mJ
130ºC	1.619 mJ	0.088 mJ
140ºC	1.827 mJ	0.103 mJ
150ºC	4.350 mJ	0.110 mJ
160ºC	2.606 mJ	0.089 mJ
170ºC	10.401 mJ	0.106 mJ
180ºC	21.190 mJ	0.158 mJ

3.3.9 Mechanical Behavior of PA11/CB/25nmSNP

Both tensile testing (ASTM D638-14) and dynamic mechanical analysis (DMA) were employed to gauge the effect of increasing SNP on the printed PA11/CB mechanical behavior. In general, all PA11/CB/25nmSNP samples demonstrated a modest increase in ultimate tensile strength and tensile modulus, with the PA11/CB/0.5wt%25nmSNP and PA11/CB/1wt%25nmSNP samples having the highest average strengths at 58.3 MPa. The PA11/CB/0.25wt%25nmSNP and PA11/CB/2wt%25nmSNP samples had slightly lower but similar values of 55.5 MPa and 55.3 MPa respectively. Tensile modulus values ranged from 1.9 GPa to 2.1 GPa, with the highest average modulus found in the PA11/CB/1wt%25nmSNP samples. When compared to the PA11/CB printed at the same printing parameters (A_{N9}), the addition of 25nm SNP led to increases in ultimate tensile strength of 5.1% to 10.8%, and increases in modulus from 5.6% to 10.5%. Elongation at break was

not as comparable to the PA11/CB A_{N9} samples. The PA11/CB/0.25wt%25nmSNP samples had an average elongation at break of 80.0%, a 26.8% increase of the elongation at break for the PA11/CB sample. The remaining PA11/CB/25nmSNP samples had much lower elongation at break, decreasing with increasing SNP content. With 0.5 wt. %, 1 wt. % and 2 wt. % SNP loadings, the average elongations to break fell to 45.2%, 21.6% and 14.6% respectively, upwards of 76.8% reduction as compared to the PA11/CB A_{N9}. It is likely again that poor polymer diffusion across the SNP boundary has led to diminished elongation at break, however previous results of rigid particle reinforced Nylons have shown a similar decreases in strain with particle loading [15]. The tensile behavior of the PA11/CB/50nmSNP composites is illustrated below in Figure 3-40, with the results summarized in Table 3-15.

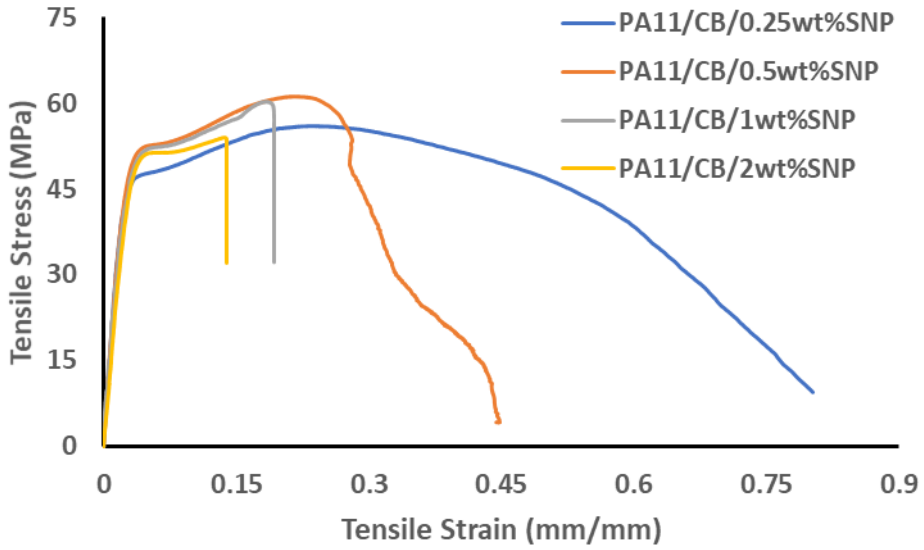

Figure 3-40: Tensile behavior of PA11/CB and PA11/CB/25nmSNP samples.

Table 3-15: Tensile behavior summary of PA11/CB and PA11/CB/25nmSNP samples.

PA11/CB Sample	Ultimate Tensile Strength (MPa)	Elongation to Break (%)	Tensile Modulus (GPa)
PA11/CB/0.25wt%25nmSNP	55.5 ± 1.5 MPa	80.0 ± 2.4%	1.9 ± 0.2 GPa
PA11/CB/0.5wt%25nmSNP	58.3 ± 1.0 MPa	45.2 ± 12.3%	2.0 ± 0.1 GPa
PA11/CB/1wt%25nmSNP	58.3 ± 1.3 MPa	21.6 ± 5.8%	2.1 ± 0.1 GPa
PA11/CB/2wt%25nmSNP	55.3 ± 1.2 MPa	14.6 ± 1.6%	2.0 ± 0.3 GPa

In addition to tensile testing, DMA was additionally performed on the composite materials, with samples generally showing increasing G′ with increasing SNP. Room temperature shear modulus values for the PA11/CB/25nmSNP samples with 0.25 wt. %, 0.5 wt. %, 1 wt. % and 2 wt. % SNP were measured to be 0.75 GPa, 0.86 GPa, 0.89 GPa and 0.99 GPa, respectively. There were no discernable changes in shear modulus relaxation with increasing SNP, with near identical differences in G′ at room temperature and the rubbery plateau. The G′ and loss modulus (G″) for each tested sample are shown below in Figure 3-41. The glass transition temperature (T_g) was additionally evaluated using the maximum of the tan(δ) peak, shown in Figure 3-42. The largest change in T_g came between the PA11/CB/0.25wt%25nmSNP and PA11/CB/0.5wt%25nmSNP samples, increasing from 55.7°C to 58.3°C. The T_g for the PA11/CB/1wt%25nmSNP and the PA11/CB/2wt%25nmSNP more modestly increased to 59.1°C and 60.3°C respectively.

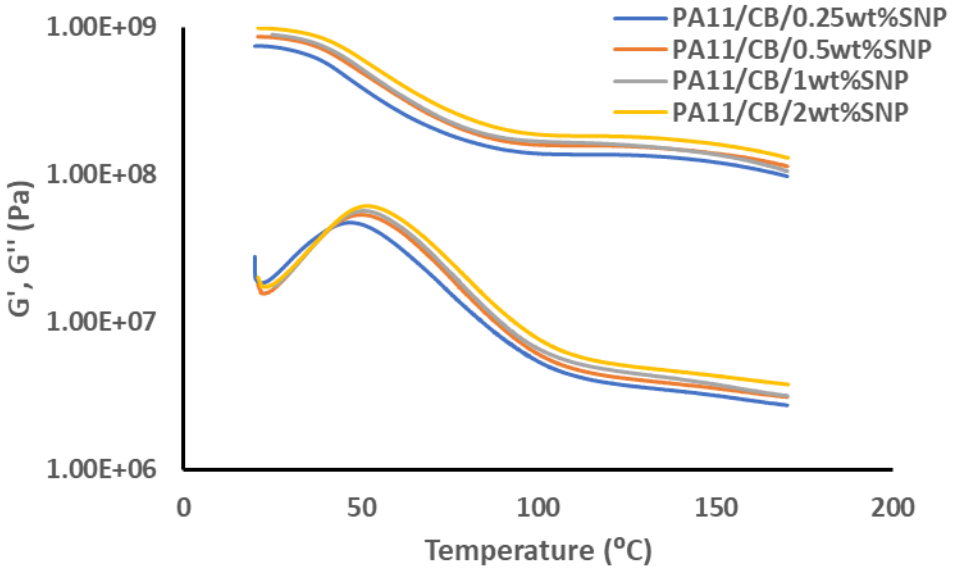

Figure 3-41: Storage and loss modulus of PA11/CB/25nmSNP samples with increasing temperature

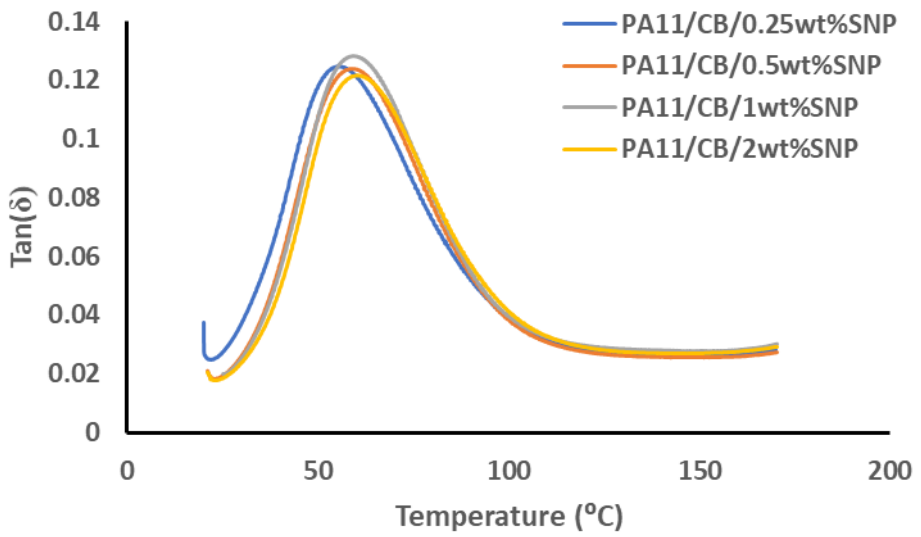

Figure 3-42: Tan(δ) of PA11/CB/25nmSNP samples with increasing temperature

The PA11/CB/25nmSNP tensile (E′) and shear (G′) modulus values were compared to those as expected by the Halpin-Tsai model, and the comparison is illustrated below in Figure 3-43. Within standard error, the PA11/CB/0.25wt%25nmSNP fall into the predicted values well. The remaining PA11/CB/25nmSNP moduli alternatively measure higher than those predicted by the Halpin-Tsai model. While the model assumes good dispersion of the rigid filler into a polymer matrix, the SNP in the SLS printed polymer composite primarily stays at the particle and layer boundaries, as identified in Section 3.3.10. This could possibly result in a skeletal-like SNP framework throughout the printed material, adding a rigid reinforcing framework that may artificially increase the stiffness in the higher loaded PA11/CB/25nmSNP samples. Had the SNP been fully dispersed throughout the PA11/CB, it is likely that the both experimental moduli would be in better agreement with the Halpin-Tsai model. Past studies on predicting mechanical performance in polyamide nanocomposites have found success using modified Halpin-Tsai equations, accounting for both fully separated/exfoliated particles as well as aggregated structures [20]. This may be a more appropriate model for future studies using SLS printing to process polymer nanocomposites.

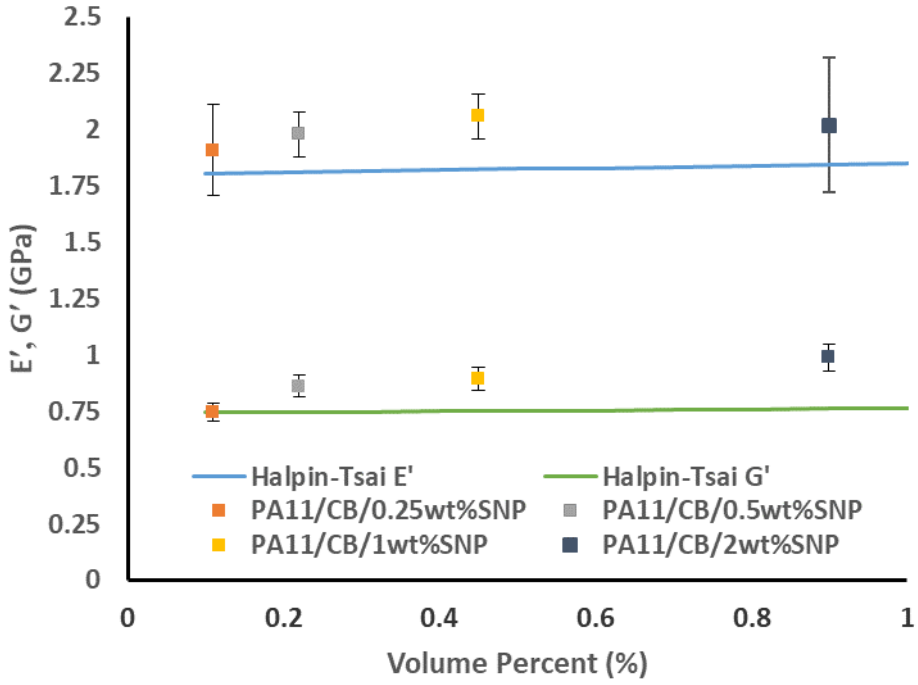

Figure 3-43: Comparison of experimental and Halpin-Tsai predicted modulus of PA11/CB/25nmSNP samples.

While essential work of fracture (EWF) was unable to be completed on the PA11/CB/50nmSNP samples, two of the PA11/CB/25nmSNP composites demonstrated yield prior to stable crack propagation, resulting in valid tests. The PA11/CB/0.25wt%25nmSNP and PA11/CB/0.5wt%25nmSNP EWF results are shown below in Figures 3-44 and 3-45, respectively. Both demonstrated similar essential work (w_e) values when compared to the PA11/CB materials in Section 2.3.5, with the PA11/CB/0.25wt%25nmSNP and PA11/CB/0.5wt%25nmSNP samples demonstrating w_e of 28.4 kJ/m^2 and 22.4 kJ/m^2 respectively. When compared to the PA11/CB A_{N9} sample w_e, the PA11/CB/0.25wt%25nmSNP showed a modest 4.4% increase, while the PA11/CB/0.5wt%25nmSNP showed a 17.6% decrease in value. In addition to the w_e values, the slope of the work of fracture line (βw_p) also varied between samples, indicative of the plastic zone size. The PA11/CB/0.25wt%25nmSNP slope was about three times larger than the w_e slope for the PA11/CB/0.5wt%25nmSNP samples, suggesting a much larger plastic zone geometry in the

PA11/CB/0.25wt%25nmSNP fracture zone. These w_e values still compare quite favorably to other toughened polyamides [21, 22], however the results highlight a sensitive optimization of SNP loading that can toughen the PA11/CB matrix without reducing the necessary ductility required to carry out the EWF test. Upwards of 1 wt. % SNP loading in the PA11/CB SLS powder seems to reduce the printed composite ductility to the point where the samples cannot be characterized by the EWF test.

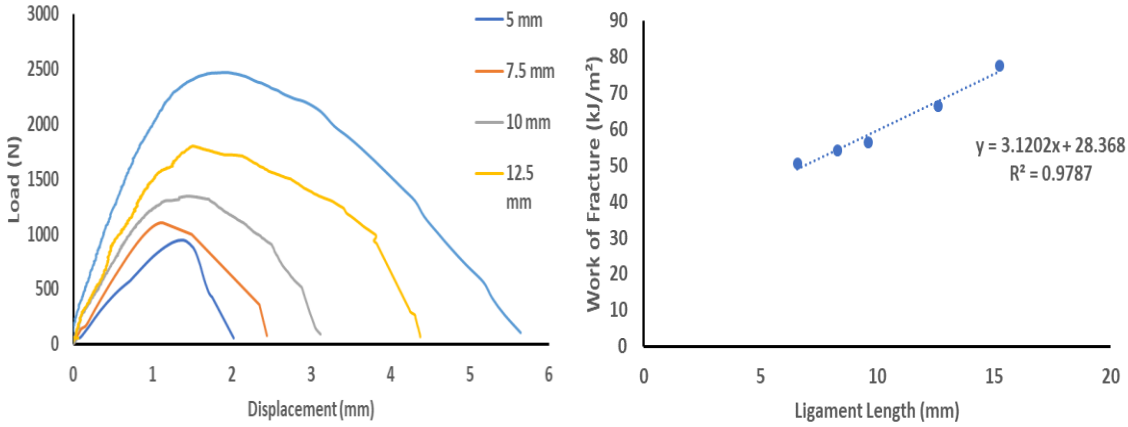

Figure 3-44: Essential work of fracture results for the printed PA11/CB/0.25wt%25nmSNP

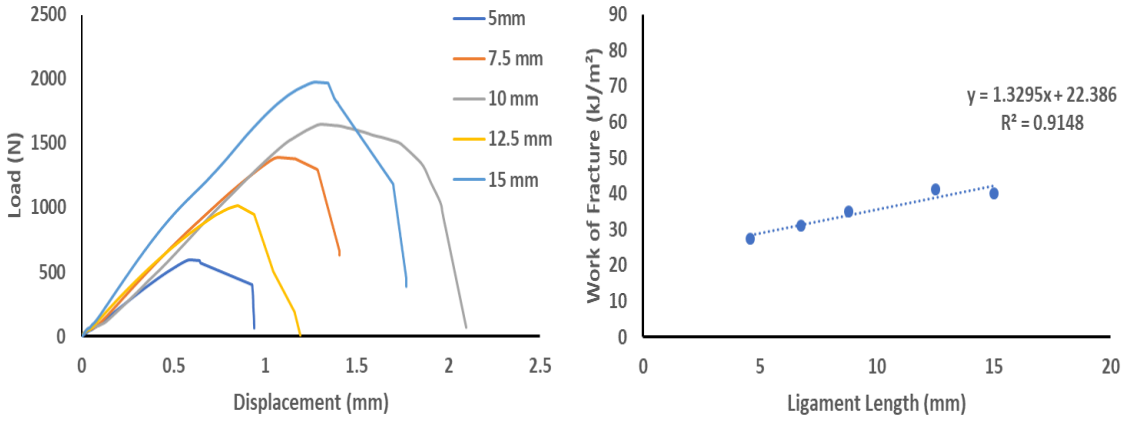

Figure 3-45: Essential work of fracture results for the printed PA11/CB/0.5wt%25nmSNP

A primary goal in reinforcing the PA11/CB powder with SNP was evaluating the effectiveness of strengthening the printed material in the build or z direction. Both compression testing and linear reciprocating wear were utilized to determine changes in mechanical behavior with printing direction and increasing SNP. As shown in Figure 3-46, the PA11/CB A_{N9} and PA11/CB/0.25wt%25nmSNP samples did not show any discernible change in compressive strength, modulus or strain behavior between the x and z direction. The PA11/CB/0.25wt%25nmSNP additionally showed a slight increase in compressive strength in both printing directions when compared to the PA11/CB A_{N9}, particularly in the z direction which saw a 10.8% increase in strength with the addition of 0.25 wt. % SNP. The remaining PA11/CB/25nmSNP samples similarly did not demonstrate a discernible change in compressive yield strength between the x and z printing directions, however the strain behavior was quite different. The PA11/CB/25nmSNP samples with 0.5 wt. %, 1 wt. % and 2 wt. % SNP experienced shear failure in the z direction, whereas the samples print in the x direction did not fail for the duration of the test. Interestingly, the samples printed in the x direction were compressed perpendicular to the printing layers, suggesting the layer adhesion and strength was actually adequate in this printing direction with increasing SNP. Because the samples in the z direction have twice the amount of layers, the likelihood of an SNP agglomerate based printing bed error is statistically more probable, possibly leading to early failure.

Another interesting trend in the PA11/CB/25nmSNP compression samples was a steady disappearance of a yield point/more rapid strain hardening with increasing SNP. The PA11/CB A_{N9} does not feature any strain softening, similar to other compression studies on PA6 and PA66 [23]. The change in yield duration is more unusual, but has been noted in PA6,6 composites due to premature debonding of particles from the polymer matrix [18]. Overall, 0.25 wt% 25nm SNP was shown to best strengthen PA11/CB in the z printing direction. Compression testing results in both the x and z directions can be summarized in Table 3-16.

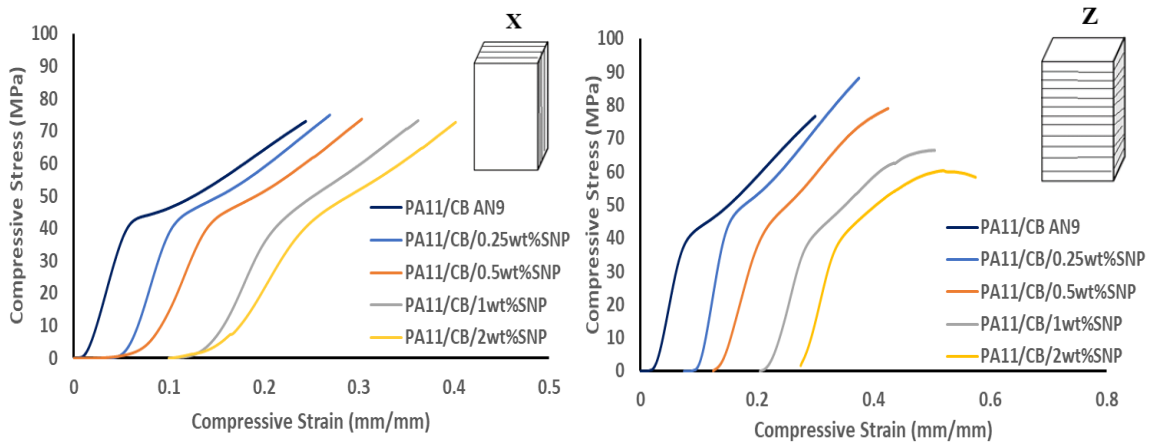

Figure 3-46: Compression testing of printed PA11/CB and PA11/CB/25nmSNP samples in the x (left) and z (right) printing directions.

Table 3-16: Summary of compression testing results of printed PA11/CB and PA11/CB/25nmSNP

PA11/CB Sample	**Compressive Yield Strength X (MPa)**	**Compressive Yield Strength Z (MPa)**
PA11/CB A_{N9}	42.9 ± 1.1 MPa	41.7 ± 1.2 MPa
PA11/CB/0.25wt%25nmSNP	45.0 ± 1.2 MPa	46.2 ± 0.9 MPa
PA11/CB/0.5wt%25nmSNP	42.6 ± 1.0 MPa	43.1 ± 1.3 MPa
PA11/CB/1wt%25nmSNP	41.6 ± 1.2 MPa	40.2± 1.1 MPa
PA11/CB/2wt%25nmSNP	41.1 ± 1.1 MPa	40.0 ± 1.2 MPa

In addition to compression testing, linear reciprocating wear was utilized to examine the ability of the 25 nm SNP to reinforce the PA11/CB particle and polymer layer boundaries. The study initially began by comparing the wear rates of PA11/CB A_{N9} in the x, y and z print orientations. Surprisingly, there were no discernible changes in wear among the three printing directions, suggesting good adhesion and strength in the z printing direction when PA11/CB is print at A_{N9}. The order of magnitude of wear is 1 x 10^{-5} mm^3/Nm, consistent with other polyamides [24], as well as other PA11 samples [25,26]. The wear rates are summarized below, in Table 17.

Table 17: Comparison of wear rates of PA11/CB A_{N9} in different printing directions.

PA11/CB Sample	**Wear Rate (mm^3/Nm)**
PA11/CB A_{N9} X	1.14 x 10^{-5} mm^3/Nm
PA11/CB A_{N9} Y	1.08 x 10^{-5} mm^3/Nm
PA11/CB A_{N9} Z	1.34 x 10^{-5} mm^3/Nm

The second iteration of wear testing focused on just the z direction wear to more directly study the effect of SNP reinforcement in the z direction. Another PA11/CB A_{N9} sample was tested and compared to that of PA11/CB/25nmSNP z direction printed specimens with increasing SNP. The PA11/CB $A_{n(}$ and PA11/CB/0.25wt%25nmSNP had similar wear magnitudes on the order of 1 x 10^{-5} mm^3/Nm, albeit at slightly elevated values as compared to the previous experiments with the PA11/CB material. This change in value could be based on slightly different humidity levels of the two testing environments, as well as using PA11/CB sourced from separate batches. The remaining PA11/CB/25nmSNP samples showed a discernible decrease in wear rate, on the 1 x 10^{-6} mm^3/Nm order of magnitude. The lowest wear was recorded for the PA11/CB/0.5wt%25nmSNP sample at 2.42 x 10^{-6} mm^3/Nm. This suggests that the SNP is actively participating in reinforcing the layer boundaries to reduce the wear of the PA11/CB. The results are in slight contrast with the compression testing results, which demonstrated shear failure of the higher SNP loaded samples with increasing strain. What has not been investigated in this study has been the role of surface defects in the SLS printed samples in prematurely failing the samples. It could be that the PA11/CB/SNP printed samples have increasing surface defects with increasing SNP, resulting in failure for surface sensitive tests like tensile testing, but not as much for wear studies. Regardless, the PA11/CB/25nmSNP z direction wear results are summarized below in Table 18.

Table 18: Comparison of wear rates of PA11/CB/25nmSNP in the z build direction.

PA11/CB Z Sample	**Wear Rate (mm^3/Nm)**
PA11/CB A_{N9}	7.49×10^{-5} mm^3/Nm
PA11/CB/0.25wt%25nmSNP	7.80×10^{-5} mm^3/Nm
PA11/CB/0.5wt%25nmSNP	2.42×10^{-6} mm^3/Nm
PA11/CB/1wt%25nmSNP	4.52×10^{-6} mm^3/Nm
PA11/CB/2wt%25nmSNP	5.41×10^{-6} mm^3/Nm

3.3.10 PA11/CB/25nmSNP Fractography

The fracture surfaces of the PA11/CB/25nmSNP DENT specimens were examined. The PA11/CN/0.25wt%25nmSNP samples demonstrated the same unique "dimpled" surface as demonstrated for the PA11/CB samples in Section 2.3.6. This suggests that crack propagation advanced primarily through microvoid coalescence, as was the case with the PA11/CB samples. The dimples generally were well oriented in the direction of crack propagation, suggesting few substantial defects acting as stress concentration sources such as poorly sintered bed layers or fully unsintered polymer particles. The average dimple size was very similar to that of the PA11/CB A_{N9} fracture surface, suggesting a similar incidence of inclusion sites or stress concentration sources between the two samples. The inclusion sources for dimple formation were also similar between the two samples, with poorly sintered particle cores and impinged spherulite nuclei as the two most prominently observed inclusions. A third inclusion source emerged in the PA11/CB/0.25wt%25nmSNP sample as a toughened particle boundary zone, as indicated by a linear and porous polymer mesh with visible SNP aggregates populating both the internal and surrounding areas of the porous zone. A collection of images showing the dimpled structure and inclusion diversity of the PA11/CB/0.25wt%25nmSNP fracture surface is shown below in Figure 3-47.

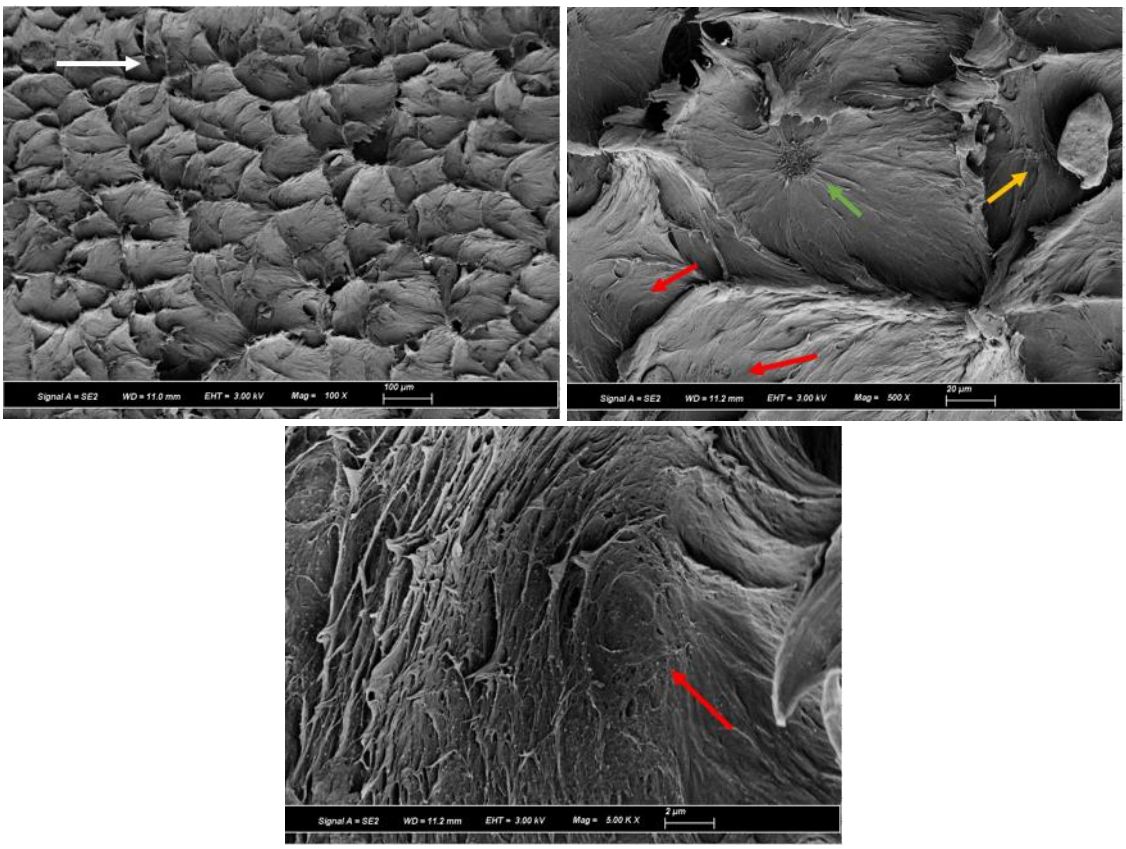

Figure 3-47: Dimple geometry and node diversity in the PA11/CB/0.25wt%25nmSNP fracture surface. The white arrows represent crack direction, the red arrows represent impinged spherulitic nodes, the green arrows represent the poorly sintered particle nodes, and the yellow arrows represent particle boundary zone nodes.

The inclusion sites in the PA11/CB/0.25wt%25nmSNP were examined further to elucidate the role of SNP in reducing crack propagation and toughening the PA11/CB polymer. SNP was found in each aforementioned inclusion site, predominantly on the edges of voids and the parabolic tears extending from the central dimple node. Due to the small size of the 25 nm SNP, it is difficult to determine any signs of particle debonding of the SNP directly seen in the PA11 matrix, however due to the high volume of SNP at the void boundaries it is likely the void growth is initiated through a debonding mechanism. This suggests the SNP may be initiating and propagating the microvoids and tears observable in the area, as concluded by previous studies on rigid particle reinforced polyamides [27]. The SNP also seems to be well separated, with only a few nano-scaled SNP aggregates observable in the parabolic tearing wake. The 25 nm SNP ultimately shows positive

signs of matrix toughening at a 0.25 wt. % SNP loading when adhered to the PA11/CB particle surface. Figure 3-48 shows a selection of observable SNP toughening in each specified inclusion site type.

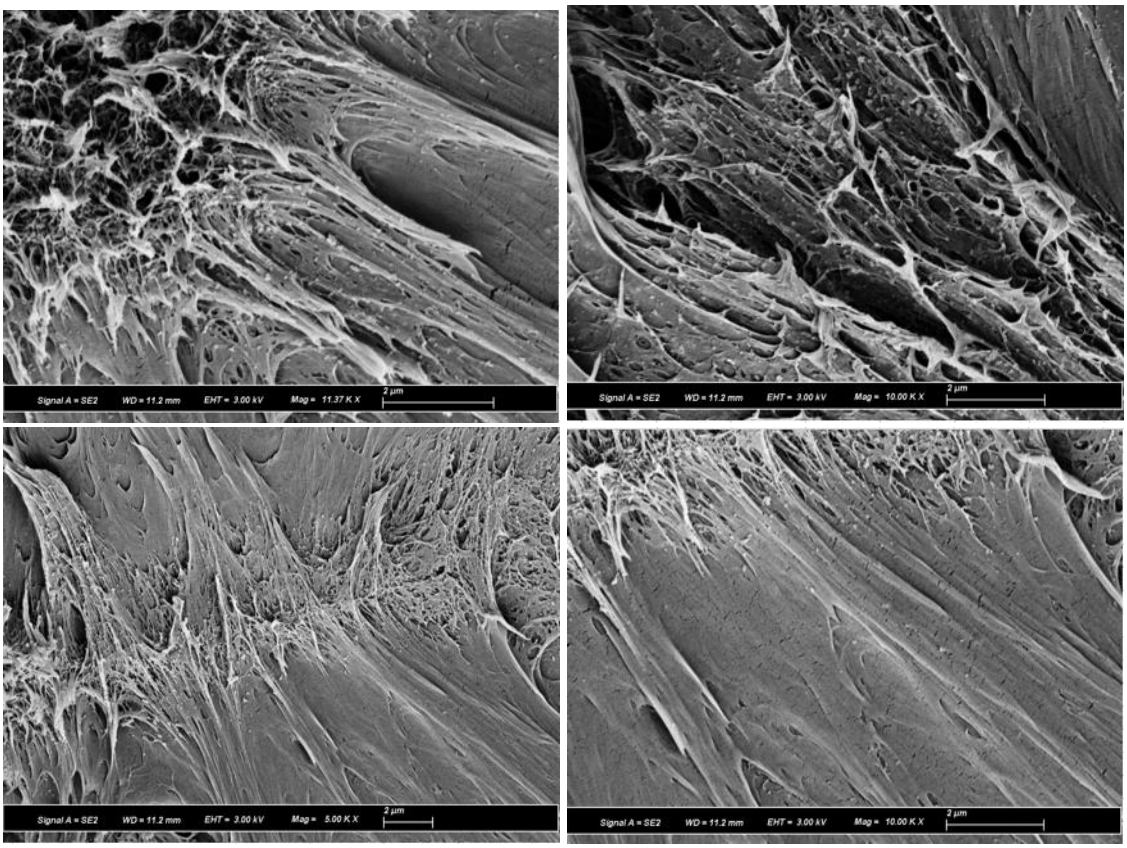

Figure 3-48: Evidence of SNP toughening and voiding on the PA11/CB/0.25wt%25nmSNP fracture surface.

The PA11/CB/0.5wt%25nmSNP fracture surface demonstrated the same dimpled surface as in the PA11/CB/0.25wt%25nmSNP samples, however with a much smaller average dimple size. There was also far less alignment of the dimples in the crack direction for the PA11/CB/0.5wt%25nmSNP sample. Both suggest a larger volume of stress concentration sources in the PA11/CB/0.5wt%25nmSNP sample as compared to the PA11/CB/0.25wt%25nmSNP fracture surface. The inclusion sources for dimple formation included the were also similar between the two samples, with poorly sintered particle cores, impinged spherulite nuclei and PA11/CB boundary

zones as the most prominently observed inclusions. The frequency of each inclusion type did seem to change in the PA11/CB/0.5wt%25nmSNP sample, as the poorly sintered particle cores and PA11/CB boundaries were much more prevalent in the fracture surface. Images showing the dimpled structure and inclusion diversity of the PA11/CB/0.5wt%25nmSNP fracture surface is shown below in Figure 3-49.

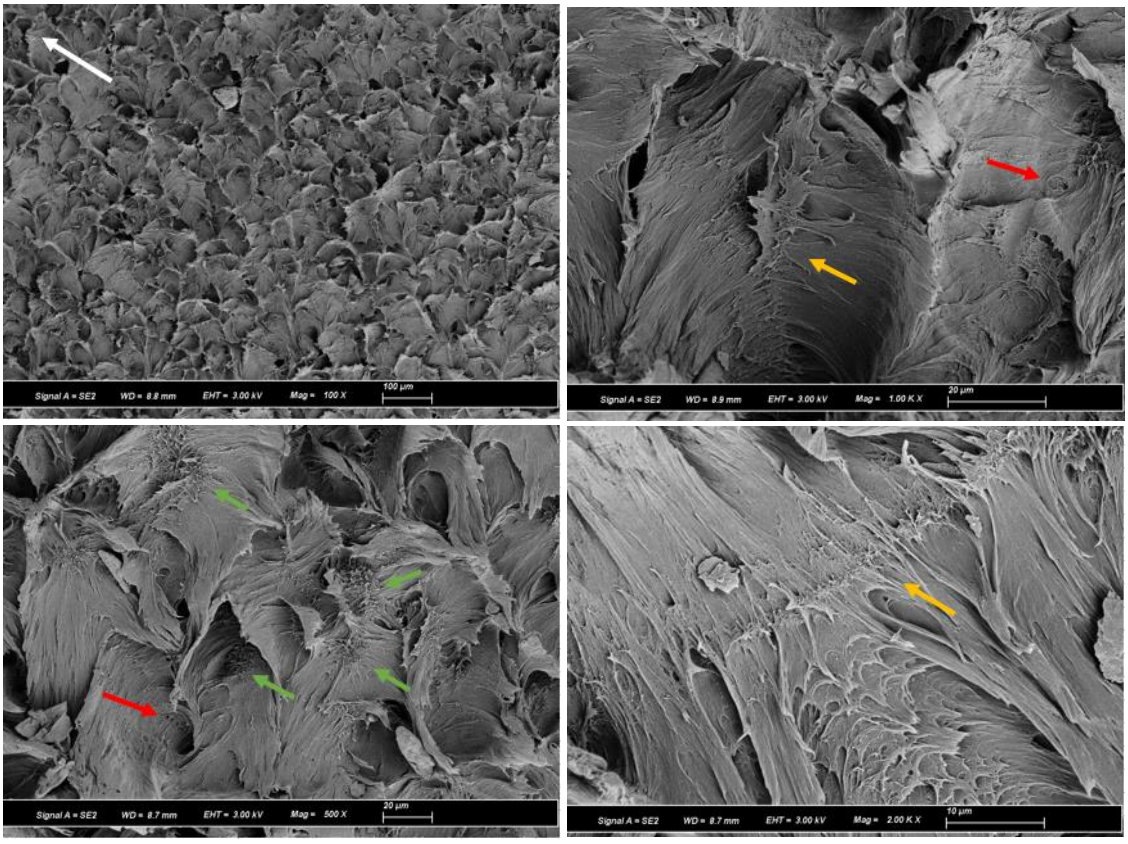

Figure 3-49: Dimple geometry and node diversity in the PA11/CB/0.5wt%25nmSNP fracture surface. The white arrows represent crack direction, the red arrows represent impinged spherulitic nodes, the green arrows represent the poorly sintered particle nodes, and the yellow arrows represent particle boundary zone nodes.

The inclusion sites in the PA11/CB/0.5wt%25nmSNP were examined further to examine the role of SNP in reducing crack propagation and toughening the PA11/CB polymer. Similar to the PA11/CB/0.25wt%25nmSNP sample, SNP was found predominantly on the edges of voids and the parabolic tears extending from a central dimple node. However, unlike the PA11/CB/0.25wt%25nmSNP sample, the SNP was primarily visible in plate-like aggregate

structures, with singular nanoparticles appearing with less frequency. Agglomeration of nanoparticles have been readily studied before, with higher occurrence with particles of smaller size [28]. This seems to differ slightly from the PA11/CB/50nmSNP samples, which did show some SNP agglomerates on the tensile fracture surface but good SNP dispersion directly in the polymer matrix. Due to the larger SNP aggregate size in the PA11/CB/0.5wt%25nmSNP sample, the voids and parabolic tears surrounding the SNP were noticeably larger than the ones observed in the PA11/CB/0.25wt%25nmSNP fracture surface. Although the PA11/CB/0.5wt%25nmSNP show increased SNP aggregation, the continued contribution of the SNP to microvoid formation at the 0.5 wt. % SNP loading shows good signs of PA11/CB matrix reinforcement. Figure 3-50 shows an area of observable SNP toughening at increasing magnification.

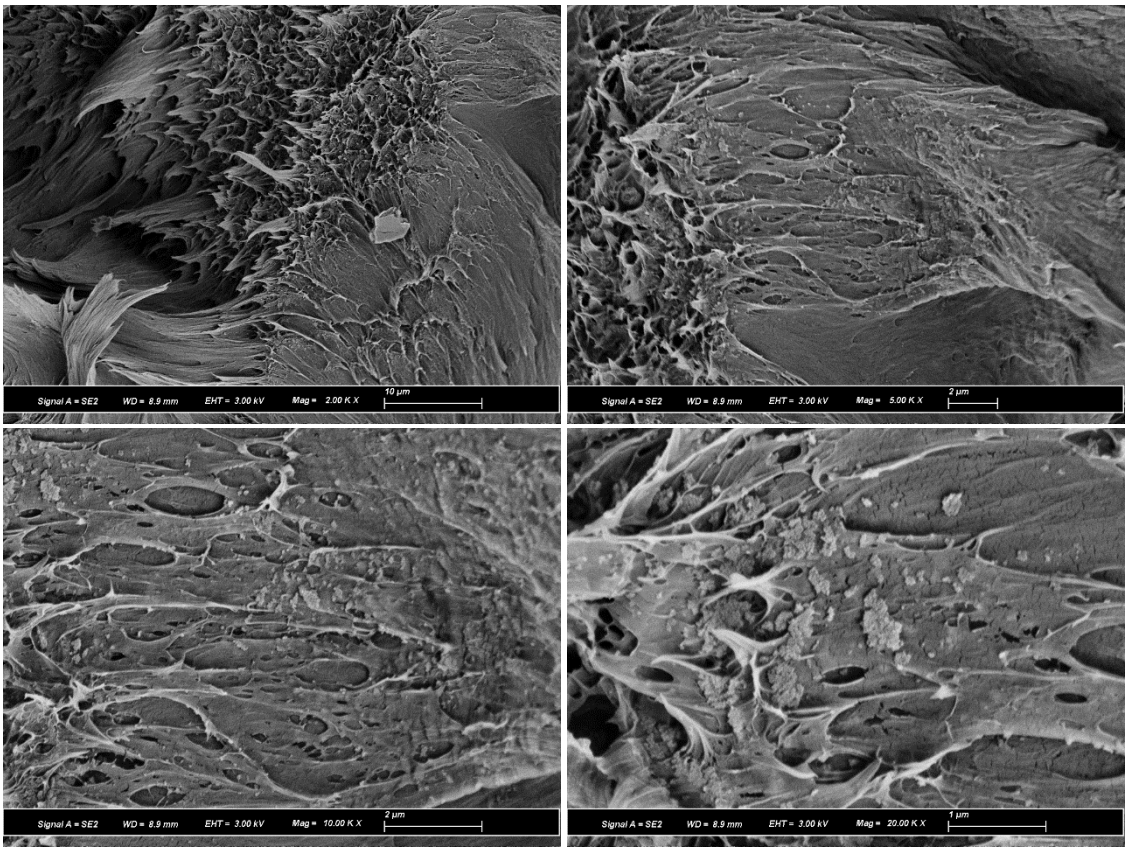

Figure 3-50: Evidence of SNP voiding and aggregation on the PA11/CB/0.5wt%25nmSNP fracture surface.

The PA11/CB/1wt%25nmSNP and PA11/CB/2wt%25nmSNP fracture surfaces were quite similar to each other, and contrasted greatly with the PA11/CB/25nmSNP sample fracture surfaces with 0.25 wt. % and 0.5 wt. % SNP loading. Initially, each sample showed ductile tearing of the PA11/CB following the notch, but soon transitioned to a ring of planar brittle fracture followed by rapid crack propagation. The crack propagation presented with three dimensional ridges organized radially, suggesting some minor ductility as opposed to a completely planar fracture surface. Similar ridged surfaces have been documented in polycarbonate EWF surfaces [29], as well as kaolin reinforced polypropylene EWF samples [30]. Some observable crazing occurs laterally across separate ridged structures, macroscopically observable by horizontal fissures perpendicular to the crack path. Upon higher magnification, oriented fibrils can be observed populating these horizontal cervices, suggesting a crazed region. Both the transitions from ductile tearing to brittle crack propagation, and the ridged brittle fracture surfaces of the PA11/CB/1wt%25nmSNP and PA11/CB/2wt%25nmSNP samples are shown in Figure 3-51.

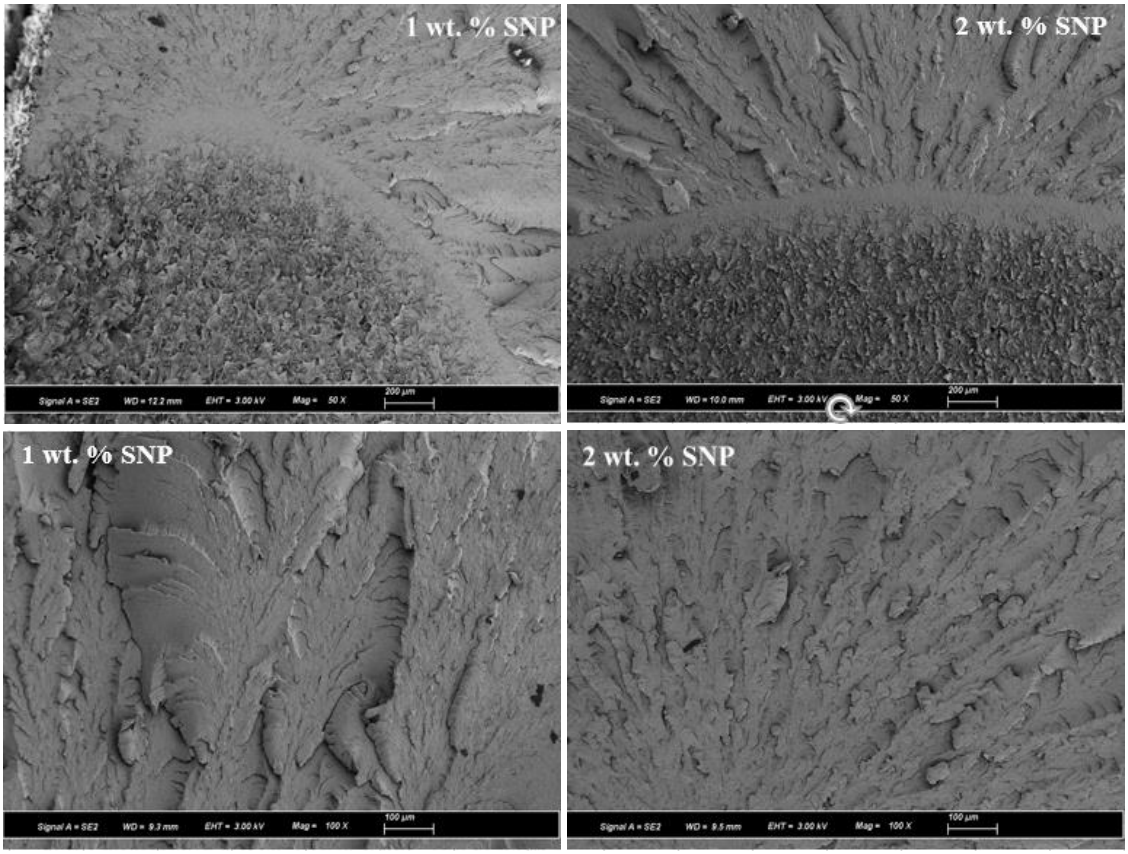

Figure 3-51: Ductile tearing and brittle crack propagation as observed in the PA11/CB/1wt%25nmSNP (left) and PA11/CB/2wt%25nmSNP (right) fracture surfaces.

The SNP was easily identified on the fracture surface for both the PA11/CB/1wt%25nmSNP and PA11/CB/2wt%25nmSNP samples in the form of large and planar SNP agglomerates. These agglomerates were found both between elongated fibril tears in the initial ductile region, and embedded into the matrix of the brittle fracture surface. The planar agglomerates were often on the micron scale, and could measure upwards of 4 μm to 5 μm in diameter. It is probable that crack propagation was accelerated through these planar SNP layers and the boundaries shared with the PA11/CB matrix. The 25 nm SNP size was specifically chosen to diffuse more easily into the PA11/CB/ matrix upon printing, as the PA11/CB50nmSNP samples showed large SNP boundaries between adjoining PA11/CB particles. While the 25 nm SNP coated the PA11/CB particles incredibly well, it has shown increased agglomeration at lower weight percent loadings into the PA11/CB matrix upon printing. There is likely an optimization of colloidal SNP size and surface

treatment that allows for easier diffusion into the PA11/CB matrix without excessive agglomeration during the printing process. Examples of SNP agglomeration in the PA11/CB/1wt%25nmSNP and PA11/CB/2wt%25nmSNP samples are shown below in Figure 3-52.

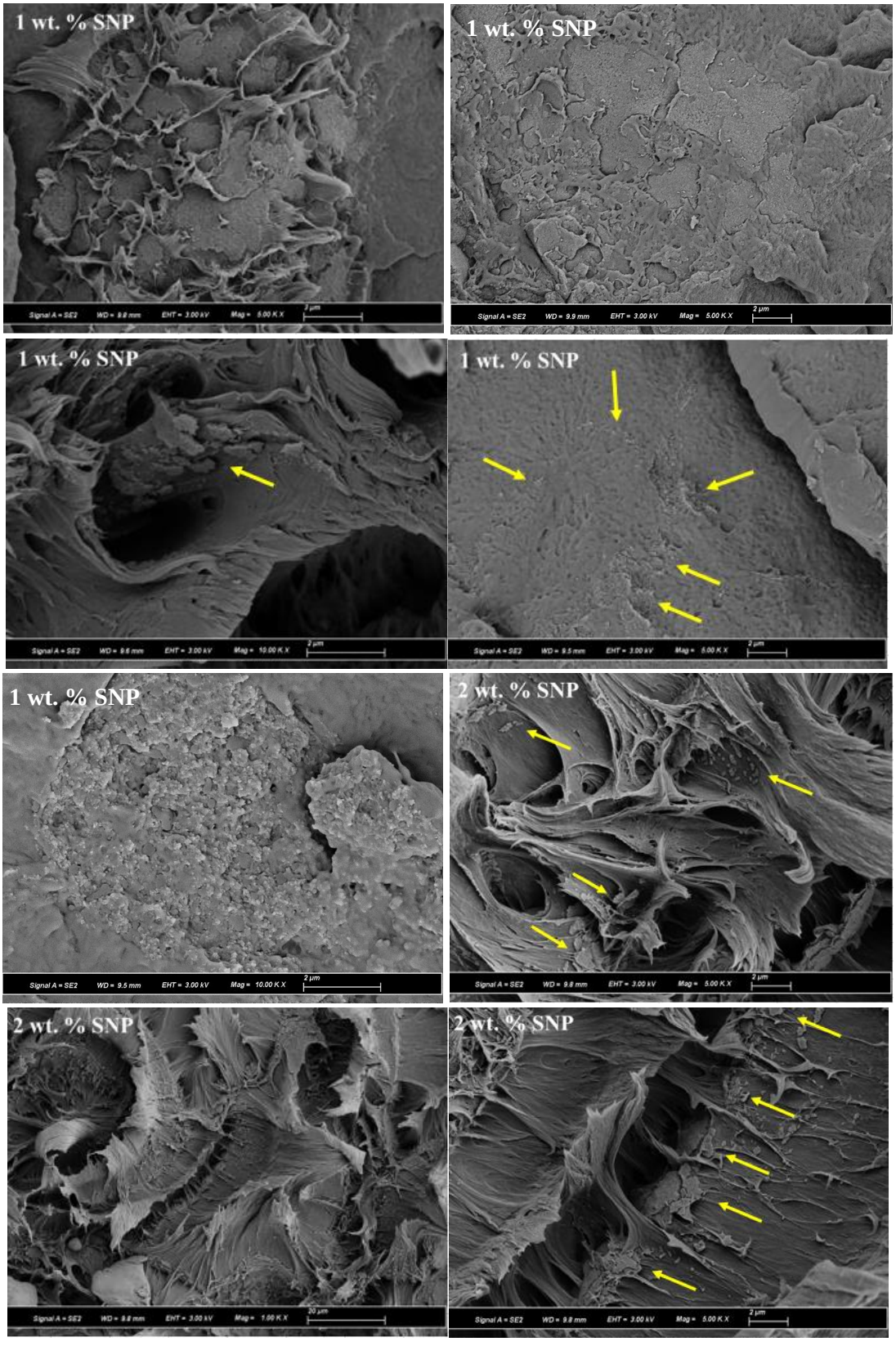

Figure 3-52: Evidence of plate-like SNP agglomeration on the PA11/CB/1wt%25nmSNP and PA11/CB/2wt%25nmSNP fracture surface.

3.4 Conclusions

Two separate PA11/CB/SNP nanocomposite powders were developed with increasing SNP loading to diversify available SLS printing powders, strengthen the PA11/CB polymer particularly in the build direction, and improve powder flow at typical printing temperature. The first iteration of creating the nanocomposite powder involved using 50 nm SNP surface treated with amine terminated silane in 2 wt. % and 4 wt. % loadings, combined through a proprietary solid state shear pulverization process. It was shown through SEM imaging of the PA11/CB/50nmSNP powder that solid state shear pulverization yielded good adhesion of the SNP to the PA11/CB polymer surface, with slight agglomeration observed in the PA11/CB/4wt%50nmSNP sample. Key differences in T_m were noticed between the PA11/CB/50nmSNP samples and the PA11/CB A_{N9} standard, as the SNP loaded samples showed a much larger residual powder peak suggesting poor sintering across the SNP boundary. Both the confined and unconfined powder flow at 180°C reduced with increasing SNP. The PA11/CB/2wt%50nmSNP had measured stiffness well predicted by the Halpin-Tsai model, while the PA11/CB/4wt%50nmSNP modulus was much lower. Both PA11/CB/50nmSNP samples saw a great reduction in elongation at break, likely due to SNP agglomerates and unsintered PA11/CB particles acting as sources of stress concentration. Summaries of the heated confined powder flow results and SNP agglomerated boundaries are shown below in Figures 3-53 and 3-54.

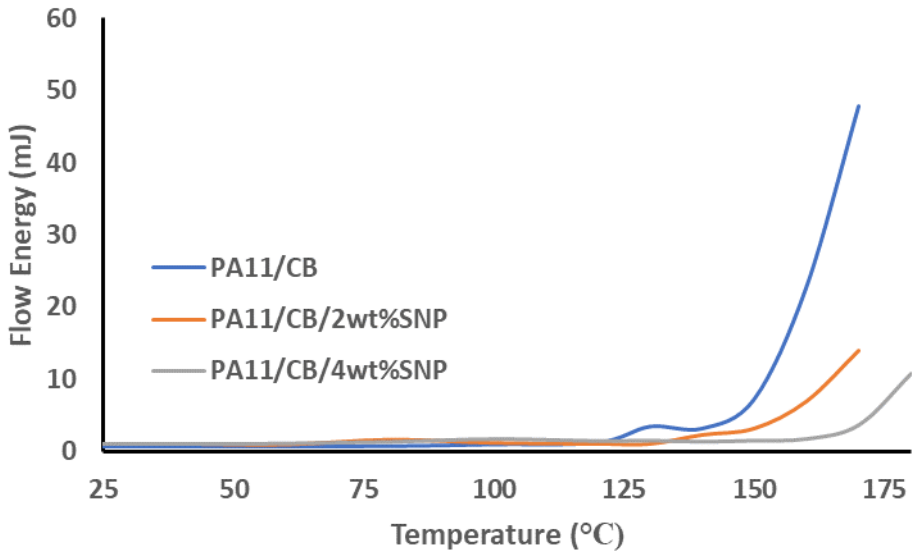

Figure 3-53: Changes in confined flow energy with increasing temperature for PA11/CB and PA11/CB/50nmSNP Powders.

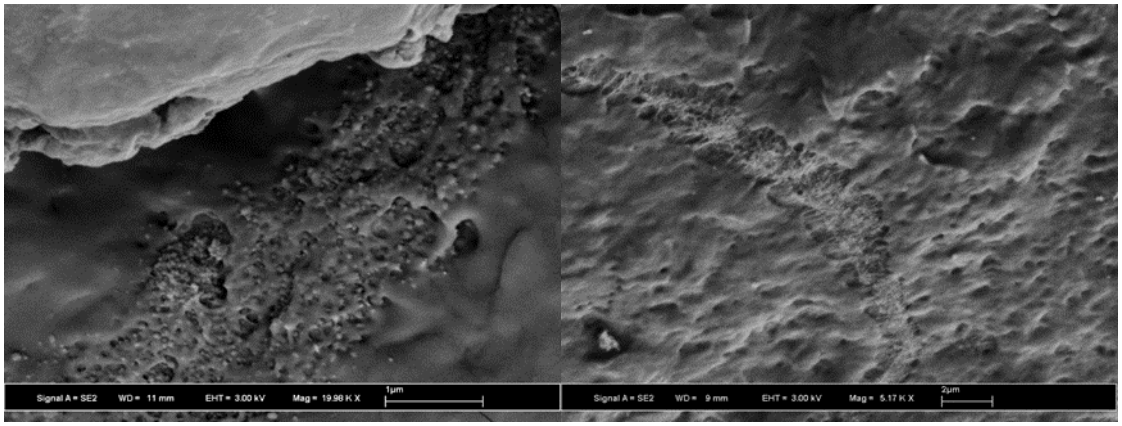

Figure 3-54: SNP boundaries in the PA11/CB/2wt%50nmSNP (left) and PA11/CB/4wt%50nmSNP (right) tensile fracture surfaces.

The second iteration of developing a PA11/CB/SNP printing powder involved combining the PA11/CB powder with 25 nm SNP surface treated with amine terminated silane using centrifugal mixing. Both SEM and TGA revealed great dispersion of SNP on the PA11/CB polymer particles at 0.25 wt. %, 0.5 wt. %, 1 wt. % and 2 wt. % SNP loading. Thermal behavior was much more similar to the PA11/CB A_{N9} sample, with residual powder melting peaks still increasing with increasing SNP loading but with much lower area than the PA11/CB/50nmSNP samples. Confined powder flow was markedly improved with increasing SNP, with measurable flow at 180°C

observed starting at the 0.25 wt. % SNP loading. Both tensile testing and DMA revealed increases in stiffness and strength with increasing SNP, with stiffness values larger than those predicted by the Halpin-Tsai model. The elongation at break for the PA11/CB/0.25 wt%25nmSNP was 26.8% larger than that of the PA11/CB A_{N9}, whereas the remaining PA11/CB/25nmSNP samples exhibited increasingly brittle behavior. Both the PA11/CB/0.25wt%25nmSNP and PA11/CB/0.5wt%25nmSNP samples met requirements for essential work of fracture, with the PA11/CB/0.25wt%25nmSNP sample showing a modest 4.4 % increase. Compression testing perpendicular and parallel to the build layer exhibited increases in compressive strength upon 0.25 wt. % SNP loading, suggesting good reinforcement of SNP at the layer boundaries. Lastly, brittle behavior in the PA11/CB/25nmSNP samples with 0.5 wt. %, 1 wt. % and 2 wt. % SNP loading was sourced to planar and plate-like agglomerations of SNP at the fracture surface, revealing little to no observable diffusion of separate SNP into the polymer matrix. Summaries of the heated confined powder flow results and SNP agglomerated boundaries are shown below in Figures 3-55 and 3-56

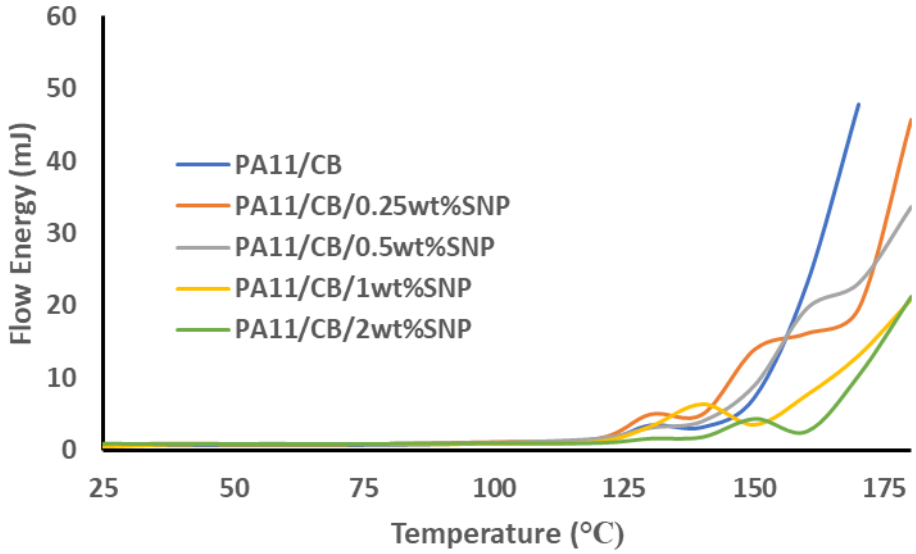

Figure 3-55: Changes in confined flow energy with increasing temperature for PA11/CB and PA11/CB/25nmSNP Powders.

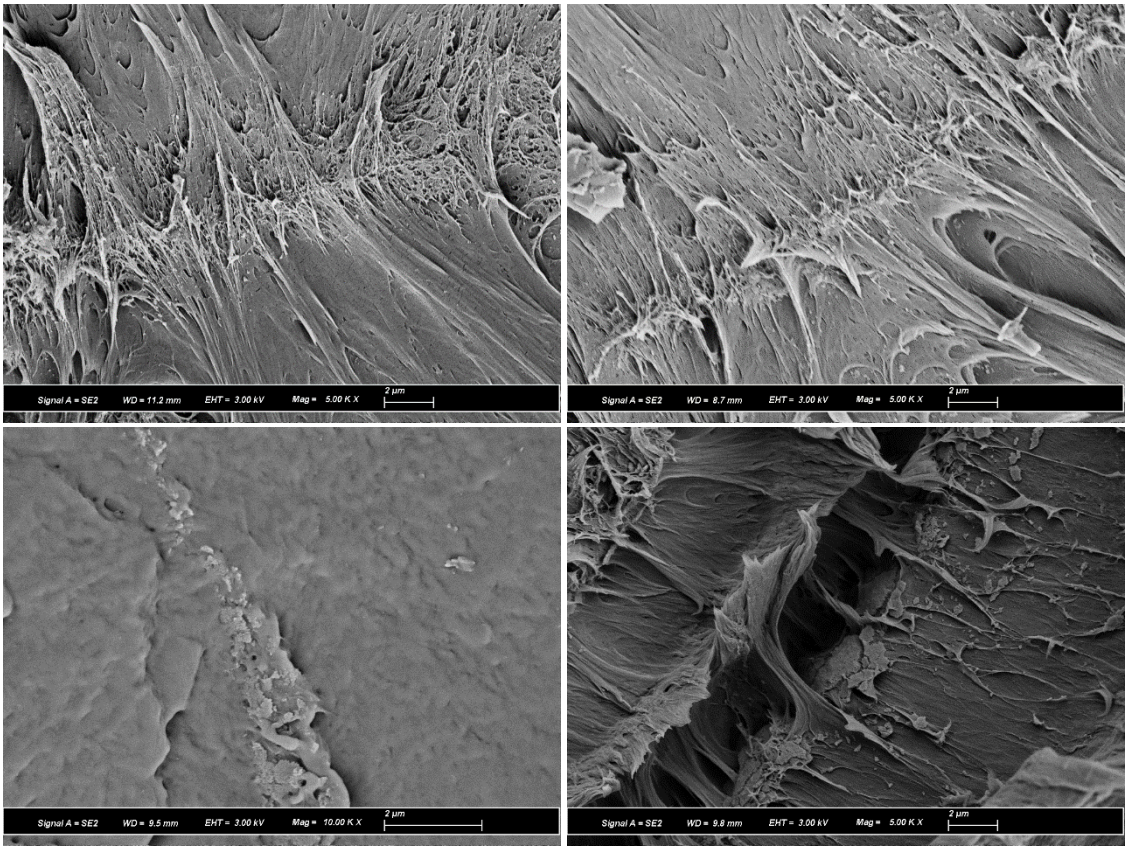

Figure 3-56: SNP boundaries in the PA11/CB/25nmSNP DENT fracture surfaces.

These studies have provided a framework for the feasibility of processing and printing nanoparticle coated polymer powders. Both solid state shear pulverization and centrifugal mixing proved very effective in blending SNP with the PA11/CB polymer powder, with fairly even layers of SNP observable on the PA11/CB surface. A larger difference was determined through fracture surface analysis, which was the ability of the 50 nm and 25 nm SNP separately to integrate into the PA11 matrix upon printing of the powder. Although particle boundary layers of SNP were observable in the PA11/CB/50nmSNP samples, the particles themselves were well surrounded by polymer matrix, and seemed to debond from the PA11/CB matrix. While promising signs of SNP strengthening and toughening was observed in the PA11/CB/0.25wt%25nmSNP samples in both the x and z build direction, the 25 nm SNP at higher wt. % loadings demonstrated significant agglomeration, with minimal polymer diffusion through the surface layer of SNP. This difference in behavior between SNP size could alternatively be due to higher density packing of 25 nm SNP,

leading to difficulties in properly diffusing through the barrier. Interestingly, the PA11/CB/25nmSNP samples demonstrated lower linear reciprocating wear rates, as well as tensile and shear modulus greater than that predicted by the Halpin-Tsai model despite poor SNP diffusion and agglomeration. The SNP at the PA11/CB particle boundaries could have formed a secondary particle aggregate framework in the matrix, leading to better reinforcement in the printed material than what the Halpin-Tsai model would predict.

The powder flow measurement results were expected, with higher SNP content leading to better confined and unconfined powder flow at SLS processing temperatures. This is in slight contrast with previous studies on heated powder flow tests, with results ranging from being highly material dependent [31], to not being temperature dependent at all [32]. The powder flow results in the current study, however, did not correlate well to improvements in mechanical behavior as the PA11/CB/4wt%50nmSNP and PA11/CB/2wt%25nmSNP samples were remarkably brittle despite enhanced flow behavior. Much of this has already been explained by the lack of polymer diffusion through the SNP boundary layers, however there could be a powder flow related explanation as well. It was determined that the confined flow of the PA11/CB powder at 180°C was so poor that the test could not be completed without reaching the torque limit of the instrument. The poor flow is due to pre-diffusion and cohesion of the polymer powder, which may be a nontrivial step in effectively melting the polymer through the SLS process. It may be that for the SLS process, the best flow characteristics would be higher confined flow energy and lower unconfined energy so that the powder bed can densify, but the new layer of powder can be placed smoothly.

In summary, it is possible to use colloidal silica to greatly change both powder flow and mechanical properties of a SLS printing powder. While further optimization of the correct size and volume percent of SNP would be suggested, it has been shown that as little as 0.25 wt. % SNP added to the

PA11/CB particle surface can have a significant effect in improving the printed polymer mechanical properties.

3.5 References

[1]. Schmid, M., Amado, A., Wegener, K. (2015). Polymer powders for selective laser sintering (SLS). *AIP Conference Proceedings 1664*, 160009-1 – 160009-5.

[2]. Ligon, S. C., Liska, R., Stampfl, J., Gurr, M. and Mülhaupt R. (2017). Polymers for 3D Printing and Customized Additive Manufacturing. *Chemical Reviews*, 117, 10212-10290.

[3]. Drummer, D., Wudy, K., and Drexler, M. (2015). Modelling of the Aging Behavior of Polyamide 12 powder during Laser Melting Process. *AIP Conference Proceedings*, 1664, 160007

[4]. Kabasci, S. (2014). Bio-Based Plastics: Materials and Applications. *John Wiley & Sons*, London, 275-293.

[5]. Ziegelmeier S., Christoua, P., Wölleckea, F., Tuck, C., Goodridge, R., Hague, R., Krampec, E. and Wintermantel, E. (2015). An Experimental Study into the Effects of Bulk and Flow Behaviour of Laser Sintering Polymer Powders on Resulting Part Properties. *Journal of Materials Processing Technology*, 215, 239–250.

[6]. Patel, B. (2016). *Toughening mechanisms in silica-filled epoxy nanocomposites*. Dissertation, Lehigh University.

[7]. Freeman Technology. Measuring and understanding the flow properties of powders with the FT4 Powder Rheometer. FM 85958, 1/2018.

[8]. Hare, C., Zafar, U., Ghadiri, M., Freeman, T., Clayton, J. and Murtagh M.J.(2015). Analysis of the dynamics of the FT4 powder rheometer. *Powder Technology*, 285, 123-127.

[9]. Okamba-Diogo, O., Richaud, E., Verdu, J., Fernagut, F., Guilment, J. (2016). Investigation of polyamide 11 embrittlement during oxidative degradation. *Polymer, Elsevier*, 82, 49-56.

[10]. Loos, M. (2015). Carbon Nanotube Reinforced Composites. *William Andrew*, Norwich, 125-170.

[11]. Sidebottom, M., Pitenis, A., Junk, C., Kasprzak, D., Blackman, G., Burch, H., Harris, K., Sawyer, W. and Krick, B.(2016). Ultralow wear Perfluoroalkoxy (PFA) and alumina composites. *Wear*, 362-363, 179-185.

[12]. Majewski, C., Zarringhalam, H. and Hopkinson, N. (2008). Effect of the degree of particle melt on mechanical properties in selective laser-sintered Nylon-12 parts. *J. of Eng. Manufacture*, 222, 1055.

[13]. Zou, H., Wu, S., and Shen, J. (2008). Polymer/Silica Nanocomposites: Preparation, Characterization, Properties, and Applications. *Chemical Reviews*, 108 ,3893-3957

[14]. Freeman, T., Brockbank, K., and Sabathier, J. (2017). Characterizing powder flow properties –the need for a multivariate approach. *Powders & Grains 2017*, 140, 03008-1 – 03008-5

[15]. Mahfuz, H., Hasan, M., Dhanak, V., Beamson, G., Stewart, J., Rangari, V., Wei, X., Khabashesku, V. and Jeelani, S. (2008). Reinforcement of nylon 6 with functionalized silica nanoparticles for enhanced tensile strength and modulus. *Nanotechnology*, 19, 1-7.

[16]. Awaja, F., Zhang, S., Tripathi, M., Nikiforov, A. and Pugno, N. (2016). Cracks, microcracks and fracture in polymer structures: Formation, detection, autonomic repair. *Progress in Materials Science*, 83, 536-573.

[17]. Burford, R. P., and Williams, D.R.G. (1988). Environmental crazing in polyamides. *Journal of Materials Science Letters*, 7, 59-62.

[18]. Cayer-Barrioz, J., Ferry, L., Frihi, D., Cavalier, K., Seguela, R. and Vigier, G. (2006). Microstructure and mechanical behavior of polyamide 66-precipitated calcium carbonate composites: influence of the particle surface treatment. *Journal of Applied Polymer Science*, 100, 989 –999.

[19]. Yoshioka,Y. and Tashiro, K. (2003). Structural change in the Brill transition of Nylon m/n (1) Nylon 10/10 and its model compounds. *Polymer*, 44, 7007-70019.

[20]. Garofalo, E., Russo, G.M., Di Maio, L. and Incarnato, L. (2009). Modelling of mechanical behaviour of polyamide nanocomposite fibres using a three-phase Halpin-Tsai model. *E-Polymers*, 55, 1-16.

[21]. Pegoretti, A and Ricco, T. (2006). On the essential work of fracture of neat and rubber toughened polyamide-66. *Engineering Fracture Mechanics*, 73, 2486-2502.

[22]. Ching, E., Li, R., Tjong, S.C., and Mai, Y. W. (2003). Essential Work of Fracture (EWF) Analysis for Short Glass Fiber Reinforced and Rubber Toughened Nylon-6. *Polymer Engineering and Science*, 43, 558-569.

[23]. Haward, R.N. (1993). Strain Hardening of Thermoplastics. *Macromolecules*, 26, 5860-5869.

[24]. Apichartpattanasiri, S., Hay, J.N. and Kukureka, S.N. (2001). A study of the tribological behaviour of polyamide 66 with varying injection-moulding parameters. *Wear*, 251, 1557-1566.

[25]. Bello, J. O. and Wood, R. J. K. (2003). Grooving micro-abrasion of polyamide 11 coated carbon steel tubulars for downhole application. *Wear*, 255, 1157-1167.

[26]. Mukaida, J., Nishitani, Y., and Kitano, T. (2015). Effect of addition of plants-derived polyamide 11 elastomer on the mechanical and tribological properties of hemp fiber reinforced polyamide 1010 composites. *AIP Conference Proceedings*, 1664, 060008-1 – 060008-5.

[27]. Yang, J.L., Zhang, Z., Zhang, H. (2005). The essential work of fracture of polyamide 66 filled with TiO_2 nanoparticles. *Composites and Science Technology*, 65, 2374-2379.

[28]. Tadano, T., Zhu, R., Muroga, Y., Hoshi, T., Sasaki, D., Yano, S. and Sawaguchi, T. (2014). A new mechanism for the silica nanoparticle dispersion–agglomeration transition in a poly(methyl methacrylate)/silica hybrid suspension. *Polymer Journal*, 46, 342–348.

[29]. Oliveria, C. J. V., Weber, R.P., Monteiro, S.N., Vital, H.C. and Dias, S.L. (2018). Evaluation of Fracture Toughness of Ultraviolet-Irradiated Polycarbonate Using the Essential Work of Fracture Method. *Materials Research*, 21, 1-9.

[30]. Wetherhold, R.C. and Mouzakis, D. E. (1999). Fracture Behavior of Kaolin Reinforced High Density Polyethylene. *Journal of Engineering Materials and Technology*, 121, 483-487.

[31]. Amado Becker A. (2016). *Characterization and prediction of SLS processability of polymer powders with respect to powder flow and part warpage.* Thesis, ETH Zurich.

[32]. Van den Eynde M., Verbelen L., Van Puyvelde, P. (2017). Influence of temperature on the flowability of polymer powders in laser sintering. *AIP Conference Procedings 1914*, 190007-1 – 190007-5.

CHAPTER FOUR: CONCLUSIONS AND FUTURE WORK

4.1 Conclusions

The overarching goal of this dissertation was to elucidate structural changes in a PA11/CB printing powder through the SLS printing process, and use these results as a benchmark from which to develop and compare a PA11/CB/SNP nanocomposite powder for SLS printing.

In Chapter 2, various characterization techniques were employed to elucidate significant changes to the PA11 microstructure during the SLS printing process. The Rilsan Invent Black PA11/CB powder was processed using a Sintratec Kit SLS printer, printing samples at increasing A_N from A_{N7} to A_{N11}. It was shown that there are specific microstructural changes that occur in PA11, some gradual and others more striking between the PA11/CB powder and printed material. The T_m, X_c, l_c and d_{hkl} spacing of PA11/CB were all shown to have changed significantly upon printing, whereas the molecular weight was shown to have a rather gradual increase between the PA11/CB powder and printed parts. Amongst the printed samples, elongation to break, ultimate tensile stress and essential work of fracture were shown to modestly increase with increasing A_N from A_{N7} to A_{N11}. These values compared quite well to available literature on PA11, with the exception of elongation to break which was quite lower than values for injection molded PA11. Subtle structural differences were particularly seen in the A_{N8} and A_{N9} samples, with the appearance of a shoulder on the melting peak and complimentary changes in d_{hkl} spacings and several FTIR peak shifts. The A_{N7} sample was shown to have significant unmelted powder within the sample from poorly sintered layers, likely skewing DSC, XRD and FTIR data with the highly crystalline unmelted powder. Polymer chain rigidity, as characterized by RAP, was also seen to reduce at A_N above the A_{N9}. Fractography proved useful in determining the sources of stress concentration within the printed samples, with all tested samples showing a “dimpled” surface characteristic of ductile fracture. The A_{N7} and A_{N8} samples were largely defect driven, with the unmelted cores of PA11 particles acting as a major source of voiding and crack propagation on the fracture surface. Other sources of stress concentrations include carbon black aggregates and impinged spherulite nuclei.

These results helped to create a better understanding of the printing process, specifically the effect of partial sintering on PA11 structure and mechanical performance. A theorized transitional phase at the polymer melt/additional powder layer interface is proposed to exist, characterized by the changes in melt behavior, RAP, d_{hkl} spacing and FTIR peak shifting of the A_{N8} and A_{N9} samples. It is proposed that it is not until A_{N10} when laser power penetrates deep enough to successfully remelt the transitional layer and not just the top layer of powder. It is concluded that to maximize mechanical performance, it is not just imperative to print at an that fully melts the PA11 powder, but also the more rigid transitional phase that is proposed to germinate at the PA11 melt/powder interphase. With this proposed mechanism in mind, it is also concluded that characterization techniques other than tensile testing prove immensely helpful in optimizing the printing process. Namely, characterizing the melt behavior, RAP and fractography of the w_e surface are enormously useful in determining the existence of poorly sintered powder, a rigid transitional phase and the sources of failure in printed PA11/CB. Using these characterization techniques in tandem can create a fuller picture of the printing process, and help identify sources of error within the printed samples to further help optimize the printing parameters to create high performance printed parts.

In Chapter 3, Two separate PA11/CB/SNP nanocomposite powders were developed with increasing SNP loading to diversify available SLS printing powders, reinforce the PA11/CB polymer particularly in the build direction, and improve powder flow at typical printing temperature. The first iteration of creating the nanocomposite powder involved using 50 nm SNP surface treated with amine terminated silane in 2 wt. % and 4 wt. % loadings, combined through a proprietary solid state shear pulverization process. The second iteration involved combining the PA11/CB powder with 25 nm SNP surface treated with amine terminated silane using centrifugal mixing. It was shown through SEM imaging of the PA11/CB/50nmSNP and PA11/CB/25nmSNP powders that both solid state shear pulverization and centrifugal mixing yielded good adhesion of

the SNP to the PA11/CB polymer surface, with slight agglomeration observed in the PA11/CB/4wt%50nmSNP sample. Key differences in T_m were noticed between the PA11/CB/SNP samples and the PA11/CB A_{N9} standard, as the SNP loaded samples showed larger residual powder peaks for the 2 wt. % and 4 wt. % SNP samples, suggesting poor sintering across the SNP boundary. Both the constrained and unconstrained powder flow at 180°C reduced with increasing 25 nm and 50 nm SNP, suggesting enhanced flow at processing temperatures.

The PA11/CB/2wt%50nmSNP had measured stiffness well predicted by the Halpin-Tsai model, while the PA11/CB/4wt%50nmSNP modulus was much lower. Both PA11/CB/50nmSNP samples saw a great reduction in elongation at break, likely due to SNP agglomerates and unsintered PA11/CB particles acting as sources of stress concentration. Both tensile testing and DMA revealed increases in stiffness and strength with increasing SNP in the PA11/CB/25nmSNP samples, with stiffness values larger than those predicted by the Halpin-Tsai model. Linear reciprocation wear testing additionally demonstrated a decrease in wear rate when increasing 25 nm SNP content from 0.25 wt. % to 0.5 wt. %. The elongation at break for the PA11/CB/0.25 wt%25nmSNP was 26.8% larger than that of the PA11/CB A_{N9}, whereas the remaining PA11/CB/25nmSNP samples exhibited increasingly brittle behavior. Both the PA11/CB/0.25wt%25nmSNP and PA11/CB/0.5wt%25nmSNP samples met requirements for essential work of fracture, with the PA11/CB/0.25wt%25nmSNP sample showing a modest 4.4 % increase. Compression testing perpendicular and parallel to the build layer exhibited increases in compressive strength upon 0.25 wt. % SNP loading, suggesting good reinforcement of SNP at the layer boundaries. Lastly, brittle behavior in the PA11/CB/25nmSNP samples with 0.5 wt. %, 1 wt. % and 2 wt. % SNP loading was sourced to planar and plate-like agglomerations of SNP at the fracture surface, revealing little to no observable diffusion of separate SNP into the polymer matrix.

These studies have provided a framework for the feasibility of processing and printing nanoparticle coated polymer-based SLS powders. The powder flow results in the current study, however, did not correlate well to improvements in mechanical behavior as the PA11/CB/4wt%50nmSNP and PA11/CB/2wt%25nmSNP samples were remarkably brittle despite enhanced flow behavior. The poor flow of the standard PA11/CB powder due to pre-diffusion and cohesion of the polymer powder was concluded to possibly be a nontrivial step in effectively melting the polymer through the SLS process. It may be that for the SLS process, the best flow characteristics would be higher confined flow energy and lower unconfined energy so that the powder bed can densify, but the new layer of powder can be placed smoothly. Ultimately it was concluded that colloidal silica can be utilized to greatly change both powder flow and mechanical properties of a SLS printing powder. While further optimization of the correct size and volume percent of SNP would be suggested, it has been shown that as little as 0.25 wt. % SNP added to the PA11/CB particle surface can have a significant effect in improving the printed polymer mechanical properties.

4.2 Future Work

4.2.1 In-depth comparison of crystallization kinetics, microstructure and mechanical behavior between PA11 and PA12

For SLS printing of polymers, PA12 remains the polymer powder most often used and reported on in literature. This is due to a number of factors including availability, attractive processing windows, and relatively good strength and stiffness values as compared to other commonly printed polymers. Unfortunately, SLS processed PA12 has continued to demonstrate limited ductility, with elongation at break of SLS printed PA12 rarely reported greater than 20%. This is in contrast with PA11, which in the current study have reached elongation to break upwards of 80% while maintaining comparable strength and stiffness values to the more commonly printed PA12. This stark contrast in mechanical behavior is surprising, considering the monomer units of the two polymers only differ only by a single CH_2 alkyl group in the monomer backbone. Aside from

commonly referenced printing errors, there have not been many concrete studies studying investigating the brittle behavior of PA12 compared to other readily used polyamides.

To address this gap in information a more direct comparison of the readily available printing polyamides PA11 and PA12 would be proposed as a future project. Printing powder with similar molecular weight would be processed and studied side by side, particularly the crystallization kinetics and molecular weight increase of each printing powder at increasing temperature. The microstructure and mechanical behavior of the resulting PA11 and PA12 polymer would then be characterized in an attempt to relate the separate crystallization and molecular weight kinetic processes to the final structure and performance of the polymer. These polymers would be initially processed via traditional manufacturing (compression molding, injection molding etc.) for a more controlled processing environment, better equipped to discern differences between the two polymers. These findings would then be utilized a benchmark to compared SLS printed samples of the two separate polyamides. The goal of this study would be to better explain the behavioral differences between the two very similar SLS polymers, and use this information to guide future processing and use of the two powders for maximum mechanical performance.

4.2.2 Development of polyamide copolymer SLS powders.

Commercially available SLS powders currently exist of homogenous polymer matrices, with possible particulate additions to enhance laser absorption, thermal stability, and powder flow. While limited studies have been performed on the SLS printing of polymers with very high T_m such as PEEK and PEKK, the majority of available SLS polymer powder is limited by the melting temperature as extended exposure to high temperature will begin degrading the material. This has reduced the available engineering polymer powders for SLS printing to those that can melt in heated environments approximately 200°C and below. While PA12 and PA11 have emerged as the primary engineering SLS polymer powders that can be processed in this temperature range, there

is plenty of room for improvement to enhance the mechanical behavior of the printed parts closer to that of PA 6 or PA66.

To address these deficiencies, PA11 and PA12 based polyamide copolymers could be studied for development of a new SLS printing powder. It should be noted that PA11/PA12 and PA6/PA,6 /PA11 random copolymers have separately been studied, with extrusion grades of PA6/PA66 copolymers commercially available [1,2]. For SLS printing, PA12/PA6, PA12/PA66, PA11/PA6 and PA11/PA66 copolymers would be synthesized and characterized with increasing PA6 and PA66 monomer content. The goal would be to optimize the PA6 and PA66 content to increase the solid material mechanical properties, but not raise the melting temperatures too high as to need a processing temperature that enables thermo-oxidative degradation. Besides successfully synthesizing the copolymers, much attention would be payed to the resulting polymer microstructure after melting to determine the homogeneity of the copolymer through processing. If successful, this material would be one uniquely designed for the SLS process, and could lead to the utilization of SLS printing for more high performance and weight bearing polymer parts.

4.2.3 Development of highly filled PA11/SNP powder for SLS printing

The present study focused on developing PA11/CB/SNP composite powders with upwards of 4 wt. % SNP added to the surface of the PA11/CB particles. While good adhesion was observed of the SNP to the polymer surface, there were clear deficiencies in fully integrating the SNP into the printed polymer matrix, as evidenced by SNP particle boundary lines and agglomerates on the fracture surface. This lead to poor polymer diffusion in the SNP rich areas, resulting in larger sources of stress concentration and ultimately failure in the printed PA11/CB/SNP samples with higher SNP loading. There is certainly a limit to how much SNP can be added to the polymer particle surface to increase powder flow and toughen the particle boundaries without negatively impacting polymer diffusion during the SLS printing process. Significant increases in PA11

mechanical properties such as modulus and strength however would likely not begin until much higher volume of SNP, which with the present methods of combining the SNP and polymer powder would not result in a printable powder.

Instead of adding SNP to the surface of the PA11/CB particle, a future study could be to create a highly SNP loaded PA11 particle for SLS printing. PA11 and SNP would be combined to form a nanocomposite polymer particle in two methods with increasing SNP. The first would consist of melt extruding the polymer and SNP together, followed by cryogenic grinding of the solid into 50 µm particles. The second method would be to use an emulsion polymerization process to polymerize PA11 in the presence of SNP, creating more of a rigid core/polymer shell hybrid particle. SNP content would start at 1 wt. %, but would increase to 5 wt. %, 10 wt. % and 15 wt. % loadings to highly fill the PA11 matrix. After a high enough yield of PA11/SNP powder is synthesized, the material would be print and fully characterized. The goal of this project would be developing a highly filled PA11 polymer specifically for the SLS process, reaching mechanical properties compatible with high performance and load bearing application needs.

4.2.4 Studying diffusion kinetics of varying sized SNP in PA11

It was determined through the present study on PA11/CB/SNP that there is limited diffusion of 25 nm and 50 nm surface treated SNP through PA11 during the SLS printing process. Optimally, however, the SNP would be present on the PA11/CB particle surface during the administering of a new powder layer and start to diffuse into the polymer matrix upon sintering. Besides optimizing the laser energy to excite an SNP particle in a viscous melted polymer, another challenge in SNP diffusion during the SLS process includes the post-polymerization of PA11 during printing. As the PA11 molecular weight increases, it will be increasingly difficult for SNP to diffuse as shown through previous diffusion studies [3]. For future use of SNP in PA11 in SLS printing, it would be imperative to not just study SNP diffusion in PA11 of a single molecular weight, but one that will demonstrate molecular weight increase at varied rates as well.

A future study could therefore focus on the diffusion rates of SNP in a PA11 matrix, and alternatively the diffusion of PA11 through a SNP saturated boundary. Particularly, focusing on a range of colloidal SNP sizes and measuring the distance travelled in a PA11 polymer film after exposure to melting temperature for increasing amounts of time. End-capped PA11 of different fixed molecular weight would first be utilized to establish diffusivity rates of SNP at separate PA11 molecular weights. Afterwards, the kinetics of post-polymerization of the Rilsan Invent Black would be modeled and used to measure SNP diffusion lengths in PA11 with increasing molecular weight. Once a silica of appropriate size was optimized, SNP with varied surface treatments would be studied to determine any effect on SNP diffusion in the PA11 matrix. The goal would be to optimize the best size of SNP to promote both SNP and polymer diffusion within the composite material, and use this information to further develop a PA11/CB/SNP nanocomposite for SLS printing.

4.2.5 SLS printing of PA11/CB/SNP composite powder with bimodal SNP size

During the study on PA11/CB/SNP composite materials in chapter 3, it was found that there was a limit to how small the SNP could be before agglomeration dominates at higher volumes. Alternatively, it was shown that 25 nm SNP was quite effective in increasing powder flow at processing temperature at very low volumes. It is possible that separate sizes of SNP are best fit to improve several SLS polymer powder properties like powder flow, dispersion and diffusion, as well as separate printed material properties like strength, stiffness, and toughness. Limited studies have been performed on using bimodal particle sizes to improve powder flow [4], however the particles are of micron size and may not be as comparable to nanoparticles. If separate sizes of SNP can be optimized to improve separate properties of SLS polymers, then combining both may allow for the optimization of all properties of interest.

Instead of adding SNP of a single size to the PA11/CB particle surface, a future study could investigate using SNP blends of separate sizes to improve upon a diverse array of powder and printed material properties. This study would be best to follow one as suggested in 4.2.4, as separate optimization studies would need to be completed to decide the best size SNP to improve powder flow, diffusion, and mechanical properties in a printed or melted solid composite. Once separate SNP sizes had been optimized, SNP powder blends of two different sizes could be mixed and then added to the PA11/CB particle surface. Alternatively, if following the study proposed in 4.2.3, one size of SNP could be optimized for mechanical performance and distributed throughout the PA11 particle, while a second could be distributed on the surface for improved powder flow and diffusion. If successful, multiple SLS parameters could be improved upon through adding the same rigid reinforcement at differing sizes, leading to SLS printed PA11 with enhanced mechanical properties for high performance applications.

4.3 References

[1]. Telen, L.,Van Puyvelde, P., and Goderis, B. (2016). Random Copolymers from Polyamide 11 and Polyamide 12 by Reactive Extrusion: Synthesis, Eutectic Phase Behavior, and Polymorphism. *Macromolecules*, 49, 876-890.

[2]. Jin, X. D., Hu, G., Yang, Y., Zhou, X. and Wang, B. (2009). Nylon 6/66/11 Copolymer Used for Hot-Melt Adhesives: Synthesis and Properties. *Journal of Adhesion Science and Technology*, 23, 779-785.

[3]. Griffin, P. J., Bocharova, V., Middleton, L.R., Composto, R.J., Clarke, N., Schweizer, K.S and Winey, K.I. (2016). Influence of the Bound Polymer Layer on Nanoparticle Diffusion in Polymer Melts. *ACS Macro Letters*, *5*, 1141-1145.

[4]. Bai, Y., Wagner, G., and Williams, C. B. (2017). Effect of Particle Size Distribution on Powder Packing and Sintering in Binder Jetting Additive Manufacturing of Metals. *Journal of Manufacturing Science and Engineering*, 139, 081019-1 – 081019-6.

APPENDIX

A more recent additive manufacturing technique showing promise in manufacturing nanocomposite materials is direct ink writing. Direct ink writing is describes the layer by layer building up approach to make three dimensional parts, however instead of more solid thermoplastic based polymer, an "ink" is robotically extruded through a micron scale nozzle [1]. These inks are typically much lower in viscosity than traditional FDM filaments, and require quick dilatant or shear thickening recovery to preserve printing shape [1]. This method has been used more readily in manufacturing biomimetic and bioenabled scaffolds [2], however it has been utilized sparingly to increase the orientation of particles and fibers in polymer composites and nanocomposites. Of real potential is the direct ink writing of polymer composites with very high aspect ratio fillers or fibers, as the ejction from the nozzle can often lead to much higher anisotropy as compared to traditional manufacturing. This was observed in a 2012 study using a modified direct ink writing setup to produce epoxy/carbon nanotube nanocomposites. The modification involved adding a UV radiation source to the nozzle to immediately cure the epoxy as it was printed. Both freestanding and tensile electrical conductance increased with 1 and 2 wt % loadings of the carbon nanotubes with promise in applications such as elctromechanical sensors [3].

Success with an even higher aspect ratio filler was observed in a 2016 study by the Jet Propulsion Laboratory (JPL). Direct ink writing was employed to produce carbon fiber reinforced epoxy, in an attempt to increase the alignment of carbon fiber and create more intricate composite parts [1]. The epoxy used was a Bisphenol-F diglycidyl ether based resin, with grade HTS40 carbon fiber. There was great importance placed and characterization of the rheology of the composite resin, with fumed silica added to create a shear thinning rheological response. It was found at 15 wt % fumed silica loading, the shear relaxation of the matrix provided the best orientation of the carbon fiber as it was extruded from the printing nozzle [1]. Orientation of the carbon fiber was reported at 80% alignment with the full optimized epoxy matrix and printing parameters. As compared to

randomly pressed composites, the printed composite material demonstated much higher tensile modulus, with the printed 15 wt % carbon fiber filled system nearing 5.5 GPa in modulus. Figure A-1 compares the random pressed (RP) and printed (AM) composite modulus values, and shows the printed composite crossection.

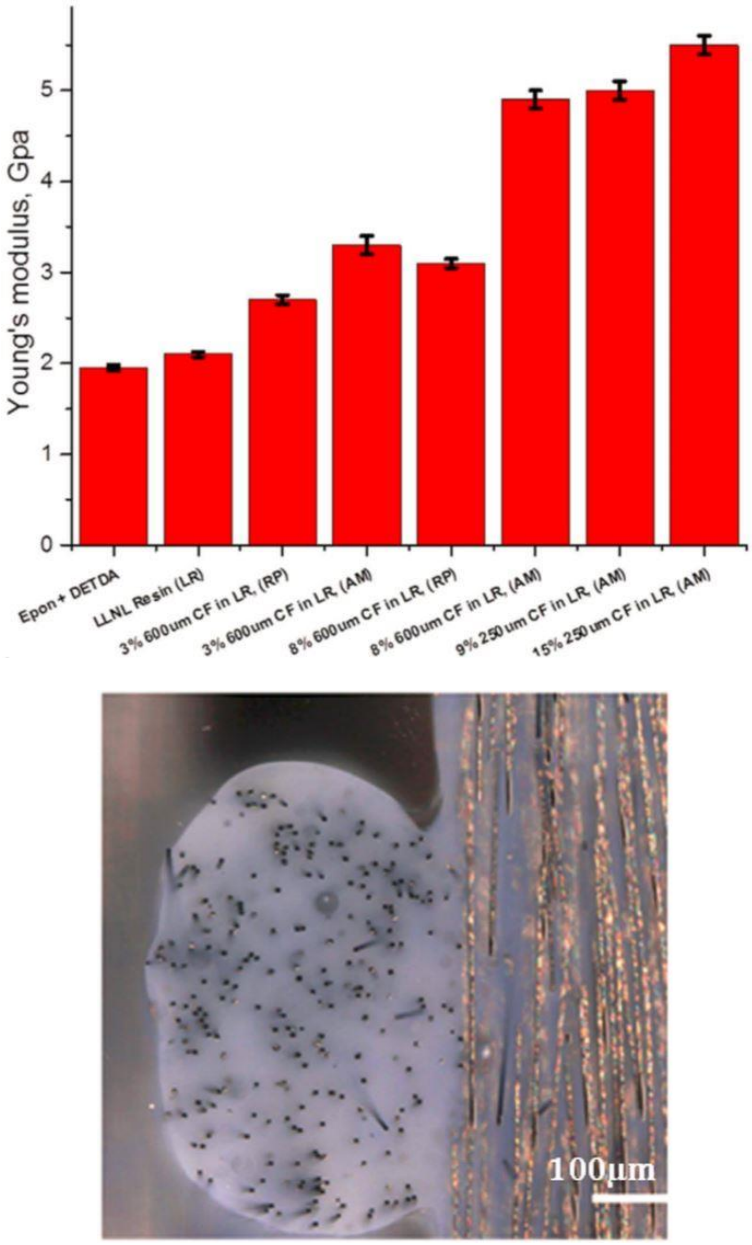

Figure A-1: Modulus values and crossection of a carbon fiber filled epoxy processed by direct ink writing [1].

As a separate, independent study to the main content of this dissertation, SNP was additionally utilized to enhance a polymer composite system for a direct ink writing (DIW) based additive manufacturing process. The composite was initially designed to consist of a diglycidyl ether of bisphenol-A (DGEBA) based epoxy, short carbon fiber (CF) and fumed silica (FS) to compare with the results shown from JPL using a similar composite system and processing technique [1]. The CF used was grade HTS40, supplied by Toho Tenax. To get a better representation of the CF dimensions, images of the CF adhered to tape were taken with a digital microscope at 250x magnification. The distribution of CF lengths proved to be very wide, with lengths ranging from 25 μm to 250 μm. The average size appeared to be between 60 μm and 80 μm. Representative images of the CF with measured fiber lengths are shown below in Figure A-2.

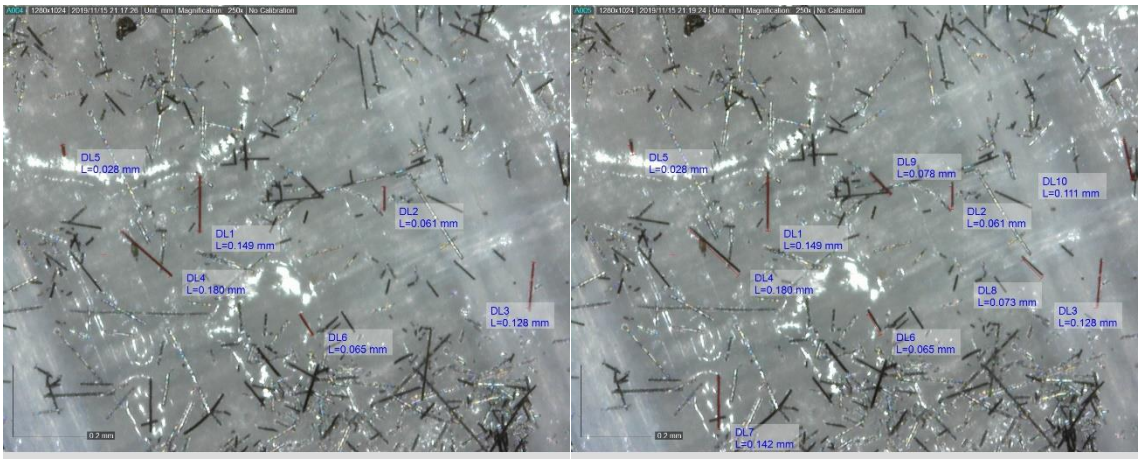

Figure A-2: Images highlighting the dimensions of CF as supplied by Toho Tenax.

To first determine the effect of CF on the epoxy rheological response, steady state shear viscosity was measured on a DGEBA based epoxy with increasing short milled carbon fiber content. Weight percents tested were 1, 5, 10 and 20 weight percent carbon fiber. The epoxy used was DER 331, with the same grade HTS40 carbon fiber supplied by Toho Tenax as mentioned previously. 50 gram batch samples were mixed using a centrifugal mixer at 2000 rpm for 1 minute, and degassed at an additional minute at 2200 rpm. The viscosity results at room temperature are shown below in Figure A-3.

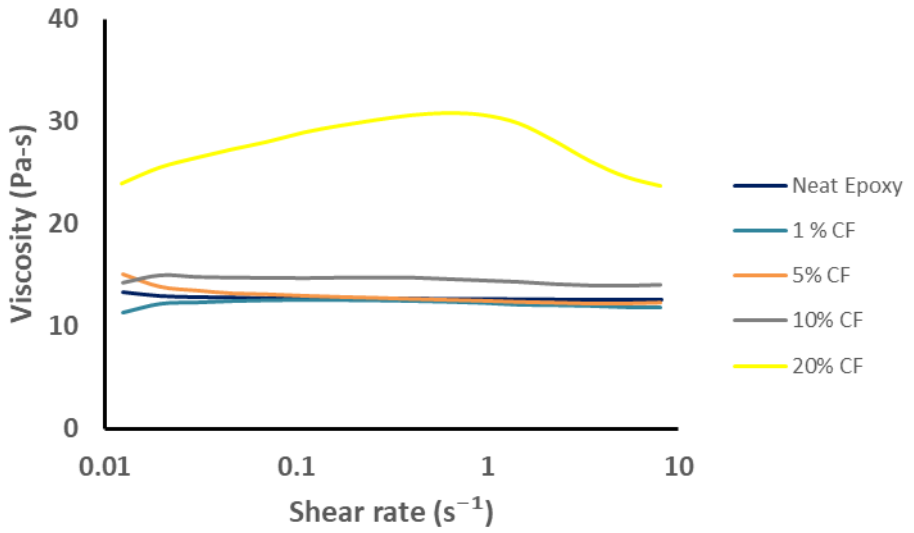

Figure A-3: Viscosity response of DER 331 epoxy with increasing carbon fiber at room temperature.

As seen in Figure A-3, the neat epoxy and composites demonstrated very Newtonian flow, until the 20 wt. % CF composite sample showing a maximum of viscosity close to 1 s^{-1}. This could be due to some structure formation of the CF at this weight percent loading, disassembling after reaching the 1 s^{-1} strain.

Both calorimetry and rheology were utilized to characterize the cure kinetics of diethylmethylbenzenediamine (DETDA) in diglycidyl ether of bisphenol A (DGEBA). To follow the study performed at JPL, a cure study on a very low phr of DETDA in DGEBA was attempted [1]. While a slight exothermic peak was detected using differential scanning calorimetry, the rheological cure studies yielded no increase in viscosity after 4 hours at elevated temperature. The cure kinetic studies then shifted to the stoichiometric volume of DETDA in the DER 331 DGEBA used for this study. This value was determined by dividing the amine hydrogen equivalent weight of DETDA (45) by the epoxy equivalent weight in DGEBA (187), and multiplying by 100. The stoichiometric value was determined to be 23.8 phr of DETDA in DGEBA, and was utilized in the remainder of the study. Another differential scanning calorimetry experiment on the 23.8 phr

DETDA in DGEBA revealed the exothermic cure peak, starting at 100°C and with a maximum occurring at approximately 200°C. The epoxy was tested in a TA Instruments Q2000 with heating and cooling cycles ranging from 25ºC to 230ºC at 10ºC/min, with heating curves comparing the 1 and 23.8 phr DETDA in DGEBA shown below in Figure A-4.

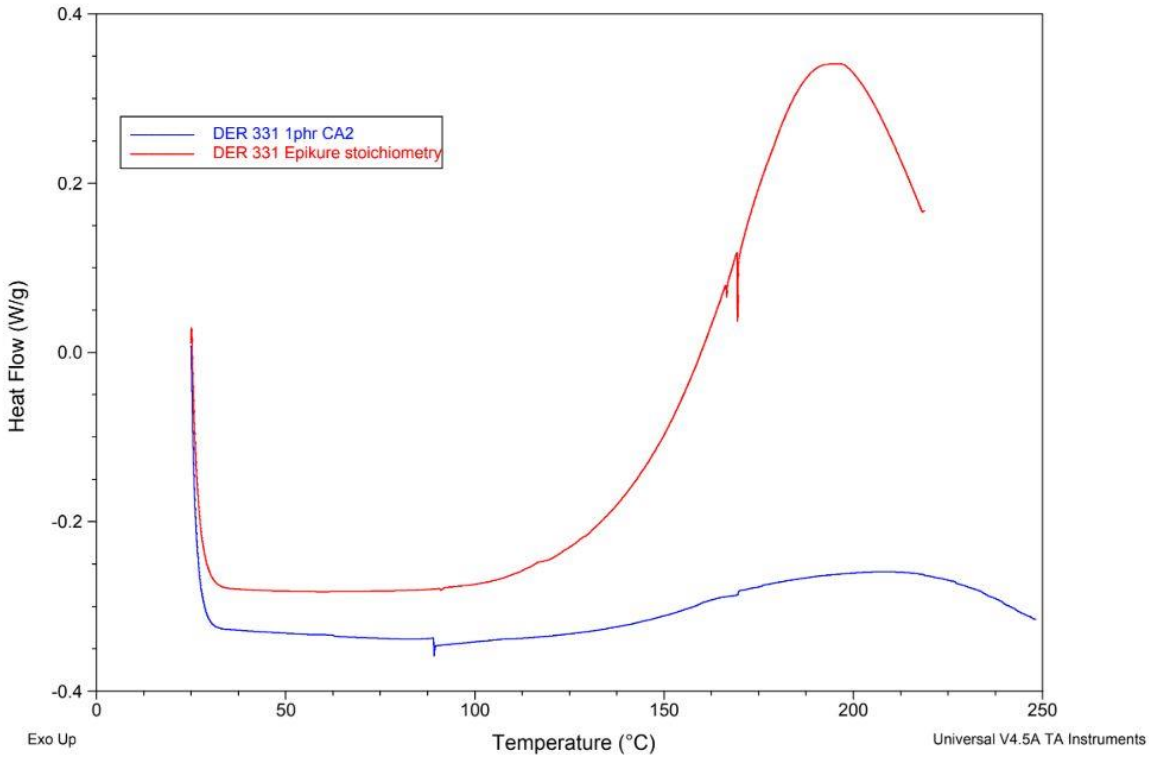

Figure A-4: DSC thermograms of the 1 phr (blue) and 23.8 phr (red) DETDA in DGEBA epoxy.

Cure studies continued using the TA Instruments DHR-2 rheometer with 25 mm parallel plates at 1 mm spacing. Of interest was finding the gel point, defined in this study as the time taken for the epoxy to reach 1000 Pa-s. Viscosity was measured as a function of time under oscillation at 50% strain and 1 Hz frequency. The viscosity results at 80°C, 100°C, 120°C and 140°C are shown below in Figure A-5.

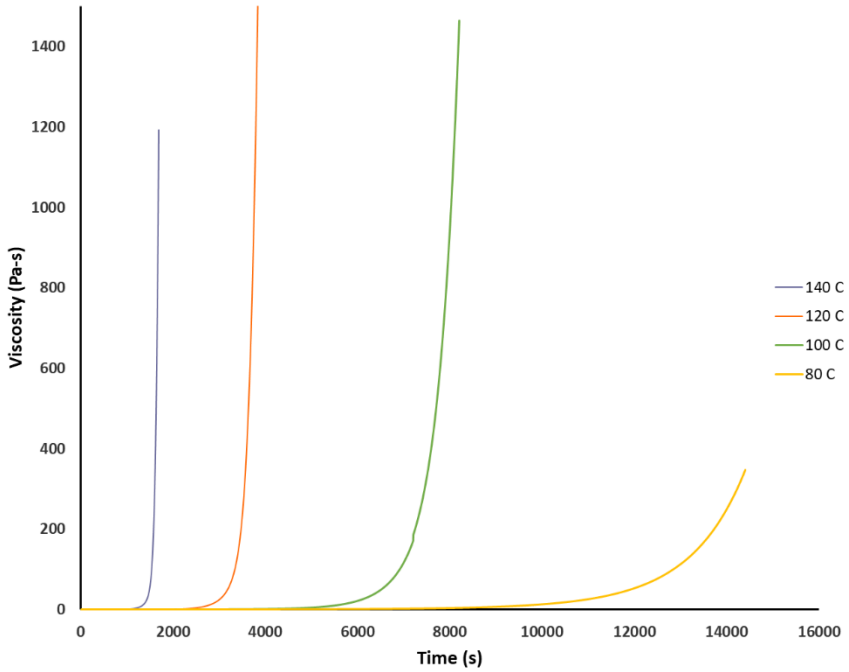

Figure A-5: Viscosity increases of 23.8 phr DETDA in DGEBA at increasing temperature.

The activation energy was determined for the reaction using the Arrhenius equation, using the time at gel point (1000 Pa-s) at 100°C, 120°C and 140°C. The natural log of the reciprocal times were plot against the reciprocal temperatures in Kelvin, with the slope proportional to the activation energy divided by the gas constant. The activation energy was calculated to be 50.2 kJ, and the gel times and Arrhenius plot are shown below in Table A-1 and Figure A-6, respectively.

Table A-1: Gel times of 23.8 phr DETDA in DGEBA at 100°C, 120°C and 140°C.

Temperature (°C)	**Gel Time (s)**
100°C	8023 s
120°C	3758 s
140°C	1670 s

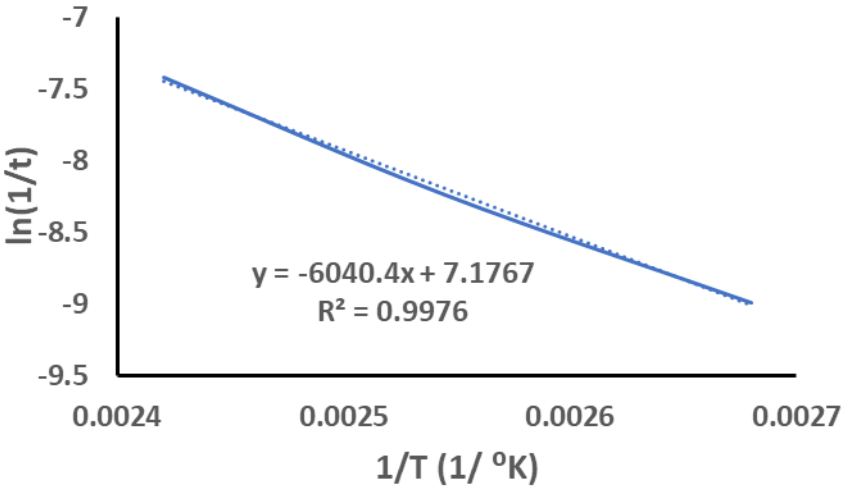

Figure A-6: Arrhenius plot of 23.8 phr DETDA in DGEBA.

The stoichiometric ratio of DETDA to DGEBA was used for the remainder of epoxy formulations for this study. To help gauge low temperature cures of the DETDA/DGEBA system, samples were cured for 24 hours at 100ºC, 120ºC and 140ºC to evaluate as potential cure schedules. Low temperature cures were initially studied to hopefully avoid an initial lowering of viscosity after printing that would distort the intended printed shape. The glass transition temperature is shown to move higher with higher cure temperature, and is illustrated below in Figure A-7.

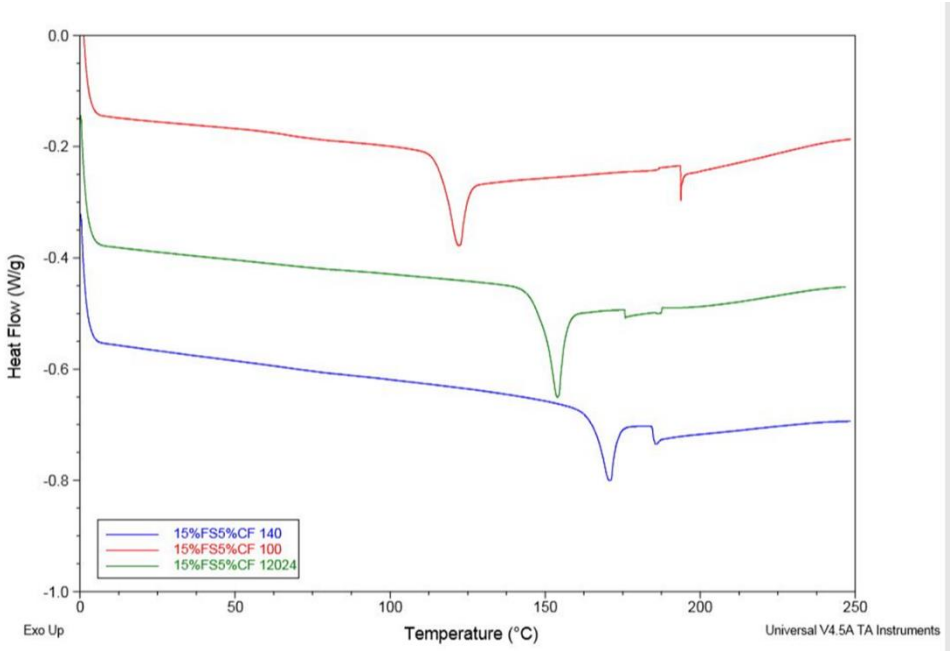

Figure A-7: Glass transition of DETDA/DGEBA cured for 24 hours at 100°C (red), 120°C (green) and 140°C (blue).

Select batches of filled DETDA/DGEBA were cured for increasing time close to the reaction maximum temperature (190°C) to observe any change in dimensions upon curing at a higher temperature. It was found that there was very little change in shape upon rapid heating, leading to 190°C being used as the temperature for the remainder of cure studies for the DETDA/DGEBA system. The epoxy was tested in a TA Instruments Q2000 with heating and cooling cycles ranging from 25ºC to 230ºC at 10ºC/min for samples cured for increasing time at 190ºC, in hopes of maximizing the glass transition temperature. It was shown that increasing cure time at 190°C resulted in smoother glass transition regions and maximizing Tg at 175ºC. A cure schedule of 6 hours at 190°C was chosen for the remainder of DETDA/DGEBA based epoxy composite systems. The DSC results are shown below in Figure A-8.

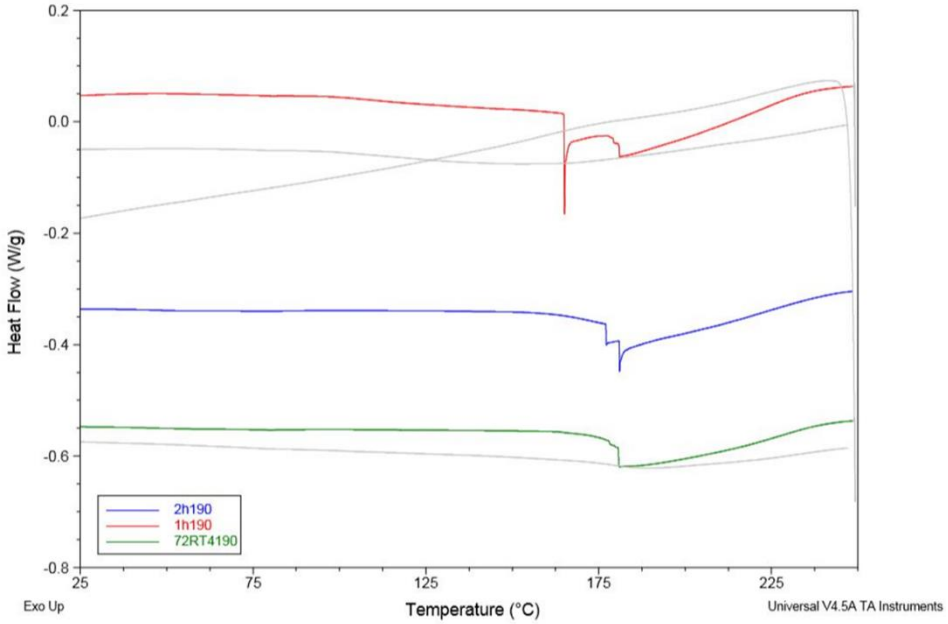

Figure A-8: Glass transition of DETDA/DGEBA cured at 190°C for 1 hour (red), 2 hours (blue) and 4 hours (green).

Rheology studies were also performed on the DGEBA with increasing fumed silica (FS). The FS used was the TPX 1450 as provided by Cabot, and was added to DGEBA in 1, 5, 10, and 15 wt % amounts through centrifugal mixing at room temperature. Epoxy composites were combined at 2000 rpm for 15 minutes, and 2200 rpm for another 15 minutes. Composites were left to cool to room temperature prior to testing, as measured using an IR thermometer. The composites were tested using similar 25 mm parallel plates and 1 mm spacing as the cure study. A steady state shear viscosity experiment was performed to study the viscosity profile with increasing fumed silica. The 1 and 5 wt % FS samples demonstrated Newtonian behavior, with slight shear thinning occurring in the 5 wt % sample beginning at 0.1 s^{-1}. The 10 and 15 wt% samples showed clear shear thinning behavior and behaved characteristically like a Bingham plastic. Both viscosity profiles fit a standard power law profile, both with a best of fit R^2 value of 0.998. The modeled viscosity behavior for the 10 wt. % and 15 wt. % samples are shown below in Equations 2 and 3 respectively, with the standard power law equation shown in Equation 1

$$\eta = k(\dot{\gamma})^{n-1} \quad (1)$$

$$\eta = 718.9(\dot{\gamma})^{-0.61} \quad (2)$$

$$\eta = 2965.1(\dot{\gamma})^{-0.63} \quad (3)$$

The k (flow consistency index) values for the 10 wt. % and 15 wt. % FS samples were slightly different at 718.9 Pa-s^n and 2965.1 Pa-s^n respectively. The n (flow behavior index) values, alternatively, were quite similar with respective values of 0.39 and 0.37. The 15 wt. % FS sample specifically reached levels of k and n closer to those modeled by JPL at 2033 Pa-s^n and 0.18 respectively, suggesting attractive flow behavior for fiber orientation in the DIW process [1]. The viscosity profiles for each DGEBA/FS sample are shown below in Figure A-9.

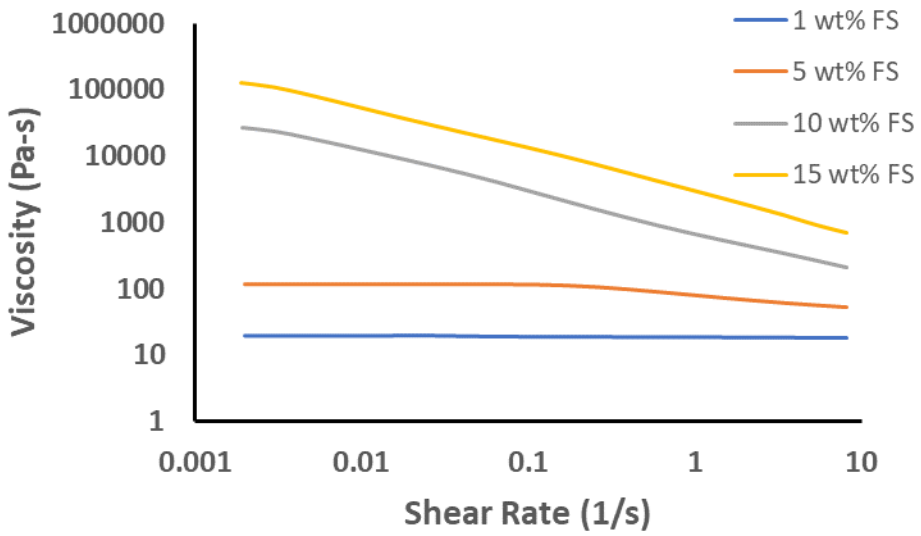

Figure A-9: Viscosity response of DER 331 epoxy with increasing FS at room temperature.

Steady state shear experiments were then performed on composites with increasing carbon fiber (CF) and FS. Epoxy composites with 1, 5 and 10 wt% CF were mixed and test with 1, 5, 10 and 15 wt% FS. The increase in carbon fiber had a minimal effect of increasing the overall viscosity, with the effect more noticeable at the composites with 1 and 5 wt% FS. The rheological profile seamed relatively unchanged, with the increases in FS having a much larger impact than the increase in CF.

This is likely due to the aspect ratio of CF used in the present study, which may not be large enough to significantly increase the filled epoxy viscosity. The shear testing results of the Epoxy/FS composites with 1, 5, and 10 wt% CF are shown respectively in Figures A-10, A-11, and A-12.

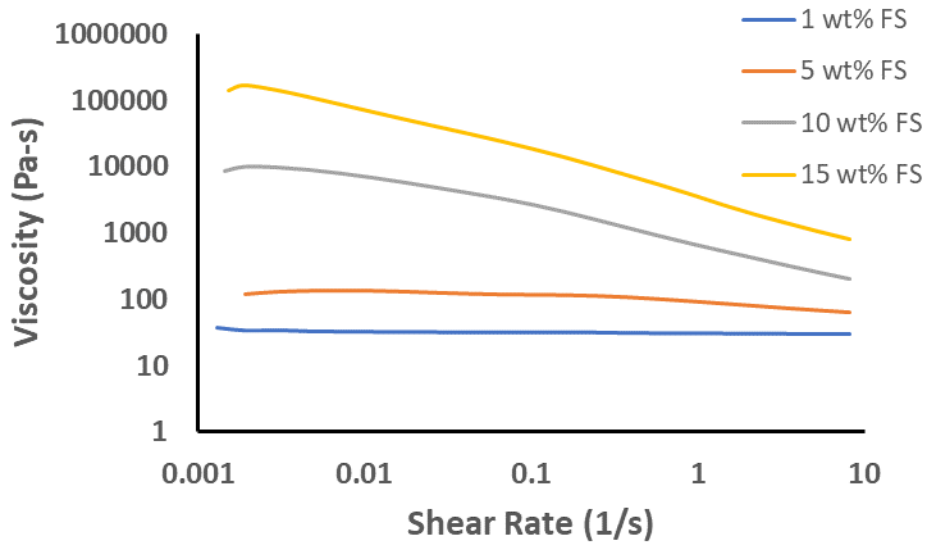

Figure A-10: Viscosity response of DER 331 with 1 wt% CF and increasing FS.

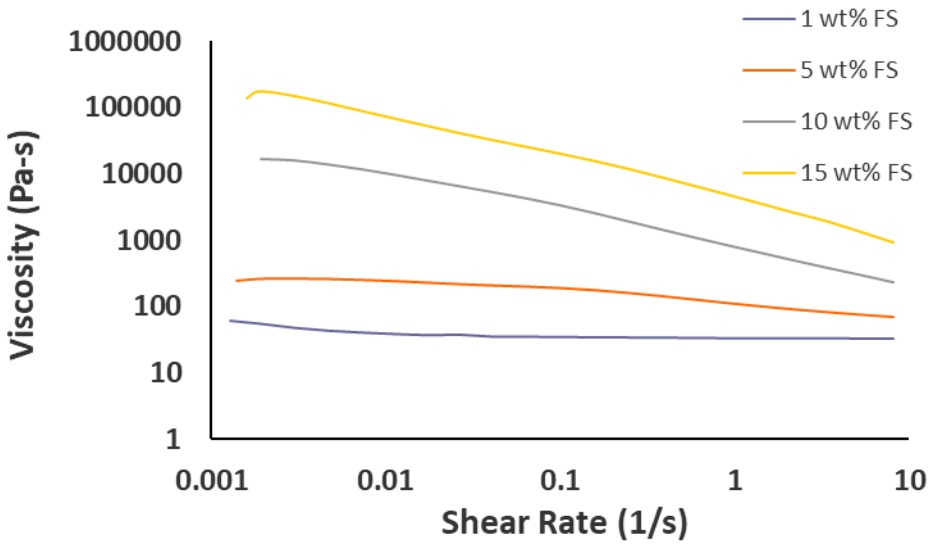

Figure A-11: Viscosity response of DER 331 with 5 wt% CF and increasing FS.

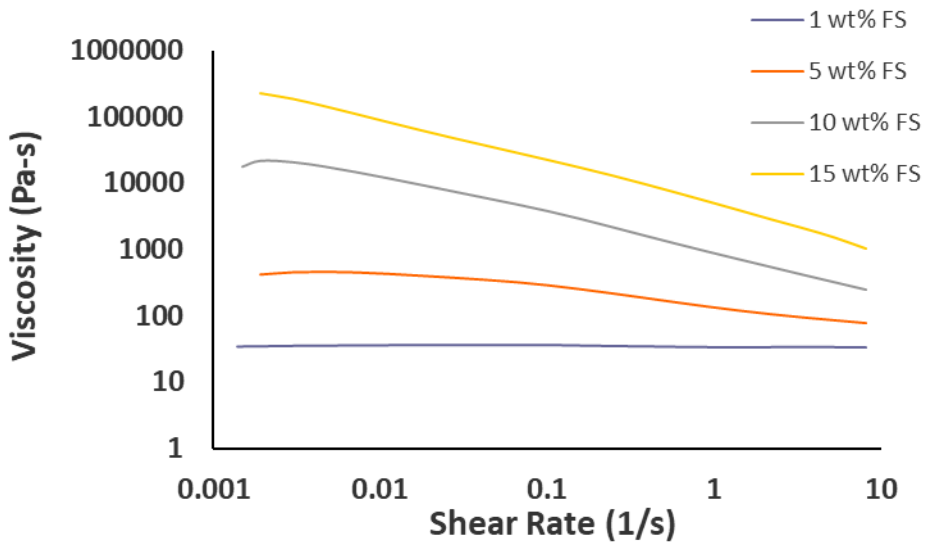

Figure A-12: Viscosity response of DER 331 with 10 wt% CF and increasing FS.

Rheology studies were performed on the DGEBA with 15 wt. % FS and increasing CF. CF was added to DGEBA/FS in 5, 10, and 15 wt % amounts, and combined with a centrifugal mixer at room temperature. Epoxy composites were combined at 2000 rpm for 15 minutes, and 2200 rpm for another 15 minutes. Composites were left to cool to room temperature prior to testing, as measured using an IR thermometer. The composites were tested using similar 25 mm parallel plates and 1 mm spacing as previously mentioned rheology studies. Of interest was the fit to the power law, and its relation to that published by JPL. All viscosity profiles fit a standard power law profile, both with a best of fit R^2 values ranging from of 0.977 to 0.998. The modeled viscosity behavior for the 5 wt. % CF, 10 wt. % CF and 15 wt. % CF samples are shown below in Equations 4-6.

$$\eta = 4412.8(\dot{\gamma})^{-0.61} \quad (4)$$

$$\eta = 7769.2(\dot{\gamma})^{-0.58} \quad (5)$$

$$\eta = 3601.4(\dot{\gamma})^{-0.72} \quad (6)$$

The k (flow consistency index) values for the 5 wt. %, 10 wt. % and 15 wt. % CF samples were slightly different at 4412.8 Pa-s^n , 7769.2 Pa-s^n and 3601.4 Pa-s^n respectively. The n (flow behavior index) values for the 5 wt. % and 10 wt. % samples were quite similar with respective values of

0.39 and 0.42. The 15 wt. % CF sample specifically reached attractive values of k and n of 3601.4 Pa-s^n and 0.28 respectively, close to those modeled by JPL at 2033 Pa-s^n and 0.18 respectively, suggesting attractive flow behavior for fiber orientation in the DIW process [1]. The viscosity profiles for each DGEBA/FS/CF sample are shown below in Figure A-13.

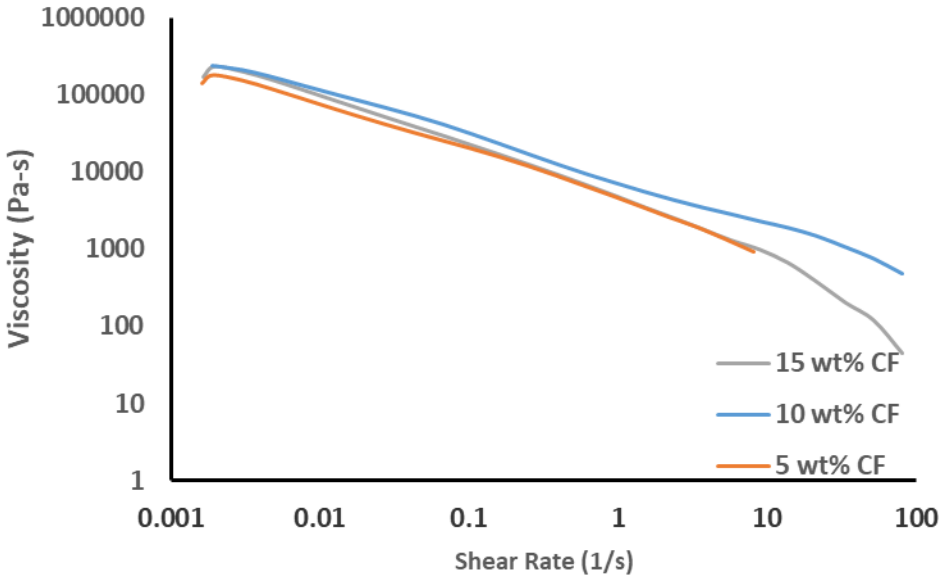

Figure A-13: Viscosity response of DER 331 with 15 wt% FS and increasing CF.

Preliminary processing of the DGEBA/DETDA/15wt%FS/15wt%CF system proved challenging, as extremely high pressure was required to push the epoxy composite through a syringe. A temperature sweep was performed to identify a processing temperature that could reduce viscosity without prematurely curing the epoxy system. Steps of 10^{o}C were taken with 5 minutes of averaging data at 1 Hz oscillation. Temperatures as low as 35^{o}C were shown to reduce the viscosity by 50%, with minimum viscosity of 190.1 Pa-s measured at 100^{o}C. Curing began at 115^{o}C, with rapid gelation occurring at 155^{o}C, as evidenced by the large increase in viscosity and the G′, G″ crossover point. Direct ink writing processed anywhere from 35^{o}C to 60^{o}C should provide enough of a viscosity decrease to better push the viscous epoxy composite through the syringe. The temperature sweep of the DGEBA/DETDA/15wt%FS/15wt%CF system is shown below in Figure A-14.

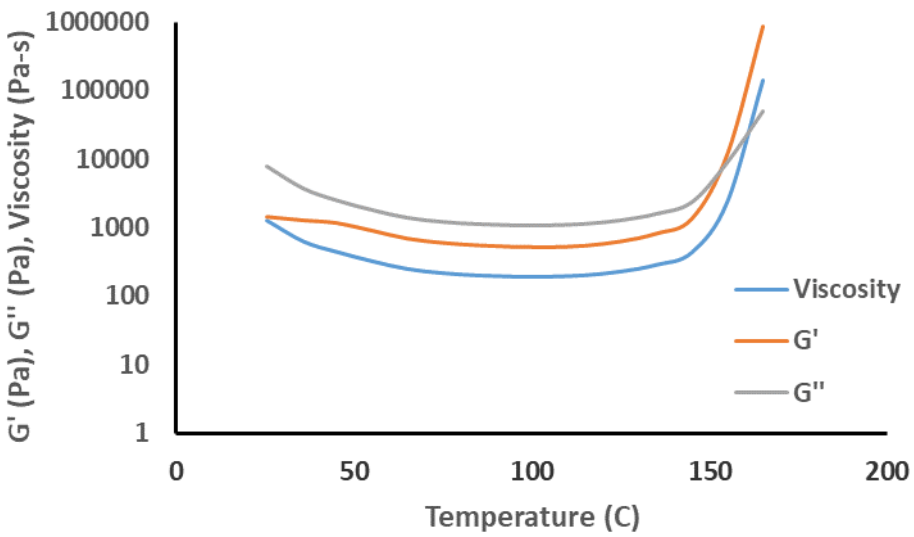

Figure A-14: Temperature sweep of the DGEBA/DETDA/15wt%FS/15wt%CF system.

Lastly, SNP was utilized in place of FS to determine its effect on controlling the flow behavior of DGEBA. The SNP used was the same amine terminated silane coated 50 nm colloidal silica provided by Cabot as described in Chapter 3. Surprisingly, the SNP did not have as essential of an effect on flow behavior as the FS did, with inclusions of 30 wt. % SNP still not reaching the zero shear viscosity as met by the 15 wt. % FS. The DGEBA/SNP samples did shear thin, but not at the rates favorable for the direct ink writing process. It is possible that the FS is contributing more to aggregation, which could be more effective in facilitating shear flow. It is concluded that a combination of FS and SNP will likely be most successful in both orienting the CF in a direct ink writing process, and further toughening the DETDA/DGEBA epoxy matrix. The viscosity profiles for the DGEBA/SNP samples are shown below in Figure A-15.

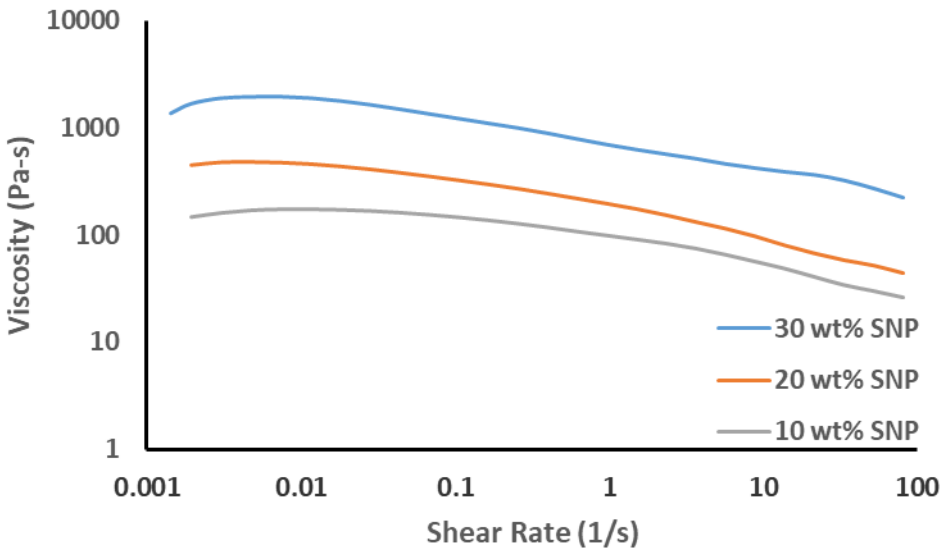

Figure A-15: Viscosity profiles of DGEBA/SNP with increasing SNP content.

References

[1]. Lewicki, J P., Rodriguez, J., Zhu, C., Worsley, M., Wu, A.S., Kanarska, Y., Horn, J.D., Duoss, E.B., Ortega, J.M., Elmer, W., Hensleigh, R., Fellini, R. and King, M. (2017). 3D-Printing of Meso-Structurally Ordered Carbon Fiber/Polymer Composites with Unprecedented Orthotropic Physical Properties. *Scientific Reports*, 7, 43401.

[2]. Lewis, J. A. (2006). Direct Ink Writing of 3D Functional Materials. *Advanced Functional Materials*, 16(17), 2193–2204.

[3]. Farahani, R. D., Dalir, H., Le Borgne, V., Gautier, L.A., El Khakani, M.A., Levesque, M. and Therriault, D. (2012). Direct-Write Fabrication of Freestanding Nanocomposite Strain Sensors. *Nanotechnology*, 23(8), 1-9.

VITA

Gabrielle Esposito was born on February 7th, 1992 in Athens, Georgia. She and her family moved between Georgia and Pennsylvania before settling in Louisville, Kentucky. She and her brother Mike wer raised by her parents Michael and Grace Esposito. Gabrielle enrolled at Georgia Institute of Technology in 2010. During her undergraduate studies, she participated in research under Ica Mana-Zloczower at Case Western University, beginning her interest in Polymer Science research. Gabrielle earned a Bachelor of Science in Polymer and Fiber Engineering in 2014, the same year she started her graduate studies under Professor Ray Pearson at Lehigh University. In April 2018, she was inducted into the P. C. Rossin Doctoral Fellows Program. Gabrielle's research has investigated a number of studies into the formulation, processing and performance of polymer nanocomposites, particularly epoxy and polyamide-11 based polymer nanocomposites. Both were the focus of her Ph. D dissertation which was completed in December 2019.

Research & Industry Experience

POLYMER NANOCOMPOSITES FOR SLS PRINTING 10/2017-8/2019

- Characterized a polyamide 11/carbon black (PA11/CB) printing based nanocomposite powder, using surface treated nanosilica as both a processing aid and toughening agent to produce high performance polymer nanocomposites.
- Utilized Differential Scanning Calorimetry (DSC), x-ray diffraction (XRD), small angle x-ray scattering (SAXS), matrix assisted laser desorption/ionization (MALDI), solution viscometry, tensile testing, compression testing, essential work of fracture, melt rheology, linear wear, Scanning Electron Microscopy (SEM) and Infrafred Spectroscopy (IR) for characterization.
- Funded through a Pennsylvania Infrastructure Technology Alliance (PITA) grant

DIRECT INK WRITING OF CARBON FIBER TOUGHENED EPOXY 7/2018-8/2019

- Developed and characterized a polymer nanocomposite for a direct ink writing based additive manufacturing process, diglycidyl ether of bisphenol-A (DGEBA) epoxy, short carbon fiber and surface treated nanosilica.
- Utilized DSC, shear and cure rheology, Light Optical Microscopy (LOM), SEM, and tensile testing.
- Funded through the Armament Research Development and Engineering Center (ARDEC).

ELÉ CORPORATION 9/2017-1/2019

- Tested provided potential toughening agents in diglycidyl ether of bisphenol-A (DGEBA) epoxy.
- Utilized K_{1c} linear fracture toughness (K_{1C}), double cantilever beam (DCB), and DSC testing.

EVONIK 5/2017-9/2017

- Evaluated fracture and fatigue performance of selected thermosetting polymers.
- Utilized four point bending, K_{1C}, and cyclic fatigue testing.

CABOT CORPORATION 9/2016-3/2017

- Synthesized epoxies with multiple grades of surface treated carbon black.
- Utilized DSC, K_{1C} testing.

REYNOLDS POLYMERS 12/2015-4/2017

- Evaluated phase separation, hazing and fracture toughness of PMMA blends.
- Utilized DCB testing, IR and SEM.

ARDEC GBIR FLEXIBLE CIRCUITS 7/2015-11/2015

- Studied polylactic acid (PLA) and polyhydroxyalkanoate (PHA) blends for use in flexible circuits.
- Dynamic mechanical analysis (DMA), DSC, fused deposition modeling based additive manufacturing, film extrusion and melt rheology.

BERRY PLASTICS 9/2015-11/2015

- Evaluated thermal transitions in various epoxy systems.
- Utilized DMA.

ELECTRO CHEMICAL 1/2015-1/2017

- Formulated an epoxy system for cyclic high temperature use in electrochemical tanks.
- Utilized DMA, DSC, IR, peel testing, rheology, SEM, tensile testing, Thermogravimetric Analysis (TGA) and Thermomechanical Analysis (TMA).

Awards

Recipient, Conrad Award, Lehigh University (May 2019)
Recipient, Rossin Doctoral Fellowship, Lehigh University (April 2018)
Recipient, Sperling Student Award, Lehigh University (May 2018)
Recipient, SPE Student Award, Lehigh University (February and November 2018)

Conference Presentations and Proceedings

Raymond Pearson, Gabrielle Esposito, Phacharapol Tanasarnsopaporn, and Yuanyuan Wang. "Processing behavior of polyamide nanocomposites for selective laser sintering." ABSTRACTS

OF PAPERS OF THE AMERICAN CHEMICAL SOCIETY. Vol. 256. WASHINGTON, DC, AMER CHEMICAL SOC, 2018.

Gabrielle Esposito and Ray Pearson, "Characterization and mechanical behavior of SLS processed PA-11/CB nanocomposites," SPE ANTEC, Orlando, 2018, pp. 1-5.

Gabrielle Esposito, Phacharapol Tanasarnsopaporn and Ray Pearson. "Mechanical behaviour and characterization of SLS processed PA-11 for PA-11/silica nanocomposites." DYFP, Rolduc, Netherlands, 2018. pp. 1-4

Israd H. Jaafar, Qi Li, Raymond A. Pearson, Gabby Esposito, Sabrina S. Jedlicka and John P. Coulter. Vibration assisted injection molding of poly(lactic acid) – thermal, spectroscopic and mechanical analysis of hydrolytic degradation." SPE ANTEC, Anaheim, 2017, pp. 1652-1661.